OPTIMISATION OF THE PERFORMANCE OF THIN FILM SOLAR CELLS

by

B. Gandham

Thesis submitted for the degree of Doctor of Philosophy of the Council for National Academic Awards

The research was carried out in the Department of Physics & Physical Electronics, Newcastle upon Tyne Polytechnic

October 1979

CONTENTS

ACKNOWLEDGEMENTS

I would first like to thank Mr. H. A. MacLeod (Reader, Department of Physics and Physical Electronics, Newcastle upon Tyne Polytechnic) for allowing me the opportunity and providing the idea for carrying out this research programme. I am grateful for his advice during the course of my research. I would also like to thank Dr. M. Bowden and Dr. R. Hill for supervising my work. My thanks are also due to the technicians and the secretarial staff of the Department for their assistance as and when it was needed.

ABSTRACT

OPTIMISATION OF THE PERFORMANCE OF THIN FILM SOLAR CELLS

BY B. GANDHAM

The thesis contains a short review of the theory of solar cells and optical properties of thin films. This is followed by the introduction of the "interference solar cell" which regards the cell as part of a multilayer structure and considers the effects of multiple reflections at each interface of the cell. Models for normal and oblique incidence of light are presented both in the presence of drift fields and in their absence.

This involves a complete novel approach resulting in the solution for the photogeneration rate as a function of position, computed by solving Maxwell's equations in a cell assumed to be composed of optically flat parallel layers. The photogenerated current is computed and the effects of varying the transport parameters and layer thicknesses are shown for Cu_2S-CdS Cds-InP and Cds-CuIn Se_2 cells with silver, zinc, and molybdenum substrates. It is shown that the optimum thickness of Cu_2S and $CuInSe_2$ is 0.1 µm- 0.2 µm whilst the optimum for InP is about 3 µm. Experimental evidence is presented to support an additional prediction that silver is superior to zinc or molybdenum substrates.

The effect of various antireflective coatings has been analysed theoretically and the conditions for maximum transmittance through a metal layer into an absorbing substrate have been derived. In order to compare theory with experiment, a small programme on Schottky barrier cells is described and comparisons made.

CHAPTER 1

INTRODUCTION AND BACKGROUND

1.1 Introduction

The search for alternative energy sources is being pursued with increasing vigour with the realisation of the fact that reserves of fuels have only a limited lifetime. Nuclear energy could go a long way towards satisfying the world's energy needs but there is concern over the dangers to the environment and the long term hazards associated with the disposal of nuclear waste. The sun, the wind and the waves are alternatives, that provide an essentially clean source of power and do not deplete the world's natural resources. This project is concerned with solar radiation as an energy source and in particular its direct conversion into electricity using solar cells. A solar cell is a photovoltaic device which converts sunlight directly into electrical power. There are a number of alternatives to solar cells, some of which are more economic at the moment, and so it is important to improve upon the cost per unit energy ratio in order to compete successfully. This project is directed towards that goal. Optical effects which can occur in thin film solar cells have until now been ignored in their design. In the course of this work an analysis has been carried out which takes into account these optical effects, using techniques similar to those used in the analysis of thin film multilayer devices. It will be shown that when optical interference is taken into account, the optimum thickness of the solar cell is smaller and the expected maximum current is larger than when these effects are ignored.

The thesis will present a brief review of photovoltaic devices and optical thin film multilayers, followed by theoretical analysis of the thin film 'interference solar cell'. This will include models for both normal and oblique incidence of light. Theoretical analysis

when electric fields are present and for when they are absent will be carried out. Computed results of this novel theory when applied to real thin film solar cells are presented and the effects on the efficiency of altering the various parameters will be examined. These include the very important part played by the substrate in thin film solar cells. This will be followed by theoretical analysis for antireflecting solar cells with the introduction of the concept of the potential transmittance, the inclusion of the 'effective complex refractive index' diagrams and the optimum index and thickness values for the antireflecting layers. A small experimental programme carried out on Schottky barrier cells carried out in order to compare the theory with experiment will also be presented. This will be followed by the concluding chapter.

1.2 Background

A semiconductor has the property that it can absorb a photon whose energy is greater than the band gap. During this process an electron is excited into the conduction band leaving behind a hole in the valence band. Energy conversion has taken place but in order to extract the energy of the electron it has to flow through an external circuit rather than let the energy be lost either through the emission of radiation or through its dissipation to the semiconductor lattice as the electron and hole recombine. This can be achieved by using a semiconductor rectifying device. The potential barrier present in such a device, which when used as a rectifier prevents the flow of current in one direction but in a solar cell it serves as the mechanism by which the electron and hole are separated. In general any rectifying structure, be it P-N homojunction, heterojunction or Schottky barrier diode, can be used in a solar cell.

It should be pointed out that one of the parameters that will

influence the choice of the semiconductor is its energy gap. For a given radiation there will exist an optimum value for the band gap, E_g, for which the integrated quantum efficiency over all wave-lengths is a maximum. For direct AMI radiation the calculated value for this is 1.5 eV (Loferski, 1956). Under diffuse, UK conditions the calculated value is 1.78 eV (Mallinson and Landsberg, 1977).

A. P-N Homojunction

A P-N homojunction is represented schematically below. It is operating at voltage V and current I into R, the load resistance.

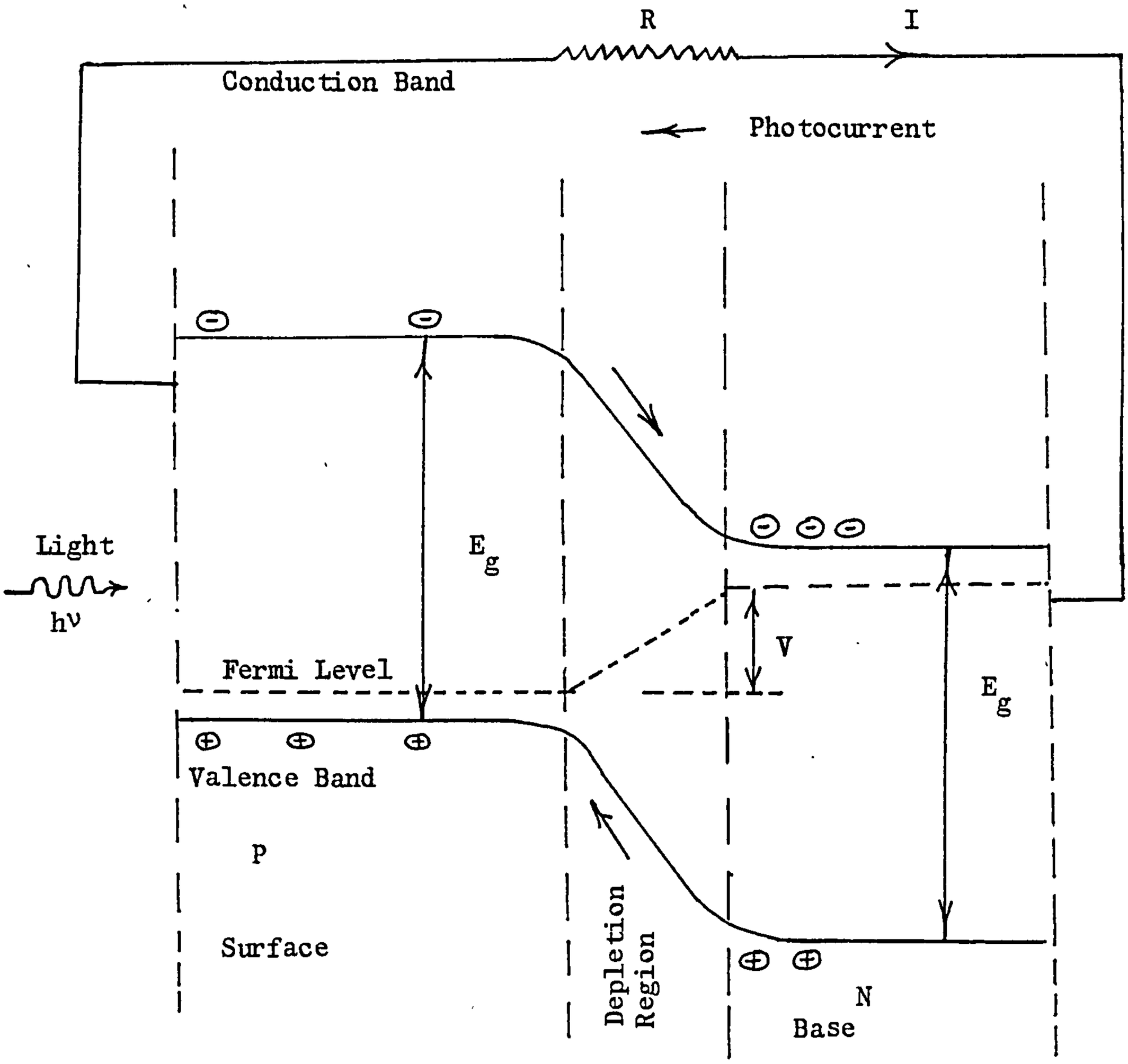

Figure 1.1

In the illustration above the device is illuminated from the P side and photons with energy greater than the band gap E_g, are absorbed throughout the material creating electron-hole pairs. On the P side of the device the minority carrier electrons move randomly as they are scattered by impurities, photons and other electrons. Any minority carrier electron reaching the junction is swept into the N type semiconductor by the large electric field present within the depletion region. This is accompanied by the transfer of an electron through the external circuit maintaining charge neutrality and in this way a photocurrent is generated. The electron could, of course, recombine with a hole in the valence band and a photogenerated electron only contributes to the total photocurrent if it reaches the junction within the lifetime of the recombination process.

If the device represented by the above diagram is maintained in an open circuit condition so that no current flows, then the transfer of charge across the junction continues until the electric field generated by the space charge prevents any further transport. Under these conditions the device exhibits the photovoltaic effect and generates its open circuit voltage V_{oc}. This is shown in the diagram below which contains the current-voltage curve for a cell operating into a load. Under short circuit conditions the current density J_{sc}, is the full photocurrent produced by the cell. The curve for the illuminated device is, to a good approximation (Rothwarf, 1978) the characteristic of a forward biased diode displaced into the fourth quadrant by an amount equal to the photocurrent. For open circuit conditions there is no flow of current and the photocurrent is equal in magnitude but opposite in sense to the dark current that the diode would pass under a forward bias of V_{oc}.

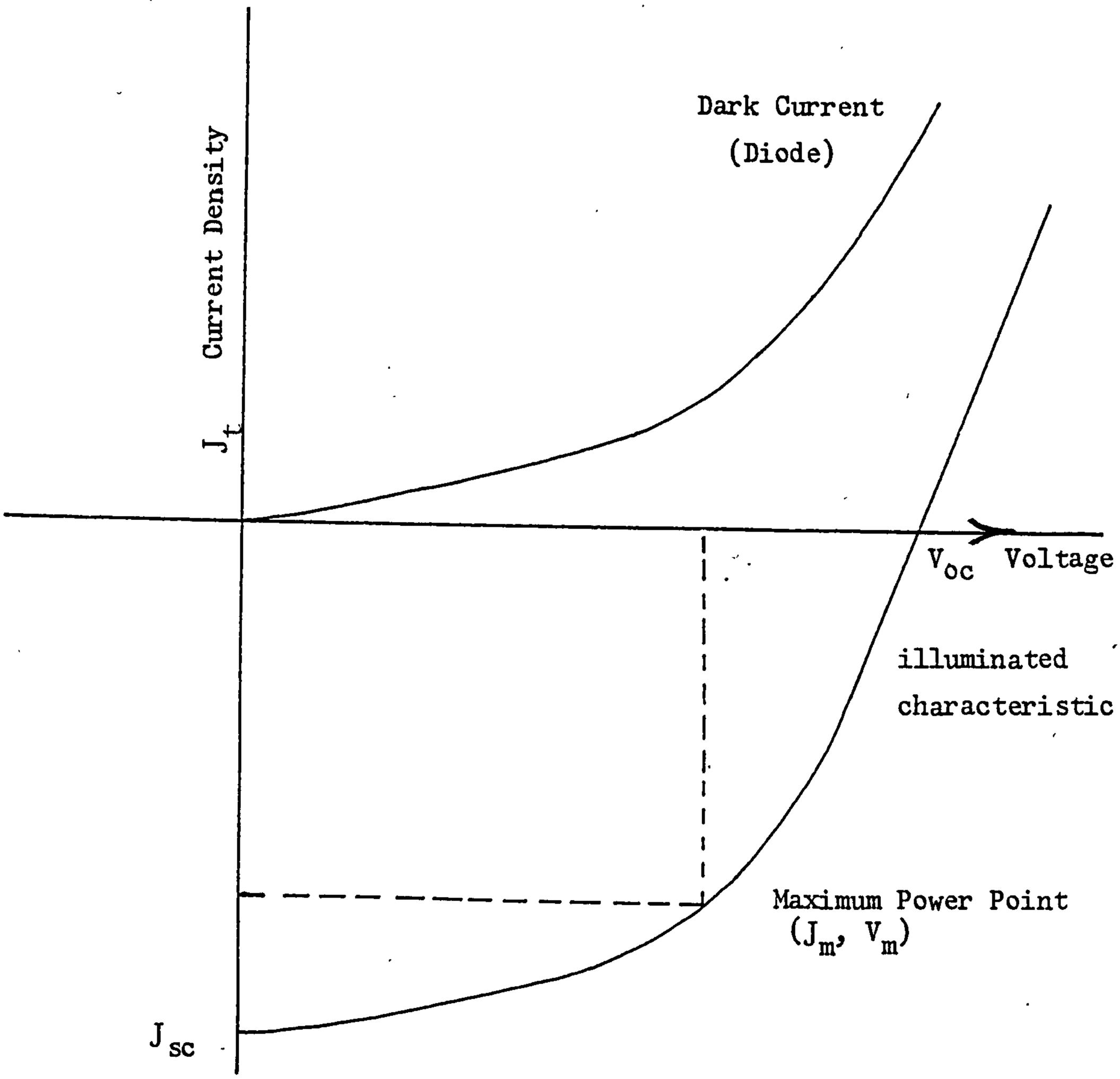

Figure 1.2 Current - Voltage characteristics for a solar cell

The power conversion efficiency ξ of a solar cell is defined as

$$\xi = \frac{V_{oc} \cdot J_{sc} \cdot FF}{P_{in}} \qquad \text{- - -} \quad 1.1$$

Where P_{in} is the power density illuminating the cell, the parameter FF, referred to as the fill-factor, is a measure of the degree of 'squareness' of the current-voltage curve, and relates the maximum

power which a cell can deliver to the short circuit current and the open circuit voltage. The fill-factor is given by

$$FF = J_m \cdot V_m / J_{sc} \cdot V_{oc}$$

The current density J_t is given by the expression

$$J_t = J_d - J_e \qquad \text{---} \quad 1.2$$

Where J_e is the photocurrent generated by the cell and J_d is the diode current of the cell when in the dark.

In a P-N homojunction there are three main dark current mechanisms, namely, injection, space-charge recombination and tunnelling.

The injected current component consists of electrons injected from the N-type region over the potential barrier at the junction into the P-type region. These excess minority carriers then diffuse and drift away from the junction and eventually recombine either at a surface or in the bulk. There is also a similar injected current of holes injected from the P-type region over the junction into the N-type region.

During the process of injection some of the carriers recombine inside the depletion region because of the impurity levels within the energy gap, resulting in an increase in the dark current through the device. This 'recombination current' was first discussed by Sah et al (1957) but their treatment has since been extended by a number of workers.

Tunnelling in a P-N homojunction is usually negligible unless the junction is highly doped. Tunnelling can occur when an empty state is separated by a short distance and a relatively small barrier from a filled electron state.

B. Schottky Barrier

From the point of view of the photocurrent the Schottky barrier can be thought of as a P–N homojunction with a zero junction depth (top layer) but having an attenuating metal coating at the front instead.

The standard expression for the dark current in the Schottky barrier is

$$J(\text{dark}) = A^* T^2 \exp(-e \Phi_B/AkT) \quad (\exp(eV/AkT)-1) \qquad - - - 1.3$$

Where A* is the effective Richardson constant and Φ_B is the barrier height, approximately equal to the difference between the metal work function and the electron affinity of the semiconductor. A is the diode factor.

This current is mostly due to thermionic emission from the semiconductor to the metal and it is a majority carrier current, whereas in the case of the P–N homojunction, the dark current is a minority carrier current. The tunnelling mechanisms do not come into effect until the doping concentration reaches about 10^{17} cm^{-3} (Sze,1969). Above this doping level the dark current rises very rapidly with doping. Below this doping level the dark current remains approximately constant although some slight variations may arise due to changes in the image potential with doping. The effect of the image potential is to lower the barrier height value (Milnes and Feucht, 1972). The latest account of the theory of the Schottky barrier solar cell can be found in Landsberg and Klimpke (1977).

C. P–N Heterojunction

The difference between a P–N heterojunction and a homojunction is that the band gaps on either side of the junction are not equal.

This is due to the top and base layers being composed of different semiconducting materials. There are now complications as a result of the presence of interface states and defects due to lattice mismatches. Recombination of the minority carriers may occur in and around the depletion regions because of interface states. Good heterojunctions need good thermal expansion match and small energy discontinuities ΔE_C and ΔE_V (figure 1.3), arising from the energy gap and electron affinity differences of the two semiconductors, in addition to a good lattice match. ΔE_C and ΔE_V impede the flow of minority carriers across the junction.

D. P-N heterojunction energy band diagram

Photons of energy less than E_{g1} but greater than E_{g2} will pass through the first material which acts as a 'window' and be absorbed by the second material. The collection of minority carriers occurs in the same way as in the homojunction. The heterojunction can nevertheless have an advantage over the homojunction in the short wavelength response, particularly when E_{g1} is large, as then the photons of high energy can be absorbed in the depletion region of the second material. The dark current mechanisms are somewhat more complex than in the homojunction case. Various different models exist (e.g. Milnes and Feucht, 1972) that attempt to explain the experimental behaviour. Tunnelling has been shown to be the most dominant in nearly all heterojunctions except in the cases where the lattice mismatch is very small.

Tunnelling varies weakly with temperature in contrast to the injected and the space charge recombination currents which vary rapidly with temperature. Different types of tunnelling current may exist. For instance, there is the tunnelling recombination model where tunnelling via empty states is followed by recombination. A series of

such steps may occur. This is the "temperature independent" tunnelling model. Tunnelling may also occur part of the way up the barrier. These tunnelling currents have a temperature dependence but this is not as strong as the thermal currents (injected and the space charge recombination). The thermal currents have now also to include the effects of ΔE_C and ΔE_V discontinuities as well as the interface states. All these different possibilities make it very difficult to predict the exact nature of the dark currents for a particular heterojunction.

For a good solar cell the dark currents must be as small as possible.

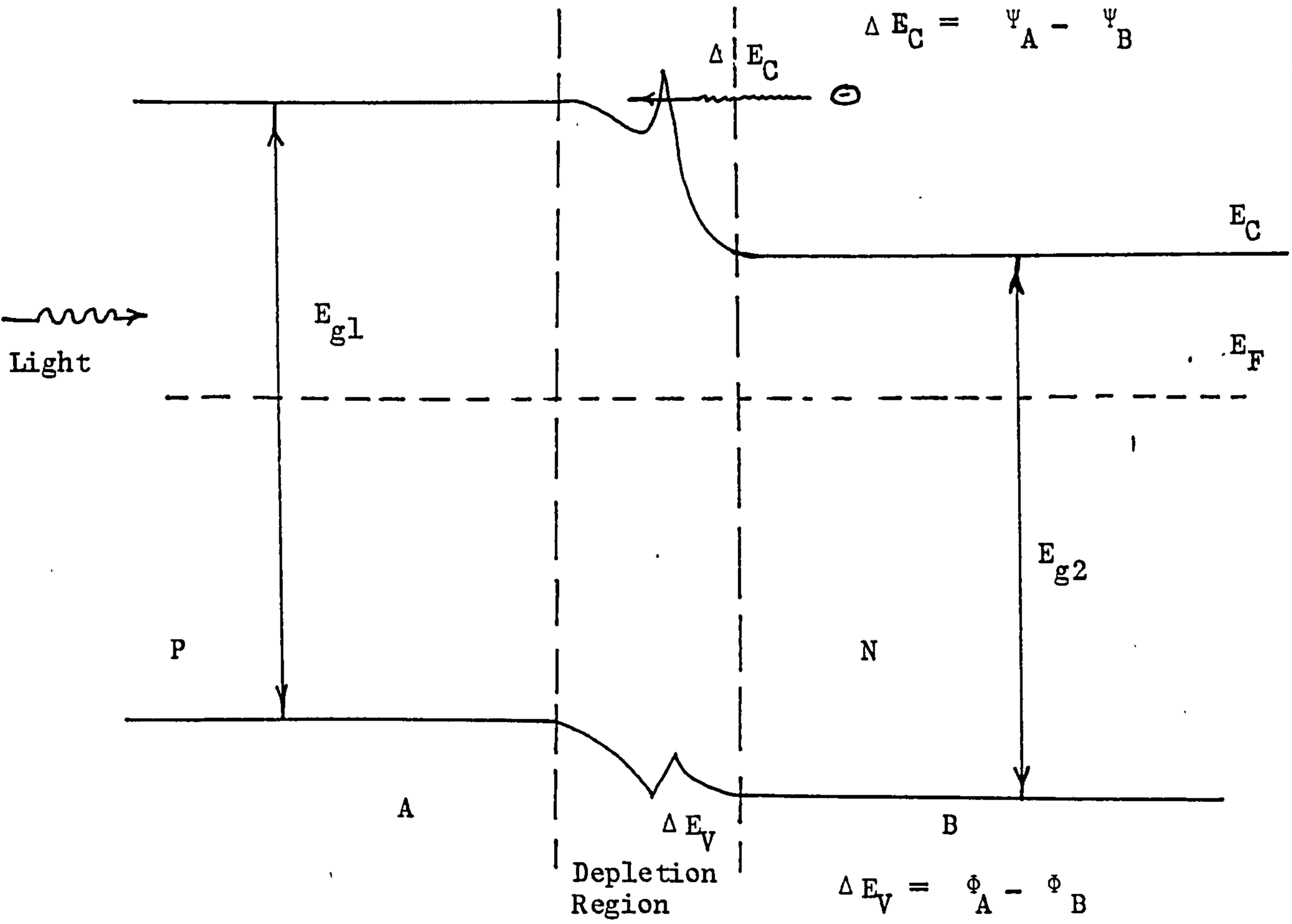

$E_{g1} > E_{g2}$

Ψ is the electron affinity

Φ is the photoelectric threshold

Figure 1.3

CHAPTER 2

THEORETICAL BACKGROUND

2.1 Introduction

The magnitude of the photocurrent obtained from the mechanism outlined in Chapter One can be determined by studying the behaviour of the minority carriers which are electrons in the P-type and holes in the N-type material. Diffusion theory is applicable for describing their motion and under steady state conditions a constant current of electrons to the right and holes to the left is established in a P-N junction solar cell, be it homojunction or heterojunction. The formulation and solution of this problem has been discussed by many workers including Cummerow (1954), Prince (1955), Lofersky and Wysocki (1961), Moss (1961), Dale and Smith (1961), Wolf (1960, 1963), Ellis and Moss (1970), Landsberg (1975), Rothwarf and Boer (1975), Hovel (1975), Mallinson and Landsberg (1977) and Rothwarf (1978).

2.2 Derivation of the Photocurrent in P-N junction devices for Monochromatic light

The one dimensional continuity equations that govern the minority carriers when the light is shining on the junction are

$$\frac{\partial N_p}{\partial t} = \frac{1}{q}\frac{dJ_n}{dx} - (N_p - N_{po})/\tau_n + g \qquad \text{- - - 2.1a}$$

$= 0$ in a steady state (for electrons on the P side)

and

$$\frac{\partial P_n}{\partial t} = -\frac{1}{q}\frac{dJ_p}{dx} - (P_n - P_{no})/\tau_p + g \qquad \text{- - - 2.1b}$$

$= 0$ in a steady state (for holes on the N side).

(g is the rate of generalisation of electron hole pairs)

P_n and N_p are the photogenerated minority carrier densities, q is the charge on the minority carrier, P_{no} and N_{po} are the minority carrier densities in equilibrium in the dark, T_p and T_n are the life times of the minority carriers and J_n, J_p are the electron and the hole currents respectively.

These currents are defined as

$$J_n = q\ \mu_n N_p E_p + q D_n \frac{dN_p}{dx} \qquad --- 2.2a$$

and

$$J_p = q\ \mu_p P_n E_n - q D_p \frac{dP_n}{dx} \qquad --- 2.2b$$

where E_p and E_n are the electric fields in the P-type and N-type regions respectively, D_n and D_p are the diffusion constants of the minority carriers and μ_n, μ_p are their mobilities.

Under steady state conditions substitution of 2.2 into 2.1 results in

$$D_n \frac{d^2N_p}{dx^2} + \mu_n E_p \frac{dN_p}{dx} + \mu_n N_p \frac{dE_p}{dx} - \frac{(N_p - N_{po})}{T_p} + g = 0 \qquad --- 2.3a$$

and

$$D_p \frac{d^2P_n}{dx^2} - \mu_p E_n \frac{dP_n}{dx} - \mu_p P_n \frac{dE_n}{dx} - \frac{(P_n - P_{no})}{T_n} + g = 0 \ . \qquad --- 2.3b$$

The first term in equations 2.3 represent the diffusion of minority carriers whilst the second term represents transport due mainly to an external applied electric field. The third term describes transport under the influence of the photogenerated internal electric field or Dember field which is the result of the different mobilities of electrons and holes. The fifth term is the rate of generation of electron hole pairs, whilst the fourth term describes the bulk recombination rate of the photogenerated pairs (Hill, 1978).

By making the assumption that the mobilities and lifetimes are independent of position within the solar cell, equations 2.3 can be solved analytically subject to the following boundary conditions (figure 2.1).

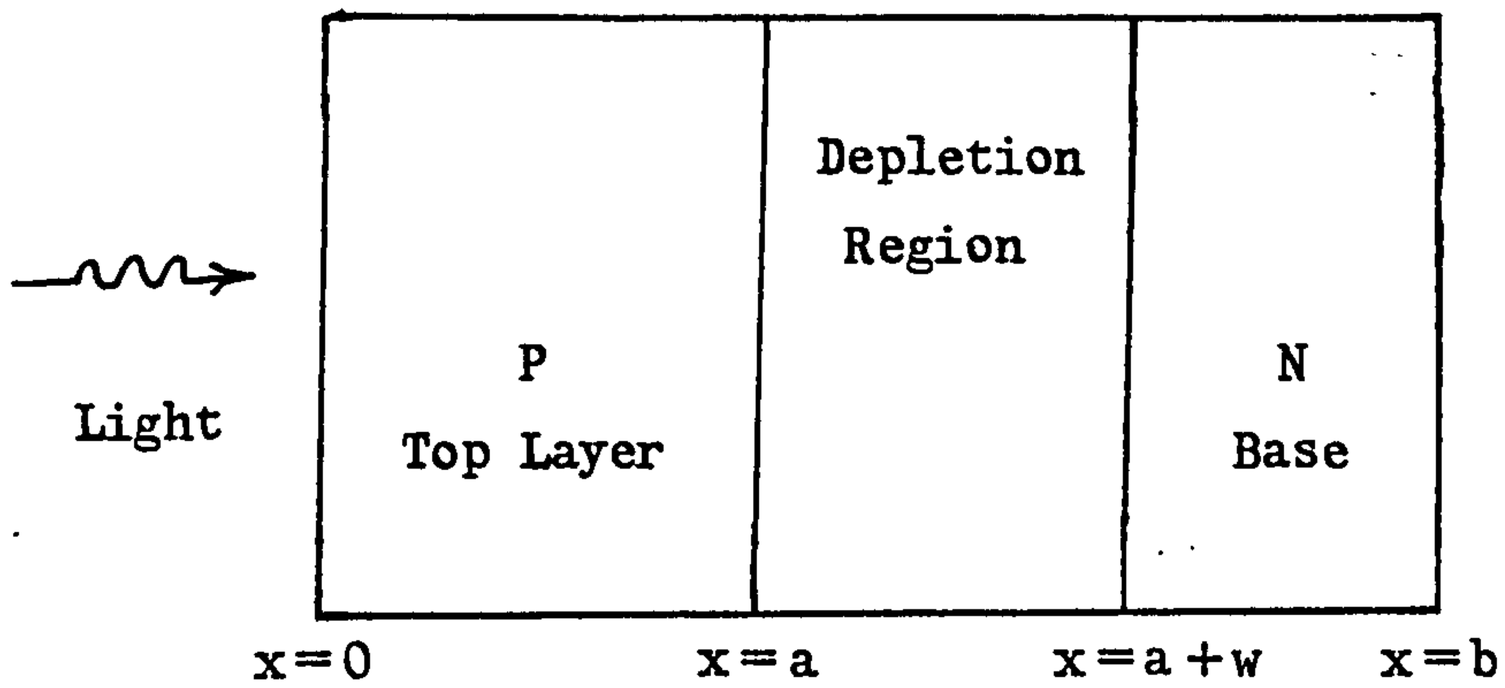

Figure 2.1

1. At the front surface, x=0, recombination occurs

$$(\frac{1}{q})\ J_n = S_n\ (N_p - N_{po})$$

where S_n is the surface recombination velocity at the front surface. It is the rate at which the generated carriers are lost at the surface. These are due to the presence of surface states which arise from "dangling bonds", chemical residues, metal precipitates, oxides and so on.

2. At the junction edge at the front at x=a,

$$N_p - N_{po} = 0\ .$$

This is the zero bias condition. The electrons which arrive at x=a are swept across the junction by the junction field and the excess electron density is taken to be zero.

3. Similarly for the junction edge facing the base layer

$$(P_n - P_{no}) = 0 \text{ at } x=(a+w)\ .$$

4. At the back surface recombination also occurs and

$$(\frac{1}{q})\ J_p = S_p\ (P_n - P_{no}),\ \text{at } x=b$$

where S_p is the surface recombination velocity at the back surface of the cell.

The current generated is then given by the sum of the currents collected in the P-layer, the N-layer and the depletion region.

This can be written as:

$$J_l = J_e + J_h + J_d$$

where

$$J_e = q\, D_n \frac{d(N_p - N_{po})}{dx} \quad \text{at } x = a \text{ (electron current)}$$

and

$$J_h = -\, q\, D_p \frac{d(P_n - P_{no})}{dx} \quad \text{at } x = (a+w) \text{ (hole current)}.$$

J_d is the current collected inside the depletion region and is equal to the product of number of photons absorbed within it and the charge q on the carrier. The electric field inside the depletion layer is assumed to be sufficiently high to accelerate out of it any photo-generated carriers before they could recombine.

When light of intensity I_o is incident on a semiconductor of absorption coefficient α, the intensity as a function of the distance x below the surface of the conductor is given by

$$I = I_o\, e^{-\alpha x} \quad \text{(Lambert's law)}$$

where α is a function of wavelength.

Differentiating I with respect to x we get

$$\frac{dI}{dx} = -\, \alpha\, I_o\, e^{-\alpha x} .$$

This is the absorption rate for the light at x.

It follows then that the magnitude of the generation rate of electron hole-pairs as a function of x is given by

$$g = \alpha\, N_o\, e^{-\alpha x} \qquad \text{- - - 2.4}$$

here N_o is the incident number of photon per unit area per sec at wavelength λ per unit band width on the surface of the semiconductor.

By letting $n = N_p - N_{po}$ and $p = P_n - P_{no}$, then equation 2.3 in the case when E_n and E_p are equal to zero can be rewritten as

$$D_n \frac{d^2n}{dx^2} - \frac{n}{T_n} + g = 0 \qquad \text{- - - 2.5a}$$

and

$$Dp \frac{d^2p}{dx^2} - \frac{p}{T_p} + g = 0 \qquad \text{- - - 2.5b}$$

where

$g = \alpha_n N_o e^{-\alpha_n x}$ for electrons on P-side

and

$g = \alpha_p N_o e^{-\alpha_p x}$ for holes on N-side .

(α_n and α_p are the respective absorption coefficients)

The general solution to equation 2.5a is

$$n(x) = C_1 e^{x/Ln} + C_2 e^{-x/L_n} - \frac{\alpha_n N_o e^{-\alpha_n x}}{D_n(\alpha_n^2 - 1/L_n^2)} \qquad \text{- - - 2.6}$$

for $\alpha_n \neq \frac{1}{L_n}$

where C_1 and C_2 are constants to be determined from the boundary conditions on page 12 with reference to figure 2.1.

$$\frac{dn}{dx} = \frac{C_1}{L_n} e^{x/L_n} - \frac{C_2}{L_n} e^{-x/L_n} + \frac{\alpha_n 2 N_o e^{-\alpha_n x}}{D_n(\alpha_n^2 - 1/L_n^2)}$$

$$n(0) = C_1 + C_2 - \frac{\alpha_n N_o}{D_n(\alpha_n^2 - 1/L_n^2)}$$

$$n(a) = C_1 e^{a/L_n} + C_2 e^{-a/L_n} - \frac{\alpha_n N_o e^{-\alpha_n a}}{D_n(\alpha_n^2 - 1/L_n^2)}$$

$$\left.\frac{dn}{dx}\right|_{x=o} = \frac{C_1}{L_n} - \frac{C_2}{L_n} + \frac{\alpha_n^2 N_o}{D_n (\alpha_n^2 - 1/L_n^2)}$$

$$\left.\frac{dn}{dx}\right|_{x=a} = \frac{C_1 e^{a/L_n}}{L_n} - \frac{C_2 e^{-a/L_n}}{L_n} + \frac{\alpha_n^2 N_o e^{-\alpha_n a}}{D_n (\alpha_n^2 - 1/L_n^2)}$$

From the boundary condition 2 on page 12

$$n(a) = 0 \ .$$

From the boundary condition 1 on page 12

$$S_n n(0) = D_n \frac{dn}{dx} \ .$$

From which

$$C_1 = \frac{-C_2 e^{-a/L_n}}{e^{a/L_n}} + \frac{\alpha_n N_o e^{-\alpha_n a}}{D_n (\alpha_n^2 - 1/L_n^2) e^{a/L_n}}$$

and

$$C_2 = \frac{\alpha_n N_o L_n (D_n \alpha_n + S_n) e^{a/L_n} - \alpha_n N_o e^{-\alpha_n a} (S_n L_n - D_n)}{D_n (\alpha_n^2 - 1/L_n^2)((D_n + S_n L_n) e^{a/L_n} - (S_n L_n - D_n) e^{-a/L_n})} \ .$$

Then the electron current J_e (page 13) is given by

$$J_e = q D_n \left.\frac{dn}{dx}\right|_{x=a}$$

$$= q D_n \left\{ \frac{C_1 e^{a/L_n}}{L_n} - \frac{C_2 e^{-a/L_n}}{L_n} + \frac{\alpha_n^2 N_o e^{-\alpha_n a}}{D_n (\alpha_n^2 - 1/L_n^2)} \right\}$$

$$= q D_n \left\{ \frac{-2 C_2}{L_n} + \frac{\alpha_n . N_o e^{-\alpha_n a}}{D_n (\alpha_n - 1/L_n)} \right\}. \qquad --- 2.7$$

The hole current J_h (page 13) is calculated in the same way as the electron current but with the application of the boundary conditions 3 and 4 to equation 2.6, with p substituted for n everywhere.

The hole current is then given by

$$J_h = q\, D_p \left.\frac{dp}{dx}\right|_{x=(a+w)}$$

$$= -\, q\, D_p \left\{ -\frac{2\, C_2}{L_p}\, e^{-(a+w)/L_p} + \frac{\alpha_p N_o\, e^{-\alpha_p(a+w)}}{D_p\,(\alpha_p - 1/L_p)} \right\}$$

$$\text{for} \quad \alpha_p \neq 1/L_p$$

where C_2 now is given by

$$C_2 = \frac{\alpha_p N_o L_p (D_p \alpha_p + S_p) e^{-\alpha_p b}\, e^{(a+w)/L_p} - \alpha_n N_o e^{-\alpha_p(a+w)} (S_p L_p - D_p) e^{b/L_p}}{D_p(\alpha_p^2 - 1/L_p^2)((D_p + S_p L_p)\cdot f^* - (S_p L_p - D_p) e^{b/L_p}\, e^{-(a+w)/L_p})}$$

In the case when $\alpha_n = 1/L_n$ and $\alpha_p = 1/L_p$ the general solution to 2.5a is

$$n(x) = C_1\, e^{x/L_n} + C_2\, e^{-x/L_n} + \frac{N_o\, e^{-\alpha_n x}\, x}{2D_n}$$

The electron and hole currents are then calculated as in the case when $\alpha_n \neq 1/L_n$.

Electric fields E_n and E_p can be introduced outside the depletion region in order to assist the minority carriers to reach the junction and thereby overcome some of the losses from both the surface and bulk

*$f = \exp((a+w)/L_p)$

recombination. They can be introduced by forming non-constant doping profiles (see page 53). E_n and E_p may also include the 'Dember field' due to the different rates of diffusion for the holes and electrons. This may or may not be significant depending upon the material in question.

Ellis and Moss (Ellis and Moss, 1970), Landsberg (Landsberg, 1975) and others have derived expressions for the light generated current in the case for constant electric fields E_n and E_p using similar analyses to the above. The expression 2.4 was used for the generation rate g.

In the case of Schottky barrier cells, the expressions for the photogenerated current outside of the depletion region are similar to those for P-N junction cells.

2.3 Dark currents in P-N junctions

This section digresses from the main theme of the thesis in presenting a rather brief review of the dark current mechanisms mentioned in Chapter One.

For a P-N homojunction assuming uniform doping profiles and that all donors and acceptors are ionised, the forward dark injected current is

$$J_{\substack{\text{dark}\\\text{injection}}} = J_o \left(e^{eV/kT} - 1\right) \qquad \text{- - - 2.8}$$

where

$$J_o = eN_i^2 \left\{ \left\{ \frac{L_p}{T_p N_d} \left\{ \frac{S_p T_p}{L_p} \cosh\left(\frac{X_n}{L_p}\right) + \sinh\left(\frac{X_n}{L_p}\right) \right\} \right/ \left\{ \frac{S_p T_p}{L_p} \sinh\left(\frac{X_n}{L_p}\right) + \cosh\left(\frac{X_n}{L_p}\right) \right\} \right\}$$

$$+ \left\{ \frac{L_n}{T_n N_a} \cdot \frac{\frac{S_n T_n}{L_n} \cosh\left(\frac{X_p}{L_n}\right) + \sinh\left(\frac{X_p}{L_n}\right)}{\frac{S_n T_n}{L_n} \sinh\left(\frac{X_p}{L_n}\right) + \cosh\left(\frac{X_p}{L_n}\right)} \right\} \cdot \qquad \text{- - - 2.9}$$

X_n and X_p are the thickness of N and P layers outside of the depletion layer. N_a and N_d are the acceptor and donor concentrations in P and N regions respectively and N_i is the intrinsic carrier concentration. Equation 2.8 is found in standard textbooks on semiconductors (e.g. Sze, 1969). Equations 2.8 and 2.9 are derived from the continuity equations 2.1 and 2.2 subject to the boundary conditions that

$$(\tfrac{1}{q})\ J_n = S_n\ (N_p - N_{po}) \quad \text{at the front surface,}$$

$$N_p - N_{po} = N_{po}\ (e^{eV/kT} - 1) \quad \text{at the junction edge with the P layer,}$$

$$P_n - P_{no} = P_{no}\ (e^{eV/kT} - 1) \quad \text{at the junction edge with the base N layer,}$$

and $$(\tfrac{1}{q})\ J_p = S_p\ (P_n - P_{no}) \quad \text{at the junction between the back contact and the base layer.}$$

V is the potential drop across the junction.

An expression for J_o with constant built-in electric fields E_n and E_p can be found in Ellis and Moss (Ellis and Moss, 1970).

When the base region is highly doped near the back surface contact, the dark current can be reduced due to an effective reduction in the back surface recombination velocity at this contact. The expression for J_o has been shown to be similar to 2.9 except that S_p in the N-type base region is replaced by an effective surface recombination velocity given by

$$S_e = \frac{N_d D_p^+}{N_d^+ L_p^+} \left\{ \left(\frac{S_p L_p}{D_p^+}\right) \cosh\left(\frac{X_n^+}{L_p^+}\right) + \sinh\left(\frac{X_n}{L_p^+}\right) \right\}$$

$$/\left(\cosh\left(\frac{X_p^+}{L_p^+}\right) + \frac{S_p L_p^+}{D_p} \sinh\left(\frac{X_n^+}{L_p^+}\right)\right) \qquad \text{- - - 2.10}$$

where the asterisked parameters refer to the highly doped region (Godlewski et al, 1973). Expressions for the dark recombination currents can be found in Sah (Sah et al, 1957 and Choo, 1968) where

$$J_d = \frac{2N_{iW}}{(T_{po}\,T_{no})^{\frac{1}{2}}} \cdot \frac{\sinh(\frac{eV}{2kT})}{(V_d - V)/kT} \cdot f(b) \quad - - - 2.11$$

$V_d = \frac{kT}{e} \ln(\frac{N_a N_d}{N_i^2})$ where V_d is the theoretically maximum photovoltage possible, otherwise known as the built in voltage, w is the thickness of depletion layer and T_p and T_n are minority carrier lifetimes on the N and P sides of the junction ; f(b) is a complicated expression of bias, trapping levels, dopant concentrations and carrier lifetime. Sah (Sah et al, 1957) considered the case of a symmetrical P–N homo-junction with recombination centres in the centre of the energy gap having approximately equal capture cross-sections for electrons and holes. Evans and Landsberg (Evans and Landsberg, 1963) extended their treatment to include Auger recombination. Choo (Choo, 1968) considered the general case of non-symmetrical junctions with recombination centres away from the centre of the energy gap and with non-equal capture cross sections.

The first model for P–N heterojunction was proposed by Anderson (Anderson, 1962) using a method similar to that used to derive the injection current of an ideal P–N junction. He derived an expression for the forward current density. His model ignores the effects of re-combination and tunnelling due to interface states.

Dolega (Dolega, 1963) proposed a model of a heterojunction formed between semiconductors having different crystal lattices and in which fast recombination occurs at the interface, of electrons and holes which reach the recombination centres by thermal activation. Dolega's expression for the forward dark current as given by Van Opdorp

(Van Opdorp, 1969) is

$$J_d = B \exp\left(\frac{-eV_d}{kT}\right)\left\{\exp\left(\frac{eV}{AkT}\right) - 1\right\} \quad \text{- - - 2.12}$$

B is a weak function of temperature and the value of A depends on the ratio of the density of defects in the two materials, but in fact A always lies between 1 and 2.

An expression for the tunnelling current derived by Newman (Newman, 1965) is

$$J_d = J_{so} \exp\left(\frac{T}{T_o}\right) \exp\left(\frac{V}{V_o}\right) \quad \text{- - - 2.13}$$

where the electrons tunnel through the spike ΔE_C (Chapter 1.2C) to the conduction band of the P-type material, where they subsequently recombine either close to the interface or after thermal excitation out of the depletion region. J_{so}, T_o and V_o are constants. Equation 2.13 describes the I-V characteristics of some heterojunctions reasonably well but in the majority of cases the current seems to be a mixture of both tunnelling and recombination.

The model containing both the latter mechanisms has been proposed by Riben and Feucht (Riben and Feucht, 1966) assuming a single step tunnelling process and a linear barrier. Their expression is not however in good agreement with experiment (Sharma and Purohit, 1974).

A multi-step tunnelling process gives an expression for the dark current which is in better agreement with experiment (Riben and Feucht, 1966) (Martinuzzi and Mallen, 1973).

2.4 Equivalent Circuit Analysis

The figure below shows an equivalent circuit diagram for a solar cell and includes both the series and shunt resistances.

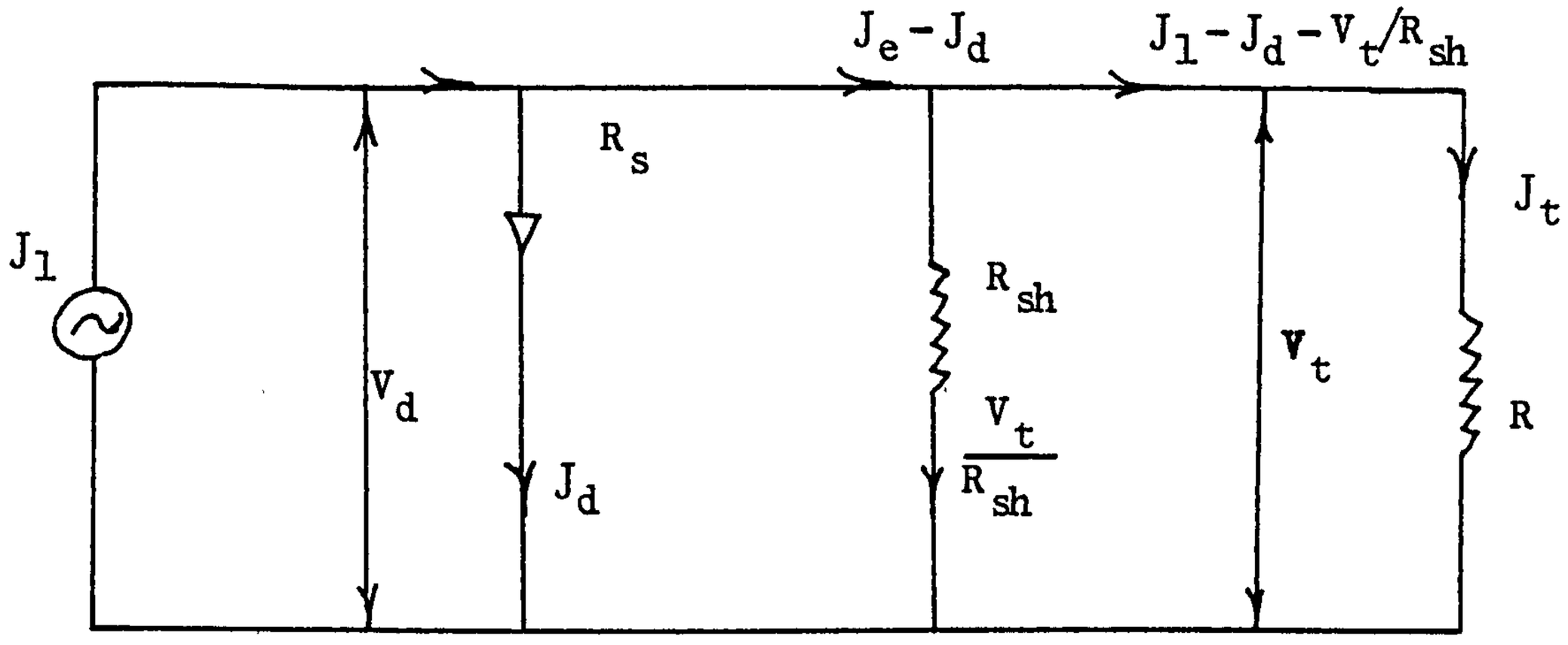

The series resistance R_s is due to the sheet resistance of the top layer combined with the bulk resistance of the base layer. The shunt resistance is due to leakage currents (Hill, 1978).

From Kirchoff's Law

$$J_t = J_l - J_d - \frac{V_t}{R_{sh}} .$$

Representing the forward diode current J_d by

$$J_d = J_o \left(\exp \left(\frac{eV_d}{AkT}\right) - 1\right).$$

The voltage V_d across the diode is greater than the terminal voltage V_t since

$$V_d = V_t + J_s R_s + \frac{R_s}{R_{sh}} V_t .$$

$$\text{Thus } / J_t / = J_o \left(\exp \frac{e}{AkT} \left(V_t + J_s R_s + \frac{R_s}{R_{sh}} V_t\right) - 1\right) + \frac{V_t}{R_{sh}} - J_l \text{ - - - 2.14}$$

Under short circuit conditions the shunt has no effect since the terminal voltage $V_t = 0$, and the short circuit current, J_{sc}, is given by the root of the equation

$$J_{sc} \quad R_s = \frac{AkT}{e} \ln\left(1 + \frac{J_l - J_{sc}}{J_o}\right). \qquad \text{- - - 2.15}$$

It can be seen that short circuit current is reduced by the series resistance but is unaffected by the shunt resistance. When the terminal current is zero, the open circuit voltage V_{oc} is given by the root of the equation

$$V_{oc} = \frac{AkT}{e} \left(R_{sh}/(R_s + R_{sh})\right) \ln \left(\frac{1}{J_o}\left(\frac{J_l}{J_o} - \frac{V_{oc}}{R_{sh}}\right) + 1\right) \text{- - - 2.16}$$

The open circuit voltage is little affected by the series resistance since $R_{sh} \gg R_s$ but is reduced when the shunt resistance values approach V_{oc}/J_l. For zero resistance 2.15 reduces to $J_{sc} = J_l$ and for infinite shunt resistance 2.16 reduces to

$$V_{oc} = \frac{AkT}{e} \ln\left(J_l/J_o + 1\right).$$

The shunt and series resistance also affect the shape of the I-V characteristics. Differentiating equation 2.14 with respect to V_t and assuming J_l does not vary with V_t

$$\frac{dJ_t}{dV_t} = \frac{e}{AkT} \cdot J_d - \left(\left(1 + R_s/R_{sh}\right) - \frac{dJ_s}{dV_t} R_s\right) + \frac{1}{R_{sh}} \cdot \qquad \text{- - - 2.17}$$

In short circuit condition $J_d \approx 0$, and

$$\left.\frac{dJ_t}{dV_t}\right|_{V_t = 0} = \frac{1}{R_{sh}} . \qquad \text{- - - 2.18}$$

Rewriting equation 2.17 and putting $J_s = J_t$ (assuming infinite shunt resistance)

$$dJ_t \left(AkT + eJ_d R_s\right) = eJ_d \, dV_t$$

$$\frac{dJ_t}{dV_t} = \frac{1}{\frac{AkT}{e.J_d} + R_s} . \qquad \text{- - - 2.19}$$

Under open circuit conditions

$$\left|\frac{AkT}{e.J_d}\right| << 1$$

therefore

$$\frac{dJ_t}{dV_t} \simeq \frac{1}{R_s} . \qquad \text{- - - 2.20}$$

From equations 2.19 and 2.20 respectively, estimates of the series and shunt resistances could be made directly from the I–V characteristic under illumination. No output power is obtained when the solar cell is operating under short circuit conditions or open circuit conditions. Maximum power point on the I–V curve is illustrated in figure 1.2 on page 5. J_m and V_m are the current and voltage values respectively at that point. The values J_m and V_m can be found by optimising the power with respect to the load resistance R.

The optimum value for J_m is given by the root of the equation

$$\frac{AkT}{e} \ln\left(1+\frac{J_l}{J_o}+\frac{J_m}{J_o}\left(1+\frac{R}{R_{sh}}\right)\right) + J_m\left(R_s+R\left(1+R_s/R_{sh}\right)\right) = 0$$

(Mallinson and Landsberg, 1977)

where

$$R = \frac{\frac{R_s}{1+\frac{R_s}{R_{sh}}}}{} - \frac{1}{2J_m}\left\{R_{sh}(J_l + J_o + J_m) + \frac{AkT/e + J_m R_s}{1 + R_s/R_{sh}}\right\}$$

$$x\left\{1 - \left\{1 + \frac{4J_m R_{sh} AkT/e}{\left\{(J_l + J_o + J_m)(R_s + R_{sh}) + J_m R_s + AkT/e\right\}^2}\right\}^{\frac{1}{2}}\right\}.$$

V_m can be evaluated using ohms law, $\therefore$ ($V_m = J_m R$).

The efficiency of the cell can therefore be found from the relation

$$P_{max}/P_{incident} = J_m V_m / P_{incident} = J_m^2 R / P_{incident} .$$

In equation 2.14 it is assumed that the photogenerated current J_l is independent of V_d, the voltage drop across the junction. Rothwarf (Rothwarf, 1978) points out that this condition is not valid under all conditions but only when the mobility, the field in the space charge region and the diffusion constant are independent of carrier concentration. He therefore points out that equation 2.14 should more generally be replaced by

$$J_t(V_d) = J_d(V_d) - J_l(V) - \frac{V_t(V_d)}{R_{sh}} . \qquad --- 2.21$$

$J_d(V_d)$ is the current-voltage relation for the diode that would exist in the dark if the conditions present in the light could be maintained in the dark, and $J_l(V)$ is the voltage dependent light generated current. In his conclusion he states that 2.21 should replace 2.14 in almost all cells except in P-N homojunctions.

The material properties of thin film solar cells are discussed in detail in a recent review by Hill (Hill, 1978), and before developing the theory of the interference thin film solar cell a brief account of the optical theory of thin solid films will be given.

2.5 Optical Theory of Thin Films

A thin film is understood to be a material structure extended in two dimensions whilst the third dimension, the thickness of the film is of the order of magnitude of few wavelengths of light. In a homogeneous thin film the optical constants are everywhere the same, whereas in an inhomogeneous thin film they vary in some way. When light is incident on one or several superposed films some of it is reflected, some absorbed, some diffused and some transmitted. One of the methods of determining the amplitudes and intensities of beams of light reflected or transmitted by a homogeneous thin film or by a system of homogeneous thin films is by solving Maxwell's equations subject to the appropriate boundary conditions (Macleod, 1969).

In SI units, Maxwell's equations can be written as

$$\nabla \times \underline{H} = \dot{\underline{D}} + \underline{J} \qquad - - - 2.26$$

$$\nabla \times \underline{E} = - \dot{\underline{B}} \qquad - - - 2.27$$

$$\nabla \cdot \underline{D} = \rho \qquad - - - 2.28$$

$$\nabla \cdot \underline{B} = 0 \qquad - - - 2.29$$

where $\underline{D} = \varepsilon \varepsilon_o \underline{E}$

$\underline{B} = \mu \mu_o \underline{H}$

and $\underline{J} = \sigma \underline{E}$

$$\nabla \cdot \underline{J} = \frac{\partial \rho}{\partial t} .$$

$\underline{B}$ is the magnetic induction, $\underline{D}$ the electric displacement, $\underline{E}$ the electric field, $\underline{H}$ the magnetic field, σ the conductivity, μ the relative permeability, ε the relative permitivity and ρ the electric charge density. ε_o and μ_o respectively are the permitivity and permeability in a vacuum.

J is the current density.

Assuming no space charge in a dielectric medium where $\sigma = 0$

$$\nabla \times \underline{H} = \dot{\underline{D}} \quad \text{and} \quad \nabla \times \underline{E} = -\dot{\underline{B}}$$

$$\nabla \times (\nabla \times \underline{E}) = - \nabla \times \dot{\underline{B}} = (\nabla . \underline{E}) - \nabla^2 \underline{E} .$$

From Maxwell's equation 2.29

$$\nabla . \underline{E} = 0$$

$$\nabla \times (\nabla \times \underline{E}) = - \nabla^2 \underline{E}$$

$$- \nabla \times (\mu \mu_o \dot{\underline{H}}) = - \nabla^2 \underline{E} = \mu \mu_o \frac{\partial}{\partial t} (\nabla \times \underline{H})$$

$$= - \mu \mu_o \frac{\partial}{\partial t} \dot{D}$$

$$= - \mu \mu_o \ddot{\underline{D}}$$

$$\nabla^2 \underline{E} = \mu \mu_o \varepsilon \varepsilon_o \ddot{\underline{E}} . \quad - - - 2.30$$

comparing 2.30 with $\nabla^2 \underline{E} = \frac{1}{v^2} \ddot{\underline{E}}$

the differential equation describing the motion of a transverse wave, the phase velocity of an electromagnetic wave is given by

$$v = \frac{1}{(\mu \mu_o \varepsilon \varepsilon_o)^{\frac{1}{2}}} \quad - - - 2.31$$

in the dielectric medium

and

$$v = c = \frac{1}{(\mu_o \varepsilon_o)^{\frac{1}{2}}} \qquad \text{in a vacuum.}$$

In a light absorbing medium where the conductivity is finite

$$\underline{J} = \sigma \underline{E}$$

$$-\nabla^2 \underline{E} = -\mu \mu_o \sigma \frac{\partial}{\partial t} (\nabla \times \underline{H})$$

$$\nabla^2 \underline{E} = \mu \mu_o \varepsilon \varepsilon_o \ddot{\underline{E}} + \mu \mu_o \sigma \ddot{\underline{E}} . \quad --- 2.32$$

A solution to 2.32 is

$$\underline{E} = \underline{E}o \exp (i \omega (t - \frac{\underline{x}}{v})) \qquad --- 2.33$$

which represents a plane wave of angular frequency ω , travelling in the x direction with a velocity v. Substitution of 2.33 into 2.32 results in

$$\frac{1}{v^2} = \mu \mu_o \varepsilon \varepsilon_o - i \frac{\mu \mu_o \sigma}{\omega} \qquad --- 2.34$$

defining $N = \frac{c}{v}$ as the complex refractive index of the absorbing medium we find

$$N^2 = c^2 \mu \mu_o \varepsilon \varepsilon_o - i \frac{\mu \mu_o \sigma c^2}{\omega} \qquad --- 2.35$$

writing $N = n - ik$

$$n^2 - k^2 = c^2 \mu \mu_o \varepsilon \varepsilon_o$$

$$2nk = \mu \mu_o \sigma c^2/\omega$$

at optical frequencies $\mu \simeq 1$ so that

$$n^2 - k^2 = \mu_o \varepsilon \varepsilon_o c^2$$

and $$2nk = \frac{\mu_o \sigma c^2}{\omega} . \qquad --- 2.36$$

n is generally known as the refractive index (real) and k as the extinction coefficient.

Rewriting equation 2.33 as

$$\underline{E} = \underline{E}_o \exp (i\omega (t - x\, N/C)) \qquad - - - 2.37$$

substituting $(n - ik)$ for N in 2.37 results in

$$\underline{E} = \underline{E}_o \exp (i\ \omega (t - \frac{nx}{c}) \exp (-\omega\ \frac{kx}{c})). \qquad - - - 2.38$$

In equation 2.38, k is a measure of the absorption of light in the medium and $\frac{c}{k}$ is the distance in which the amplitude of the wave falls to $\frac{1}{e}$ of its initial value. $\omega \frac{nx}{c} = \frac{2\pi}{\lambda}$ nx is the phase factor corresponding to an optical distance of nx. λ is the wavelength in a vacuum. Maxwell's equations can also be used to show some important relationships between $\underline{E}$ and $\underline{H}$ vectors. Consider a plane wave given by equation 2.37 where x is replaced by a vector $\underline{r} = \alpha i + \beta j + \gamma k$, i, j and k being the unit vectors along the x, y and z axis respectively and α, β, γ being their direction cosines.

$$\frac{\partial \underline{E}}{\partial t} = i\ \omega \underline{E} \qquad \text{from 2.36}$$

$$\nabla \times \underline{H} = \frac{\partial \underline{D}}{\partial t} + \sigma \underline{E} \qquad \text{(Maxwell's equation)}$$

$$= \varepsilon \varepsilon_o \frac{\partial \underline{E}}{\partial t} + \sigma \underline{E} = i\ \varepsilon\ \varepsilon_o\ \omega \underline{E} + \sigma \underline{E}$$

$$= (i\ \varepsilon\ \varepsilon_o\ \omega + \sigma)\ \underline{E}$$

$$= - \frac{i\ N^2 \omega}{c^2 \mu\ \mu_o} - i\omega\ \varepsilon\ \varepsilon_o$$

and from 2.35

$$\nabla \times \underline{H} = \frac{i \omega N^2}{c^2 \mu \mu_o} \cdot \underline{E} .$$

Now $$\nabla \times = \frac{\partial i}{\partial x} + \frac{\partial j}{\partial y} + \frac{\partial k}{\partial z} . \qquad --- 2.39$$

From equation 2.37 where x is replaced by $\underline{r}$

$$\frac{\partial \underline{E}}{\partial x} = - \frac{i \omega N}{c} \propto \underline{E} , \quad \frac{\partial \underline{E}}{\partial y} = - \frac{i \omega N}{c} \beta \underline{E} , \quad \frac{\partial \underline{E}}{\partial z} = - \frac{i \omega N}{c} \gamma E .$$

Because there is symmetry between the solutions $\underline{E}$ and $\underline{H}$ we can also write

$$\frac{\partial \underline{H}}{\partial x} = - \frac{i \omega N}{c} \propto \underline{H} , \quad \frac{\partial \underline{H}}{\partial y} = \frac{i \omega N}{c} \beta \underline{H}$$

and $$\frac{\partial \underline{H}}{\partial z} = - \frac{i \omega N}{c} \gamma \underline{H} .$$

Therefore

$$\nabla \times \underline{H} = - \frac{i \omega N}{c} \left(\frac{i \partial}{\partial x} + \frac{j \partial}{\partial y} + \frac{k \partial}{\partial z} \right) \underline{H} = - \frac{i \omega N}{c} \cdot \underline{r} \times \underline{H} \qquad --- 2.40$$

By substituting 2.40 into 2.39 we get

$$- \frac{\omega N}{c} \cdot \underline{r} \times \underline{H} = \frac{i \omega N^2}{\mu \mu_o c^2} E$$

that is

$$\underline{r} \times \underline{H} = - \frac{N \underline{E}}{c \mu \mu_o} . \qquad --- 2.41$$

Similarly,

$$\nabla \times \underline{E} = - \frac{\omega N}{c} \underline{r} \times \underline{E}$$

and

$$\nabla \times \underline{E} = - \frac{\partial B}{\partial t} \qquad \text{(Maxwell's equation)}$$

$$= - \mu \mu_o i \omega \underline{H} \qquad --- 2.43$$

where $\underline{H} = \underline{H}_o \exp i\omega (t - \frac{x}{c} N)$.

From 2.42 and 2.43 we get

$$\frac{N}{c} (\underline{r} \times \underline{E}) = \mu \mu_o \underline{H}$$

that is

$$\frac{N}{c \mu \mu_o} (\underline{r} \times \underline{E}) = \underline{H}. \qquad - - - 2.44$$

2.6 Derivation of the effective complex refractive index

From equations 2.44 and 2.41 we can see that $\underline{E}$, $\underline{H}$ and $\underline{r}$ are mutually orthogonal and form a right handed set. Let us now consider the boundary conditions of a thin film of complex index N_1 on a substrate of index N_2, where the thickness of the film is d with the incident medium having a complex index of N_o.

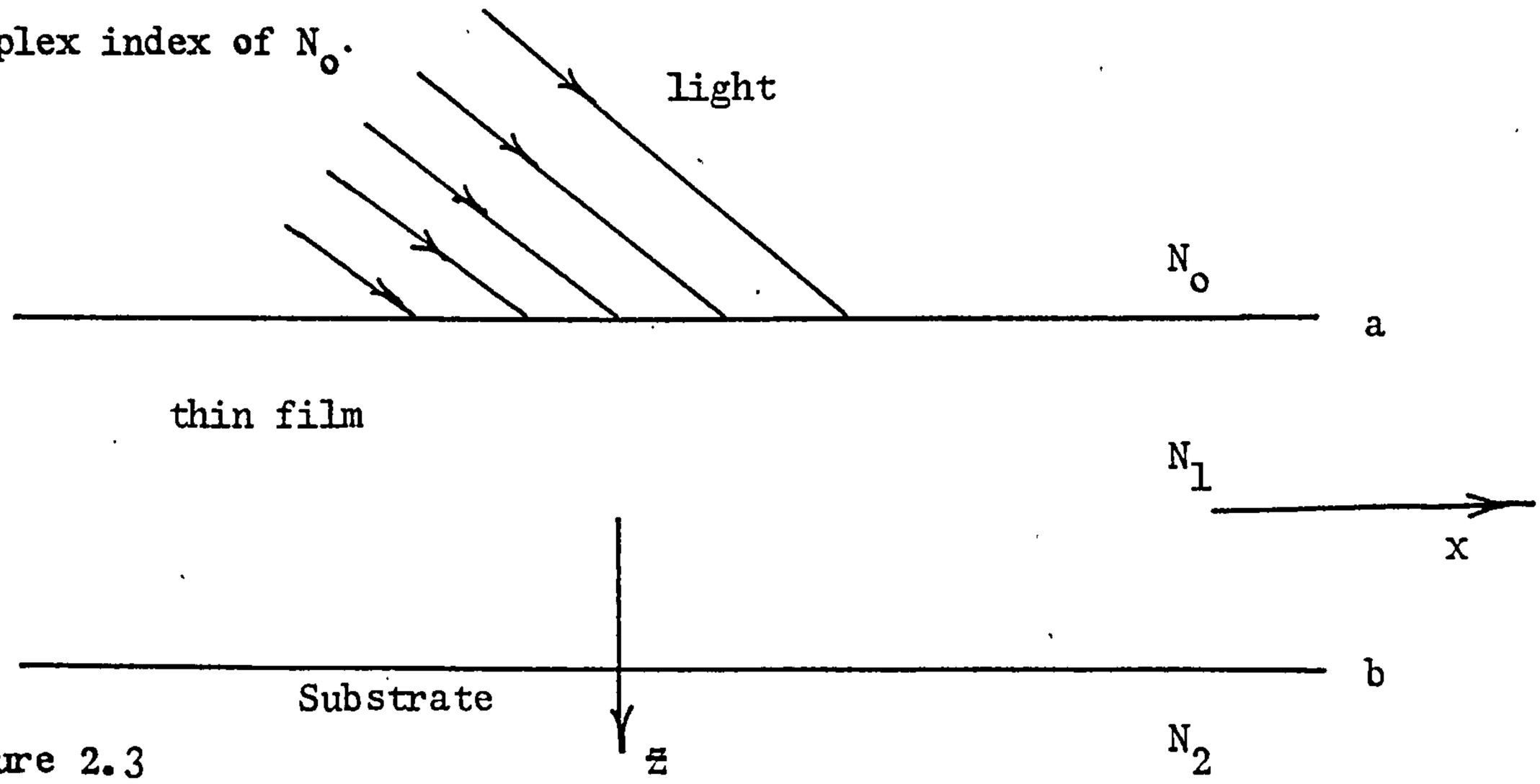

Figure 2.3

With reference to the figure 2.3 at the interface b the tangential components of $\underline{E}$ and $\underline{H}$ are $\underline{H}_b = \underline{H}^+_{1b} + \underline{H}^-_{1b}$

$$\underline{H}_b = \frac{\underline{N}_1}{c \mu \mu_o} (\hat{k} \times \underline{E}^+_{1b}) - \frac{\underline{N}_1}{c \mu \mu_o} (\hat{k} \times \underline{E}^-_{1b}). \qquad - - - 2.45$$

(by using 2.44)

The first term represents the positive going wave and the second one the negative going wave.

Also, $$\underline{E}_b = \underline{E}^+_{1b} + \underline{E}^-_{1b}$$

so that $$(\hat{k} \times \underline{E}_b) = (\hat{k} \times \underline{E}^+_{1b}) + (\hat{k} + \underline{E}^-_{1b}). \qquad \text{- - - 2.46}$$

Substituting 2.46 into 2.45

$$\underline{H}_b = \frac{N_1}{c\ \mu\ \mu_o} (\hat{k} \times \underline{E}_b - \hat{k} \times \underline{E}^-_{1b}) - \frac{N_1}{c\ \mu\ \mu_o} (\hat{k} \times \underline{E}^-_{1b})$$

$$= \frac{N_1}{c\ \mu\ \mu_o} (\hat{k} \times \underline{E}_b - 2\hat{k} \times \underline{E}^-_{1b})$$

that is

$$\hat{k} \times \underline{E}^-_{1b} = \frac{\frac{N_1}{c\ \mu\ \mu_o} (\hat{k} \times \underline{E}_b) - \underline{H}_b}{N_1/c\ \mu\ \mu_o}$$

$$= (\hat{k} \times \underline{E}_b) - \frac{\underline{H}_b}{N_1/c\ \mu\ \mu_o} . \qquad \text{- - - 2.47}$$

Similarly,

$$\hat{k} \times \underline{E}^+_{1b} = (\hat{k} \times \underline{E}_b) + \frac{\underline{H}_b}{N_1/c\ \mu\ \mu_o} . \qquad \text{- - - 2.48}$$

At the interface a in the above diagram

$$\underline{E}^+_{1a} = \underline{E}^+_{1b}\ e^{i\delta_1}$$

$$\underline{E}^-_{1a} = \underline{E}^-_{1b}\ e^{-i\delta_1}$$

$$\underline{H}^+_{1a} = \underline{H}^+_{1b}\ e^{i\delta_1} \qquad \text{- - - 2.49}$$

$$\underline{H}^-_{1a} = \underline{H}^-_{1b}\ e^{-i\delta_1}$$

where δ_1 is the phase factor equal to $\frac{2\pi}{\lambda} N_1 d$, for normal incidence.

At the boundaries a and b (figure 2.3)

$$\hat{k} \times \underline{E}_a = \hat{k} \times \underline{E}_{1a}^{+} + \hat{k} \times \underline{E}_{1a}^{-}$$

$$= \hat{k} \times \frac{\underline{E}_b}{2}) \ (e^{i\delta_1} + e^{-i\delta_1}) + \frac{\underline{H}_b}{N_1/c \ \mu \ \mu_o} \ (\frac{e^{i\delta_1} - e^{-i\delta_1}}{2}),$$

$$--- 2.50$$

using the relations 2.49, 2.47 and 2.48

$$\hat{k} \times \underline{E}_a = \hat{k} \times \underline{E}_b \cos \delta_1 + i \frac{\underline{H}_b \sin \delta_1}{N_1/c \ \mu \ \mu_o} . \qquad --- 2.51$$

Similarly,

$$\underline{H}_a = i \frac{N_1 \hat{k}}{c \ \mu \ \mu_o} \times \underline{E}_b \sin \delta_1 + \underline{H}_b \cos \delta_1 . \qquad --- 2.52$$

Equations 2.51 and 2.52 can be written in the matrix notation as

$$\begin{vmatrix} \hat{k} \times \underline{E}_a \\ \underline{H}_a \end{vmatrix} = \begin{vmatrix} \cos \delta_1, (i \sin \delta_1)/(N_1/c \ \mu \ \mu_o) \\ \frac{i \ N_1 \sin \delta_1}{c \ \mu \ \mu_o}, \qquad \cos \delta_1 \end{vmatrix} \begin{vmatrix} \hat{k} \times \underline{E}_b \\ \underline{H}_b \end{vmatrix} \qquad --- 2.53$$

where,

$$\begin{vmatrix} \cos \delta_1 & i \sin \delta_1/(N_1/c \ \mu \ \mu_o) \\ \frac{i \ N_1 \sin \delta_1}{c \ \mu \ \mu_o} & \cos \delta_1 \end{vmatrix}$$

is called the characteristic matrix of the thin film. The refractive

index N_1 can be replaced by $\frac{N_1}{\cos\theta}$ for P-waves and $N_1 \cos\theta$ for S-waves when the light is incident at an angle of incidence of θ . The phase factor is then replaced by

$$\frac{2\pi}{\lambda} N_1(\cos\ \theta)d \qquad \text{(see equation 3.1).}$$

This can only be done for homogeneous waves. The case for inhomogeneous waves will be discussed later.

If the effective refractive index of the assembly is Z_a, then by direct analogy with equation 2.44

$$\frac{Z_a}{c\ \mu\ \mu_o}\ (\hat{k} \times \underline{E}_a) = \underline{H}_a \quad , \qquad \text{- - - 2.54}$$

substituting 2.54 into 2.53

we get $(\hat{k} \times \underline{E}_a)$
$$\begin{vmatrix} 1 \\ \frac{Z_a}{c\,\mu\mu_o} \end{vmatrix} = \begin{vmatrix} \cos\delta_1 & \frac{i \sin\delta_1\ c\ \mu\ \mu_o}{N_1} \\ \frac{i\ N_1\ \sin\delta_1}{c\ \mu\ \mu_o} & \cos\delta_1 \end{vmatrix} \begin{vmatrix} 1 \\ \frac{N_2}{c\mu\mu_o} \end{vmatrix} (\hat{k} \times \underline{E}_b) \ ;$$

rewritten such that $\frac{Z_a}{c\,\mu\mu_o} = C/B$, the effective refractive index can be worked out.

$$\begin{vmatrix} B \\ C \end{vmatrix} = \begin{vmatrix} \cos\delta_1 & \frac{i \sin\delta_1\ c\ \mu\ \mu_o}{N_1} \\ \frac{i\ N_1\ \sin\delta_1}{c\ \mu\ \mu_o} & \cos\delta_1 \end{vmatrix} \begin{vmatrix} 1 \\ \frac{N_2}{c\mu\mu_o} \end{vmatrix} .$$

The matrix relations above relate the tangential components of $\underline{E}$ and $\underline{H}$ vectors at the incident interface with the tangential components at the interface with the substrate. The above treatment can easily be extended to the case for an assembly of n thin films on a substrate of refractive index N_{n+1} and

$$\begin{vmatrix} B \\ C \end{vmatrix} = \prod_{r=1}^{n} \begin{vmatrix} \cos\delta_r & \frac{c\,\mu\,\mu_o\, i \sin\delta_r}{N} \\ \frac{i\,N \sin\delta_r}{c\,\mu\,\mu_o} & \cos\delta_r \end{vmatrix} \begin{vmatrix} 1 \\ N_{r+1} \end{vmatrix} \quad \text{--- 2.57}$$

The tangential components of $\underline{E}$ and $\underline{H}$ at the incidence interface again relate the tangential components at the interface with the substrate no matter how many intermediate layers there may be. We can also calculate the effective refractive index of the whole assembly from which by the application of the Fresnel formula the reflectance of the assembly can be derived.

CHAPTER THREE

INTERFERENCE SOLAR CELL

Introduction

The interference solar cell is defined as one that takes into account the optical interference effects due to multiple reflections at each interface between the different media constituting the device. The substrate interface effects are also included. Its theory will be developed starting from the optical characteristic matrix, derived in Chapter Two, relating the electric and magnetic fields at the front surface to those at the interface with the substrate of an assembly of thin absorbing films.

3.1 Derivation of the absorption rate

In this section an expression for the rate of absorption of light at any point inside the solar cell will be derived. The solar cell is assumed to be a system of plane-parallel sided, homogeneous absorbing layers.

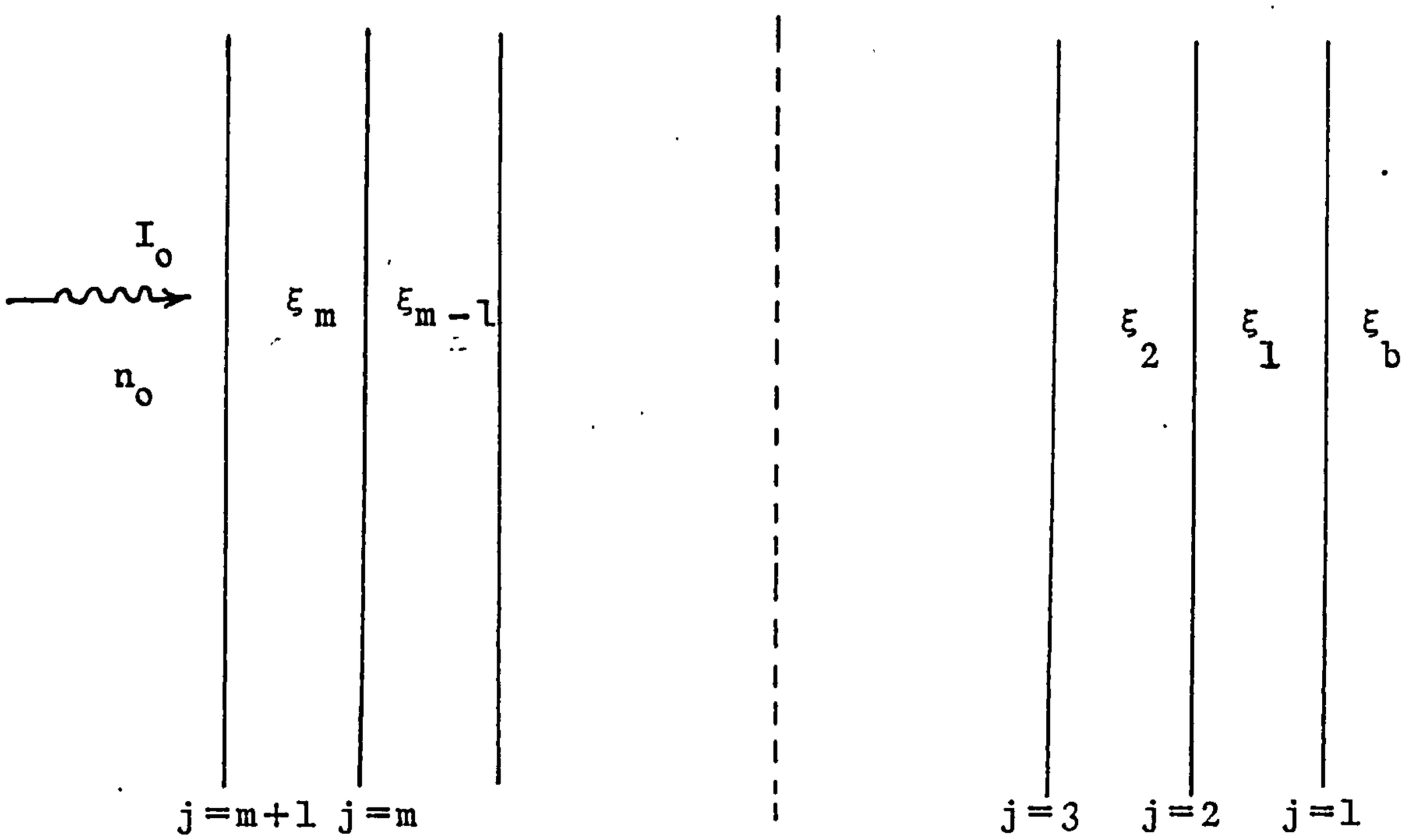

Figure 3.1 Multilayer System

Let E_a and H_a be the tangential components of the electric and magnetic vectors respectively at the boundary $j = m+1$ where light of intensity I_o is incident normally in a medium of optical admittance n_o. If N_b is the optical admittance of the substrate and E_b is the tangential component of the electric vector at the boundary $j = 1$, then from the standard characteristic matrix for an assembly of thin films

$$\begin{vmatrix} E_a \\ H_a \end{vmatrix} = \begin{vmatrix} \cos(\delta_m) & i \sin(\delta_m)/\xi_m y_v^{-1} \\ i\xi_m \sin(\delta_m) y_v^{-1} & \cos(\delta_m) \end{vmatrix} \begin{vmatrix} 1 \\ \xi_b y_v^{-1} \end{vmatrix} E_b \quad --- 3.1$$

where $y_v = (\frac{\mu_o}{\varepsilon_o})^{\frac{1}{2}}$, $\delta_m = \frac{2\pi}{\lambda}(n - i k_m) d_m \cos(\theta_m)$ and d_m is the thickness of the mth layer.

The "complex refractive" index ξ_m is defined as $\xi_m = \frac{n_m - i k_m}{\cos(\theta_m)}$ for P-waves and $= (n_m - i k_m) \cos(\theta_m)$ for S-waves.

n_m is the "real" refractive index and k_m is the extinction coefficient for the mth layer.

$N_b = n_b - ik_b$ where n_b is the "real" refractive index, and k_b is the extinction coefficient for the substrate.

For $k_m = 0$, θ_m is real

For $k_m \neq 0$, θ_m is in general complex

θ_m is in general given by the generalised form of Snells Law i.e.

$$(n_m - i k_m) \sin \theta_m = (n_{m-1} - ik_{m-1}) \sin \vartheta_m - 1,$$

For normal incidence $\theta_m = 0$.

The matrix relation 3.1 can be rewritten in the form

$$\begin{vmatrix} E_a \\ H_a \end{vmatrix} = \begin{vmatrix} M_{11} & M_{12} \\ M_{21} & M_{22} \end{vmatrix} \begin{vmatrix} 1 \\ \xi_b \; y_v \end{vmatrix} \cdot E_b \; . \qquad \text{---} \; 3.2$$

If R_a is the reflection coefficient at the boundary $j = m$

$$(1 - R_a)\, I_o = \frac{1}{2} \text{Real}\, (E_a \times H_a^*) \; . \qquad \text{---} \; 3.3$$

Substituting 3.2 into 3.3 and putting $I_o = 1$

$$E_b = \left\{ \frac{1 - R_a}{\frac{1}{2} \text{Real}\, (M_{11} + M_{12}\;\; \xi_b\, y_v)(M_{21} + M_{22}\;\; \xi_b\, y_v)^*} \right\}^{\frac{1}{2}} \; . \qquad \text{---} \; 3.4$$

For any boundary j in the assembly the relation 3.2 can be used to write,

$$\begin{vmatrix} E_j \\ H_j \end{vmatrix} = \begin{vmatrix} A_{11} & A_{12} \\ A_{21} & A_{22} \end{vmatrix} \begin{vmatrix} 1 \\ \xi_b \; y_v \end{vmatrix} \cdot E_b \; . \qquad \text{---} \; 3.5$$

R_a is given by

$$R_a = \left(\frac{(n_o - Z_a)}{(n_o + Z_a)} \right) \left(\frac{(n_o - Z_a)}{(n_o + Z_a)} \right)^* \; , \qquad \text{(Fresnel's relation)}$$

where

$$Z_a = \frac{(\mu_o)^{\frac{1}{2}}}{(\varepsilon_o)^{\frac{1}{2}}} \; \frac{H_a}{E_a} \; . \qquad \text{---} \; 3.6$$

Z_a is the effective "complex refractive index" for the whole assembly. The intensity at j , normal to the boundary is given by

$$I_j = \frac{1}{2} \text{Real } (E_j \times H_j^*). \qquad \text{- - - 3.7}$$

The electric vector E_x at any point inside the layer ξ_j is given by (see figure 3.2)

$$E_x = (\cos x'' + i \sin x'' \frac{Z_j}{\xi_j}) E_j \qquad \text{- - - 3.8}$$

where

$$Z_j = \frac{(\mu_o)^{\frac{1}{2}}}{(\varepsilon_o)^{\frac{1}{2}}} \frac{H_j}{E_j}, \text{ and } x'' = \frac{2\pi}{\lambda} \cdot (n_j - ik_j) x .$$

Z_j is the effective complex refractive index for the assembly (figure 3.2) on the left hand side of the boundary j.

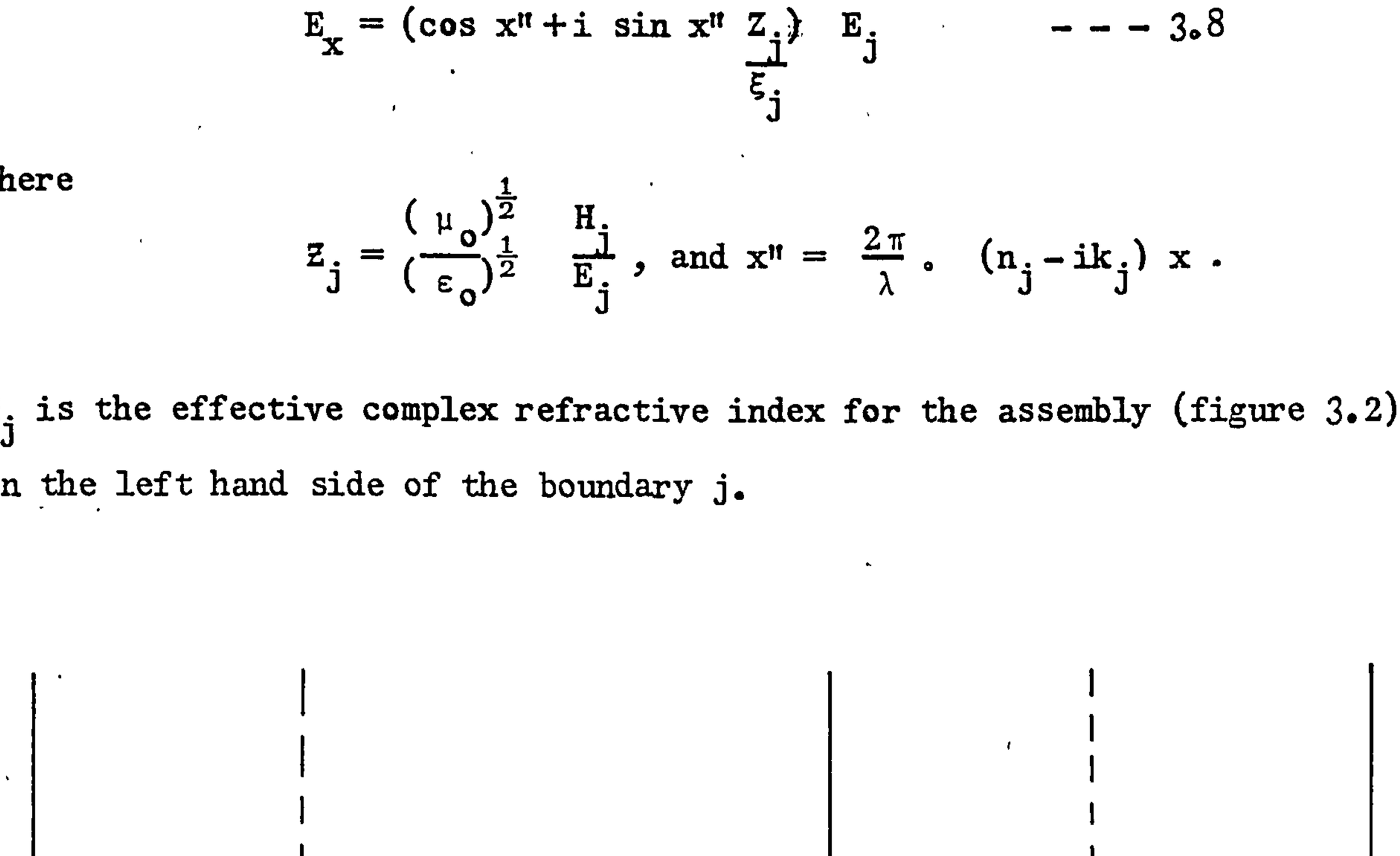

Figure 3.2

The absorption rate per square metre in a lamella dx at x in the jth layer is given by

$$\text{Absorption Rate } A(x) = \tfrac{1}{2} \quad \sigma_j \; E_x \; E_x^* \qquad \text{- - - 3.9}$$

σ_j is the conductivity in $\text{ohm}^{-1}\ \text{m}^{-1}$

E_x is in Vm^{-1}

σ_j is given by

$\sigma_j = 4\,\pi\,\varepsilon_o\,n_j\,k_j\,f$ (from Maxwell's equations)

f is the frequency of the wave.

The analytical expression for A(x) was solved out to

$$A(x) = \tfrac{1}{2}\, E_j E_j^* \; \left(\frac{P_2}{4} \left(e^{+2y} + e^{-2y}\right) + \frac{P_5}{2} \left(e^{+2y} - e^{-2y}\right) \right.$$

$$\left. + \frac{P_3}{2} \cos 2x' + P_4 \sin 2x' \right) \sigma_j \qquad \text{- - - 3.10}$$

where

$$x' = \frac{2\pi}{\lambda}\, n_j\, x \text{ and } y = \frac{2\pi}{\lambda}\, k_j\, x$$

$$z_j = (\gamma_j - i\,\beta_j)\ ,$$

$$P_1 = (\gamma_j^2 + \beta_j^2)/(n_j^2 + k_j^2).$$

$$P_2 = (1 + P_1)$$

$$P_3 = (1 - P_1)$$

$$P_4 = (\beta_j\, n_j - \gamma_j\, k_j)/(n_j^2 + k_j^2)$$

$$P_5 = (\gamma_j\, n_j + \beta_j\, k_j)/(n_j^2 + k_j^2).$$

3.2 Calculation of the short circuit current

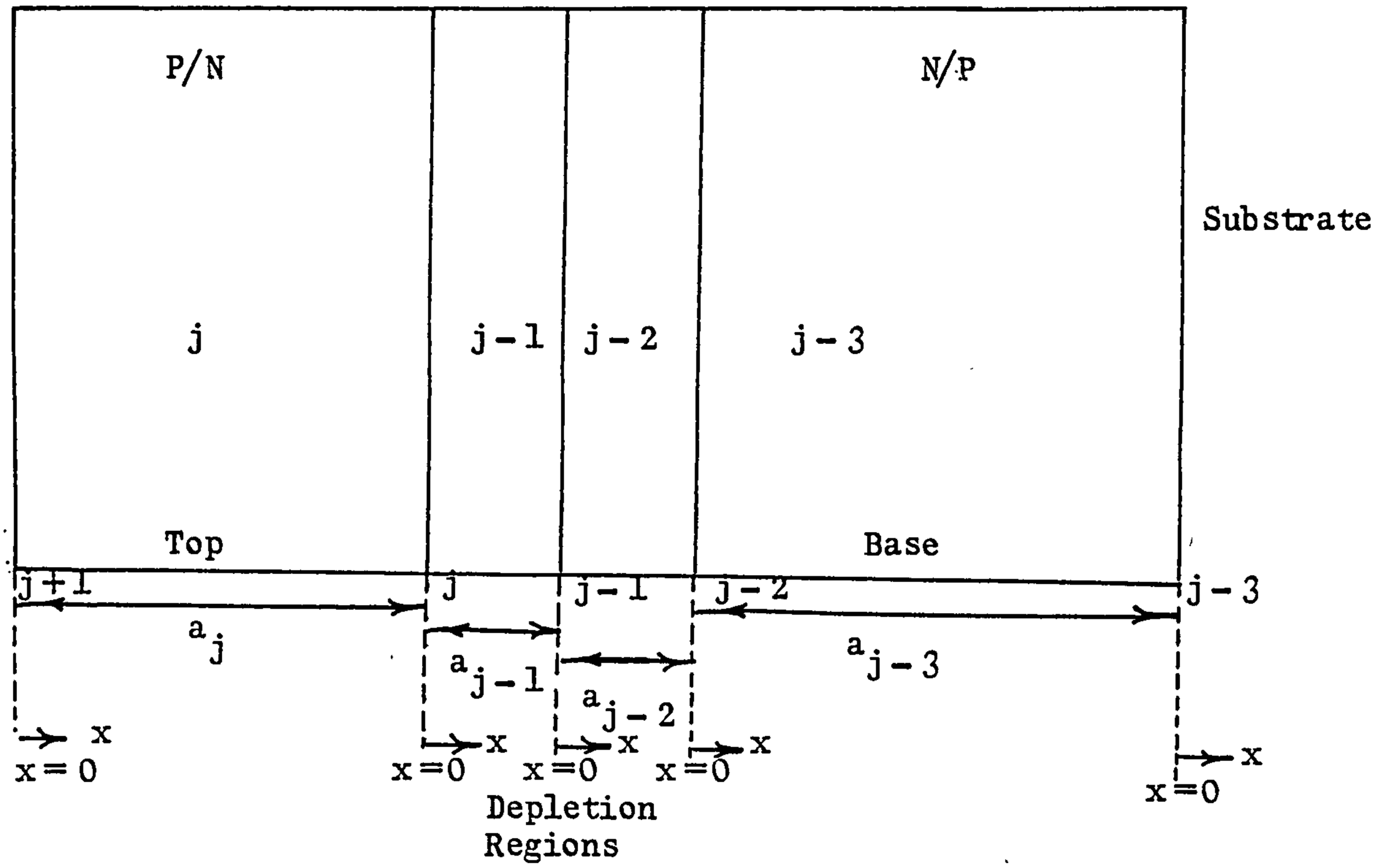

Figure 3.3

Only the case for zero electric field will be considered assuming D_n, n and L_n to be constant with both λ and x.

The continuity equation to solve for each layer is

$$D_n \frac{d^2n}{dx^2} - \frac{n}{T_n} = - A(a-x) \qquad \text{- - - 3.11}$$

(see equations 2.5)

where

$A(a-x)$ is in units of photons/m^3/sec;

n is the concentration of the generated carriers i.e. electrons on the P side. The same equation applies to holes on the N side by substituting p for n everywhere.

The boundary conditions (see page 12) applicable to the jth layer are:

(1) $n(a_j) = 0$ (for zero external bias and ignoring recombination due to interface states)

(2) $D_n \frac{dn}{dx}\Big|_{x=0} = S_n\, n(0)$ where S_n is the surface recombination velocity at the (j + 1) surface.

The boundary conditions applicable to the (j-3)th layer are:

(1) $n(0) = 0$ (for zero bias and ignoring interface states)

(2) $D_n \frac{dn}{dx}\Big|_{x=a_{j-3}} = -S_b n(a_{j-3})$ where S_b is the recombination velocity at the (j − 3) boundary.

The solution to 3.11 was found to be

$$n = C_1 e^{-x/L_n} + C_2 e^{+x/L_n} + \frac{\sigma}{4D_n}\,\frac{P_3\cos(S(a-x))}{(S^2+t^2)} + \frac{P_4}{2D_n}\,\frac{\sin(S(a-x))}{(S^2+t^2)}$$

$$- \frac{\sigma P_2}{4D_n}\,\frac{\cosh \alpha(a-x)}{(\alpha^2 - t^2)} - \frac{P_5 \sinh(\alpha(a-x))}{2D_n(\alpha^2 - t^2)} \qquad \text{---} \quad 3.12$$

where

$$\alpha = \frac{4\pi k}{\lambda} \text{ (absorption coefficient)},$$

$$S = \frac{4\pi n}{\lambda} \quad \text{and} \quad t = \frac{1}{L_n}.$$

C_1 and C_2 are found from the boundary conditions.

For a P type layer the short circuit current at j due to absorption in the jth layer is given by

$$J_j = e\, D_n \left.\frac{dn}{dx}\right|_{x = a_j} \cdot F$$

$$= e\, D_n \left(\frac{2C_2}{L_n} e^{+a/L_n} + \frac{W_1}{L_n} - \frac{\sigma_j P_4 S}{2D_n(S^2+t^2)} \right.$$

$$\left. + \frac{\sigma_j P_5}{2D_n(\alpha^2 - t^2)} \right) \cdot F$$

where

$$W_1 = \frac{\sigma_j P_3}{4D_n(S^2 + t^2)} - \frac{\sigma_j P_2}{4D_n(\alpha^2 - t^2)}$$

$$W_2 = \frac{\sigma_j P_3 \sin(Sa)}{4D_n(S^2+t^2)} - \frac{\sigma_j P_4 S \cos(Sa)}{(S^2 + t^2)} + \frac{\sigma_j P_2 \sinh(\alpha a)}{4D_n(\alpha^2 - t^2)}$$

$$+ \frac{\sigma_j P_5 \cosh(\alpha a)}{2D_n(\alpha^2 - t^2)}$$

$$W_3 = \frac{\sigma_j P_3 \cos(Sa)}{4D_n(S^2 + t^2)} + \frac{\sigma_j P_4}{2D_n(S^2 + t^2)} - \frac{\sigma_j P_2 \cosh(\alpha a)}{4D_n(\alpha^2 - t^2)}$$

$$- \frac{\sigma_j P_5 \sinh(\alpha a)}{2D_n(\alpha^2 - t^2)}$$

$$C_2 = \left(W_1 \exp(a/L_n) - \frac{S_n L_n W_3 - L_n D_n W_2}{S_n L_n + D_n} \right)$$

$$\Big/ \left(\frac{L_n S_n - D_n}{D_n + L_n S_n} - \exp(2a/L_n) \right)$$

$a = a_j$ and F is the incident photon flux at wavelength λ .

For an n type jth layer equations 3.13 still apply with p substituted for n everywhere.

Assuming that all the absorbed photons generate minority carriers in the depletion regions, the contribution to the short circuit current from these is given by

$$J_d = (I_j - I_{j-2})\ e.\ F\ . \qquad \text{- - - 3.14}$$

It is assumed that all the minority carriers are swept across before they can recombine.

The contribution from the base region is given by

$$J_{j-3} = -e\ D_n \left.\frac{dn}{dx}\right|_{x=0} .\ F$$

$$= e\ \left(\frac{2C_2}{L_n} + \frac{W_3}{2} + W_2\right) D_n\ .\ F \qquad \text{- - - 3.15}$$

where C_2 is now defined as

$$C_2 = \frac{-W_3\left(\frac{1}{L_n} - \frac{S_b}{D_n}\right) - \left(\frac{S_b W_1}{D_n} + W_4\right) e^{a/L_n}}{e^{2a/L_n}\left(\frac{S_b}{D_n} + \frac{1}{L_n}\right) + \left(\frac{1}{L_n} - \frac{S_b}{D_n}\right)}$$

where

$$W_4 = \frac{\sigma_j, P_4\ S}{(S^2 + t^2)} + \frac{\sigma_j P_5\ \alpha}{2(\alpha^2 - t^2)} \quad \text{and} \quad a = a_{j-3}\ .$$

The total short circuit current for an N–P or P–N junction solar cell

is

$$J \text{ total} = /J_j/ + /J_d/ + /J_{j-3}/ \quad \text{at wavelength } \lambda \qquad --- 3.16$$

Total current over all wavelengths is given by

$$J \text{ total (all } \lambda \text{ 's)} = \int_0^{\lambda(E_g)} J \text{ total } d\lambda$$

where $\lambda (E_g)$ is the wavelength corresponding to the cut-off band edge frequency for the junction.

A complete working computer program in Fortran IV has been written for the above analysis.

3.3 Oblique incidence

From Maxwell's equations the following relationships between $\underline{E}$ and $\underline{H}$ vectors can be derived (Stern, 1960).

$$k_1 \underline{r}_1 \times \underline{E} - i\, k_2 \underline{r}_2 \times \underline{E} = c\, \mu\, \mu_o \underline{H} \equiv k^1 \times \underline{E}$$

$$k_1 \underline{r}_1 \times \underline{H} - i\, k_2 \underline{r}_2 \times \underline{H} = \frac{-N^2}{c\, \mu\, \mu_o} \underline{E} \equiv k^1 \times \underline{H} \qquad --- 3.17$$

where $N = n - i\,k$ is a pure number.

$\underline{r}_1$ is the unit vector in the direction normal to the planes of constant phase.

$\underline{r}_2$ is the unit vector in the direction normal to the planes of constant amplitude.

$$k_1 = 2^{-\frac{1}{2}} \left((n^2 - k^2) + \left((n^2 - k^2)^2 + \left(\frac{4n^2k^2}{\cos^2 \chi} \right)^{\frac{1}{2}} \right)^{\frac{1}{2}} \right)^{\frac{1}{2}}$$

$$k_2 = 2^{-\frac{1}{2}} \left(-(n^2 - k^2) + \left((n^2 - k^2)^2 + \left(\frac{4n^2k^2}{\cos^2 \chi} \right)^{\frac{1}{2}} \right)^{\frac{1}{2}} \right)^{\frac{1}{2}}$$

χ is the angle between $\underline{r}_1$ and $\underline{r}_2$

when $\underline{r}_1$ and $\underline{r}_2$ are parallel, $\chi = 0$,

$k_1 \equiv n$ and $k_2 \equiv k$, the wave is homogeneous.

The wave is inhomogeneous when $\underline{r}_1$ and $\underline{r}_2$ are not parallel, that is when the direction perpendicular to the planes of constant phase is not parallel to the direction perpendicular to the planes of constant amplitude.

To distinguish between homogeneous and inhomogeneous waves a little more clearly we can write the $\underline{E}$ vector for the homogeneous case as

$$\underline{E} = \underline{E}_o \exp\left(i(\omega t - \frac{2\pi}{\lambda o} N.\underline{r})\right)$$

($\underline{r}$ is with respect to the direction of propagation here)

whereas for the inhomogeneous case it is

$$\underline{E} = \underline{E}_o \exp\left(i(\omega t - \frac{2\pi}{\lambda o}(\underline{r}_1 k_1 - i k_2 \underline{r}_2)\, \underline{r})\right).$$

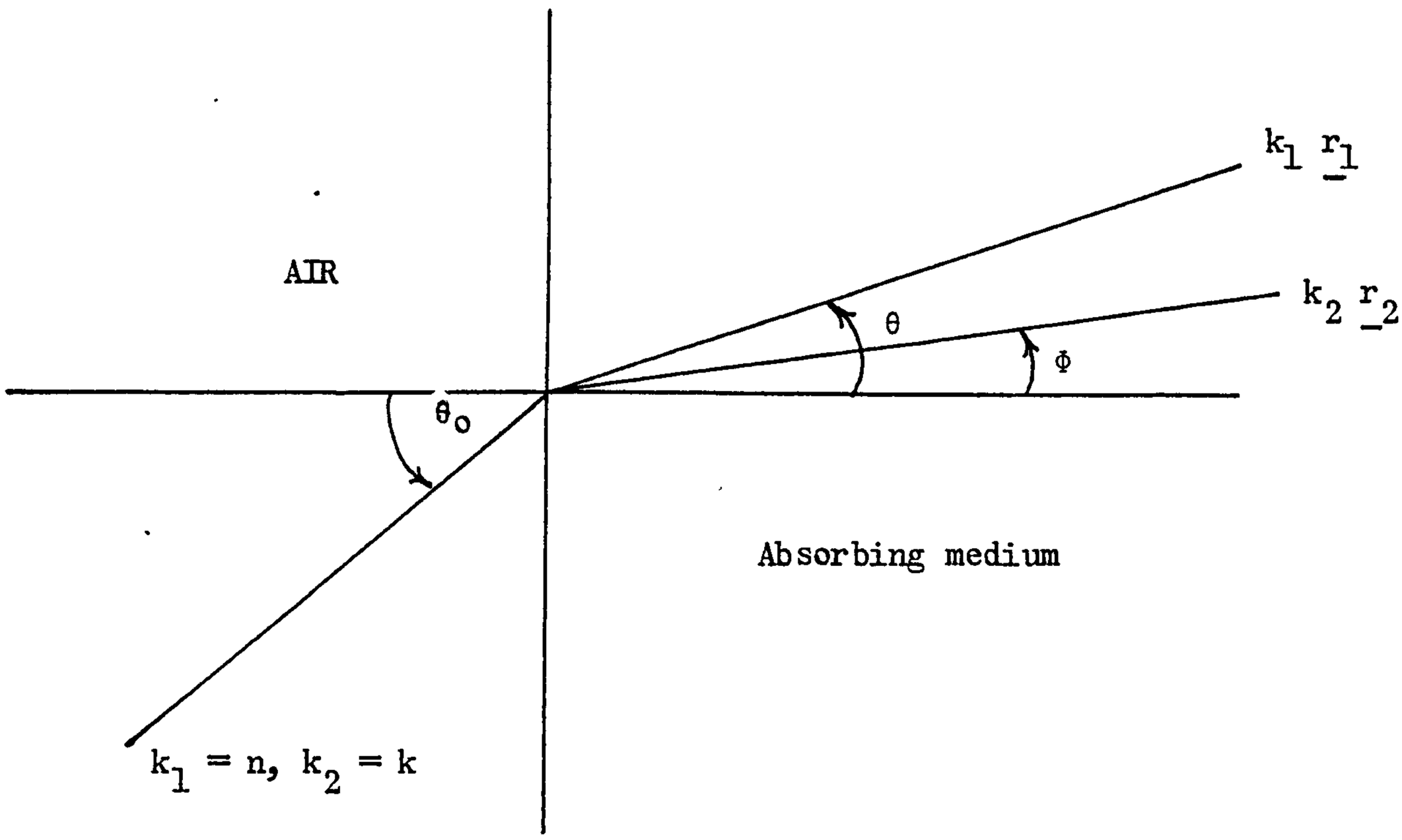

When Snells Law is written as

$$(n_m - i\,k_m)\sin\theta_m = (n_m - i\,k_{m-1})\sin\theta_{m-1}$$

where θ is in general complex as a consequence of the "refractive index" being complex. It is very difficult to attach real physical meaning to the values of θ other than that they indicate $\underline{r}_1$ and $\underline{r}_2$ are not parallel.

The second form of writing Snells Law in a generalised way is

$$k_{1\,m}\sin\theta_m = k_{1(m-1)}\sin\theta_{m-1}$$

$$k_{2\,m}\sin\Phi_m = k_{2(m-1)}\sin\Phi_{m-1} \qquad ---\ 3.18$$

where θ and Φ are real and physically represent the directions of constant phase and amplitude respectively i.e. directions of $\underline{r}_1$ and $\underline{r}_2$.

The relations 3.18 are derived from the boundary conditions for E and $\underline{H}$ at the interface.

If the medium of incidence is air then from equation 3.18 we can see that $\underline{r}_2$ is always perpendicular to the boundary.

The energy flow $\overline{S}$ is still given by the relation

$$\overline{S} = \tfrac{1}{2}\,\text{Real}\,(\underline{E}^* \times \underline{H})$$

$$= \tfrac{1}{2}\,\text{Real}\,(\underline{E}^* \times (\underline{r}_1 k_1 - i\,k_2\,\underline{r}_2) \times \underline{E}) \text{ from 3.17}$$

$$---\ 3.19$$

writing $\underline{k}^1 = k_1\,\underline{r}_1 - i\,k_2\,\underline{r}_2$ we get

$$\overline{S} = \tfrac{1}{2}\,\frac{1}{c\mu\,\mu_o}\,\text{Real}\;(\underline{E}^* \cdot \underline{E})\,\underline{k}^1 - (\underline{E}^* \cdot \underline{k}^1)\,\underline{E}$$

$$= \tfrac{1}{2}\,\frac{1}{c\mu\,\mu_o}\;(\underline{E}^* \cdot \underline{E})\,k_1\,\underline{r}_1$$

$$- \text{Real}\,((\underline{E}^* \cdot (k_1\,\underline{r}_1 - i\,k_2\,\underline{r}_2))\,\underline{E} \quad . \qquad ---\ 3.20$$

Now any incident wave can be written as a combination of P- and S-waves. For P-waves the $\underline{E}$ vector is parallel to the plane of incidence defined as the plane containing $\underline{r}_1$, $\underline{r}_2$ and the normal to the boundary.

For S-waves the $\underline{E}$ vector is perpendicular to the plane of incidence.

Let us represent the $\underline{E}_o$ vector by $\underline{E}_1 + i\,\underline{E}_2$ where $\underline{E}_1$ and $\underline{E}_2$ are the major and minor axis for the ellipse traced out by the oscillating $\underline{E}_o$ vector.

Assuming zero charge distribution and using Maxwell's equation

$$\nabla \cdot \underline{D} = \rho = 0 \text{ we find that}$$

$$(k_1 \underline{r}_1 - i\, k_2 \underline{r}_2)(\underline{E}_1 + i\, \underline{E}_2) = 0$$

from which

$$k_1 \underline{r}_1 \circ \underline{E}_1 = - k_2 \underline{r}_2 \circ \underline{E}_2 ,$$

$$k_2 \underline{r}_2 \circ \underline{E}_1 = k_1 \underline{r}_1 \cdot \underline{E}_2 .$$

In equation 3.20 above

$$\underline{E}^* \cdot (k_1 \underline{r}_1 - i\, k_2 \underline{r}_2) = (\underline{E}_1 - i\, \underline{E}_2) \circ (k_1 \underline{r}_1 - i\, k_2 \underline{r}_2)$$

$$= \underline{E}_1 k_1 \underline{r}_1 - \underline{E}_2 k_2 \underline{r}_2 - i\,(\underline{E}_2 k_1 \underline{r}_1 + \underline{E}_1 k_2 \underline{r}_2)$$

$$= - 2\underline{E}_2 k_2 \underline{r}_2 - 2\, i\, (\underline{E}_1 k_2 \underline{r}_2).$$

Substituting the latter into 3.20 where

$$- \text{Real}\,(\underline{E}^* \cdot k_1^1) \cdot \underline{E}_1$$

$$= - \text{Real}\,(-2\underline{E}_2 k_2 \underline{r}_2 - 2\, i\, \underline{E}_1 k_2 \underline{r}_2)(\underline{E}_1 + i\, \underline{E}_2)$$

$$= - \quad (2\underline{E}_1 k_2 \underline{r}_2 \cdot \underline{E}_2) - (2\underline{E}_2 k_2 \underline{r}_2 \cdot \underline{E}_1)$$

$$= - k_2 \underline{r}_2 \times (\underline{E}_2 \times \underline{E}_1) ,$$

from which

$$\bar{S} = \tfrac{1}{2} \frac{1}{c \mu \mu_o} (\underline{E}^* \underline{E}) k_1 \underline{r}_1 - k_2 \underline{r}_2 (\underline{E}_2 \times \underline{E}_1). \qquad --- 3.21$$

The latter equation shows that when $\underline{E}_o$ oscillates in the plane of incidence (P-waves), the direction of the energy flow is the vector sum of a component in the direction of constant phase plus a component given by the second term and lies in the plane of incidence.

When the $\underline{E}_o$ vector oscillates in a direction perpendicular to the plane of incidence (S-waves), the energy flow is in the direction of constant phase.

The arguements applied to normally incident light on a thin film multi-layer will now be extended to obliquely incident light. The equation 3.17 relating $\underline{E}$ and $\underline{H}$ vectors indicate that for inhomogeneous waves, $\underline{E}$ and $\underline{H}$ are not necessarily orthogonal. However, the Poynting vector is still perpendicular to the plane containing the $\underline{E}$ and $\underline{H}$ vectors.

For the two special cases when $\underline{E}$ is parallel to the plane of incidence and perpendicular to the plane of incidence the $\underline{E}$ and $\underline{H}$ vectors are orthogonal still.

Now equation 3.1 can be used to find the intensity and absorption rate for the normal components in the following way. Remembering that for P-waves $\xi_m = \dfrac{n_m - i\, k_m}{\cos \theta_m}$ and for S-waves $\xi_m = (n_m - i\, k_m) \cos \theta_m$, equation 3.2 still applies except θ_m is now complex and given by Snell's Law as mentioned earlier.

Equation 3.3 is modified to

$$(1 - R_a)\, I_o \cos \theta_o = \tfrac{1}{2}\, \text{Real}\, (E_a \times H_a^*)$$

where θ_o is the angle of incidence.

Equation 3.4 becomes

$$E_b{}^2 = \frac{(1-R_a)\cos\theta_o}{\frac{1}{2}\,\text{Real}\,(M_{11} + M_{12}\ \xi_b\ y_v)(M_{21} + M_{22}\ \xi_b\ \frac{1}{2}y_v)^*} \quad \text{for } I_o = 1$$

Equations 3.5 and 3.9 still apply for the energy components normal to the boundary with the following modifications.

$$x'' = \frac{2\pi}{\lambda}\ N_j \cos\ \theta_j\ x$$

$$N_j = (n_j - i\ k_j)$$

$$x'' = \frac{2\pi}{\lambda}\ (n_j - i\ k_j) \cos\ \theta_j\ x \text{ for S-waves and P-waves}$$

write $\theta_j = \varepsilon_j + i\,\Omega_j$.

For P-waves equation 3.10 still applies with the exception that $\underline{E}_j$ and $\underline{H}_j$ values will no longer be the same as for normal incidence and that $(\gamma_j - i\ \beta_j)$ is equal to $Z_j \cos\theta_j$; n and k should be substituted by c and d respectively by redefining x'' so that

$$x' = \frac{2\pi}{\lambda}\ (c_j - id_j)\ x$$

where

$$(c_j - id_j) = (n_j - i\ k_j) \cos\ \theta_j$$

from which

$$c_j = n_j \cos\varepsilon_j \cosh\ \Omega_j - k_j \sin\varepsilon_j \sinh\ \Omega_j$$

$$d_j = -n_j \sin\varepsilon_j \sinh\Omega_j + k_j \cos\varepsilon_j \cosh\Omega_j .$$

Equation 3.10 can now be applied by substituting c for n and d for k also in the case for S-waves with the substitutions

$$x' = \frac{2\pi}{\lambda}\ c_j\ x\ , \quad y = \frac{2\pi}{\lambda}\ d_j\ x$$

and $$P_1 = (\gamma_j{}^2 + \beta_j{}^2)/(c_j{}^2 + d_j{}^2)$$

$$P_2 = 1 + P_1$$

$$P_3 = 1 - P_1$$

$$P_4 = (\gamma_j c_j - \beta_j d_j)/(c_j^2 + d_j^2)$$

$$P_5 = (\gamma_j c_j + \beta_j d_j)/(c_j^2 + d_j^2)$$

where $$\gamma_j - i\,\beta_j = \frac{Z_j}{\cos\theta_j} \quad \text{for S-waves}$$

Equation 3.10 will now give the normal components for the absorption rate for both P- and S-waves.

The absorption rate along the direction of energy flow as a function of x (distance along the normal) can be found in the following way.

Note that the absorption rate is proportional to the intensity (equation 3.9).

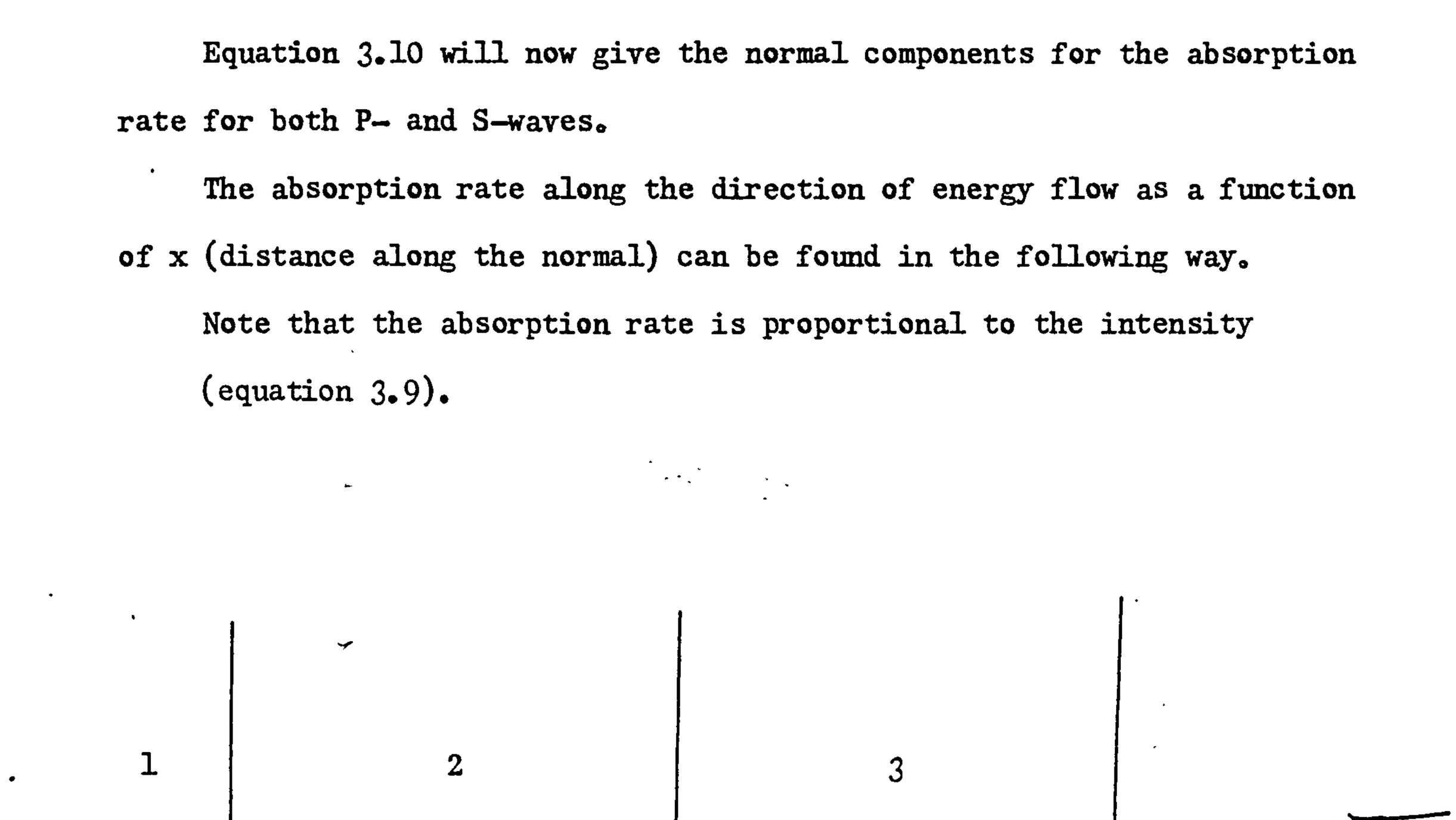

Unfortunately a simple expression for the flow of energy by an inhomogeneous wave does not exist but it should theoretically be possible to calculate α_j at each interface (diagram above) by the application of equation 3.21; $\underline{r}_1$ and $\underline{r}_2$ can be calculated using the generalised form of Snell's Law (equation 3.18); k_1 and k_2 can be evaluated from the relations given on page 45.

For the S-waves the energy flow is in the direction of $\underline{r}_1$, that is in a direction perpendicular to the planes of constant phase.

For P-waves the energy flow direction will be that of the vector equal to $A\,\underline{r}_1 + B\,\underline{r}_2$,

where
$$A = \frac{1}{2\,c\mu\mu_o}\,(\underline{E}^* \cdot \underline{E}) \cdot k_1$$
$$B = \frac{-1}{2c\,\mu\,\mu_o}\,(\underline{E}_2 \cdot \underline{E}_1) \cdot k_2 \,.$$

The absorption rate as a function of x is then given by equation 3.10 divided by the cosine (α). α is the direction of energy flow in a given layer and can be worked out as shown.

When working out the short circuit current for zero drift fields equation 3.12 gives the minority carrier concentration with the modification that σ everywhere has to be replaced by $\frac{\sigma}{\cos\alpha}$.

The short circuit current is given by equations 3.13, 3.14 and 3.15, remembering that I_j is replaced $\frac{I_j}{\cos\alpha}$ and F is the photon flux density at oblique incidence.

A computer program can be written and the short circuit current analysis for oblique incidence and zero electric field can be made.

CHAPTER 4

"INTERFERENCE" CELL WITH CONSTANT ELECTRIC FIELDS

4.1 Normal Incidence

Electric fields can be produced both in the top layer and the base layer of the cell by introducing donor or acceptor doping concentration gradients. These fields can aid the photogenerated carrier to reach the junction and so increase the photovoltaic current.

When electric fields are included the continuity equation which governs the minority carriers is

$$D_n \frac{d^2n}{dx^2} - \frac{n}{T_n} + nE_n \frac{dn}{dx} + A(a-x) = 0. \qquad ---\ 4.1$$

$A(a-x)$ is given by equation 3.10, n is the concentration of the minority carriers, T_n is the lifetime, D_n the diffusion constant, μ_n the mobility of the minority carriers and E_n the constant electric field inside the material. It is assumed that each photon absorbed generates one pair of minority carriers.

Equation 4.1 can be written as

$$(\zeta^2 - t^2 + B\zeta)\, n + \frac{A(a-x)}{D_n} = 0 \qquad ---\ 4.2$$

where $t^2 = \frac{1}{D_n T_n} = \frac{1}{L_n^2}$;

$B = \frac{\mu_n E_n}{D_n}$ and ζ is the differential operator.

The complementary function to 4.2 is

$$y = k_1 e^{+y_1 x} + k_2 e^{+y_2 x} \qquad \text{- - - 4.3}$$

$$\text{where } y_1 = \frac{-B + (B^2 + 4t^2)^{\frac{1}{2}}}{2}$$

$$y_2 = \frac{-B - (B^2 + 4t^2)^{\frac{1}{2}}}{2} .$$

The particular integral is

$$+ \frac{\sigma}{2} \frac{E_j E_j^*}{D_n} \left\{ (-P_4 BS + P_{\frac{3}{2}} (S^2 + t^2)) \cos (S(a-x)) + \right.$$

$$\left. (P_4 (S^2 + t^2) + P_{\frac{3}{2}} BS) \sin (S(a-x)) \right\}$$

$$- \frac{\sigma}{2} \frac{E_j E_j^*}{D_n} \left\{ \frac{\left(\frac{P_2}{4} + \frac{P_5}{2}\right) e^{\alpha(a-x)}}{\alpha^2 - t^2 - B\alpha} + \frac{e^{-\alpha(a-x)} \left(\frac{P_2}{4} - \frac{P_5}{2}\right)}{\alpha^2 - t^2 + B\alpha} \right\} \qquad \text{- - - 4.4}$$

The final solution is given by 4.3 + 4.4 and represents the carrier concentration as a function of x in layer j of figure 3.2. The constants k_1 and k_2 are found from the boundary conditions with reference to figure 3.3. Interface states are ignored throughout. For the jth layer the conditions are

a) $D_n \frac{dn}{dx} \Big|_{x=0} + \mu_n E_n n(0) = -S_n n(0)$ (surface recombination)

b) $n(a_j) = 0$ (zero bias condition).

For the $(j-3)$th layer the conditions are

a) $$D_n \frac{dn}{dx}\Big|_{x = a_{j-3}} + \mu_n E_n\, n(a_{j-3}) = -S_n\, n(a_{j-3})$$

(surface recombination)

b) $n(0) = 0$ (zero bias condition).

We can write the minority carrier concentration as

$$n = k_1\, e^{y_1 x} + k_2\, e^{y_2 x} + Q_1 \cos S(a-x) + Q_2 \sin S(a-x)$$

$$+ Q_3\, e^{\alpha(a-x)} + Q_4\, e^{-\alpha(a-x)} \qquad ---\ 4.5$$

where

$$Q_1 = \frac{\sigma}{2D_n}\, E_j\, E_j^* \left(-P_4 BS + P_3 \frac{(S^2+t^2)}{2}\right)$$

$$Q_2 = \frac{\sigma}{2D_n}\, E_j\, E_j^* \left(+P_4 (S^2+t^2) + P_3 \frac{BS}{2}\right)$$

$$Q_3 = \frac{-\sigma E_j\, E_j^* \left(\frac{P_2}{4} + \frac{P_5}{2}\right)}{2D_n \left(\alpha^2 - t^2 - B\alpha\right)}$$

$$Q_4 = \frac{-\sigma E_j\, E_j^* \left(\frac{P_2}{4} - \frac{P_5}{2}\right)}{2D_n \left(\alpha^2 - t^2 + B\alpha\right)}$$

The contribution to the short circuit from the jth layer is given by

$$J_j = e\, D_n \left.\frac{dn}{dx}\right|_{x = a_j} \cdot F$$

$$= e\, D_n\, F\; k_2(y_2\, e^{y_2\, a_j} - y_1\, e^{y_1\, a_j}) \quad - W_7(y_1\, e^{y_1 a_j} + W_8) \text{ - - - } 4.6$$

where $W_8 = Q_2 S - Q_3 \alpha + Q_4 \alpha$

$$W_7 = Q_1 + Q_2 + Q_4$$

and $$k_2 = (-W_7\, e^{-y_1\, a_j}) - W_6 \left(\frac{\frac{S_n}{D_n} - B) \quad + W_5}{y_1 - (\frac{S_n}{D_n} - B)}\right) \Big/$$

$$\frac{(\frac{S_n}{D_n} - B) \quad - y_2}{y_1 - (\frac{S_n}{D_n} - B)} \quad + \exp(y_2 - y_1)\, a_j$$

where $W_5 = -Q_1 S \sin(Sa) + Q_2 S \cos(Sa) - Q_3 \alpha\, e^{\alpha a} + Q_4 \alpha\, e^{-\alpha a}$

$$W_6 = Q_1 \cos(Sa) + Q_2 \sin(Sa) + Q_3\, e^{\alpha a} + Q_4\, e^{-\alpha a} .$$

The contributions from the depletion regions are again given by equation 3.14 on the assumption that all the absorbed photons generate minority carriers and that they are swept across before they have a chance to recombine.

The contribution from the base or $(j-3)$th layer of figure 3.3 is

$$J_{j-3} = -e D_n \left.\frac{dn}{dx}\right|_{x=0} \cdot F$$

$$= -e D_n F \left(k_2 (y_2 - y_1) - W_6 y_1 + W_5\right) \quad ---\ 4.7$$

where k_2 is now given by

$$k_2 = \frac{W_7 \left(\frac{S_n}{D_n} + B\right) + W_8}{\left(y_1 e^{y_1 b} + \left(\frac{S_n}{D_n} + B\right)\right)} - W_6$$

The total short circuit current is given by equation 3.16.

When the electric field is not uniform throughout the layer then the layer can be subdivided and equation 4.5 applied to each sublayer separately. The constants k_1 and k_2 would have to be worked out from the boundary conditions for each sublayer. The contribution to the current collection at the junction can then be worked out for each sublayer. The electric field is of course assumed to be constant within each sublayer.

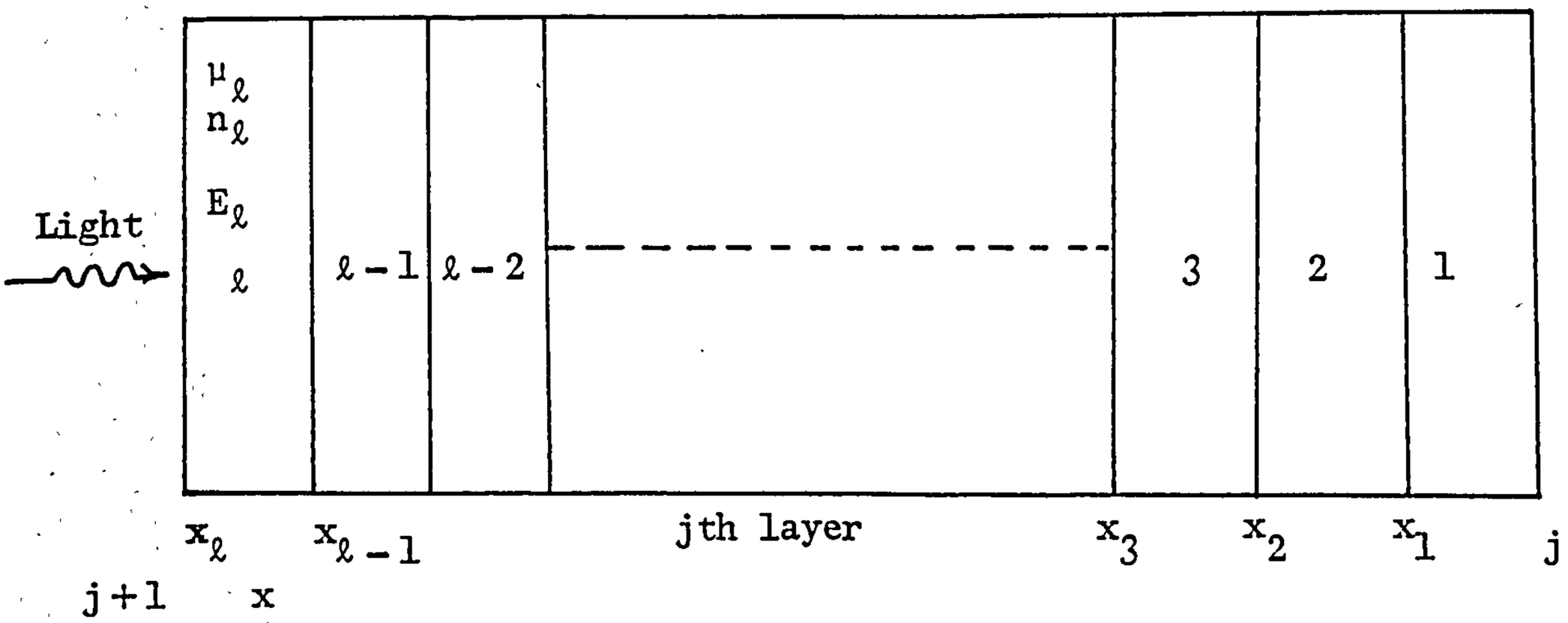

Figure 4.1

The boundary conditions for jth layer are, neglecting interface states and noting that n (x) is different for each sublayer

$$n_1 (a_1) = 0 \qquad \text{(zero bias externally)}$$

$$n_1 (0) = n_2 (a_2)$$

$$\vdots \qquad \text{(continuity of n)}$$

$$n_{\ell - 1} (0) = n_{\ell}(a_{\ell}) \quad (a_{\ell} \text{ is the thickness of } \ell\text{th sublayer})$$

$$D_{n1} \frac{dn_1}{dx}\bigg|_{x=0} + \mu_1 E_1 n_1(0) = D_{n2} \frac{dn_2}{dx}\bigg|_{x=a_2} + \mu_2 E_2 n_2(a_2)$$

$$D_{n2} \frac{dn_2}{dx}\bigg|_{x=0} + \mu_2 E_2 n_2(0) = D_{n3} \frac{dn_3}{dx}\bigg|_{x=a_3} + \mu_3 E_3 n_3(a_3)$$

$$D_{n\ell} \frac{dn_\ell}{dx}\bigg|_{x=0} + \mu_\ell E\, n_\ell(0) = S n_\ell n_\ell(0) \qquad \text{(surface recombination)}$$

For ℓ sublayers 2ℓ simultaneous equations have to be solved to find k_1 and k_2 for each sublayer. (a_ℓ is the thickness of ℓth sublayer)

The solution to a two sublayer model can be worked out from the following matrix relation

$$\begin{vmatrix} 1, & 1, & -e^{y_{12}a_2}, & -e^{y_{22}a_2} \\ D_{n1}(y_{11}+B_1), & D_{n1}(y_{21}+B_1), & -D_{n2}e^{y_{12}a_2}(y_{12}+B_2), & -D_{n2}e^{y_{22}a_2}(y_{22}+B_2) \\ e^{y_{11}a_1}, & e^{y_{21}a_1}, & 0, & 0 \\ 0, & 0, & y_{12}-W_9(2), & y_{22}-W_9(2) \end{vmatrix} \begin{matrix} k_{11} \\ k_{21} \\ k_{12} \\ k_{22} \end{matrix}$$

$$= \begin{vmatrix} W_7(2) - W_6(1) \\ D_{n2}B_2\ W_7(2) + D_{n2}\ W_8(2) - D_{n1}\ W_5(1) - D_{n1}B_1\ W_6(1) \\ -W_7(1) \\ W_9(2)\ W_6(2) - W_5(2) \end{vmatrix}$$

where the 2nd subscript and number in brackets refers to the number of the sublayer (figure 4.1) and $W_9 = \frac{S_n}{D_{n2}} - B_2$.

The current contribution from the jth layer is then given by

$$e\ D_{n1}\frac{dn_1}{dx}\Big|_{x=a_1} + e\ D_{n2}\frac{dn_2}{dx}\Big|_{x=a_2+a_1} \qquad \text{(top layer)}$$

which can be calculated from equation 4.5.

The general solution for sublayers in the jth layer is worked out as follows

$$\text{Let } M = \begin{vmatrix} a_{11} & a_{12} & a_{13} & a_{14} \\ a_{21} & a_{22} & a_{23} & a_{24} \end{vmatrix}$$

where $a_{11} = 1,\ a_{12} = 1,\ a_{13} = -e^{y_{1\ell}\ a_\ell}$

$a_{14} = -e^{y_{2\ell}\ a_\ell},\quad a_{21} = D_{n(\ell-1)}(y_{1(\ell-1)} + B_\ell)$

$a_{23} = -D_{n\ell}e^{y_{1\ell}\ a_\ell}(y_{1\ell} + B_\ell),\ a_{22} = D_{n(\ell-1)}(y_{2(\ell-1)} + B_\ell)$

$a_{24} = -D_{n\ell}e^{y_{2\ell}\ a_\ell}(y_{2\ell} + B_\ell)$

Let $\left|\phi_\ell\right| = \left|0\ ,\ 0\ ,\ --\ ,\ 0\ ,\ y_{1\ell} - W_9(\ell)\ ,\ y_{2\ell} - W_9(\ell)\right|$

$\left|\phi_1\right| = \left|e^{y_{11}\ a_1}\ ,\ e^{y_{21}\ a_1}\ ,\ 0\ ,\ 0\ ,\ ---------0\ ,\ 0\right|$

The general matrix can be written as

$$\begin{vmatrix} M_2\ ,\ 0\ ,\ ----------0 \\ 0\ ,\ 0\ ,\ M_3\ ,\ 0\ ,\ ------0 \\ 0\ ,\ 0\ ,\ 0\ ,\ M_4\ ,\ 0\ ,\ ---0 \\ ---------- \\ 0\ ,\ 0\ ,\ ---------0\ ,\ M_\ell \\ \phi_1\ ,\ ---------0\ ,\ 0 \\ 0\ ,\ 0\ ,\ ----------\phi_\ell \end{vmatrix} \begin{vmatrix} k_{11} \\ k_{21} \\ k_{12} \\ k_{22} \\ \vdots \\ k_{1\ell} \\ k_{2\ell} \end{vmatrix} = \begin{vmatrix} U_2 \\ U_3 \\ \vdots \\ U_\ell \\ -W_7(1) \\ W_9(\ell)\ W_6(\ell) - W_5(\ell) \end{vmatrix}$$

i.e. $\underline{A}\ \underline{k} = \underline{U}$ --- 4.8

where

$$U_{\ell} = \begin{vmatrix} W_7(\ell) - W_6(\ell-1) \\ D_{n\ell}W_8(\ell) + D_{n\ell}B\ W_7(\ell) - D_{n\ell-1}W_5(\ell-1) - D_{n\ell-1}B_{\ell-1}\ W_6(\ell-1) \end{vmatrix}$$

By writing a suitable computer program the k's can be calculated for each sublayer.

The contribution to the short circuit current from the jth layer is calculated in the same way as for the two layer model. The contribution from the base or $(j-3)$th layer of figure 3.3 is calculated as follows

$(j-3)$th layer

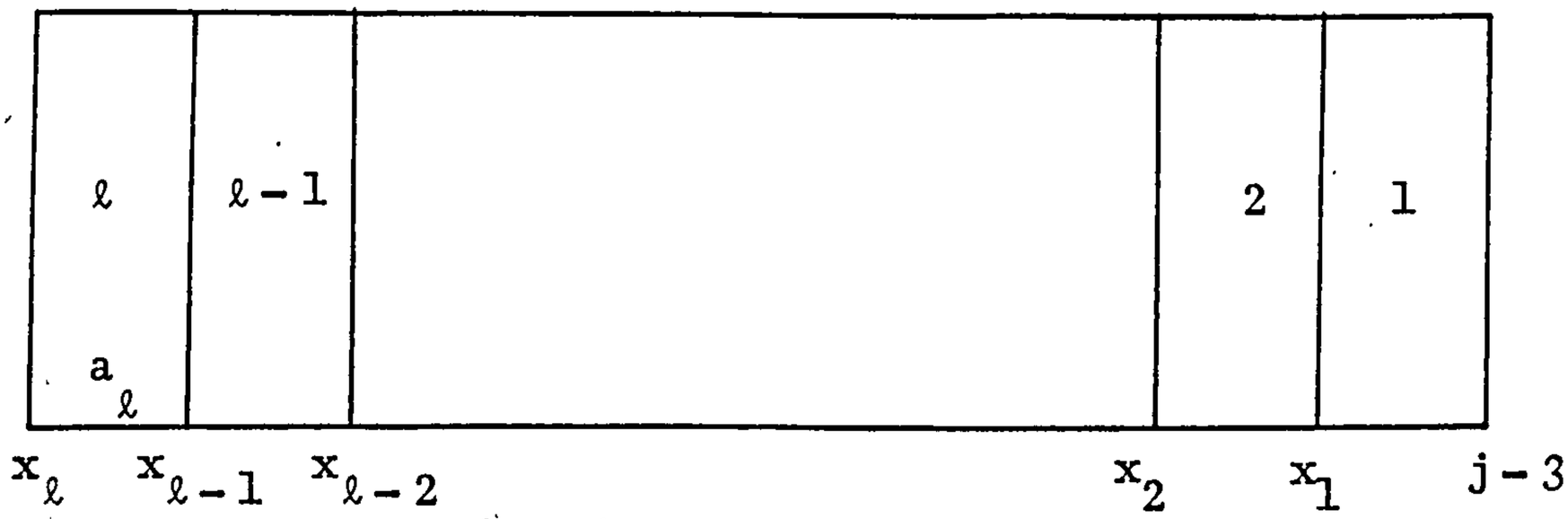

In the case of the $(j-3)$th layer an identical relation to 4.8 exists. M's are identical in form and so are U's; but ϕ_1 is now given by the boundary condition.

$$\left.\frac{dn_1}{dx}\right|_{x=a_1} = \left(\frac{-S_n}{D_n} - B_1\right)\ n(a_1) \qquad \text{and}$$

ϕ_ℓ is given by the boundary condition $n_\ell(0) = 0$

$$\phi_1 = \left| \begin{array}{cc} y_{11}\, e^{y_{11} a_1} + \frac{S_n}{D_{n1}} + B_1 & , \quad y_{21}\, e^{y_{21} a_1} + \frac{S_n}{D_{n1}} + B_1 \\ \text{- - - 0} & \end{array} \right| ,$$

$$\phi_\ell = \left| \begin{array}{cc} 0 , 0 , \text{- -} & 1 , 1 \end{array} \right|$$

The short circuit current contribution from the $(j-3)$th base layer is given by

$$J_{j-3} = -e\, D_{n1} \frac{dn_1}{dx}\Big|_{x = -(a_2 + a_3 + \text{- -} \quad a_\ell)}$$

$$-e\, D_{n2} \frac{dn_2}{dx}\Big|_{x = -(a_3 + a_4 + \text{- -} \quad a_\ell)}$$

$$\text{- - - - - - - - - - - - -} \qquad -e\, D_{n_\ell} \frac{dn_\ell}{dx}\Big|_{x = 0}$$

The total current collected at the junction is again given by

J total $= /J_j/ + /J_d/ + /J_{j-1}/$ where J_d is the contribution from the depletion regions as given by equation 3.14.

4.2 Oblique incidence with Electric Field

The same arguments apply here as in the case for the zero electric field. The absorption rates for the P- and S- waves is calculated from equation 3.10 with modifications for oblique incidence. The direction of energy flow is also calculated as discussed in the case for zero electric field. In equation 4.4 σ has to be divided by the cosine of the angle the energy flow

makes with the normal.

Graded band gap solar cell

In a graded band gap solar cell the band gap varies with thickness. If the top layer of the cell was graded in such a way that it moved the minority carriers towards the junction, there would be less left at the surface to recombine. Very high electric fields can be obtained in a graded band gap layer. For example, if the energy gap grading only affects the bottom of the conduction band, a 0.3 eV increase in the energy gap in the range 1 μm corresponds to an internal electric field of up to 300 V cm^{-1} (Makota et al 1975).

The theory described above for non-zero electric fields can equally well be applied to the graded band gap solar cell, but it has to be remembered that in the case for the graded band gap layer the absorption coefficient varies with distance i.e. it is a function of the band gap. In this model then a different value for the absorption coefficient as well as the electrical parameters have to be entered for each sublayer. This really is a correct model for a step graded gap solar cell, but the more steps that can be introduced (depending on the capacity of the computer) the more it will resemble a smooth graded band gap solar cell. T. S. Moss (1959) discusses absorption processes in semiconductors, i.e. variation of the absorption coefficient with the band gap, for instance.

CHAPTER 5

COMPUTER ANALYSIS FOR THE "INTERFERENCE" CELL

(Normal incidence and zero electric fields)

5.1 Introduction

Data for AM1 radiation was obtained from M. P. Thakaekora (1974). AM1 radiation is approximately 100 mW per cm^2 and is the sun's energy that falls on Earth on a clear day at zero zenith. Figure 5.1 is a graph for AM1 radiation in which the total integrated photon flux is plotted against the photon energy. The band gap for Si is 1.1 ev; the corresponding photon flux from figure 5.1 is 24.3×10^{20} photons per m^2 per second. Assuming all the photons are absorbed and generate minority carriers and that there are no losses due to surface and bulk recombinations the corresponding short circuit current is 38.8 mA per cm^2.

For a Cu_2S, the band gap energy is approximately 1.2 ev and the corresponding photon flux from figure 5.1 is 20.8×10^{20} photons per m^2 per second. The corresponding short circuit current is 33.3 mA per cm^2.

Therefore the maximum short circuit that a Si–Si cell can generate from AM1 radiation is 38.8 mA per cm^2 per second, whereas the Cu_2S–CdS cell can generate a maximum short circuit current of 33.3 mA per cm^2.

The smaller the band gap, the higher the maximum possible short circuit current that can be generated. However, the smaller the band gap the lower will be the open circuit voltage.

It follows then that there is an optimum band gap energy for which the overall efficiency, after taking into account dark currents, is a maximum. Such calculations have been made for a P-N homo–junction, for example by P. Rappaport (1959). The optimum band gap energy is around 1.4 ev. No such calculations exist for a Schottky barrier cell. For a heterojunction cell (de Vos, 1977) the larger band gap should be greater than 1.5 ev and the smaller one equal to 1.1 ev to give an efficiency of 30%.

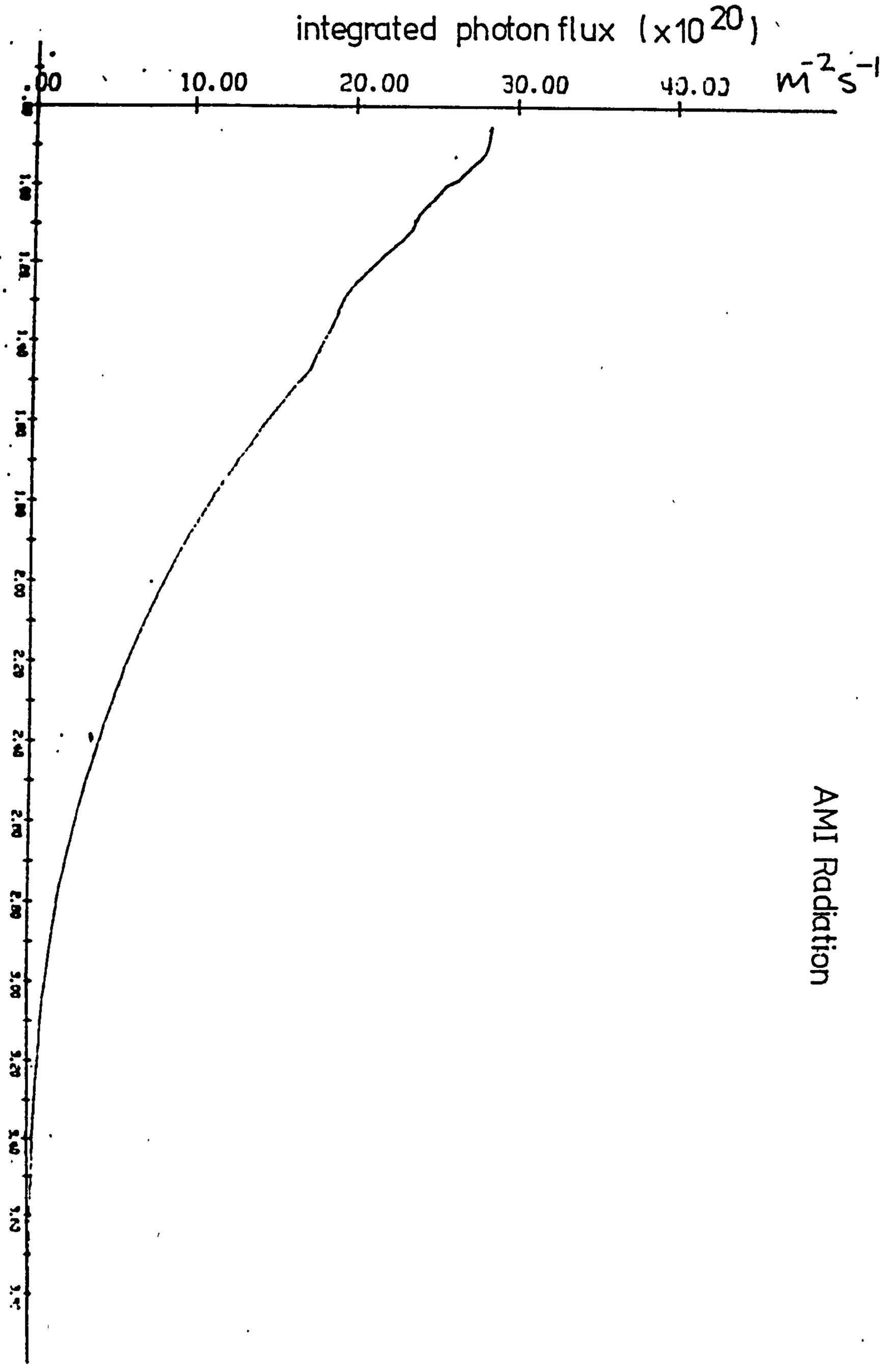

FIGURE 5.1

Figure 5.1 Photon flux V_s photon energy for AM1 radiation

5.2 Intensity and Absorption rates in a Multilayer Stack

Figure 5.2 shows graphs of intensity, the absorption rate and the mean square of the electric vector as functions of position for a Cu_2S– CdS solar cell having the following configuration.

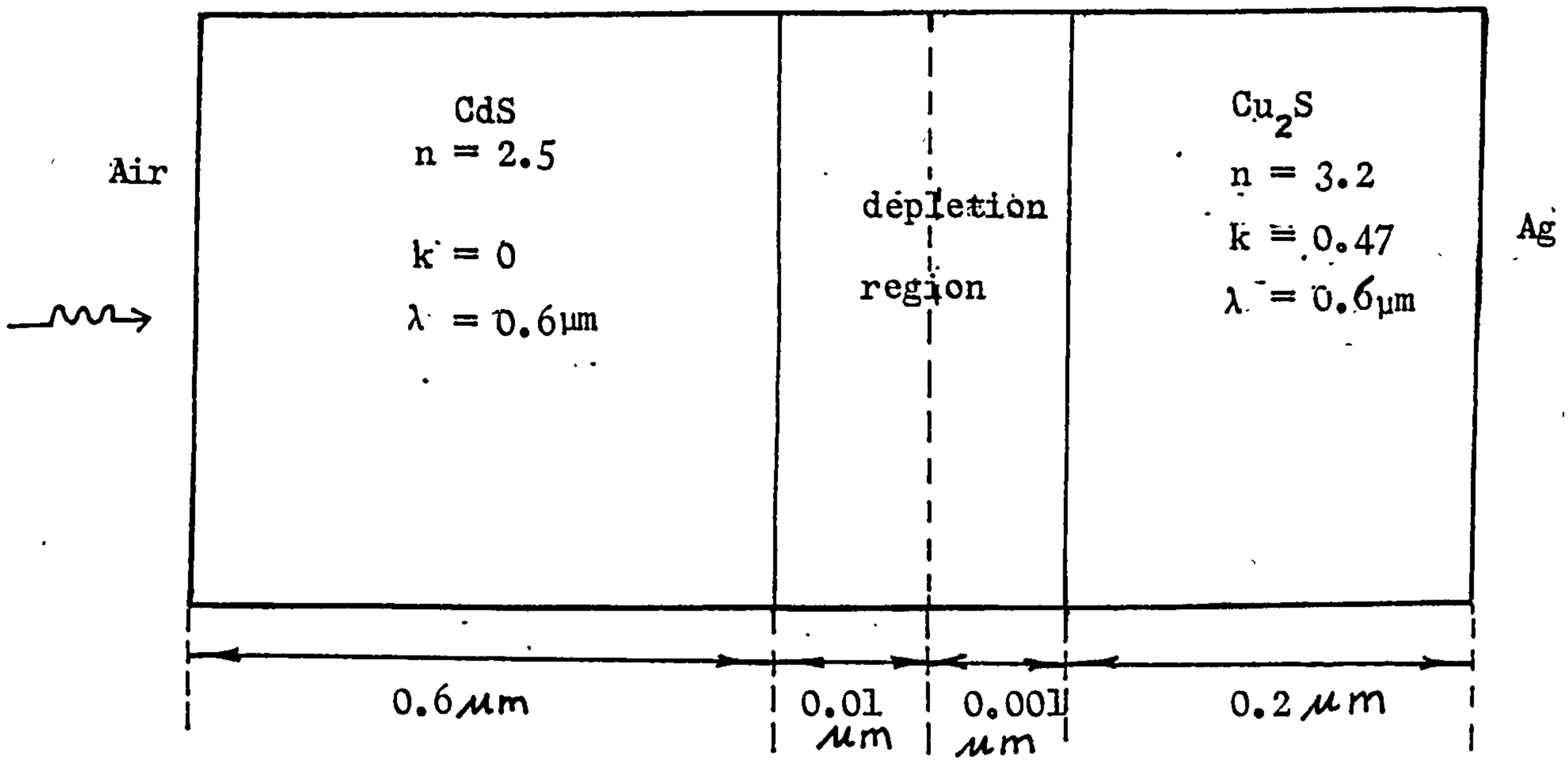

Light of wavelength 0.6μm is made to shine on the CdS side. Refractive index of Cu_2S was taken as 3.2 and the extinction coefficient calculated as 0.47 from the absorption coefficient taken as 10^5 cm^{-1} (Rothwarf and Boer 1975) and bearing in mind that such data was not well established. (B. J. Mulder 1973)

Absorption coefficient data for CdS was taken from Loferski (1963) and the remaining optical data for CdS and Ag was taken from the American Institute of Physics handbook 3rd edition.

The following notation of symbols will make it easier to identify the graphs in figures 5.2 to 5.9.

Δ – represents the mean square of the electric vector

X – represents the absorption rate

□ – represents the intensity

Figures 5.2

1. Square of electric vector Vs wavelength
2. Absorption Rate Vs wavelength
3. Intensity of light Vs wavelength
(for notation see page 66)

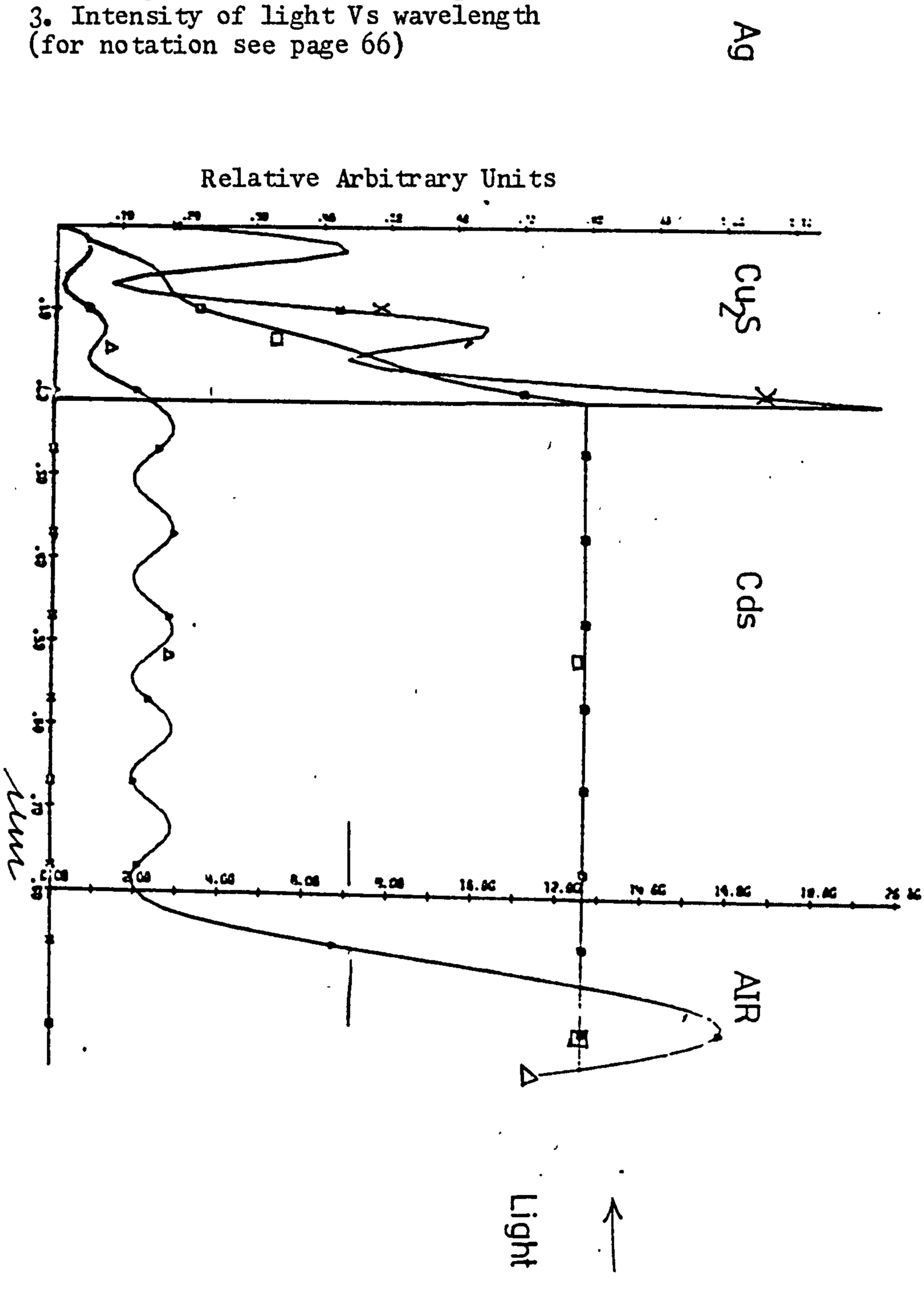

FIGURE 5.2

Looking at the $\bar{E}^2$ graph in figure 5.2 one can see a standing wave being set up in front of the CdS in air and also a standing wave with a smaller amplitude being set up in the CdS.

A standing wave can also be observed in the Cu_2S but its amplitude is attenuating.

The $\bar{E}^2$ graph is calculated from equation 3.8. The higher the reflectance at the interface between CdS and air as shown in figure 5.2, the larger will be the amplitude of $\bar{E}^2$ in front of the CdS layer in air at the expense of the amplitude in CdS.

The same argument applies to the CdS and Cu_2S interface but it has to be remembered that the amplitude in Cu_2S is also attenuating due to absorption.

The standing waves are set up as a result of multiple reflections from each interface as well as the substrate which in the case of figure 5.2 is silver. The reflected waves and the forward travelling waves superpose resulting in optical interference of the waves.

From the graphs of the intensity and absorption rate in figure 5.2 one can see that there is a total reflection of just over 20 percent for the assembly as a whole and that the absorption rate is a maximum where the slope of the curve is steepest and that it is a minimum where the intensity is least steep as expected.

The intensity is calculated from equation 3.7 and the absorption rate from equation 3.10.

Figure 5.3 shows graphs of $\bar{E}^2$, absorption rate and the intensity for the same cell as for figure 5.2, at the same wave length but with the silver substrate substituted by air.

Figure 5.3

1. Square of electric vector Vs wavelength
2. Absorption Rate Vs wavelength
3. Intensity of light Vs wavelength

(for notation see page 66)

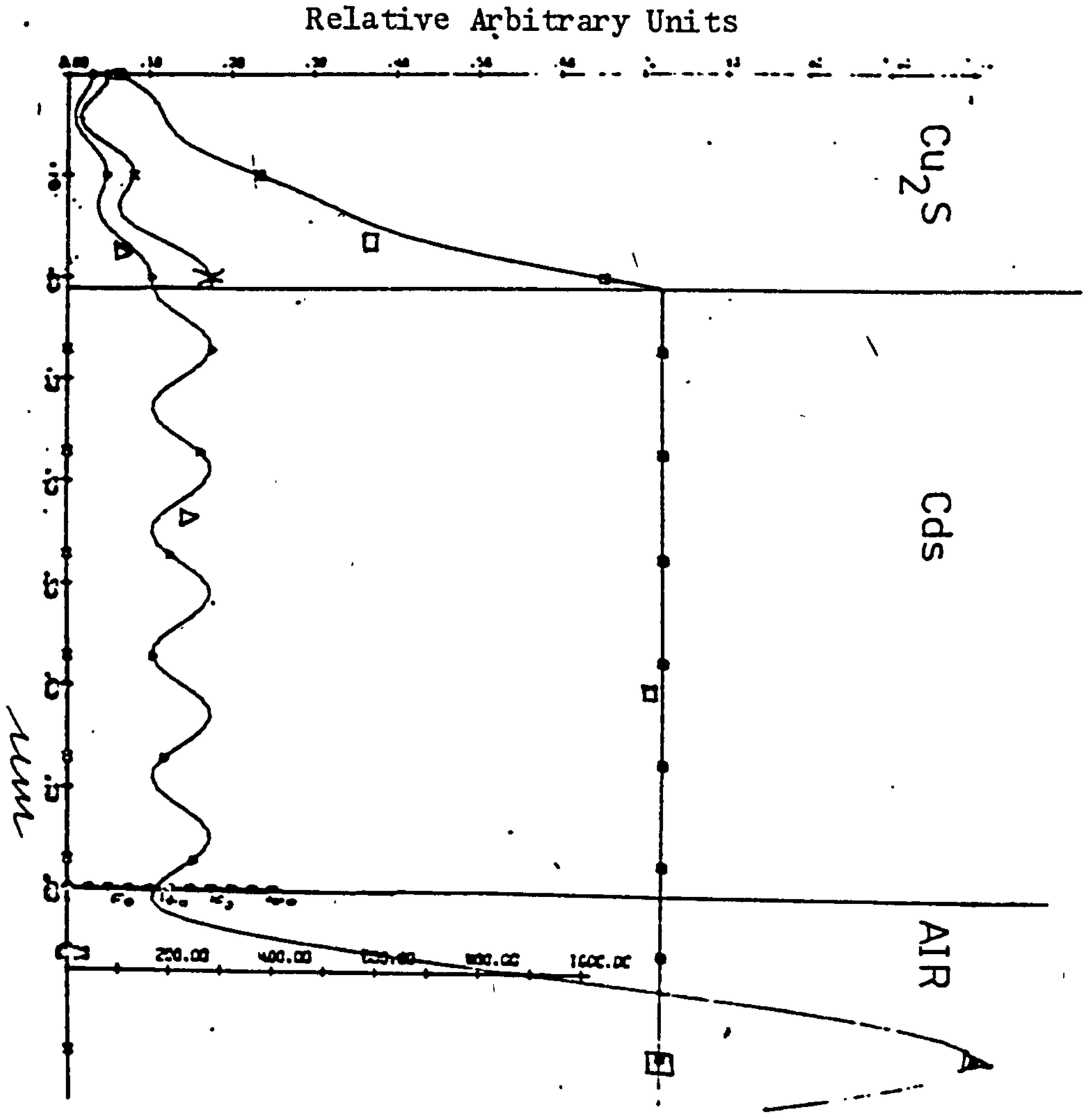

FIGURE 5.3

The absorption rate in the Cu_2S layer in figure 5.3 can be seen to have fallen in comparison to that in figure 5.2. The reason for it is that there is no longer sufficient light coming back into the Cu_2S layer after reflection at the back as in the case with a silver substrate. Even though more light enters a cell backed by an air substrate the absorption is greatest in a silver substrate case. This is an illustration of the fact that the substrate can alter the optical interference conditions and hence affect the absorption rate.

The graphs of $\bar{E}^2$, absorption rate and the intensity in figure 5.4 illustrate how altering the thickness of the CdS layer alone can affect the absorption rate in the Cu_2S layer. The thickness for the CdS layer is changed to 0.4μm and everything else kept the same as for figure 5.3. Comparing figures 5.3 and 5.4 it can be seen that in going from figure 5.3 to figure 5.4 the absorption rate has risen and the reflectance for the assembly as a whole has fallen by 50%.

The effect of altering the CdS thickness is to change the phase which in turn alters the optical interference conditions.

When the total optical thickness for the assembly is a multiple of $\frac{\lambda}{2}$ the amplitude of the standing wave in front of the assembly is a minimum, or zero if the assembly is entirely dielectric. When absorbing materials are included in the assembly an amplitude condition must also be satisfied for zero reflection.

In the examples that follow the light enters the cell from the Cu_2S side at a wave length of 0.6μm .

The graphs in figure 5.5 are for a cell with a Cu_2S thickness of 0.1μm and a CdS thickness of 0.6μm. The depletion regions are of the same thickness as in the previous examples. The substrate is silver.

Figure 5.4

1. Square of electric vector Vs wavelength
2. Absorption Rate Vs wavelength
3. Intensity of light Vs wavelength

(for notation see page 66)

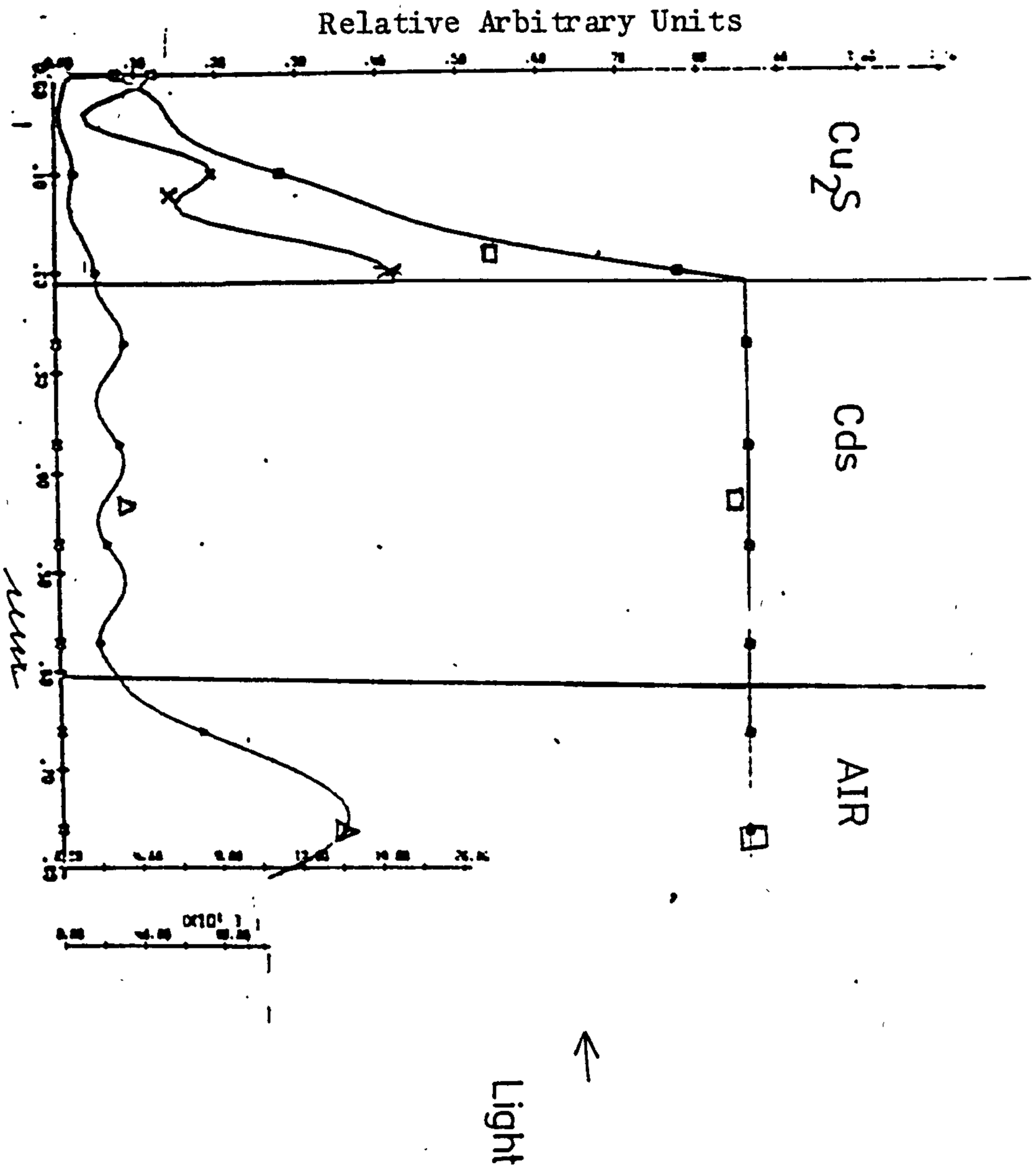

FIGURE 5.4

Figure 5.5

1. Square of electric vector Vs wavelength
2. Absorption Rate Vs wavelength
3. Intensity of light Vs wavelength

(for notation see page 66)

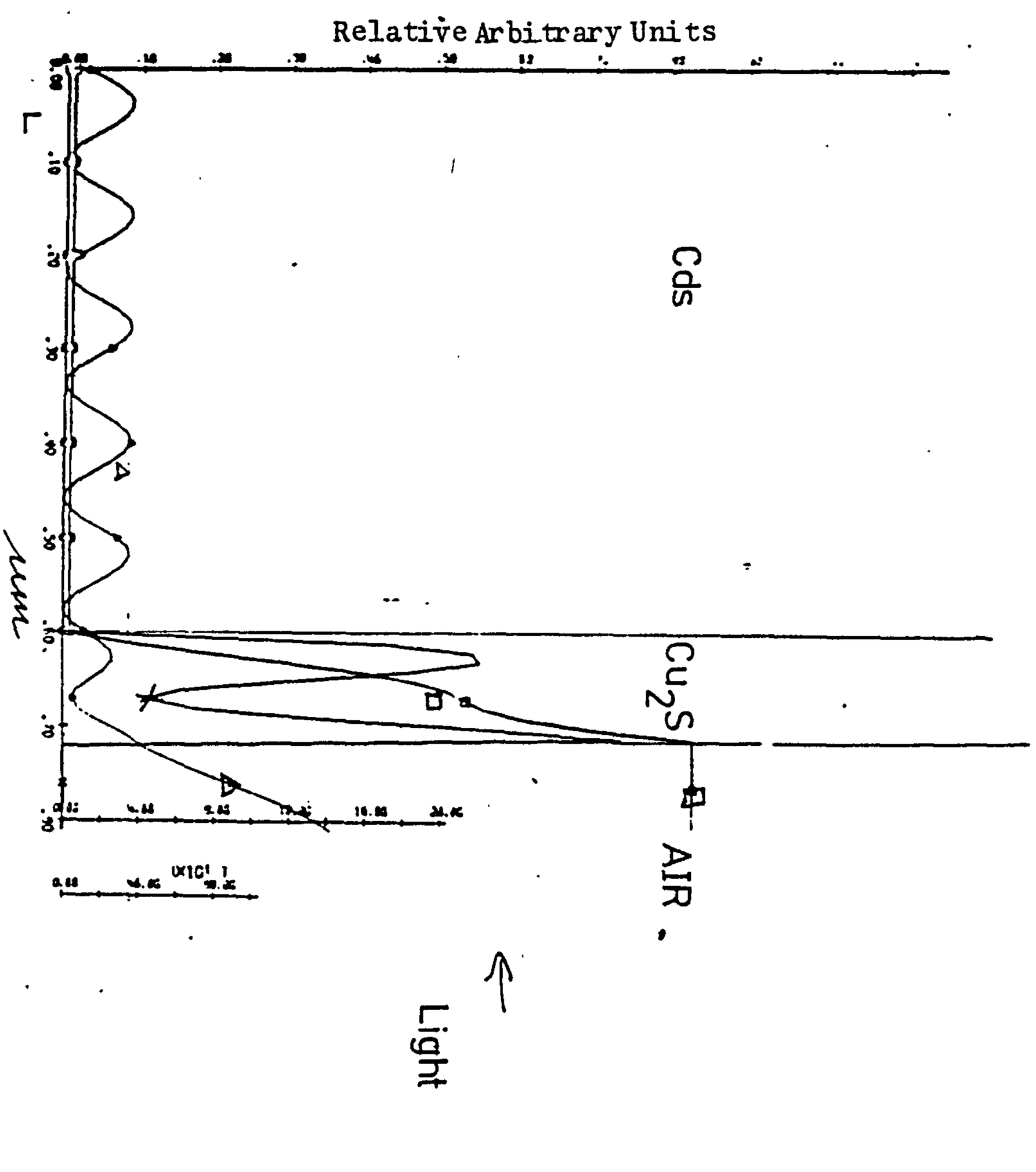

FIGURE 5.5

The graphs in figure 5.6 are for a cell identical in every respect except that it has air in place of the substrate.

In the case of figure 5.7 the CdS layer is of 0.4μ thickness, otherwise the cell is the same as for figure 5.5.

Figure 5.5 shows strong absorption in the Cu_2S layer with about 15 per cent reflectance from the assembly. Figure 5.6 shows reflectance of about 22 per cent with absorption low compared to figure 5.5. Figure 5.7 shows reflectance of about 25 per cent with good absorption in the Cu_2S layer. The absorption in figure 5.7 is low in comparison to figure 5.5 and due mostly to reflection losses as can be observed from the graphs.

The graphs in figure 5.8 are for a cell with the Cu_2S layer of 0.2μm thickness and a CdS layer of 0.4μm thickness. The substrate is silver. Figure 5.8 shows about 30 per cent reflection with good absorption in the Cu_2S layer. There are also three maximum values for the absorption rate in figure 5.8 as compared to figures 5.5, 5.6 and 5.7 in which there are only two maxima each.

In figure 5.9 the graphs are for a cell with a CdS layer of 0.2μm thickness and a Cu_2S layer of 0.1μm. The substrate is again silver. Here one notices very strong reflection of nearly 60 per cent with strong absorption in the Cu_2S layer with only a single maximum value lying roughly in the middle of the layer.

The graphs of $\bar{E}^2$, absorption rate and the intensity in figures 5.2 to 5.9 have illustrated a number of points. Firstly the absorption rate can be maximised by having a strongly reflecting back surface. It can be maximised by varying and selecting the optimum thickness of the Cu_2S and CdS layers. It can further be maximised by reducing reflection losses from the assembly as a whole. As the layers are made thinner the number of maxima for the absorption rate curve are reduced.

Figure 5.6

1. Square of electric vector Vs wavelength
2. Absorption Rate Vs wavelength
3. Intensity of light Vs wavelength

(for notation see page 66)

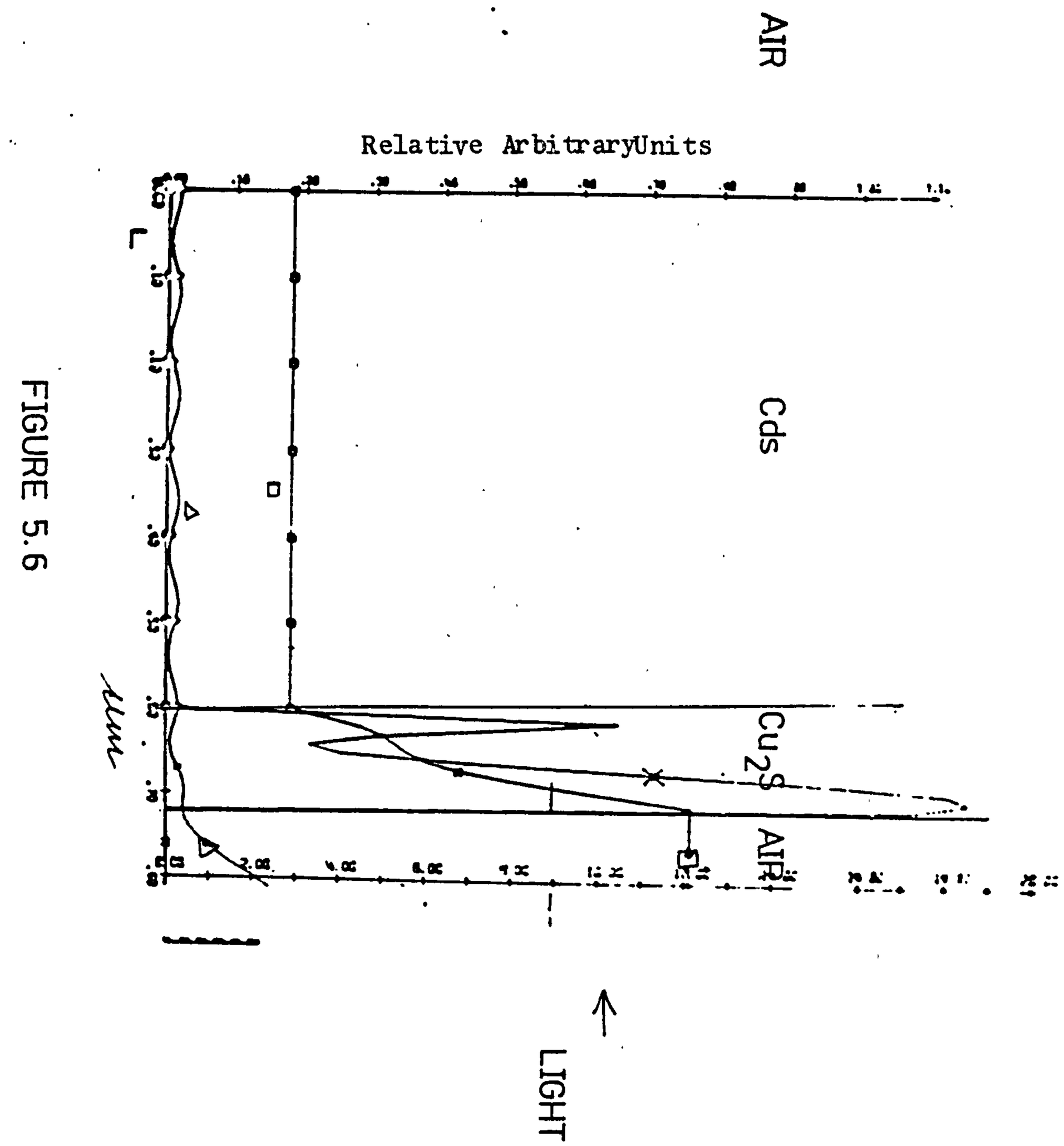

FIGURE 5.6

Figure 5.7

1. Square of electric vector Vs wavelength
2. Absorption Rate Vs wavelength
3. Intensity of light Vs wavelength

(for notation see page 66)

Ag

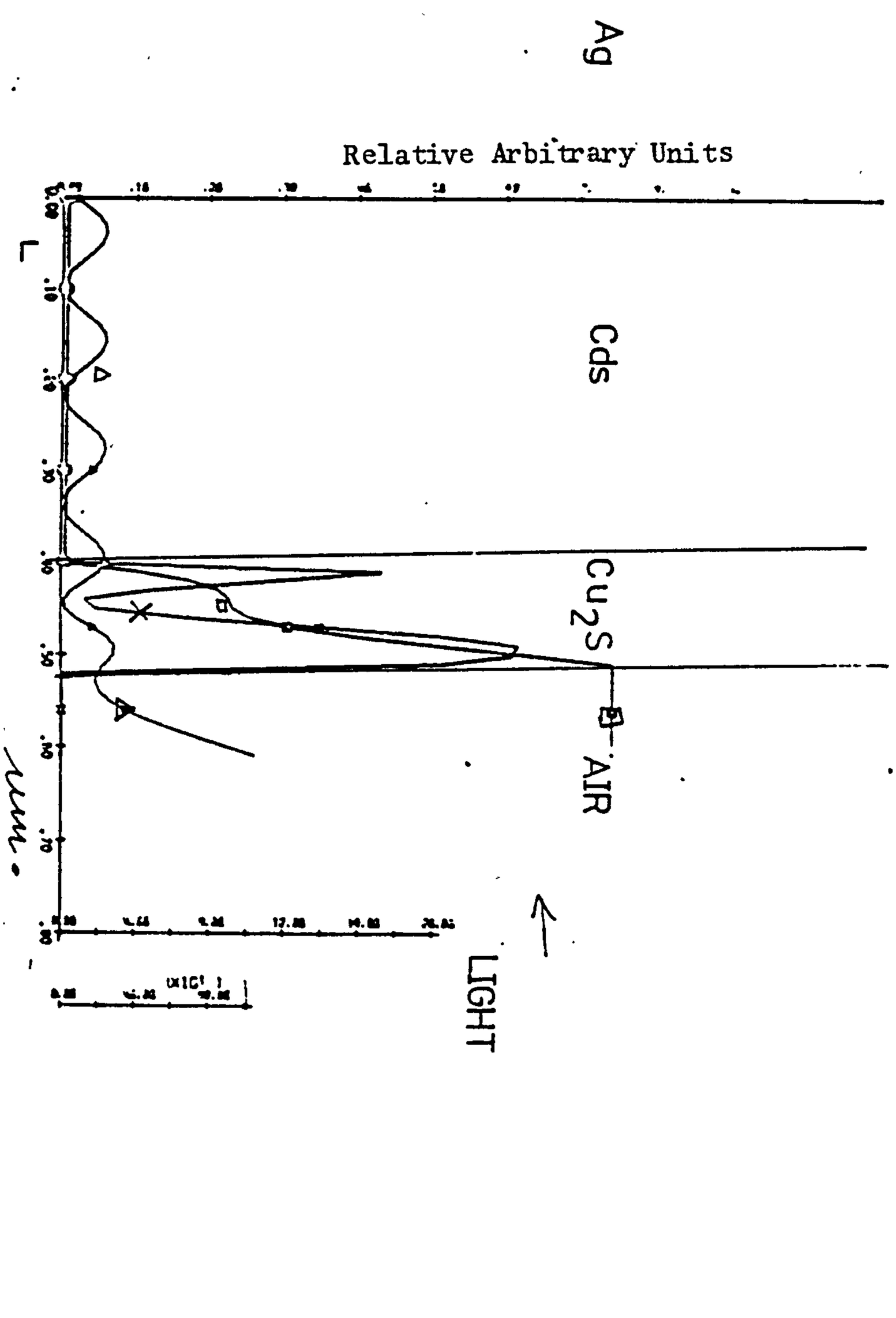

FIGURE 5.7

Figure 5.8

1. Square of electric vector Vs wavelength
2. Absorption Rate Vs wavelength
3. Intensity of light Vs wavelength

(for notation see page 66)

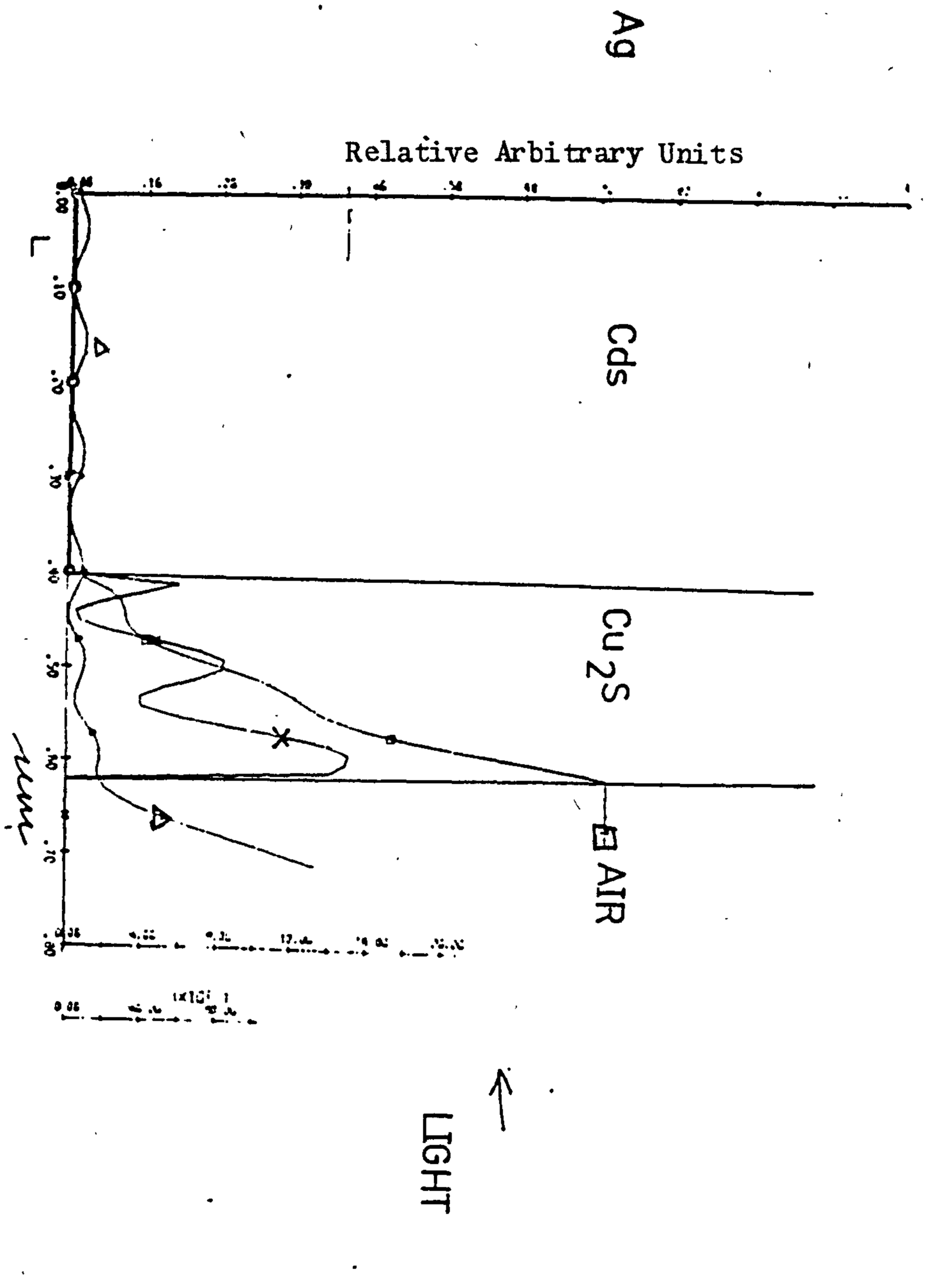

FIGURE 5.8

Figure 5.9

1. Square of electric vector Vs wavelength
2. Absorption Rate Vs wavelength
3. Intensity of light Vs wavelength

(for notation see page 66)

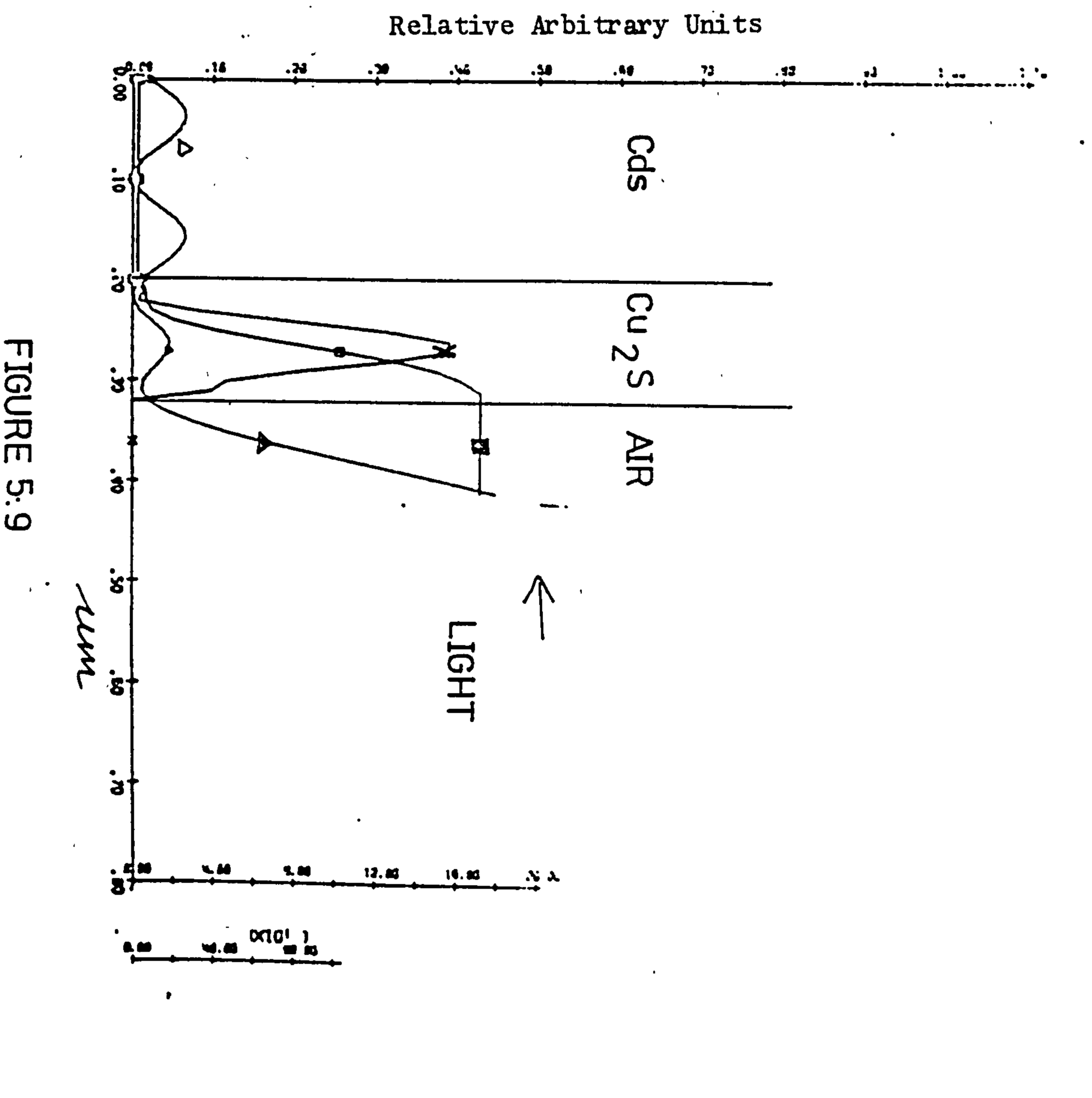

FIGURE 5.9

From the point of view of collecting minority carriers at the junction it is desirable to have the maxima, preferably a single maximum of the absorption rate curve as near as possible to the junction. This would mean that most of the absorption occurs close to the junction; thereby reducing losses from recombination, both surface and bulk.

By first maximising the absorption rate at any reflectance of the assembly, the reflectance can then be minimised by adding on suitable anti-reflection coatings.

Alternatively, the assembly including the antireflection coating layers can be analysed as a whole and the absorption rate maximised accordingly, at the same time ensuring minimum reflectance for the assembly.

As an illustration the absorption curve in figure 5.9 would be quite desirable as most of the absorption occurs nearer to the junction than the front surface, bearing in mind that antireflection coatings would have to be used to reduce the reflection losses to a sufficiently low value.

So far only single wavelength absorption has been considered. To be of practical use the above optimisation of the absorption rate must occur over a wide range of wave lengths as possible. It must be remembered that CdS becomes absorbing at wavelengths shorter than 0.5 μm and contributes to the generation of the minority carriers.

Although digressing a little it should be mentioned that the above analysis when carried out systematically would be most useful in optimising the efficiency of photocathodes also. Other methods for optimising the efficiency of photocathodes have been discussed by Kossel et al (1969).

Most of the absorption in photocathodes occurs in the first 10 Å under the surface so that a maximum of the absorption rate as near as possible to the surface is most desirable. For instance a peak in the absorption rate such as the one in figure 5.9 could be shifted towards the surface by altering for example the thickness of the dielectric layer between a back reflecting surface and the photoemmissive material. The advantage of this analysis is that the same computer program can be used for working out reflectances, transmittances and absorptances for a multi-layer with any number and order of arrangements of the constituent absorbing and dielectric layers. In fact all the different designs discussed by Kossel et al (1969) could be worked out using the analysis in this report. It also makes it possible to look for new designs whilst using the same theoretical equations.

5.3 Spectral Response curves for Cu_2S - CdS cells

Table 5A lists the values of parameters and the main results for the spectral response curves from figures 5.10 to 5.18.(definition on page 90).

For the curves in figures 5.10 to 5.18 the following notation of symbols is used;

Δ - represents the absorptance f(λ)

□ - represents the spectral response for the CdS + Cu_2S layers

0 - represents the spectral response for the Cu_2S layer

\+ - represents the spectral response for the CdS layer

X - represents the spectral response for the CdS + Cu_2S layers assuming zero reflection of the whole assembly.

AM1 radiation data is used for the light entering the cell through the Cu_2S layer first.

Table 5A Absorptance, reflectance, collection efficiency and photogenerated current for Cu_2S–Cds substrate thin film solar cells.

5.10	5.11	5.12	5.13	5.14	5.15	5.16	5.17	5.18	Figure
10.0	10.0	10.0	10.0	10.0	1.0	1.0	1.0	1.0	CdS Thickness
0.1	0.1	0.1	0.1	0.1	0.1	0.1	0.1	0.1	Cu_2S Thickness
38.1	30.8	38.1	38.1	38.1	37.5	37.5	37.5	37.5	% Reflectance R Whole assembly for $\lambda d\lambda$
61.3	51.2	61.3	61.3	60.5	61.6	61.6	61.6	61.6	% Absorption
Ag	Mo	Ag	Ag	Ag	Ag	Ag	Ag	Ag	Substrate
19.2	16.7	20.0	20.1	20.1	20.4	15.4	10.0	19.3	Total current MA cm^{-2} R ≠ 0
31.0	24.1	32.3	32.5	32.5	32.7	24.6	16.0	30.9	Total current MA cm^{-2} R = 0
93.2	72.5	97.2	97.6	97.7	98.2	74.1	48.1	93.0	% Collection efficiency over entered flux
57.7	50.1	60.2	60.5	60.5	61.4	46.3	30.1	58.1	% Collection efficiency over incident flux with $h\nu > Eg$
94.1	98.0	98.1	98.6	98.6	99.7	75.1	48.8	94.4	% collection efficiency over absorption
2.0	2.0	2.0	2.0	2.0	2.0	0.1	0.05	0.3	Diffusion length Cu_2S μm
2.0	2.0	2.0	2.0	2.0	2.0	2.0	2.0	2.0	Diffusion length CdS μm
10^5	10^4	10^4	10^0	10^0	10^0	10^4	10^4	10^4	S.R.V. front cmS^{-1}
10^{50}	10^{50}	10^{50}	10^{50}	10^0	10^0	10^{50}	10^{50}	10^{50}	S.R.V. back cms^{-1}

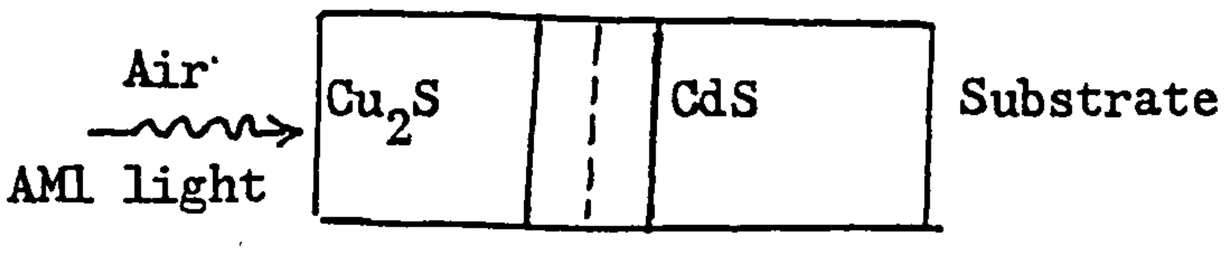

depletion regions:

Cu_2S 0.001μm thick

CdS 0.01μm thick

Figure 5.10 Absorptance and spectral response curves for Cu_2S–CdS cells
(for notation see page 79)

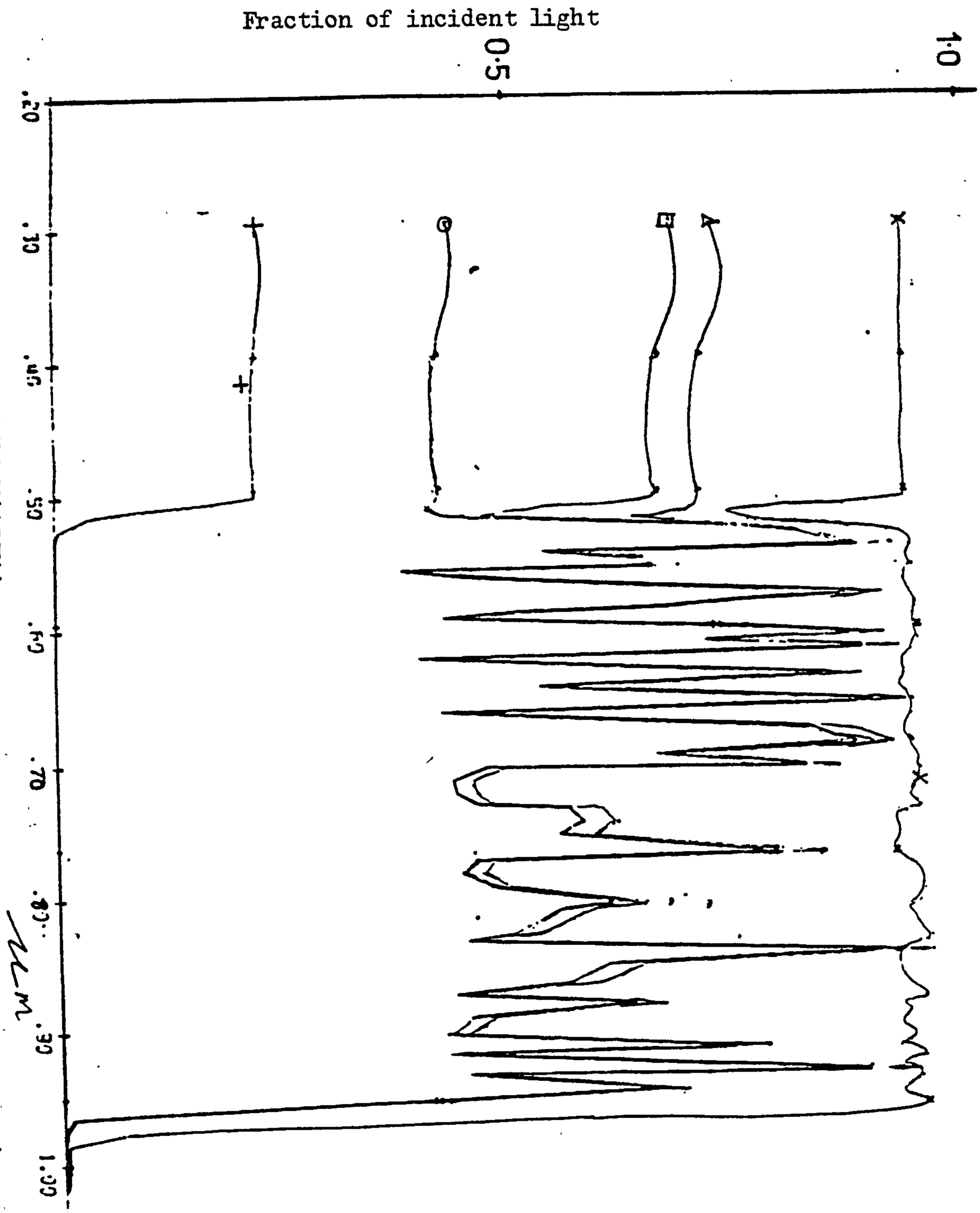

FIGURE 5.10

Figure 5.11 Absorptance and spectral response curves for Cu_2S-CdS cells
(for notation see page 79)

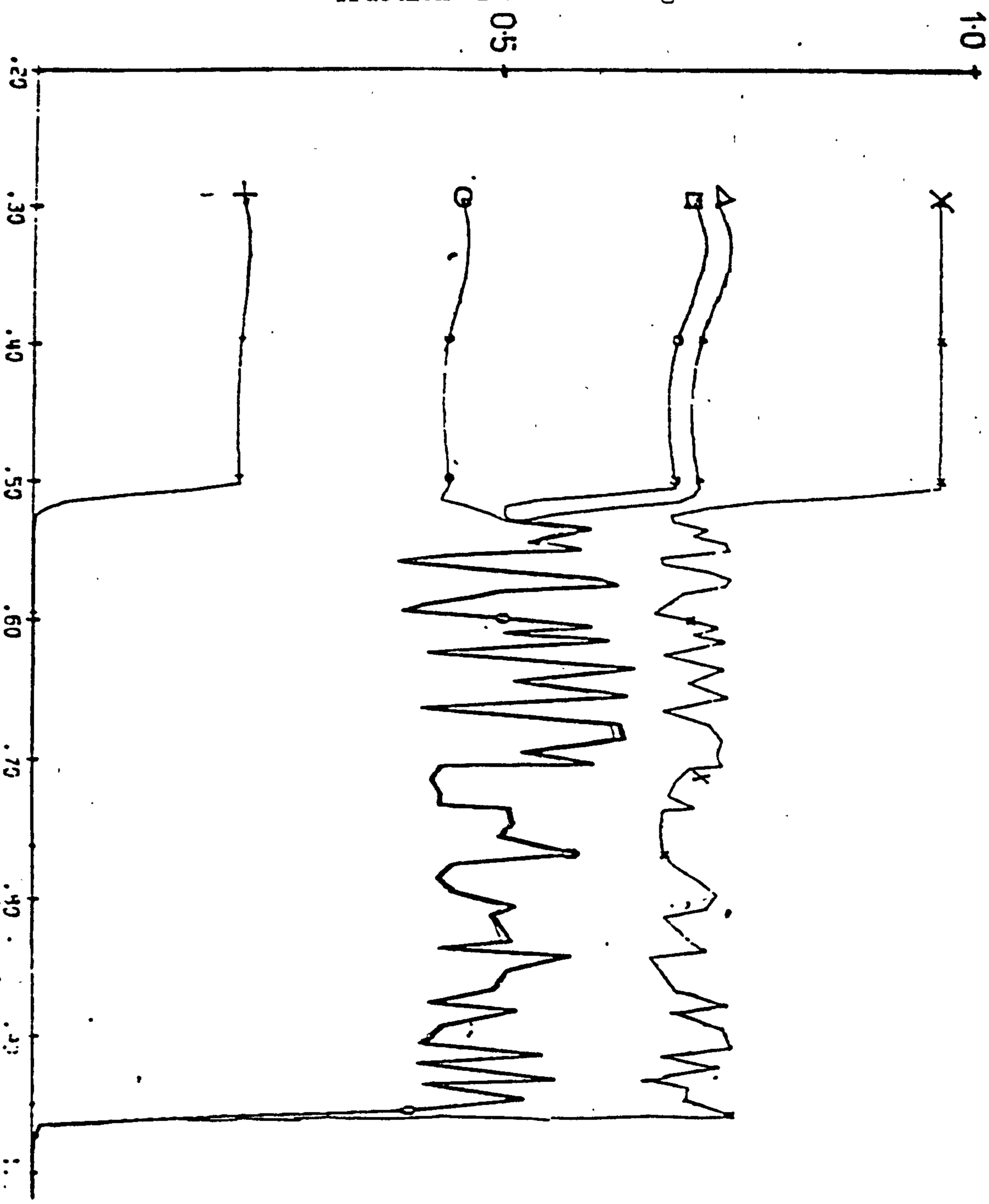

FIGURE 5.11

Figure 5.12 Absorptance and spectral response curves for Cu_2S-CdS cells
(for notation see page 79)

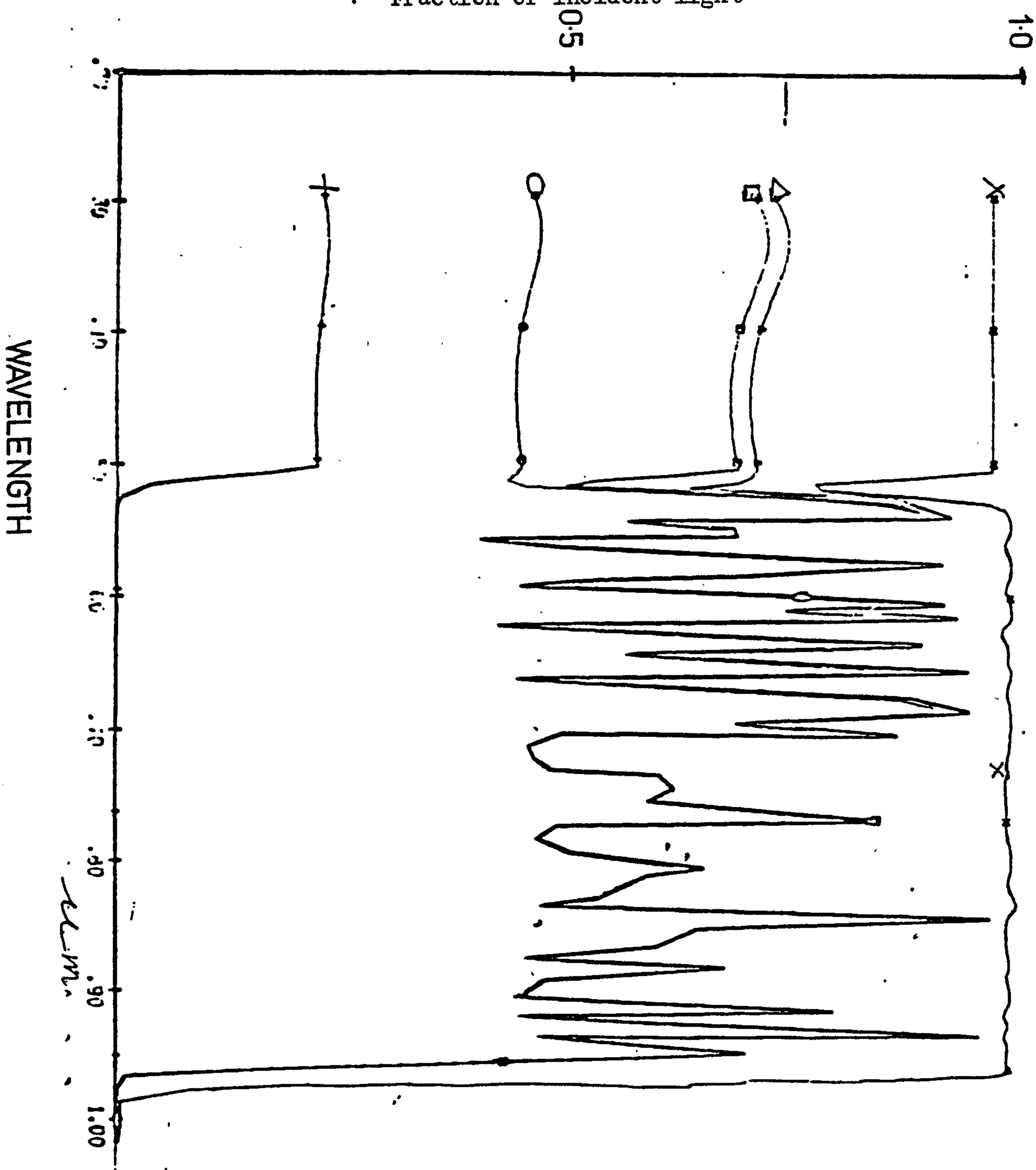

FIGURE 5.12

Figure 5.13 Absorptance and spectral response curves for Cu_2S-CdS cells
(for notation see page 79)

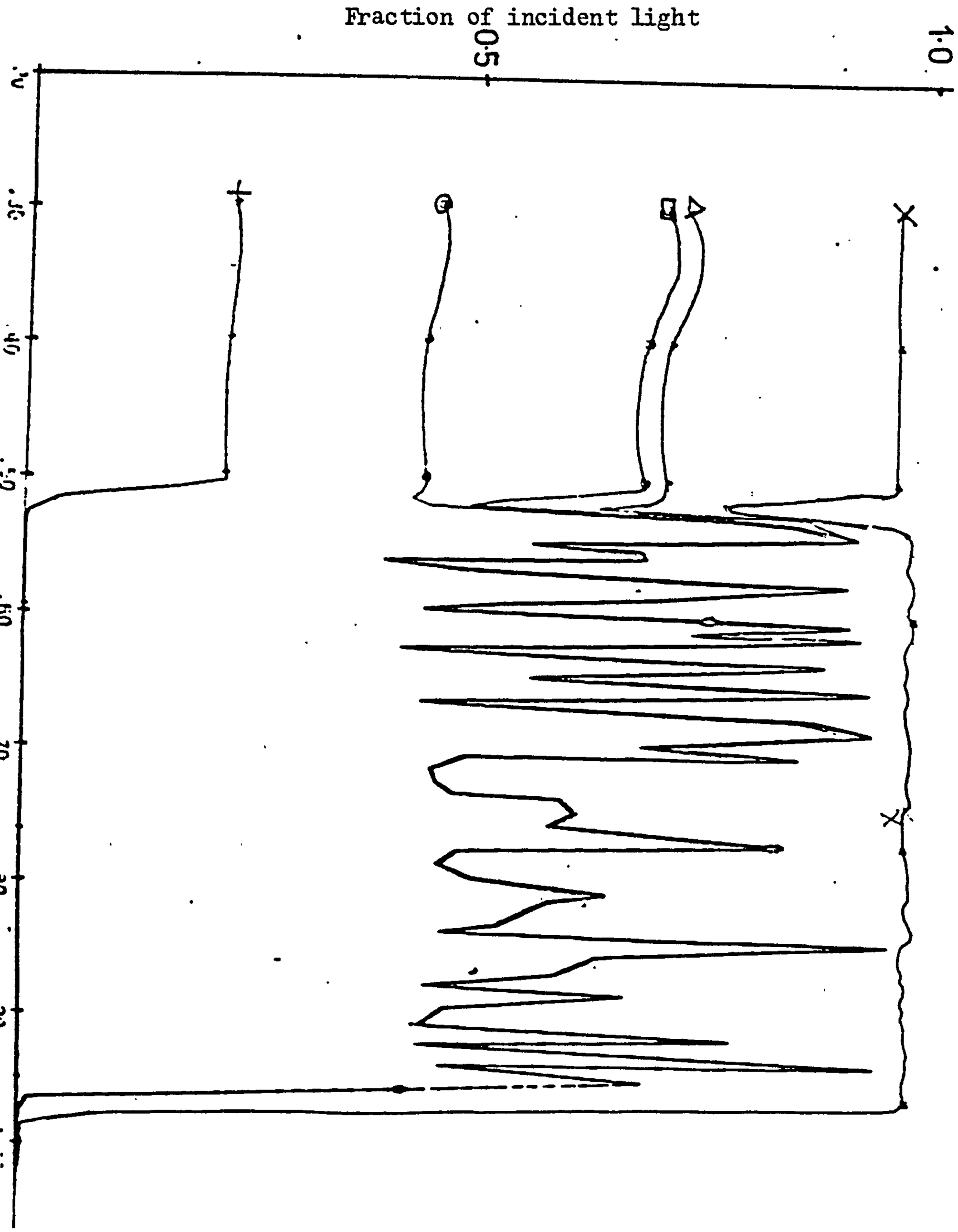

FIGURE 5.13

Figure 5.14 Absorptance and spectral response curves for Cu_2S-CdS cells
(for notation see page 79)

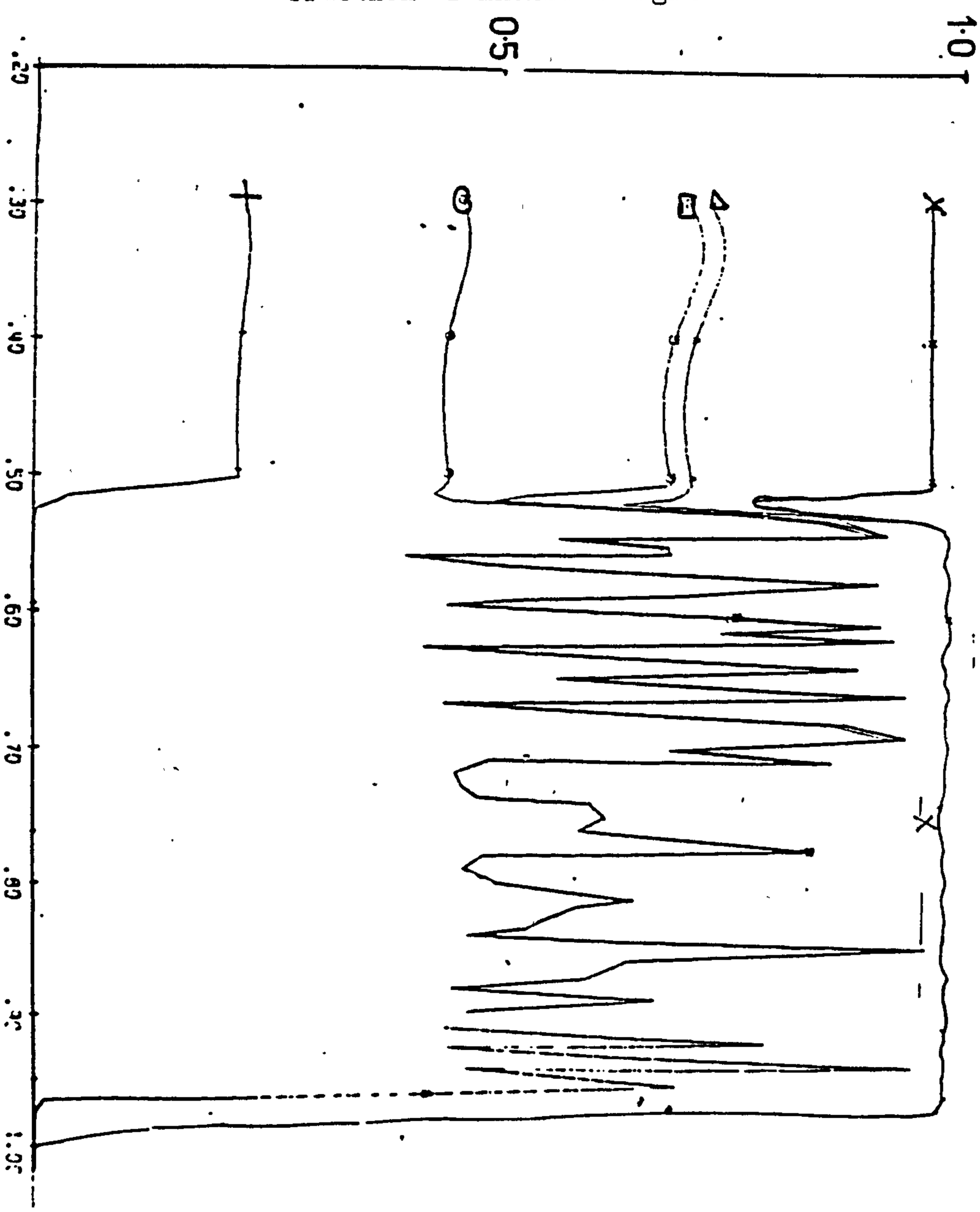

FIGURE 5.14

Figure 5.15 Absorptance and spectral response curves for Cu_2S-CdS cells''

(for notation see page 79)

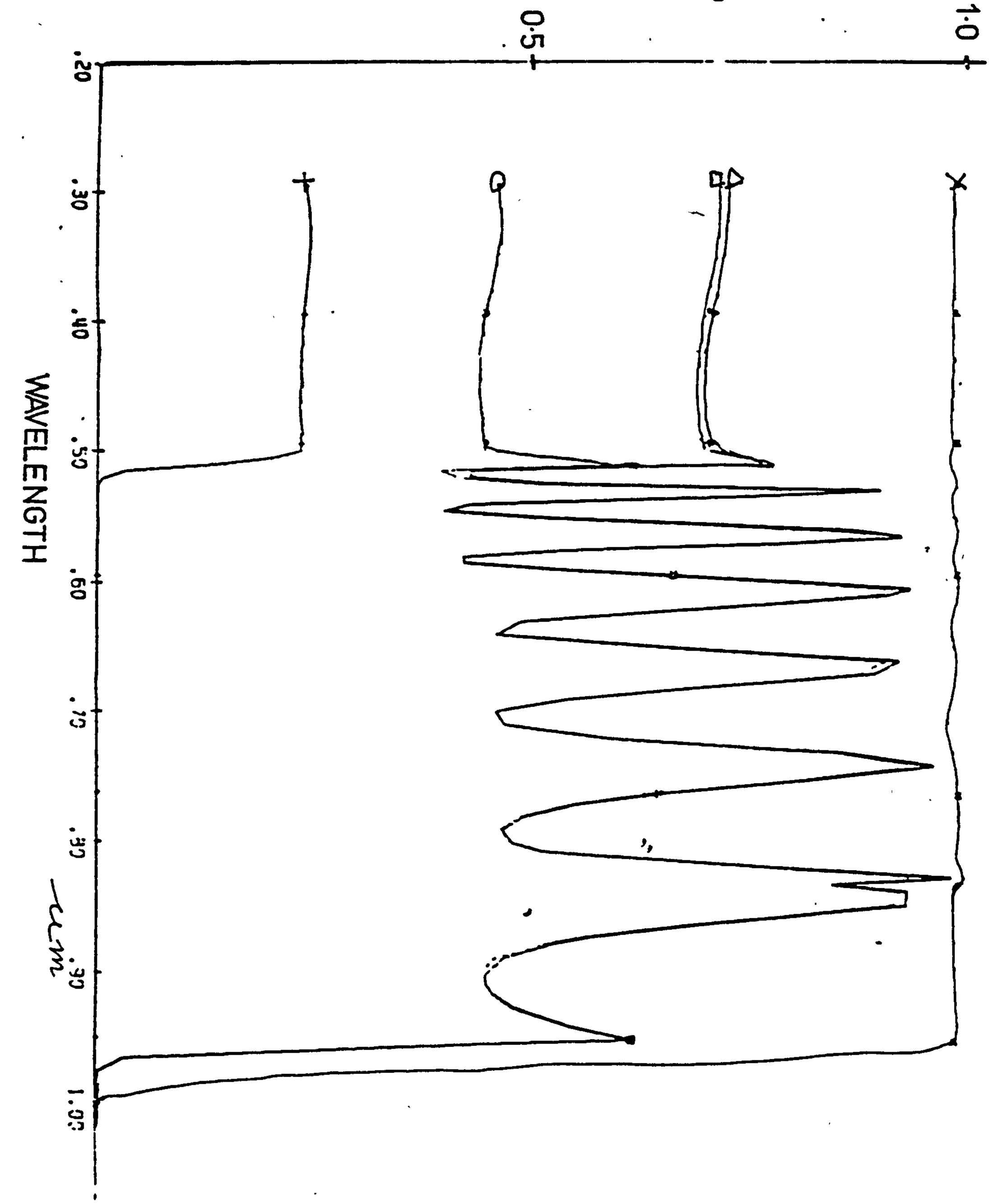

FIGURE 5.15

Figure 5.16 Absorptance and spectral response curves for Cu_2S - CdS cells
(for notation see page 79)

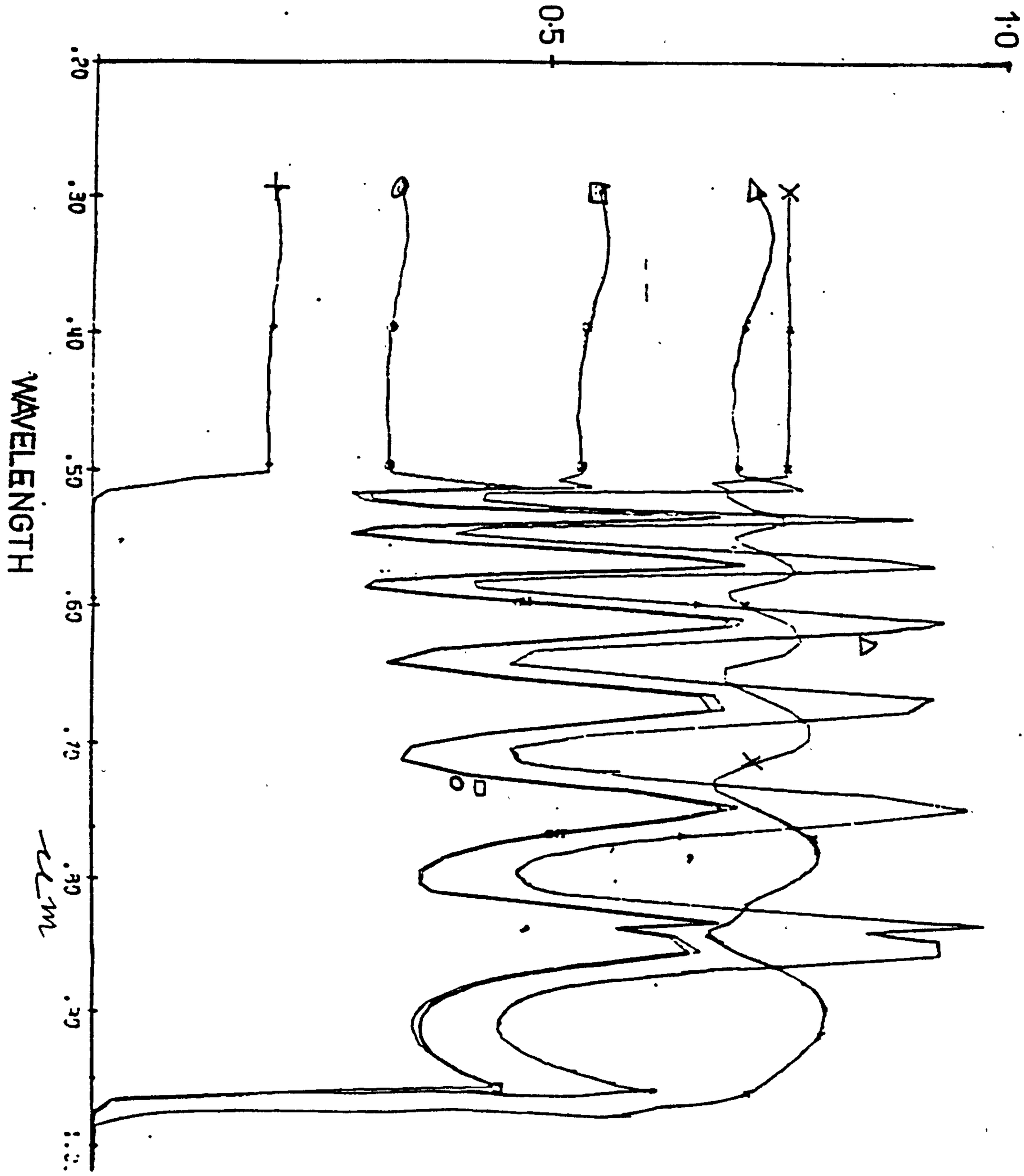

FIGURE 5.16

Figure 5.17 Absorptance and spectral response curves for Cu_2S-CdS cells
(for notation see page 79)

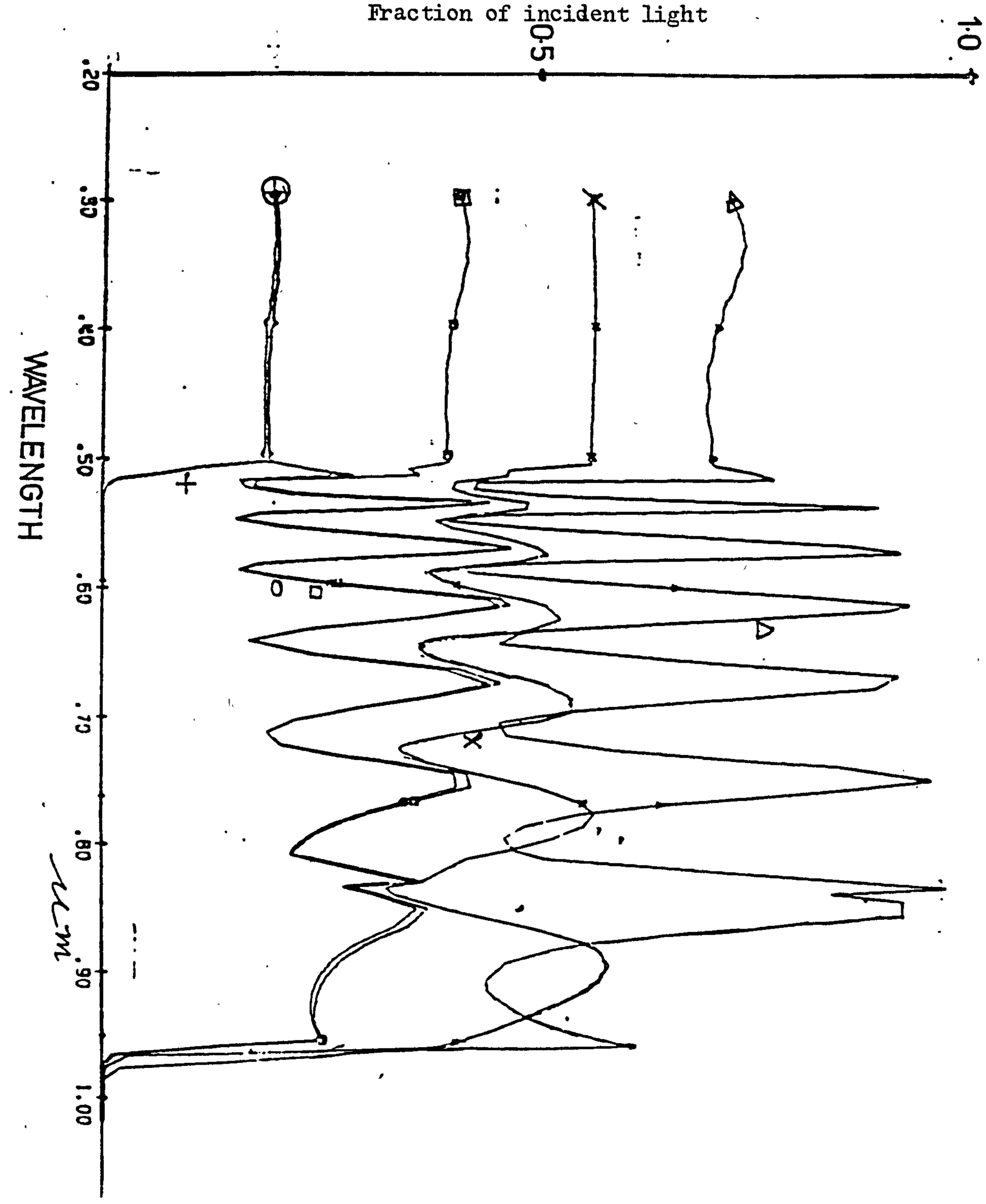

FIGURE 5.17

Figure 5.18 Absorptance and spectral response curves for Cu_2S - CdS cells

(for notation see page 79)

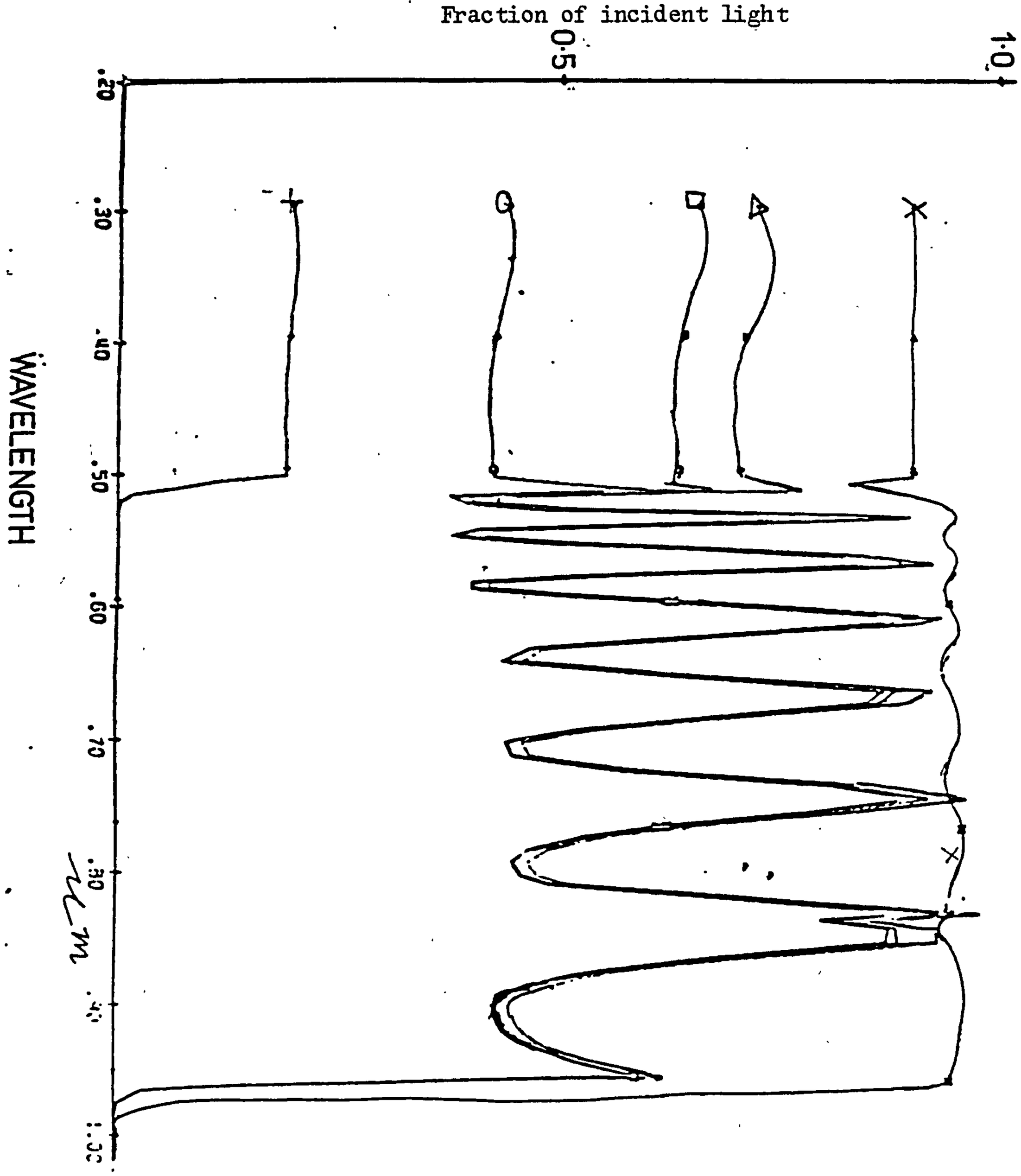

The spectral response S.R. is defined as

$$SR = \frac{(\text{short circuit current generated at the junction})}{(\text{incident flux}) \quad \times q}$$

where q is the electronic charge.

The refractive index for Cu_2S was assumed to be 3.2 for all wavelengths of interest. The extinction coefficients were calculated from the absorption coefficient data for the Cu_2S. The absorption coefficient data for Cu_2S was taken as 10^5 cm^{-1} below 0.95 μm wavelength having a very sharp absorption edge to about 1.0 μm. Above 0.95 m the absorption coefficient data for Cu_2S was taken from Loferski (1961).

The remaining optical data for both CdS and Ag was taken from (American Institute of Physics Handbook 3rd Edition 1977). The absorption coefficient for CdS was given as 5.0×10^4 cm^{-1} 0.5 μm wavelength and zero above 0.54 μm wavelength. The refractive index of CdS varied between 2.3 and 2.8.

Comparison of figures 5.10 and 5.11 show no change in the spectral response curves for the CdS layer. However there are dramatic differences in the spectral curves and the absorptance curves for the Cu_2S layer. Figure 5.10 has a silver substrate and figure 5.11 has a molybdenum substrate. The front surface recombination in figure 5.11 is 10^{-4} cm per second whereas it is 10^5 cm per second in figure 5.10, otherwise they are identical.

On comparing more closely the curves for the molybdenum backed cell to the silver backed cell (figures 5.11 and 5.12 respectively) it can be observed that in the wavelength range

below 0.5μm , both the spectral responses and the absorptances are nearly identical for the Cu_2S layer in the two cases. The value for the absorptance in the molybdenum backed cell varies around 50 per cent compared to 60 per cent in the silver backed cell. Even though the silver backed cell reflects more of the incident radiation than does the molybedenum backed cell (Table 5A) the former still absorbs more radiation for the same incident value. If both cells were perfectly anti-reflected such that the reflectance was zero, the absorptance in the case for the silver substrate would rise to 95 per cent and above whereas the corresponding value in the molybdenum case would be 70 per cent.

In the examples just discussed the diffusion length of the minority carriers in the Cu_2S layer is 20 times the Cu_2S layer thickness. Consequently one expects negligible bulk recombination losses. In the CdS layer, however, the diffusion length is $\frac{1}{5}$ times the CdS thickness and a fair amount of bulk recombination losses might be expected. The first point is varified by the fact that the spectral response curves for the Cu_2S layer almost superimpose the absorptance curves (figures 5.10, 5.11 and 5.12) in the wave length range greater than 0.5μm. For wave lengths below 0.5 μm the spectral responses for the Cu_2S layers vary from about 24 per cent below the Cu_2S absorptance values (figure 5.10) to 22 per cent below the absorptance values (figures 5.11 and 5.12). In the same wave length range the remaining absorptance takes place in the CdS layer such that the total absorptance values are 2 to 4 per cent above the total spectral responses (figures 5.10, 5.11 and 5.12).

The spectral responses of the CdS layers remain unaltered by changing the substrate from molybedenum to silver (figures 5.11 and 5.12). This can be explained by the fact that most of the radiation entering the cell within the absorption band for the CdS layer is absorbed before reaching the substrate for this particular configuration of the cell.

Generally by decreasing the front surface recombination velocity one can increase the spectral response of the cell. However there exists a limiting value for the front surface recombination velocity such that decreasing the front surface recombination further does not increase the spectral response. This is illustrated by comparison of figures 5.12, 5.13 and 5.14. This limiting value is 10^4 cm per second (table 5A). It can be further seen that most of the absorption in the CdS layers, of figures 5.12, 5.13 and 5.14, occurred far away from the back surface as lowering the back surface recombination velocity from effectively infinity to 1 cm per second made no difference to the spectral response curves for the CdS layers.

Now increasing the front surface recombination velocity from 10^4 cm per second to 10^5 cm per second lowers the spectral response (figures 5.10 and 5.12) but the differences in the Cu_2S spectral responses are not uniform. This is explained by the presence of optical interference effects interacting with surface recombination velocity (equation 3.13).

As previously mentioned bulk recombination losses occur in the CdS layer (figure 5.14) where it can be seen the total spectral curve remains a few per cent below the absorptance curve in the shorter wavelength range even when front and back surface recom-

bination velocities are negligible.

An illustration of the fact that by altering the CdS thickness and hence the optical interference conditions the spectral responses can be changed, is to be seen by comparing figures 5.14 and 5.15. Decreasing the CdS thickness from 10 μm to 1 μm has increased its spectral response but leaves the Cu_2S response and absorptance curves unaltered in the shorter wave length range. In the longer wavelength range the shape of the absorptance curve is changed and raised slightly in addition to the spectral response also being slightly increased. The reason for the CdS spectral response rising is that the diffusion length has become twice the CdS thickness (table 5A) compared to $\frac{1}{5}$ the CdS thickness previously. The implication of this is that the bulk recombination is the CdS layer is reduced. Another point to note here is that the absorption of light occurred close to the junction in the CdS layer because altering its thickness from 10 μm to 1 μm did not change its absorptance curve.

Spectral response curves and the absorptance curve for a cell with a diffusion length in the Cu_2S equal to 0.1 μm is shown in figure 5.16. The front and back surface recombination velocities are 10^4 cm per second and 10^5 cm per second, respectively. The other parameters are the same as for figure 5.15 (see table 5A). The absorptance curves in both the figures 5.15 and 5.16 are the same as the layer thickness are identical. The spectral response for the CdS is slightly lower in figure 5.16 than in figure 5.15 because of effectively infinite back surface recombination velocity in the case for figure 5.16. The back surface recombination has now come into play because the CdS thickness is only 1.0 μm thick.

The total spectral response in figure 5.16 is lower than for figure 5.15 because of the very much reduced diffusion length in the Cu_2S. The Cu_2S diffusion length for figure 5.16 is equal to the Cu_2S thickness whereas it is 20 times that for figure 5.15.

Although very similar in shape to the absorptance curve, on close examination it can be seen that the total spectral response curve in figure 5.16 does not follow the absorptance curve precisely. This can be explained from the equation for the short current (see equation 3.13 for instance) where there are optical interference terms that also include the diffusion length. It could be said then that "secondary" interference effects also take place within the diffusion length distance from the junction.

When the diffusion length is very much larger than the thickness of the layer there is good collection of the minority carriers and the total spectral response curve almost superposes the absorptance curve as already pointed out. The "secondary" interference effects are masked by the primary interference effect in that case. The total spectral response curve is divided by (1-R), i.e. zero reflectance case, there should hardly be any interference fringes present when the diffusion length is long. This is observed in figure 5.15. The few ripples in the zero reflectance total spectral response curve in figure 5.15 are due to the small amount of absorption taking place in the silver substrate. It can be seen from equation 3.13 that whenever L the diffusion length is very much larger than $\frac{\lambda}{4\pi n}$ µm the diffusion length has little or no effect on the interference terms.

When L approaches $\frac{\lambda}{4\pi n}$ or is less than $\frac{\lambda}{4\pi n}$ the "secondary" interference effects should be observable. These are observed for instance in figure 5.16 particularly when looking at the zero reflectance total spectral response curve. The diffusion length in the Cu_2S equals the Cu_2S thickness in that case.

Figure 5.17 shows curves for a cell identical to a cell with the curves in figure 5.16 with exception that the Cu_2S diffusion length in the case for figure 5.17 is 0.05 µm. Because L is less than $\frac{\lambda}{4\pi n}$ the "secondary" interference effects are again observable. L for figure 5.17 is half the size of L for figure 5.16 and the interference fringes in the zero reflectance spectral response curve are observed to be sharper and deeper in figure 5.17, although lower in value due to poorer collection of the minority carriers.

The curves are for a cell with the Cu_2S diffusion length equal to 0.3 µm i.e. three times the Cu_2S thickness are shown in figure 5.18. Again the "secondary" interference terms are observable in the zero reflectance spectral response curve but they are quite shallow with the collection efficiency over the light entered equal to 93.0 per cent. This is about 5 per cent below the case when the diffusion length is 2.0 µm, everything else being equal.

A CdS thickness of 1.0 µm is preferable to a thickness of 10.0 µm from the point of view of saving material as well as interference conditions.

5.4 Short circuit current curves. (Under AM1 radiation)

The graphs in figures 5.19 to 5.29 show the AM1 radiation equivalent current in mA x 10^2 per micron of wave length at each wave length, the short circuit current assuming zero reflection and the short circuit current taking into account the reflection.

The following notation of symbols is used to distinguish the three curves in figures 5.19 to 5.29.

\+ represents AM1 radiation current

□ represents the short circuit current with zero R

0 represents the short circuit current with non-zero R.

Table 5B shows the values of the parameters and the main results for the curves in figures 5.19 to 5.29.

AM1 radiation is incident on the Cu_2S side of the cell and the back surface reflection is provided by the silver substrate. The depletion region in the Cu_2S is assumed equal to 0.001 μm and in the CdS equal to 0.01μm.

The total current over the whole wave length range in question is given by the areas under the curves in figures 5.19 to 5.29.

If the flux entering the cell = Φ , the current collected at the junction = I and e = charge on the electron then the collection efficiency over flux entered = I / (Φ x e).(definition)

On comparing figures 5.19, 5.20 and 5.21 the effects of altering the diffusion lengths of the minority carriers in the Cu_2S on the short circuit current can clearly be seen. At a front surface recombination velocity of 10^6 cm per second the collection efficiency over the flux entered reduces from 72.5 per cent for a diffusion length of 0.5μm down to 62.2 per cent for a diffusion

Table 5B Absorptance, reflectance, collection efficiency and photogenerated current for Cu_2S – CdS – Ag thin film solar cells

5.19	5.20	5.21	5.22	5.23	5.24	5.25	5.26	5.27	5.28	5.29	Figure
10.0	10.0	10.0	10.0	10.0	10.0	10.0	10.0	10.0	10.0	10.0	Thickness CdS μm
0.1	0.1	0.1	0.1	0.1	0.1	0.2	0.2	0.2	0.2	0.2	Thickness Cu_2S μm
38.1	38.1	38.1	38.1	38.1	38.1	33.0	33.0	33.0	33.0	33.0	Reflectance R %
61.3	61.3	61.3	61.3	61.3	61.3	66.4	66.4	66.4	66.4	66.4	Absorptance A %
14.9	9.37	12.8	15.4	19.8	10.1	7.81	4.06	12.7	20.5	9.21	Total Current $MAcm^{-2}$ $R \neq 0$
24.1	15.1	20.7	24.9	31.9	16.2	11.7	6.06	18.9	30.6	13.8	Total Current $MAcm^{-2}$ $R = 0$
72.5	45.5	62.2	74.9	96.0	48.8	35.1	18.2	56.9	92.1	41.4	Collection Efficiency % over flux entered
44.9	28.2	38.5	46.4	59.4	30.2	23.5	12.2	38.1	61.7	27.7	Coll.Effic. over incident flux %
0.5	0.05	0.1	0.1	0.5	0.05	0.1	0.05	0.5	0.5	0.1	Diffusion length Cu_2S
2.0	2.0	2.0	2.0	2.0	2.0	2.0	2.0	2.0	2.0	2.0	Diffusion length CdS
10^6	10^6	10^6	10^4	10^4	10^4	10^6	10^6	10^6	10^4	10^4	SRV front cm sec^{-1}
73.2	46.0	62.8	74.9	97.0	49.3	35.4	18.4	57.4	92.9	41.7	Coll.Effic.% over absorbed flux

(Silver substrate and SRV back is infinite)

SRV = surface recombination velocity

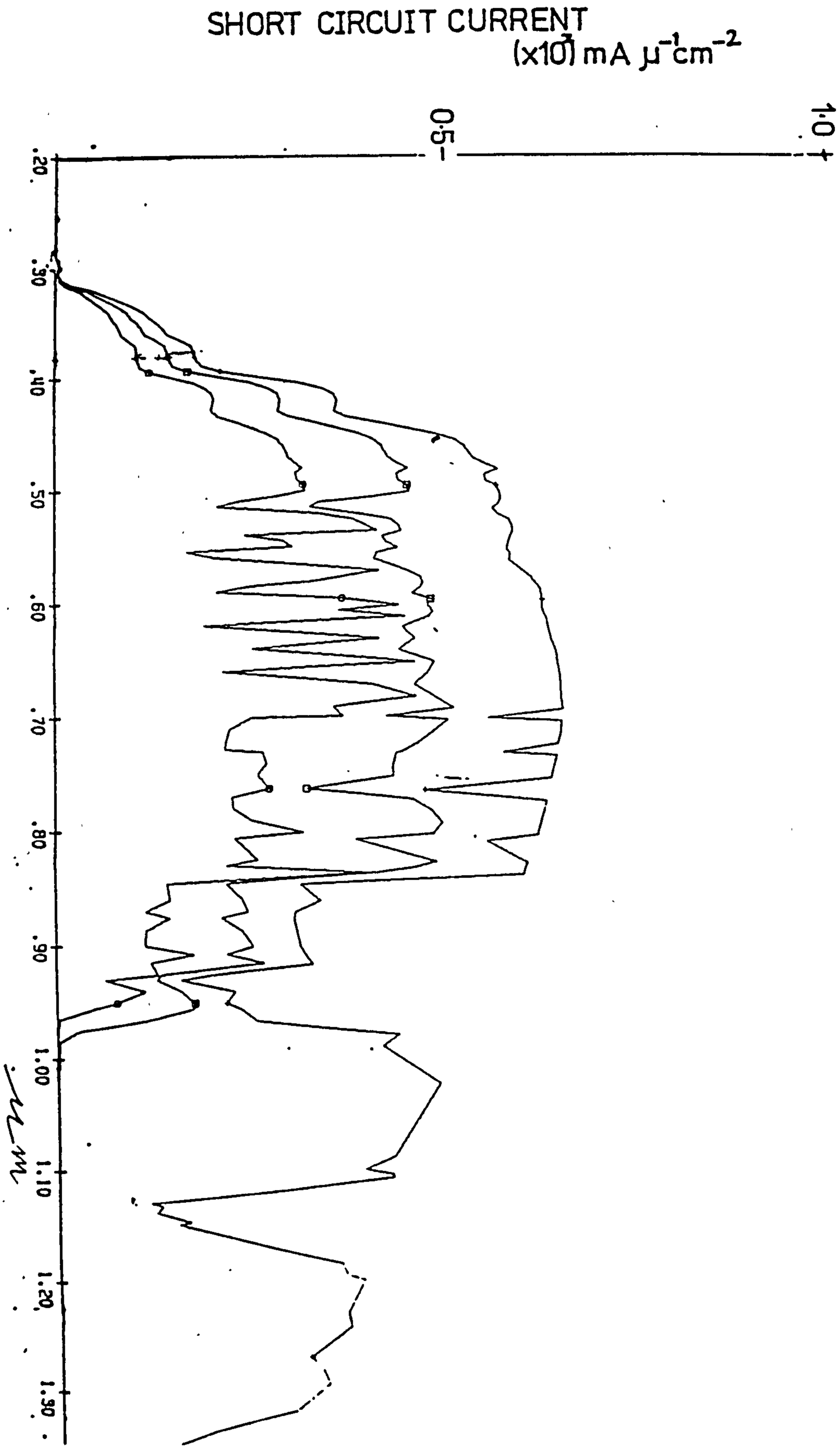

FIGURE 5.19

Figure 5.19 Photocurrent against wavelength under AM1 radiation

(see table on page 97)

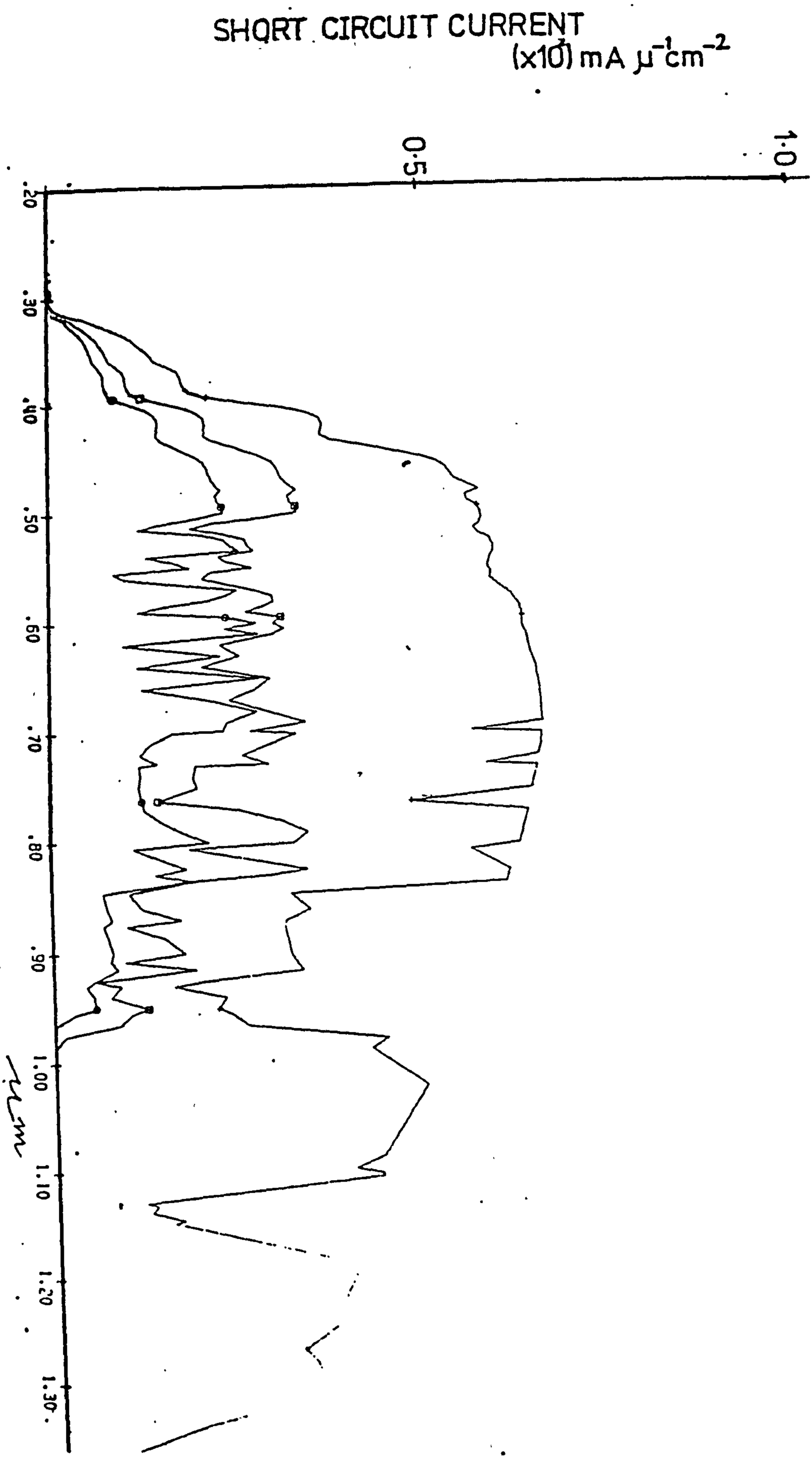

Figure 5.20 Photocurrent against wavelength under AM1 radiation

(see table on page 97)

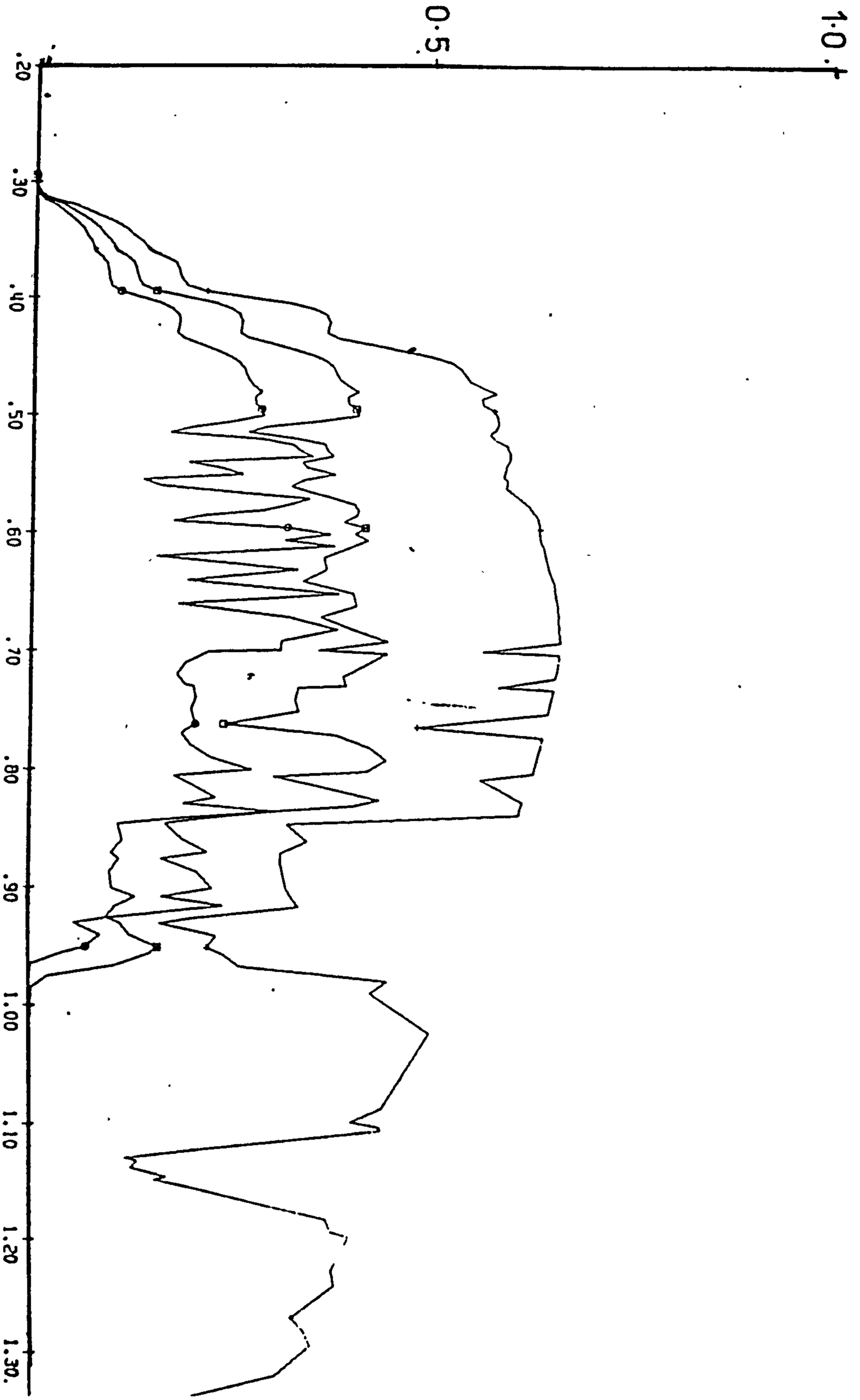

FIGURE 5.21

Figure 5.21 Photocurrent against wavelength under AM1 radiation

(see table on page 97)

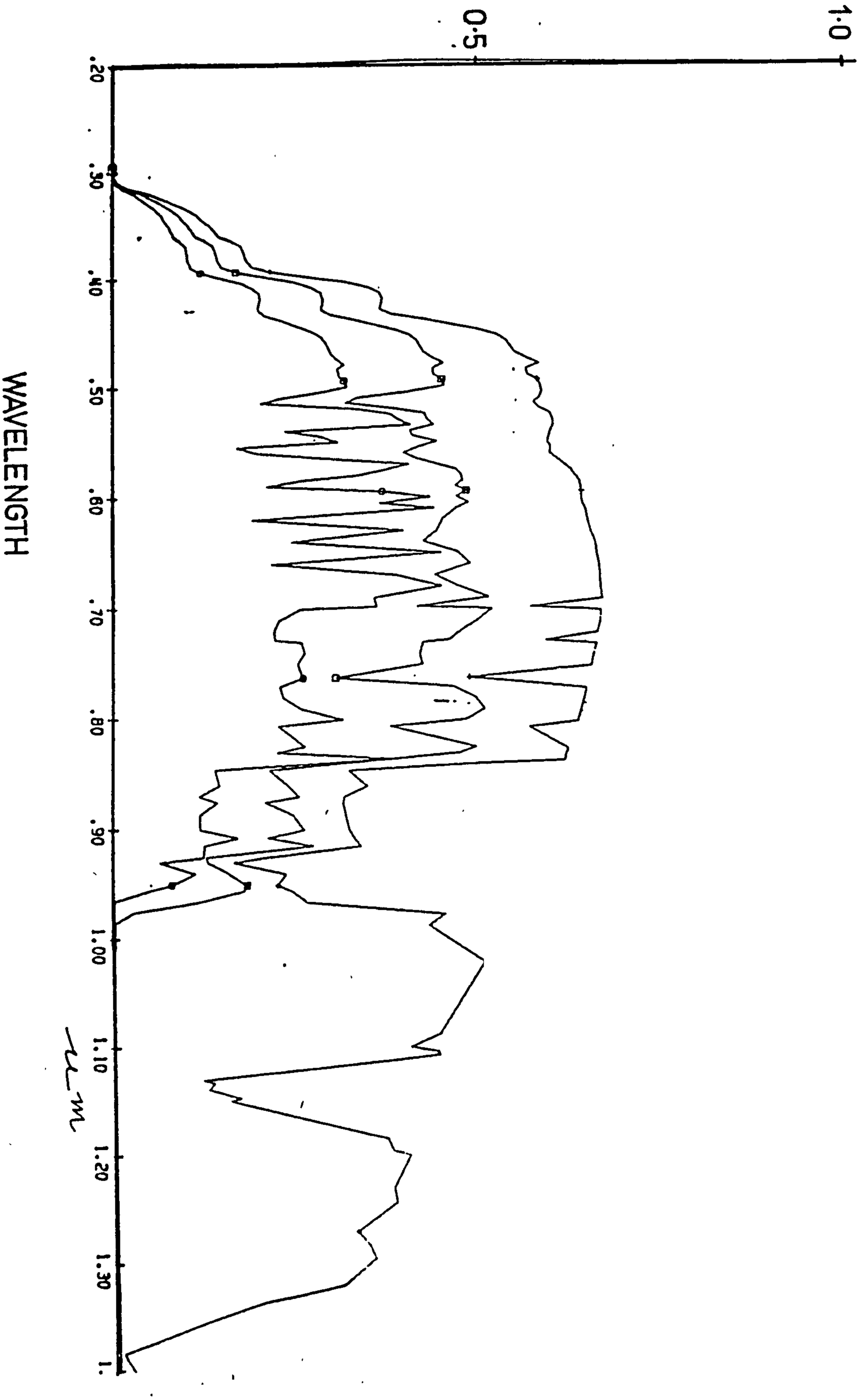

FIGURE 5.22

Figure 5.22 Photocurrent against wavelength under AM1 radiation
(see table on page 97)

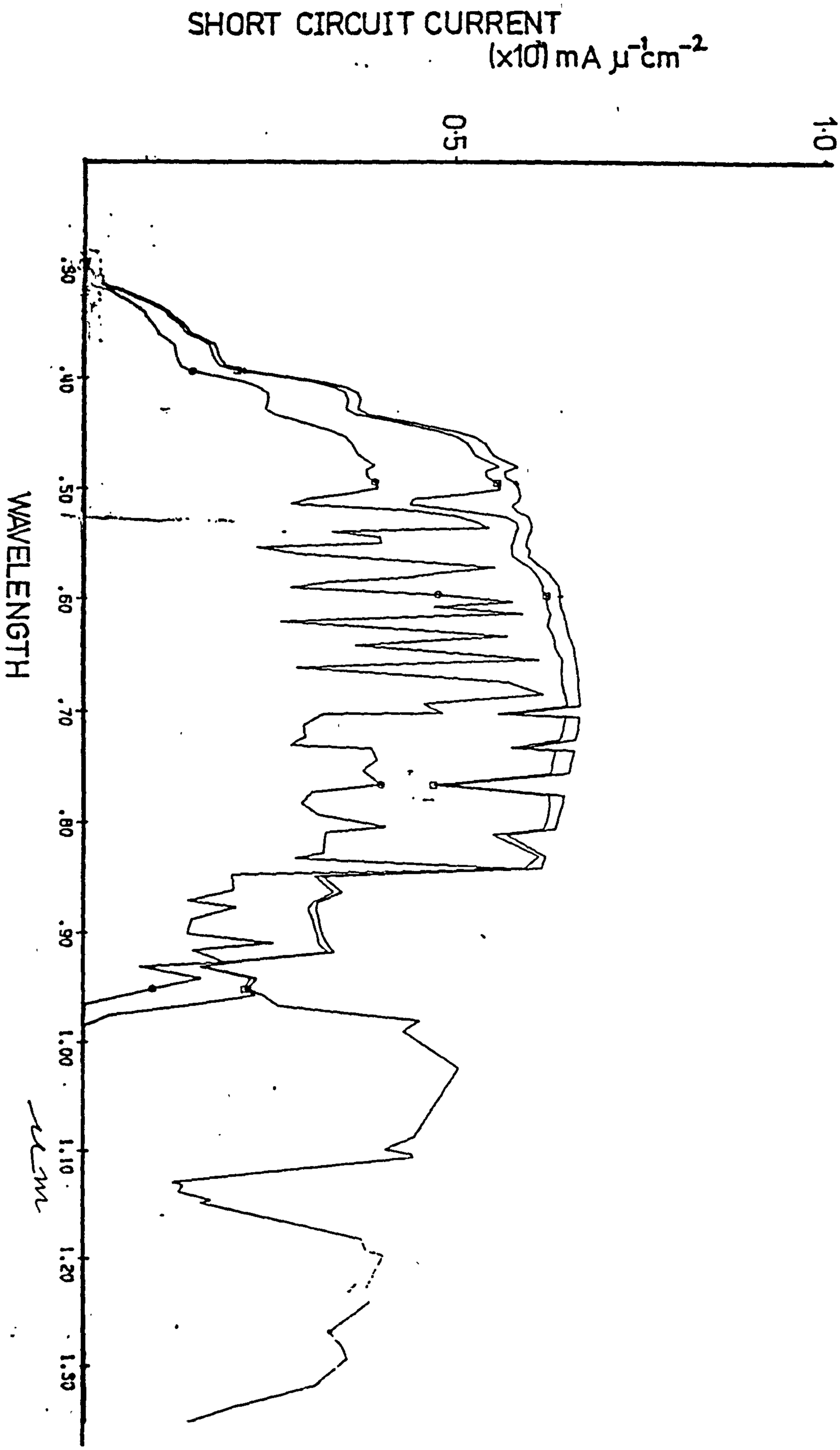

Figure 5.23 Photocurrent against wavelength under AM1 radiation

(see table on page 97)

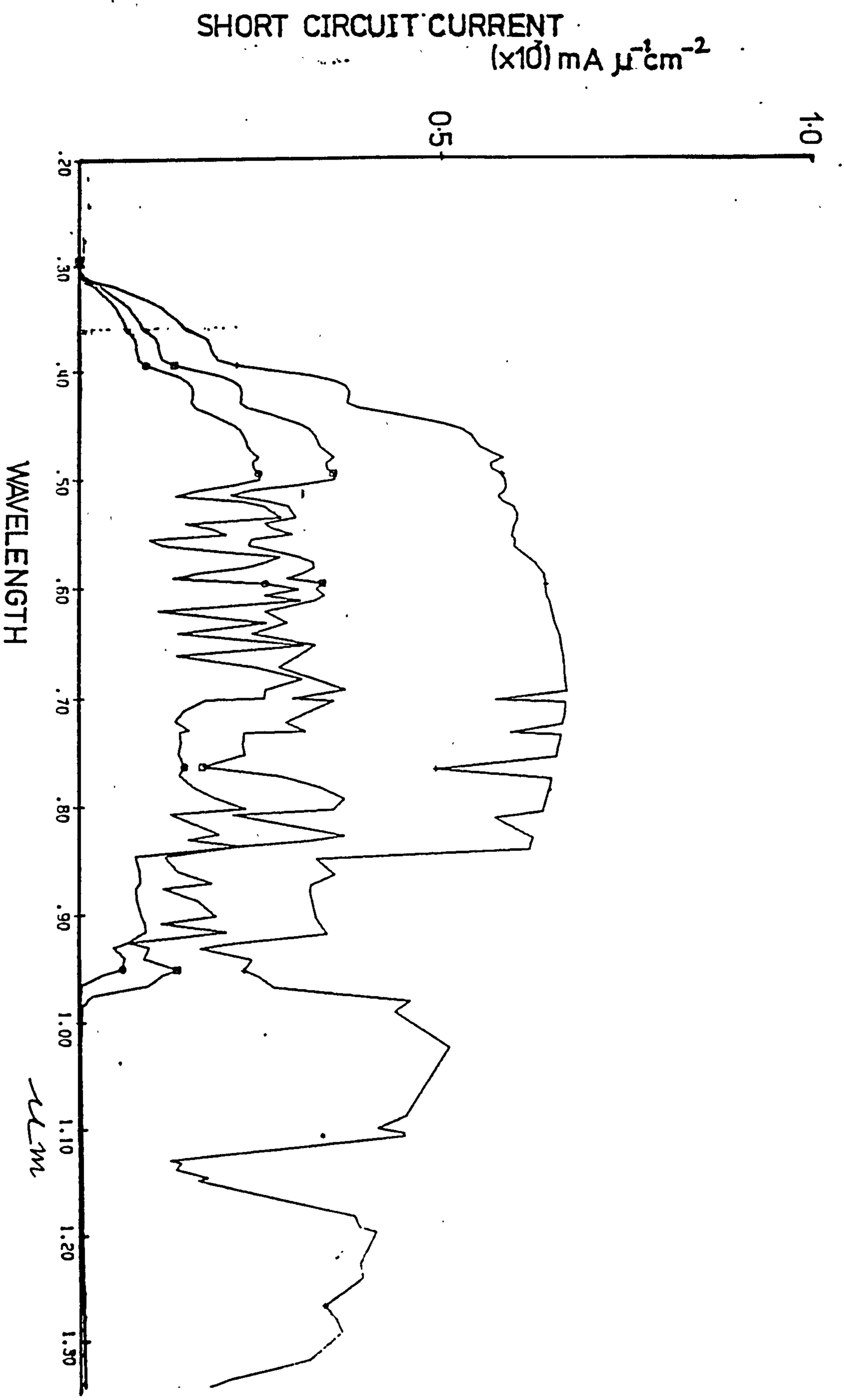

FIGURE 5.24

Figure 5.24 Photocurrent against wavelength under AM1 radiation
(see table on page 97)

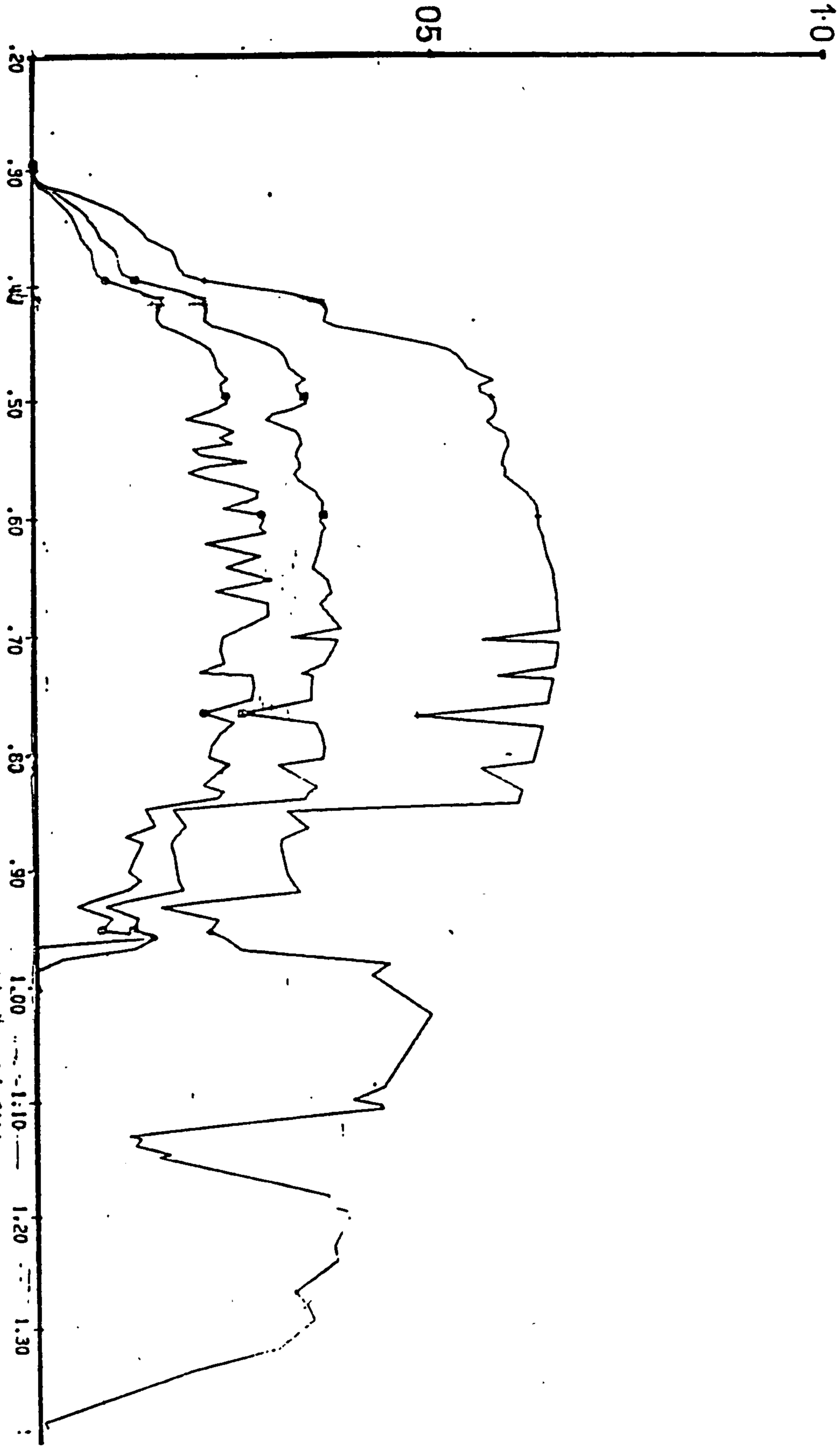

FIGURE 5.25

Figure 5.25 Photocurrent against wavelength under AM1 radiation
(see table on page 97)

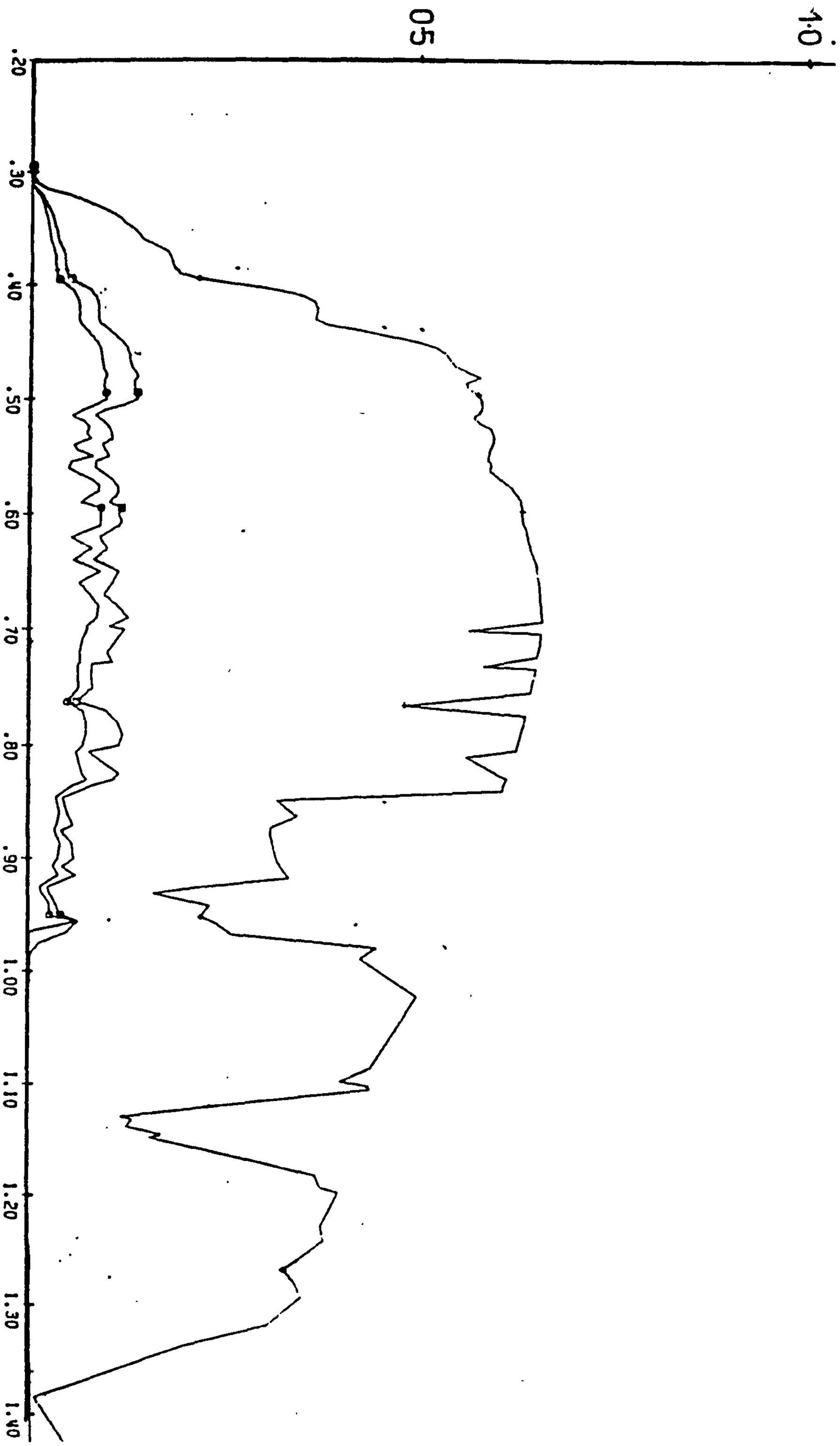

FIGURE 5.26

Figure 5.26 Photocurrent against wavelength under AM1 radiation
(see table on page 97)

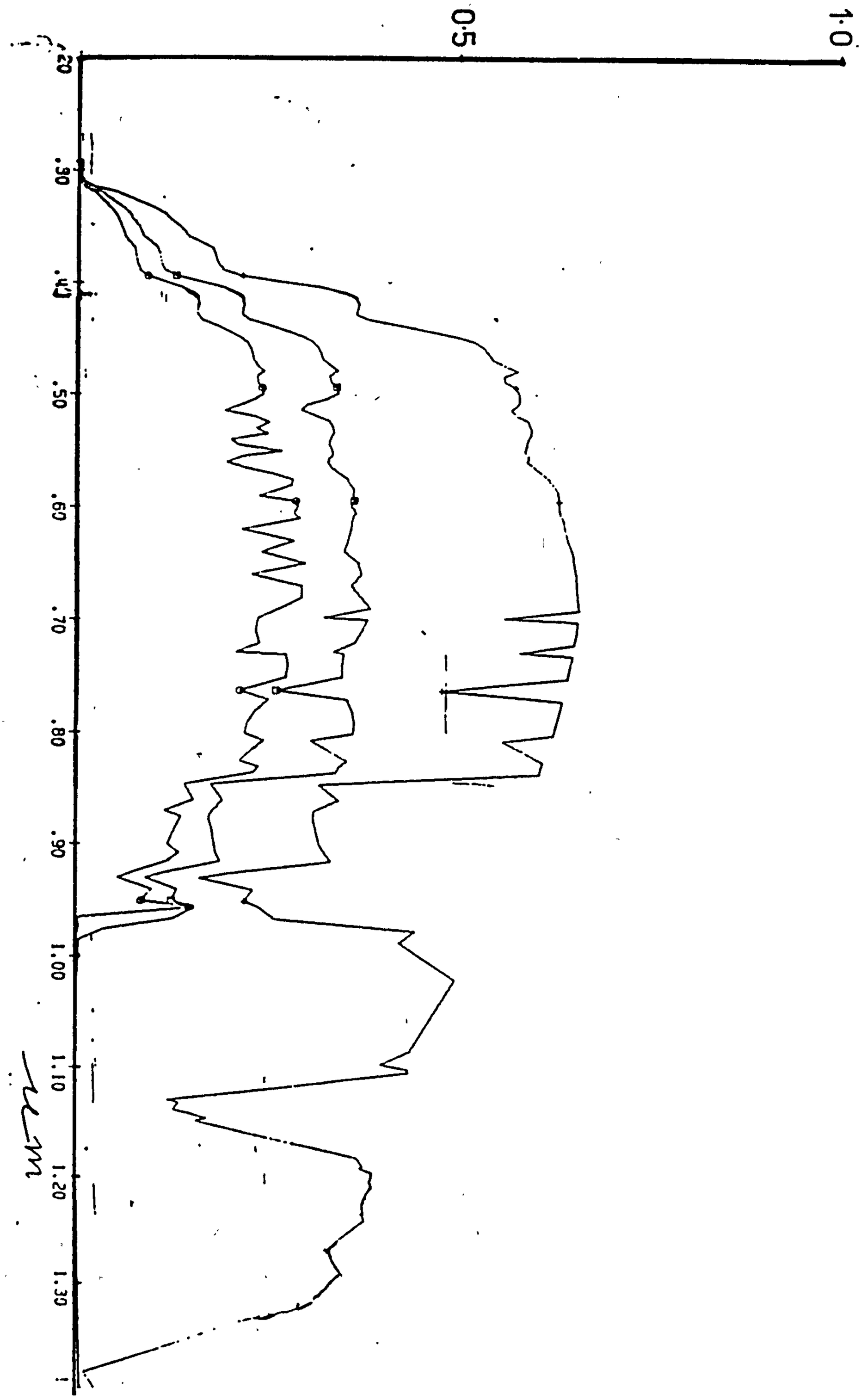

Figure 5.27 Photocurrent against wavelength under AM1 radiation
(see table on page 97)

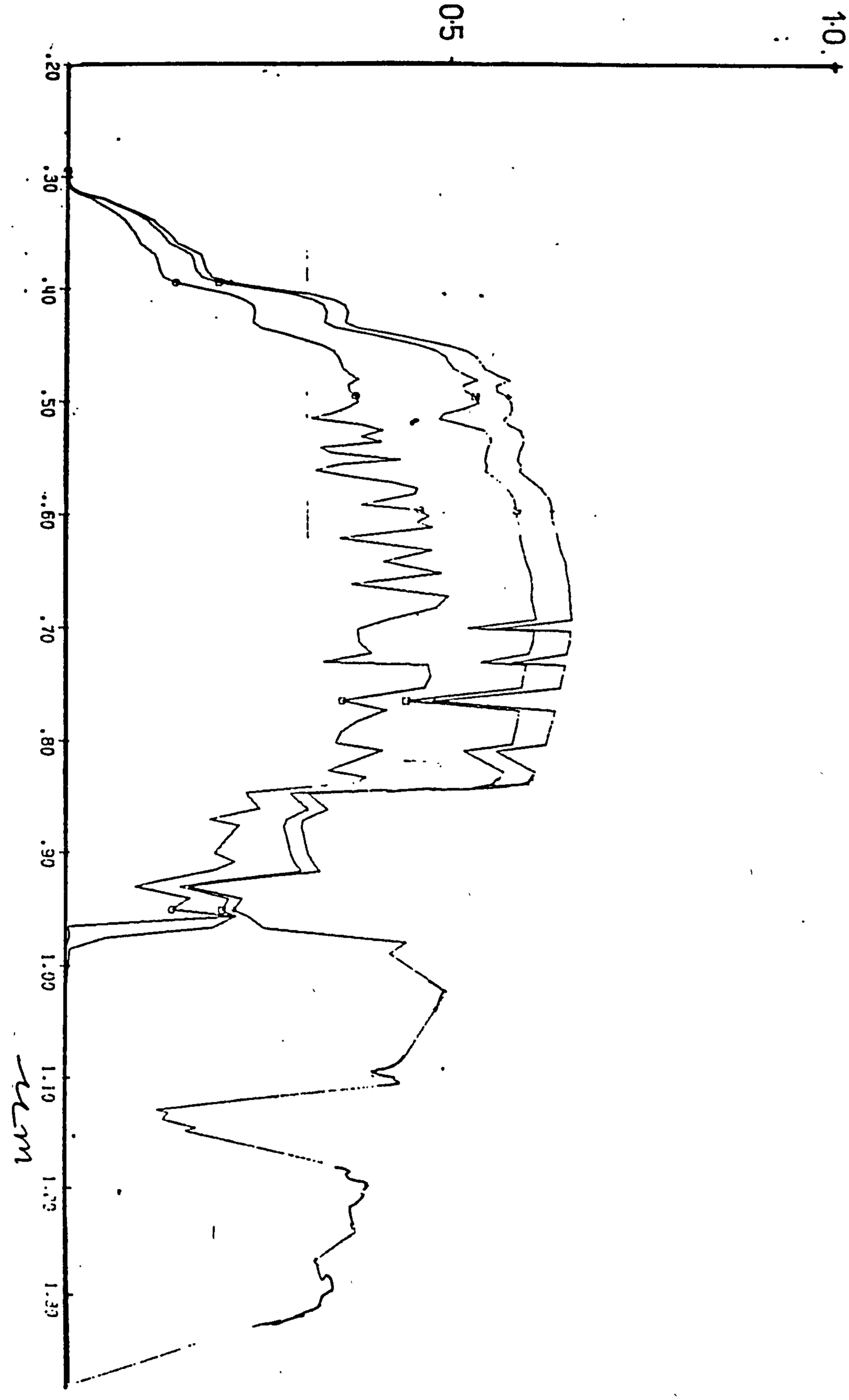

FIGURE 5.28

Figure 5.28 Photocurrent against wavelength under AM1 radiation
(see table on page 97)

PAGE NUMBERING AS ORIGINAL

length of 0.1μm. It further reduces to 45.5 per cent for a diffusion length of 0.05 μm.

Figures 5.19 and 5.23 illustrate the importance of the surface recombination velocity at the front surface. For both figures the diffusion lengths are identically 0.5 μm. For figure 5.19 the front surface recombination velocity is 10^6 cm per second and for figure 5.23 it is 10^4 cm per second. The collection efficiency as defined above is 97.0 per cent for figure 5.23 and 22 per cent below that for figure 5.19.

At a diffusion length of 0.1μm the collection efficiency over the flux entered goes up by 12 per cent in reducing the front surface recombination velocity from 10^6 cm per sec to 10^4 cm per sec. At a diffusion length of 0.05μm it goes up by only 3 per cent in reducing the surface recombination velocity from 10^6 to 10^4 cm per sec. This can be seen by comparing figures 5.22 and 5.24 with figures 5.20 and 5.21. (see table 5B.)

The shorter the diffusion length the quicker will the minority carriers recombine in the bulk of the material before reaching the junction. The shorter the diffusion length the less important becomes the surface recombination velocity as illustrated in the examples above.

When little absorption of light occurs at a distance greater than or equal to the diffusion length from the top surface the majority of the minority carriers will recombine in the bulk of the material before they could recombine at the surface. This is the reason why there is only 3 per cent increase in the collection efficiency on reducing the surface recombination velocity from 10^6 cm per sec at a diffusion length of 0.05μm. On the other hand when there

is good absorption of light within a distance equal to the diffusion length from the surface, the carriers have a good chance of getting to the surface and recombining at the surface. This explains the 22 per cent increase in the collection efficiency in reducing the surface recombination velocity from 10^6 cm per sec to 10^4 cm per sec at a diffusion length of 0.5μm.

Comparing figures 5.19 to 5.24 with figures 5.25 to 5.29 illustrate the importance of the Cu_2S layer thickness on the generated current. At a surface recombination velocity of 10^6 cm per sec and a diffusion length of 0.1μm the effect of altering the Cu_2S thickness from 0.1 to 0.2μmis to reduce the collection efficiency over flux entered by 27.4 per cent. At a surface recombination velocity of 10^6 cm per sec and a diffusion length of 0.05μmthe effect is to reduce the collection efficiency by 27.6 per cent and at a diffusion length of 0.5μmand a surface recombination velocity of 10^6 cm per sec the collection efficiency is reduced by 15.8 per cent (see table 5B).

At a surface recombination velocity of 10^4 cm per sec and diffusion length of 0.5μm, increasing the Cu_2S thickness from 0.1μm to 0.2μmreduces the collection efficiency from 97 per cent by 4 per cent. At a diffusion length of 0.1μm and the same surface recombination velocity the collection efficiency falls from 74.9 per cent by 33.2 per cent.

In the examples discussed above, increasing the Cu_2S thickness from 0.1 to 0.2μmmeans that the majority of minority carriers are generated further from the junction. That is why at shorter diffusion lengths the fall in collection efficiency is the greatest.

At longer diffusion lengths and low surface recombination velocities the fall in the collection efficiency is relatively small due to the generated carriers having longer time to reach the junction with little surface recombination.

It can be stated then that surface recombination velocity becomes less and less important as the diffusion length gets shorter and shorter and is less than the Cu_2S thickness. It becomes increasingly important as the diffusion length is increased and is greater than the Cu_2S thickness.

As the diffusion lengths and the surface recombination velocities are altered, it can be seen that the short circuit current curves do not rise or fall uniformly over the whole of the wave length range. This is caused by the "secondary" interference effects already mentioned.

5.5 Cu_2S Optimum Thickness Analysis

Tables 5C and 5D list the parameter variations in plotting the theoretical curves in figures 5.1B to 5.39B. The CdS thickness is kept at 10.0 μ and the back surface recombination velocity at 10^{50} cm per sec. AM1 radiation is incident on the Cu_2S side of the cell. The CdS depletion region is kept at 0.01 μm and that of the Cu_2S at 0.001 μm. The curves in figures 5.1B to 5.39B show the short circuit current in mA per cm^2 integrated over all wave lengths up to the absorption edge versus the thickness of the Cu_2S in μm for both zero R and non-zero R.

Figures 5.1B to 5.39B show that there is an optimum value for the Cu_2S thickness in each case, for which the value of the generated current is a maximum for both zero and non-zero reflection case.

Table 5C Parameters for Cu_2S - CdS - substrate cells (fig.5.1B to 5.29B)

Figure	SRV Front cm s^{-1}	Diffusion Length CdS μm	Diffusion Length Cu_2S μm	Substrate	Diff.constants CdS cm^2 sec^{-1}	Cu_2S	
5.1B	10^7	2.0	0.7	MO	10	10	
5.2B	10^6	2.0	0.7	MO	10	10	
5.3B	10^5	2.0	0.7	MO	10	10	
5.4B	10^4	2.0	0.7	MO	10	10	
5.5B	10^7	2.0	0.7	MO	10	10	
5.6B	10^6	2.0	0.6	MO	10	10	
5.7B	10^4	2.0	0.6	MO	10	10	
5.8B	10^7	2.0	0.5	MO	10	10	
5.9B	10^6	2.0	0.5	MO	10	10	
5.10B	10^4	2.0	0.5	MO	10	10	
5.11B	10^7	2.0	0.4	MO	10	10	
5.12B	10^6	2.0	0.4	MO	10	10	
5.13B	10^5	2.0	0.4	MO	10	10	
5.14B	10^4	2.0	0.4	MO	10	10	
5.15B	10^7	2.0	0.3	MO	10	10	
5.16B	10^6	2.0	0.3	MO	10	10	
5.17B	10^5	2.0	0.3	MO	10	10	
5.18B	10^4	2.0	0.3	MO	10	10	
5.19B	10^7	2.0	0.2	MO	10	10	
5.20B	10^6	2.0	0.2	MO	10	10	
5.21B	10^5	2.0	0.2	MO	10	10	
5.22B	10^4	2.0	0.2	MO	10	10	
5.23B	10^0	2.0	0.2	MO	10	10	
5.24B	10^5	2.0	0.5	MO	10	10	**
					40	40	**
5.25B	10^5	2.0	0.5	MO	30	30	**
5.26B	10^5	2.0	0.5	MO	20	20	**
5.27B	10^4	2.0	0.05	MO	10	10	
5.28B	10^5	2.0	0.5	Zinc	10	10	
5.29B	10^4	2.0	0.2	Zinc	10	10	

** same results obtained when CdS diff. const. kept at 10 cm^2 S^{-1}

SRV Back = 10^{50} cm S^{-1}

Table 5D Parameters for Cu_2S–CdS - Ag cells (fig. 5.30B to 5.39B)

Figure	SRV front cm S^{-1}	Diffusion Length CdS μm	Diffusion Length Cu_2S μm	Substrate	Diffusion Constant CdS cm^2S^{-1}	Diffusion Constant Cu_2S cm^2S^{-1}
5.30B	10^5	2.0	0.7	Ag	10	10
5.31B	10^4	2.0	0.7	Ag	10	10
5.32B	10^4	2.0	0.6	Ag	10	10
5.33B	10^5	2.0	0.5	Ag	10	10
5.34B	10^4	2.0	0.5	Ag	10	10
5.35B	10^4	2.0	0.4	Ag	10	10
5.36B	10^4	2.0	0.3	Ag	10	10
5.37B	10^2	2.0	0.2	Ag	10	10
5.38B	10^4	2.0	0.2	Ag	10	10
5.39B	10^5	2.0	0.2	Ag	10	10

FIGURE 5·1B

Photocurrent against Cu_2S thickness
(see tables on pages 112 and 113)

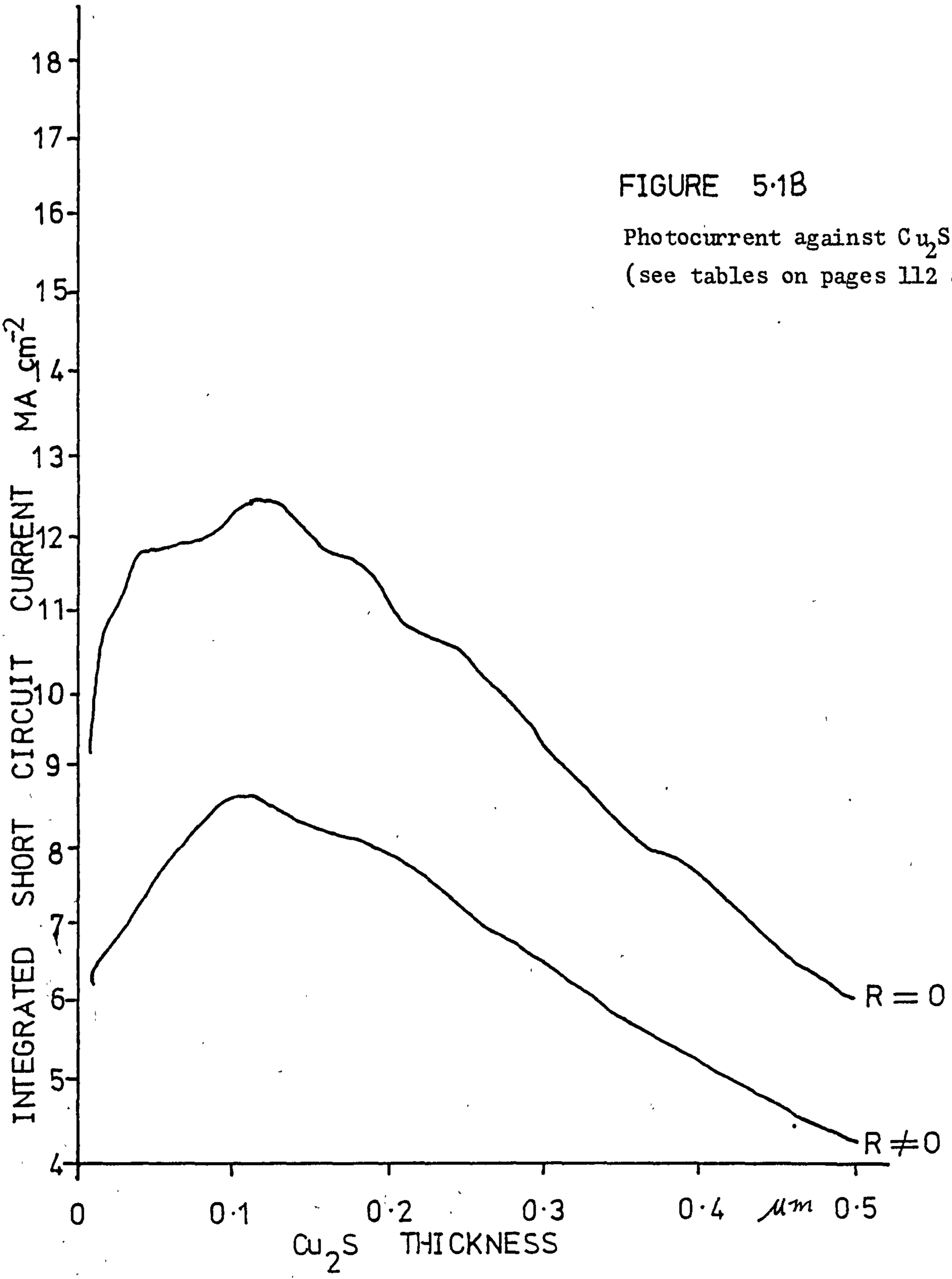

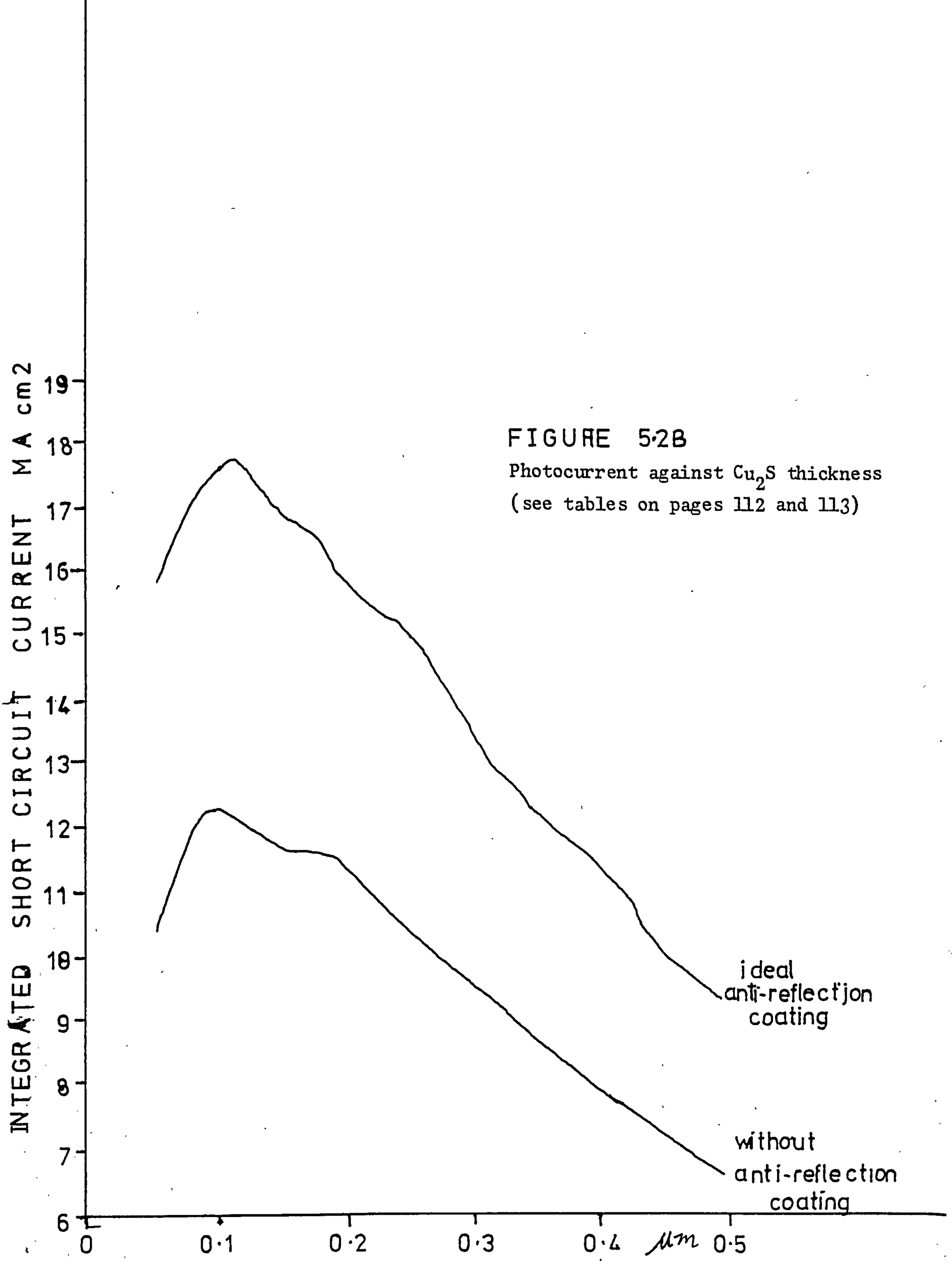

FIGURE 5·2B

Photocurrent against Cu_2S thickness

(see tables on pages 112 and 113)

Photocurrent against Cu_2S thickness (see tables on pages 112 and 113)

FIGURE 5·38

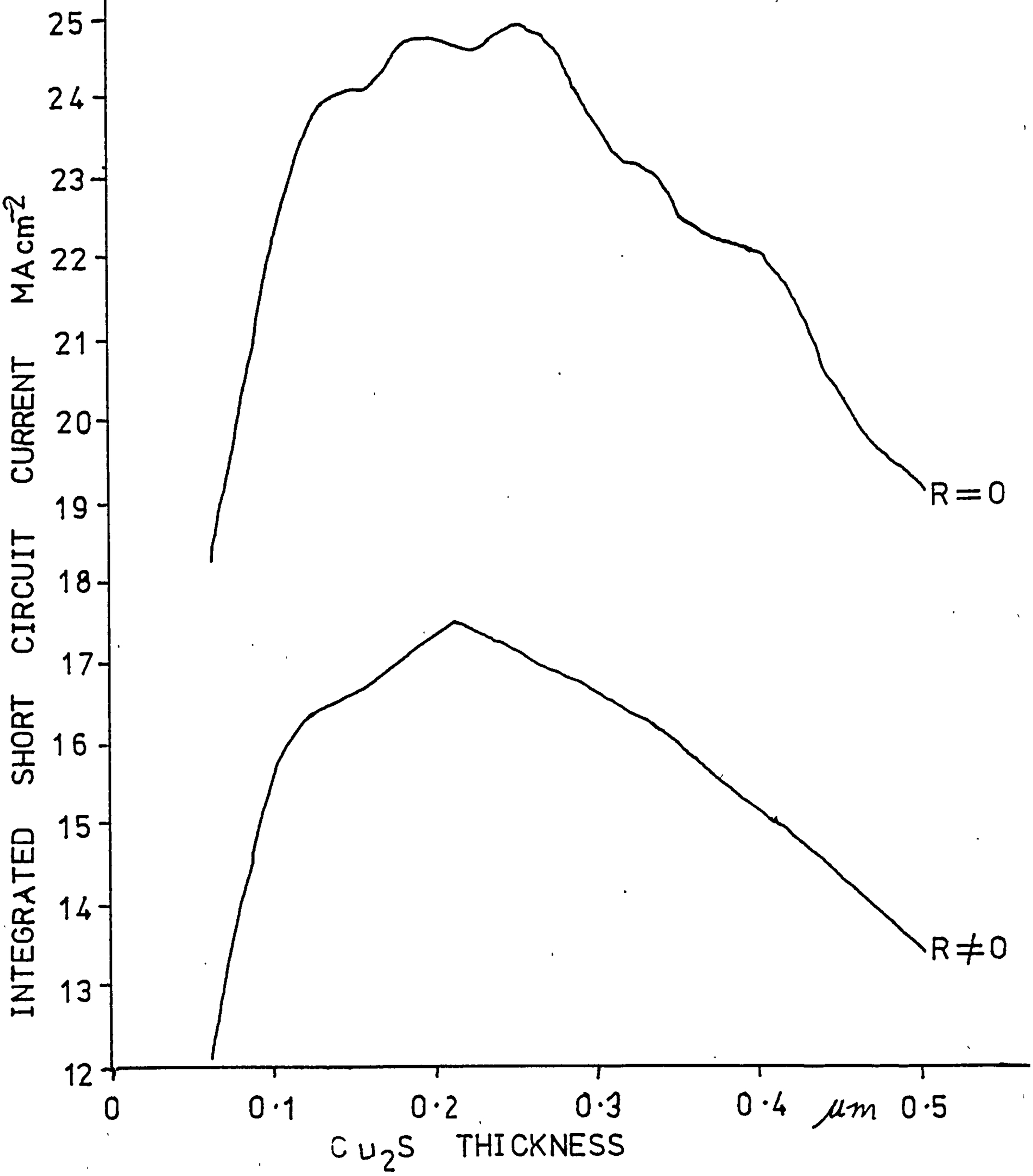

Photocurrent against Cu_2S thickness (see tables on pages 112 and 113)

FIGURE 5·48

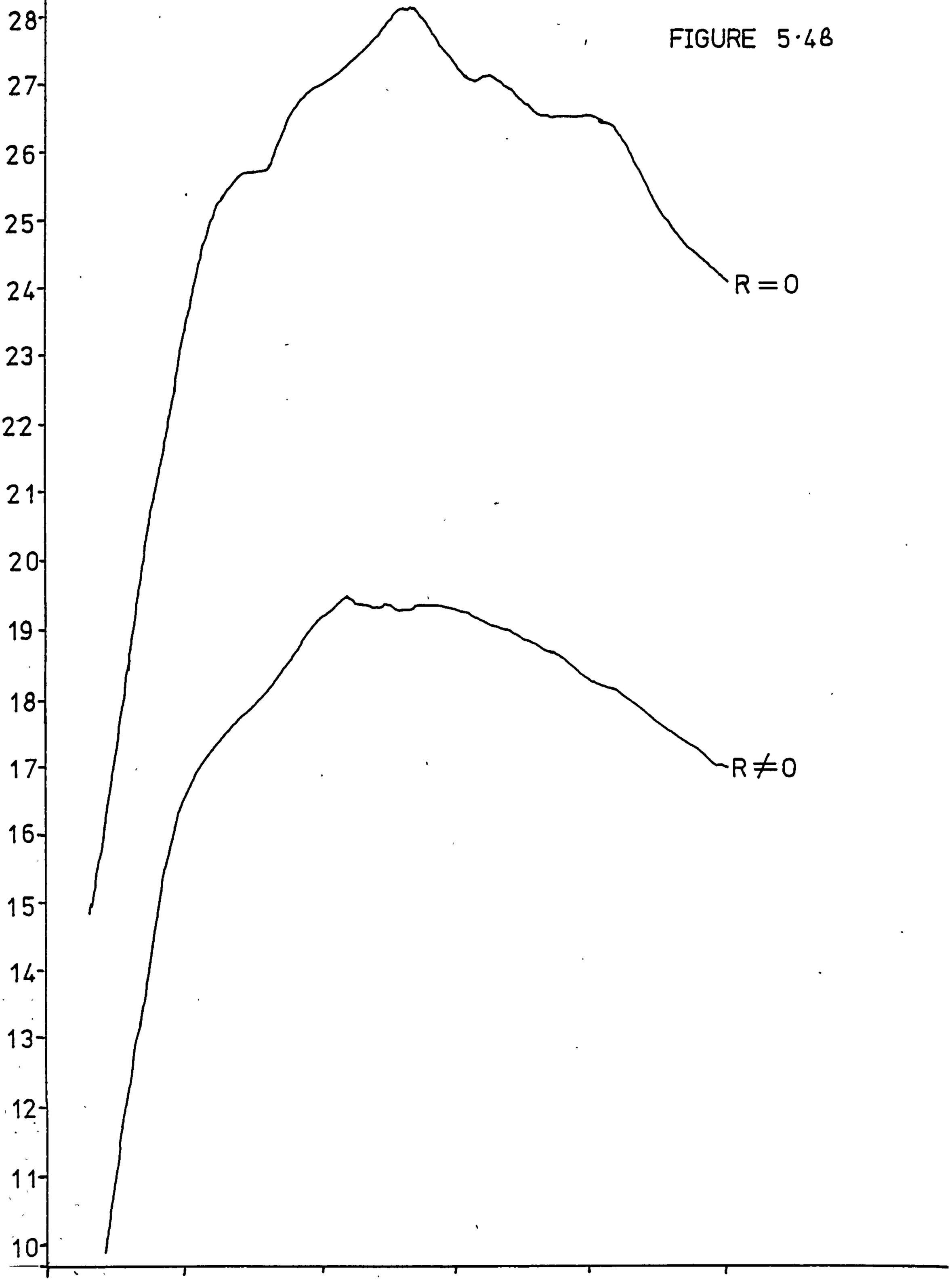

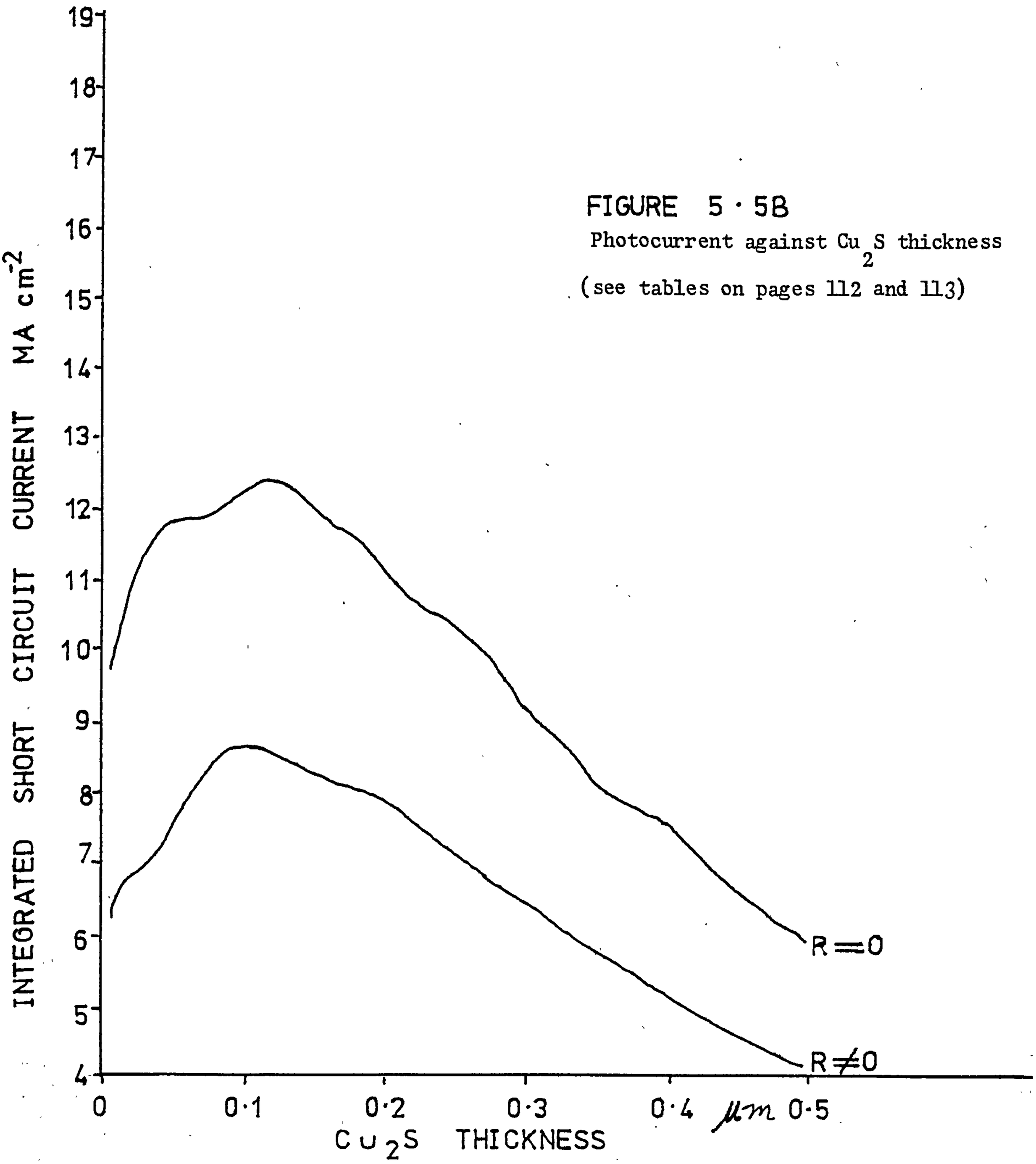

FIGURE 5·5B

Photocurrent against Cu_2S thickness

(see tables on pages 112 and 113)

FIGURE 5·6B

Photocurrent against Cu_2S thickness

(see tables on pages 112 and 113)

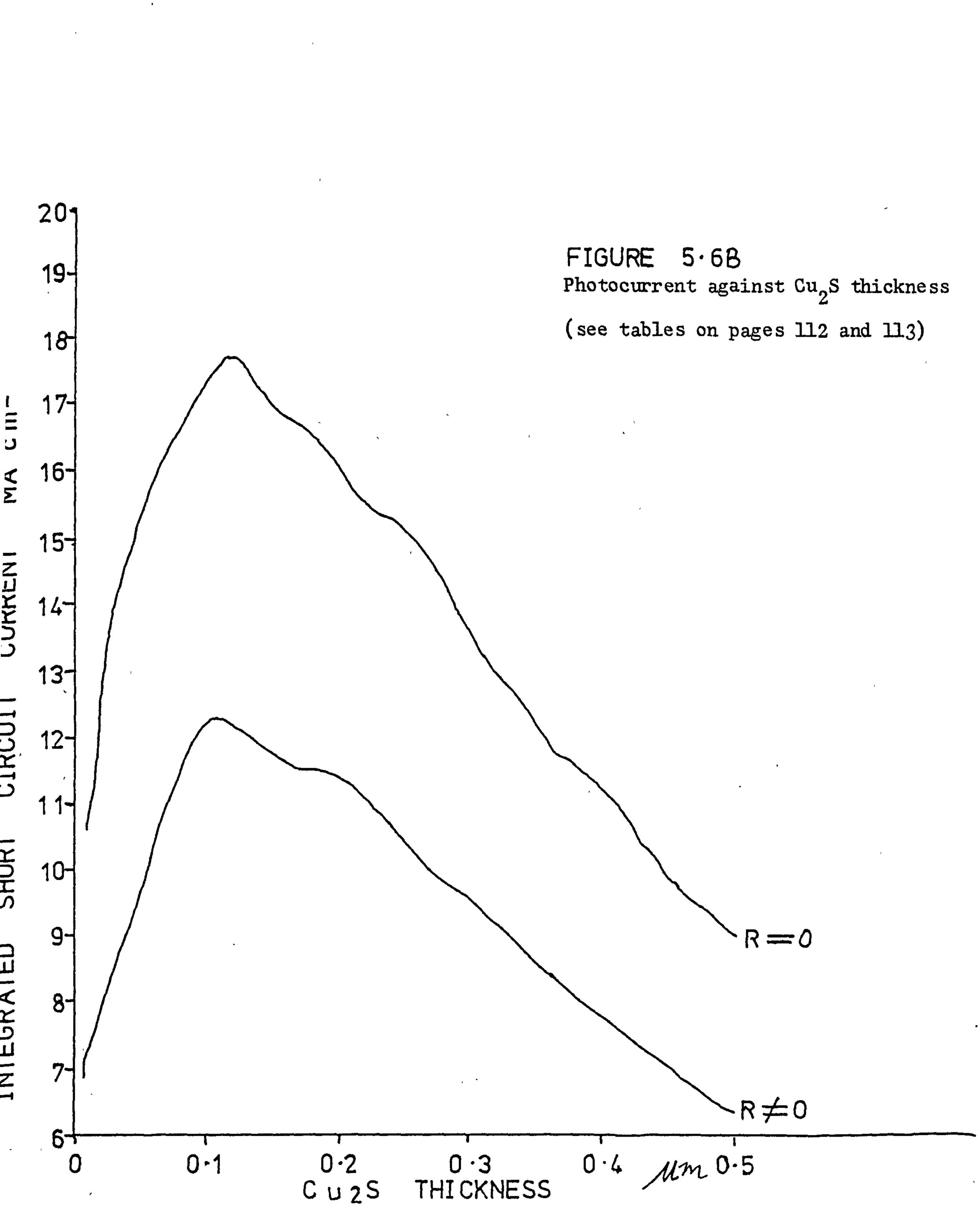

FIGURE 5·7B
Photocurrent against Cu_2S thickness

(see tables on pages 112 and 113)

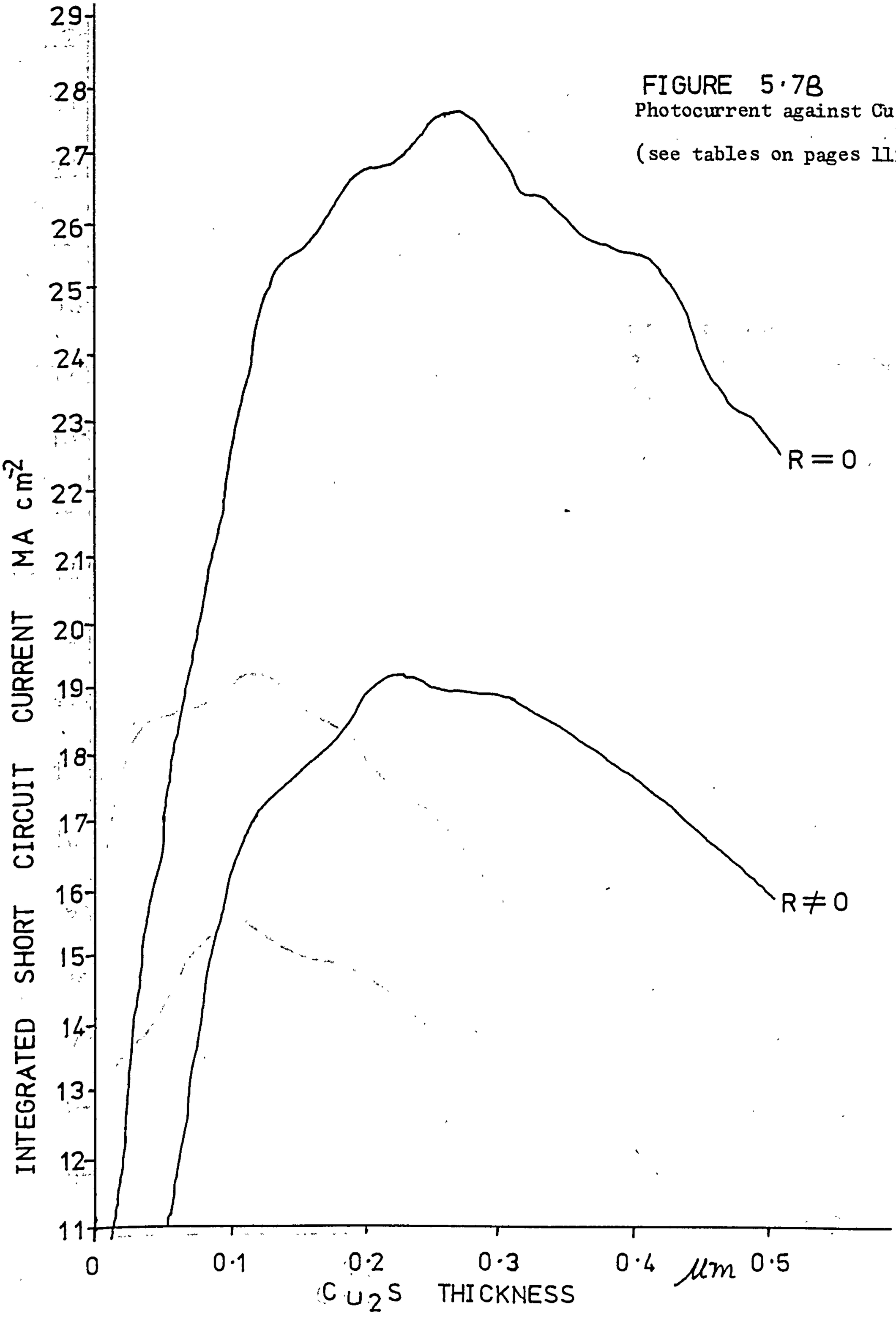

FIGURE 5·8B

Photocurrent against Cu_2S thickness

(see tables on pages 112 and 113)

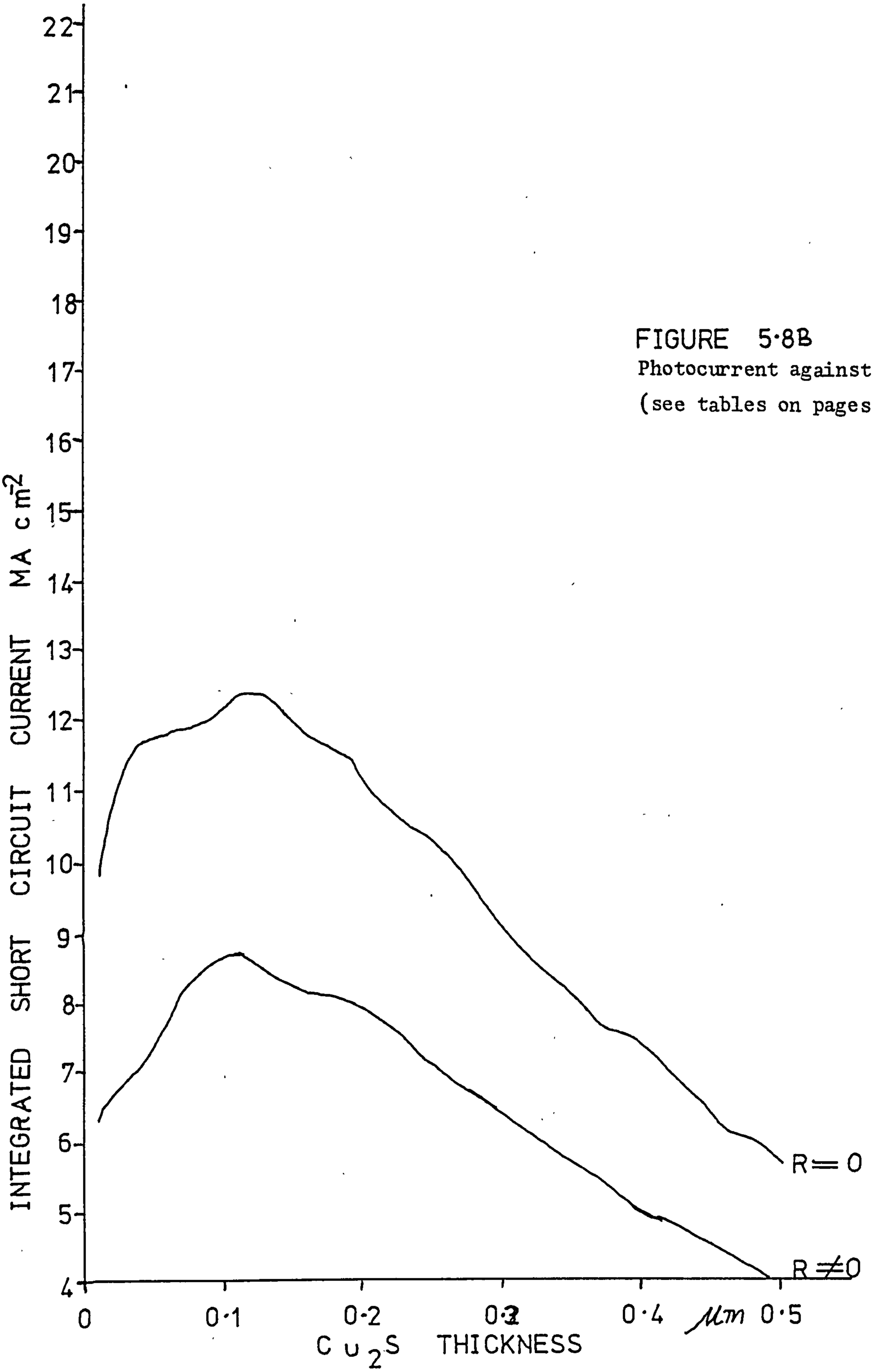

FIGURE 5·9B

Photocurrent against Cu_2S thickness

(see tables on pages 112 and 113)

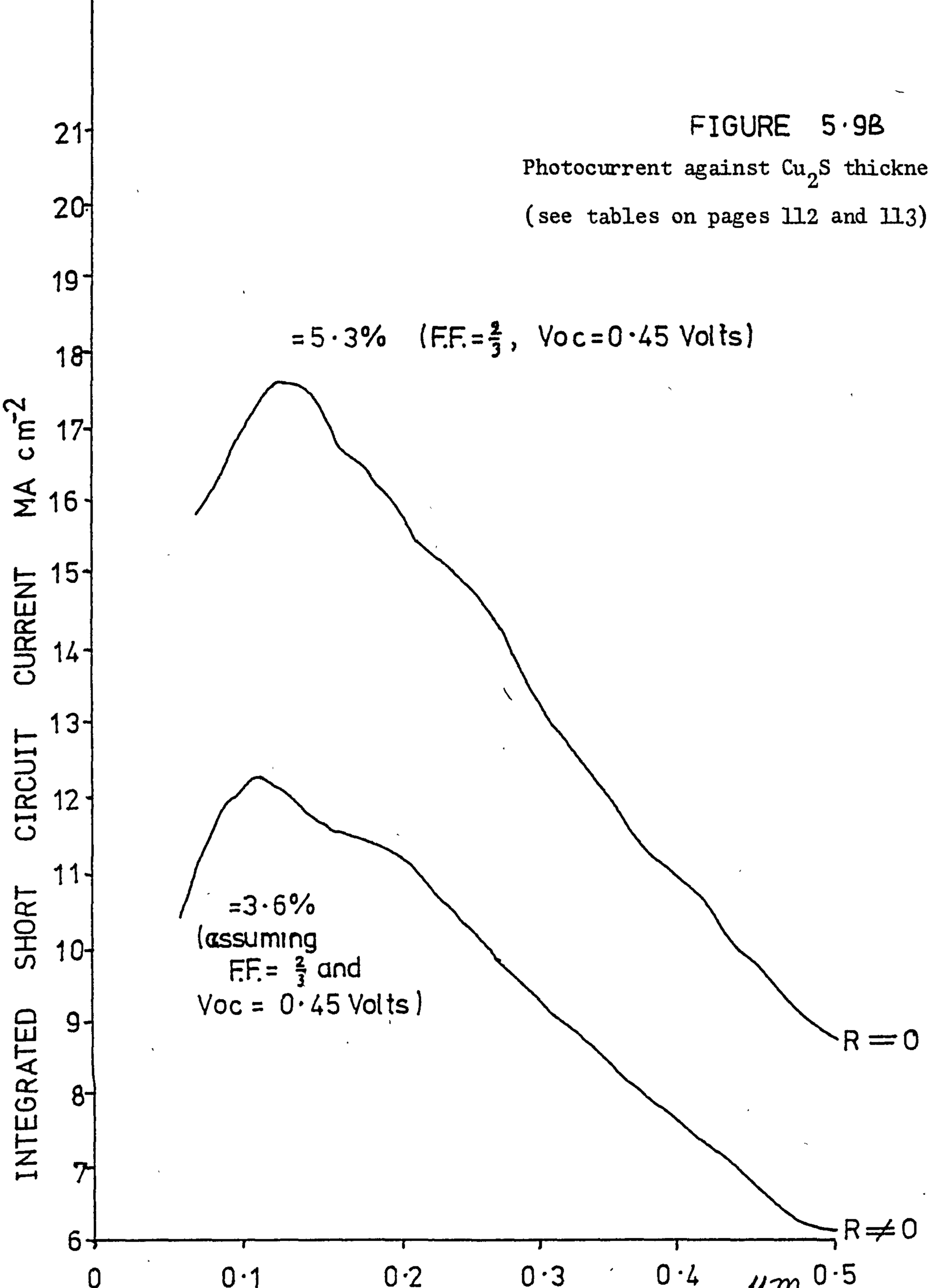

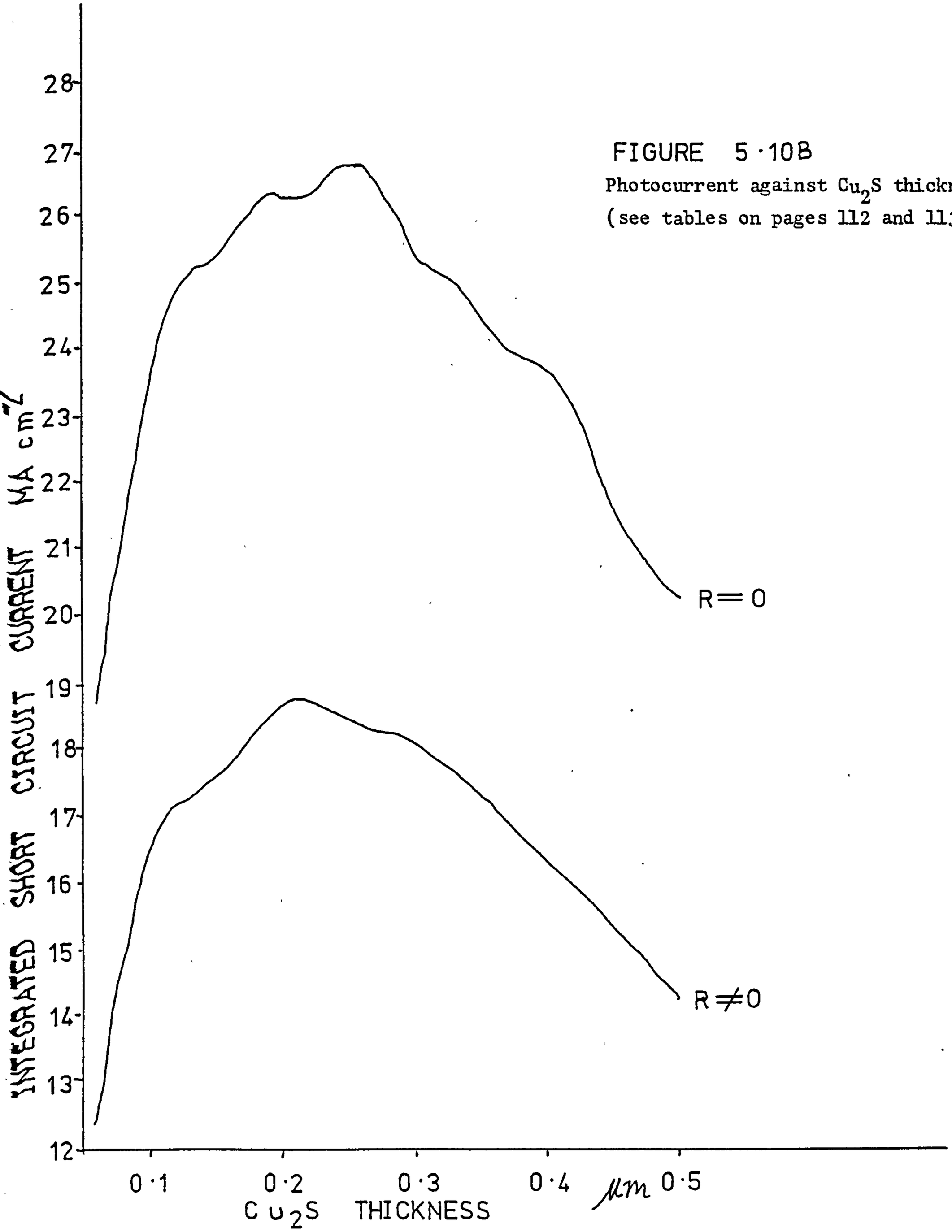

FIGURE 5·10B

Photocurrent against Cu_2S thickness

(see tables on pages 112 and 113)

FIGURE 5·11B

Photocurrent against Cu_2S thickness

(see tables on pages 112 and 113)

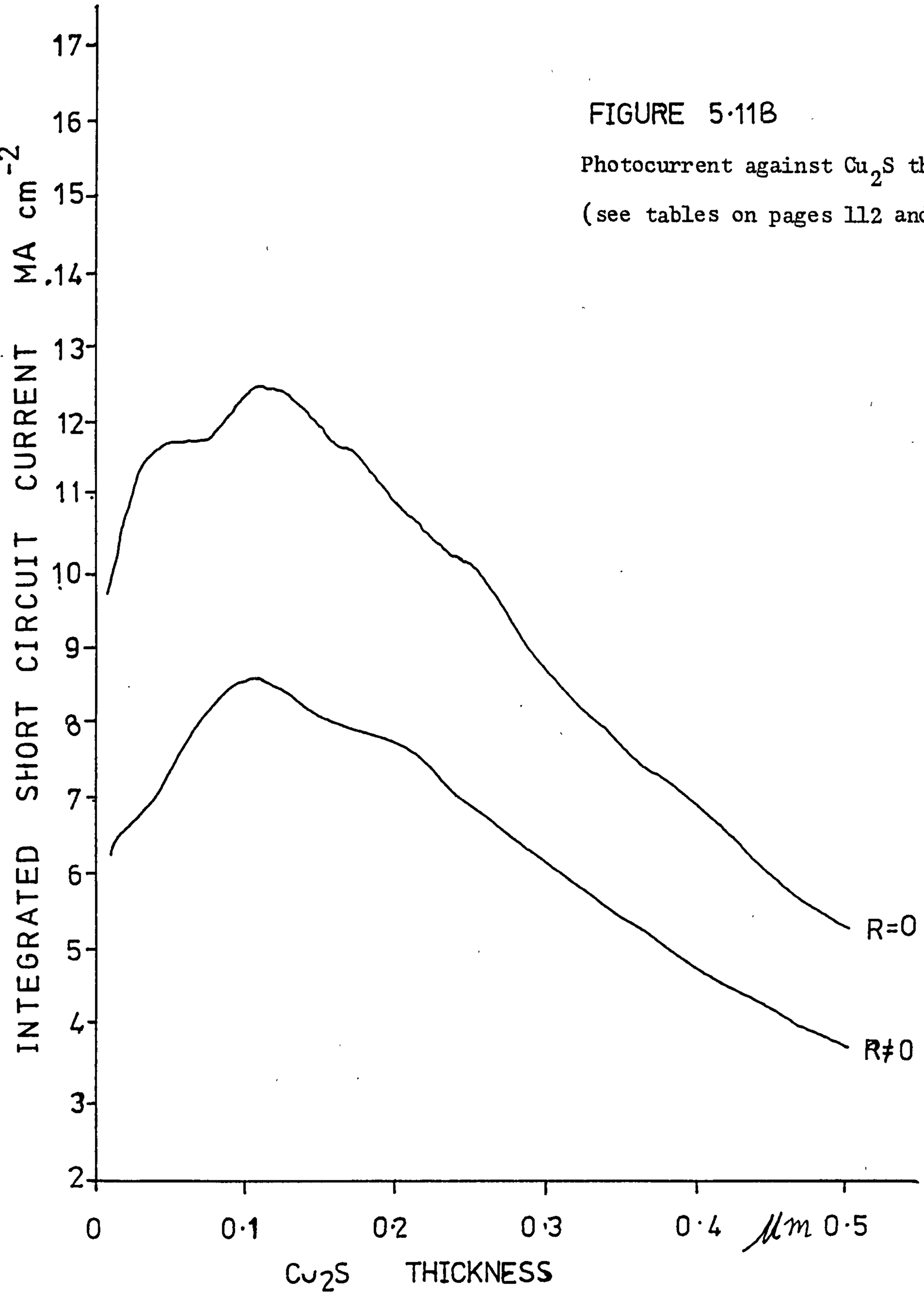

FIGURE 5-12B

Photocurrent against Cu_2S thickness

(see tables on pages 112 and 113)

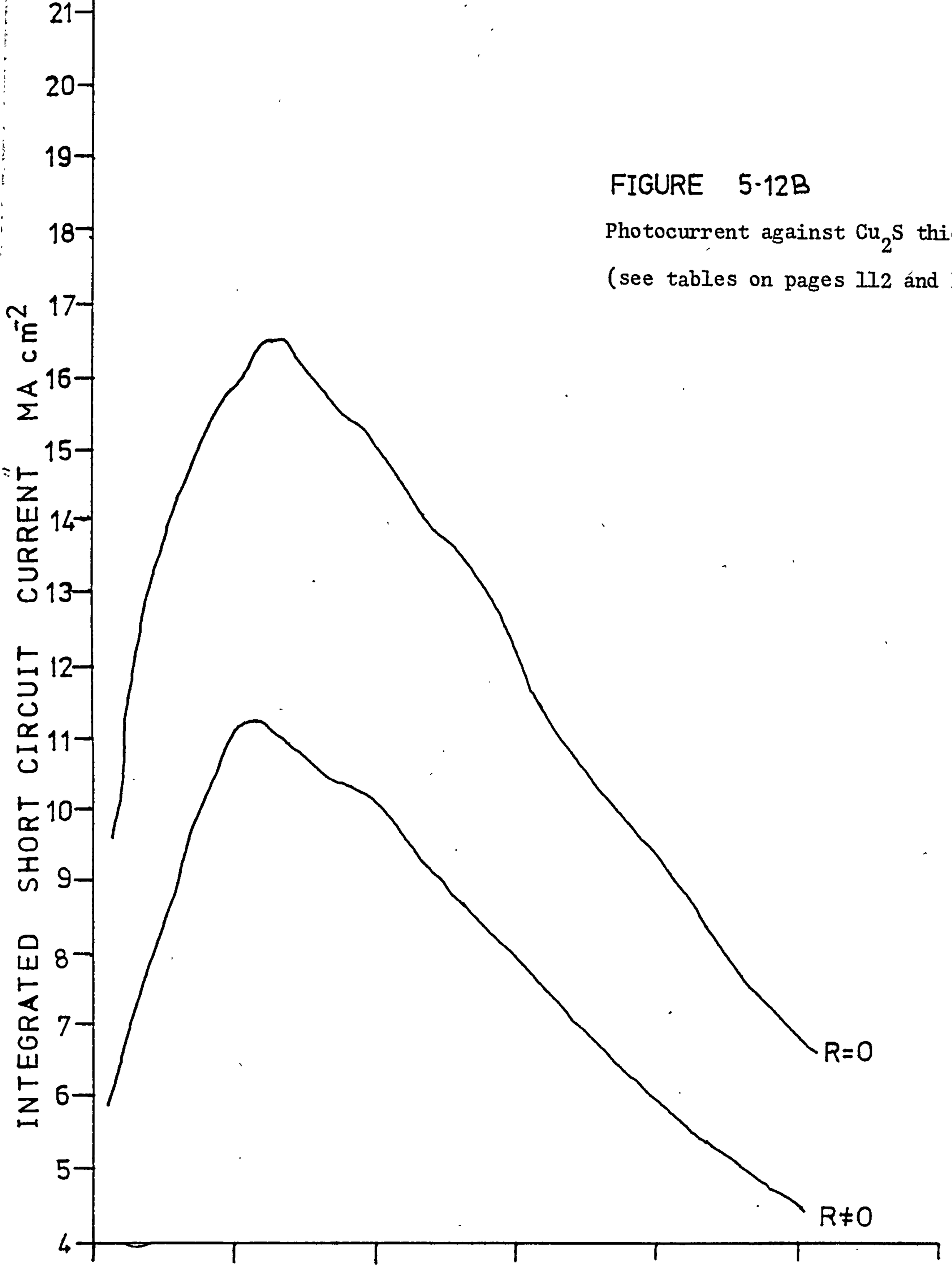

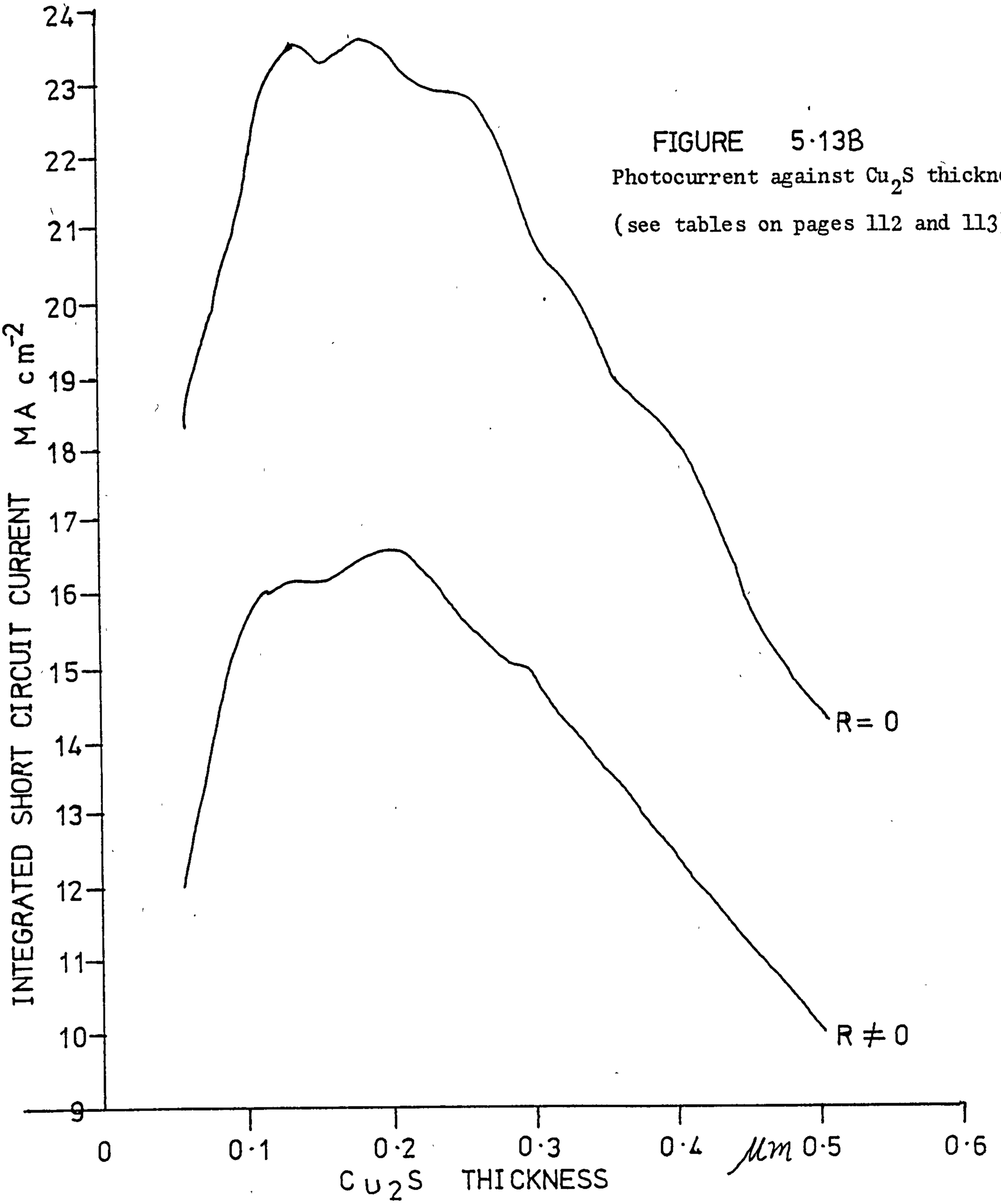

FIGURE 5·13B

Photocurrent against Cu_2S thickness

(see tables on pages 112 and 113)

FIGURE 5.14B

Photocurrent against Cu_2S thickness

(see tables on pages 112 and 113)

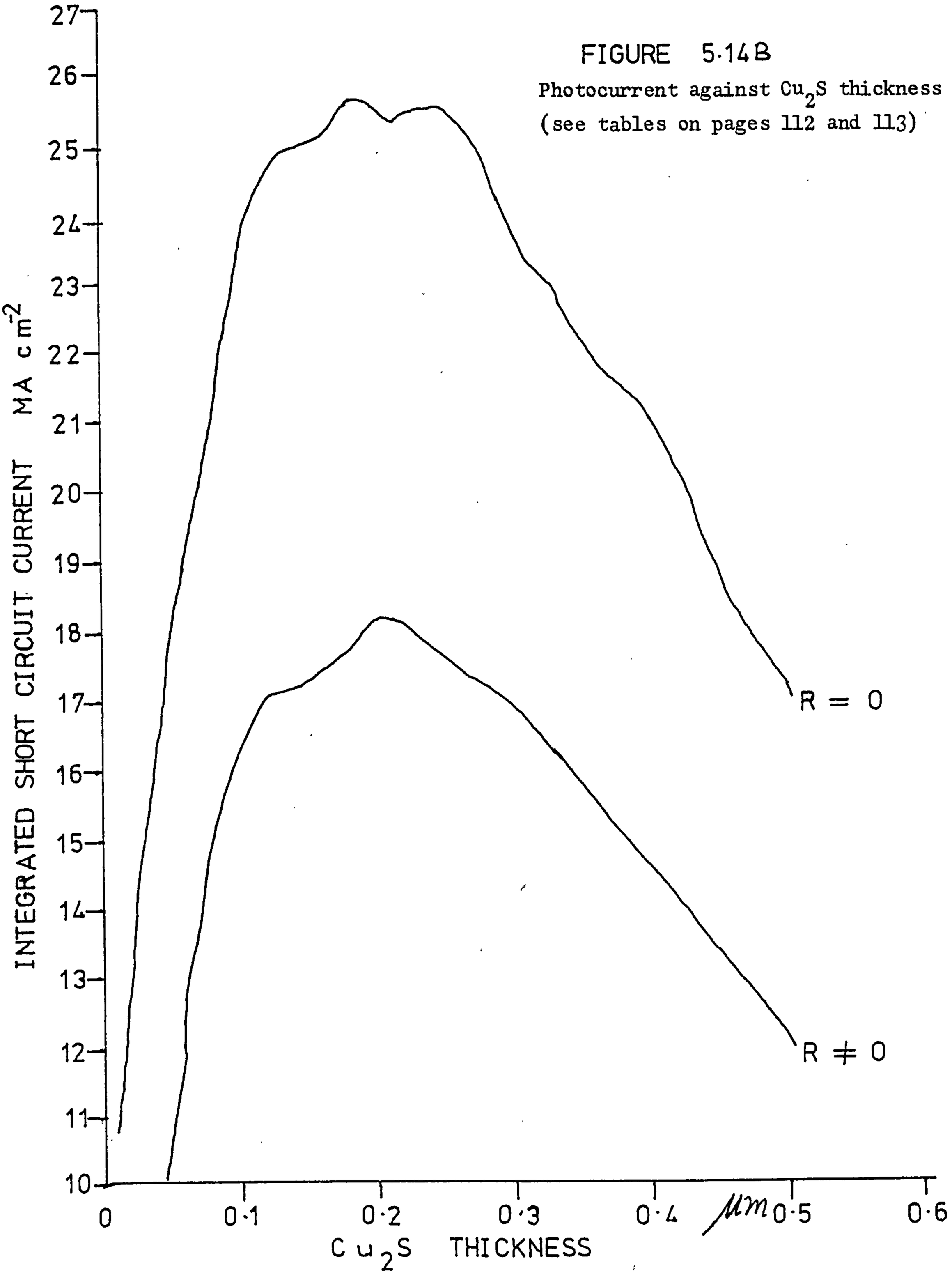

FIGURE 5·15B

Photocurrent against Cu_2S thickness

(see tables on pages 112 and 113)

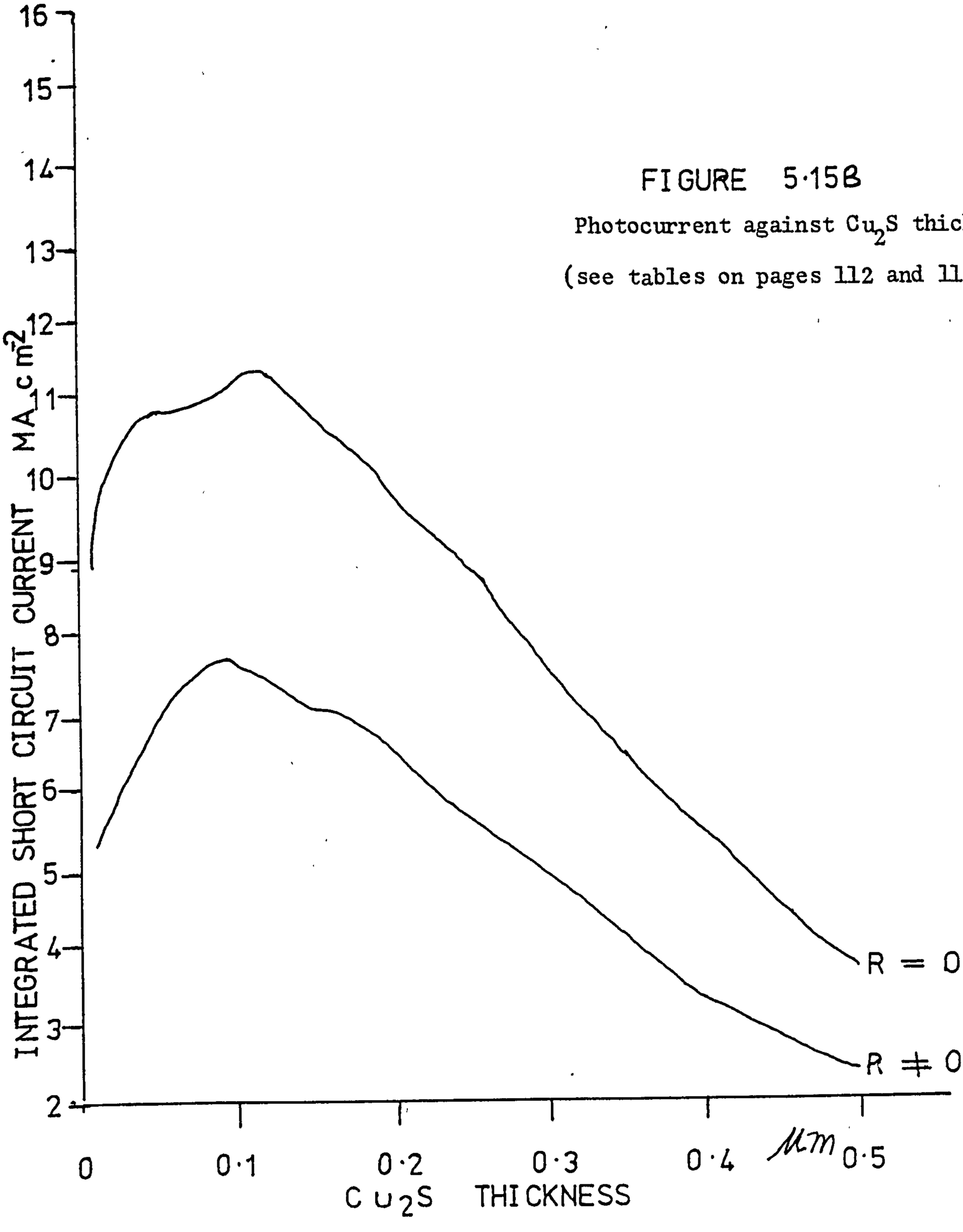

FIGURE 5·16B

Photocurrent against Cu_2S thickness

(see tables on pages 112 and 113)

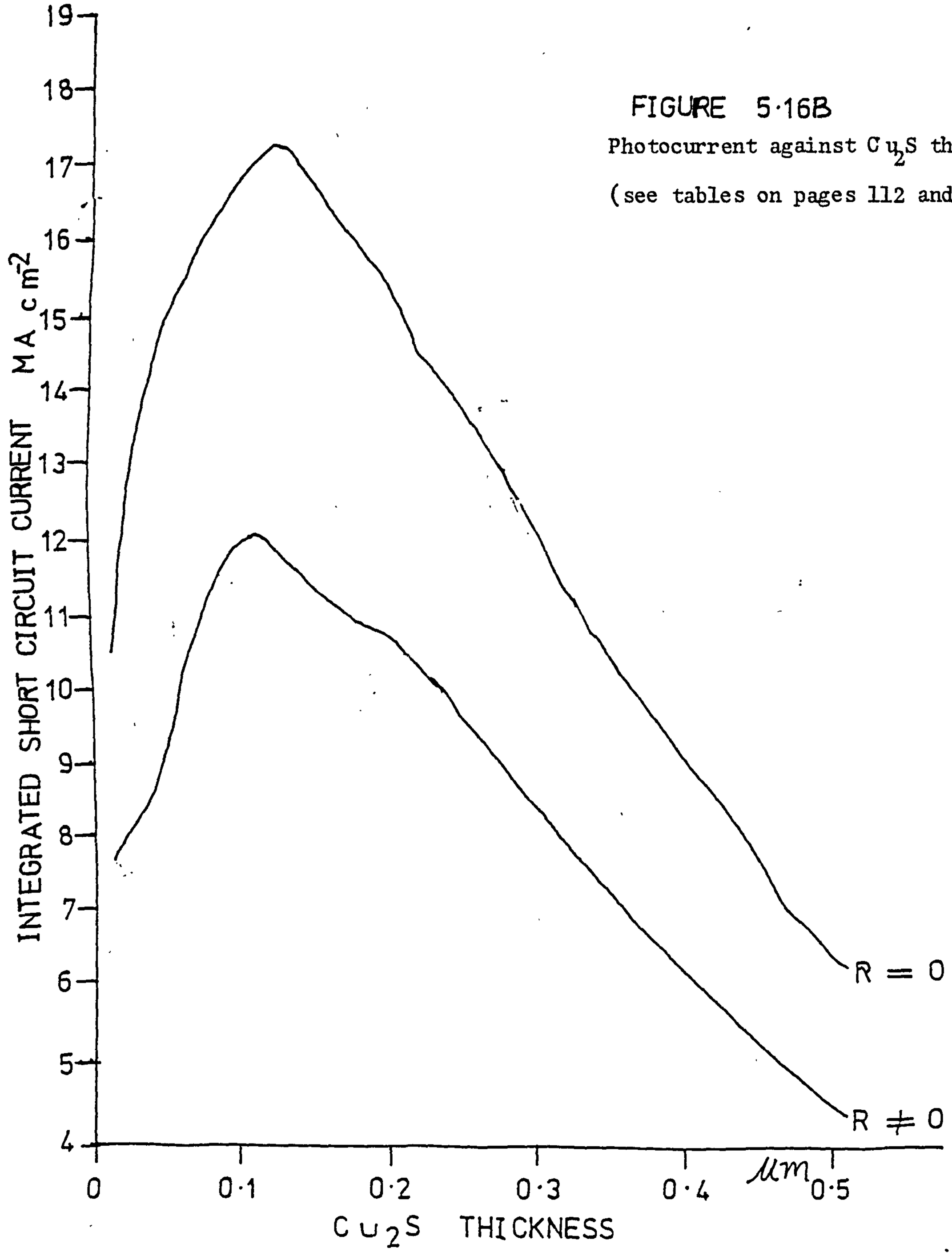

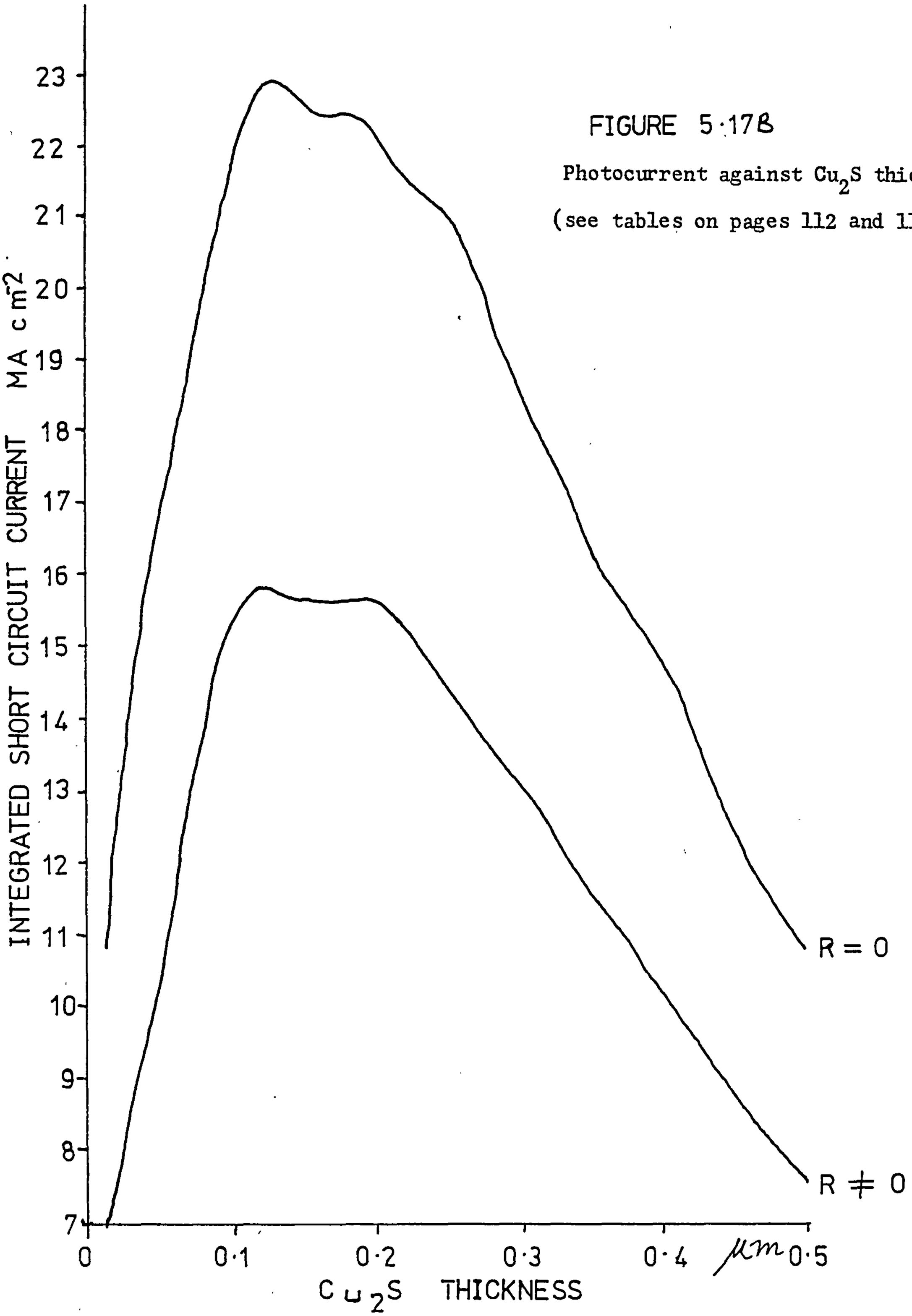

FIGURE 5·17B

Photocurrent against Cu_2S thickness

(see tables on pages 112 and 113)

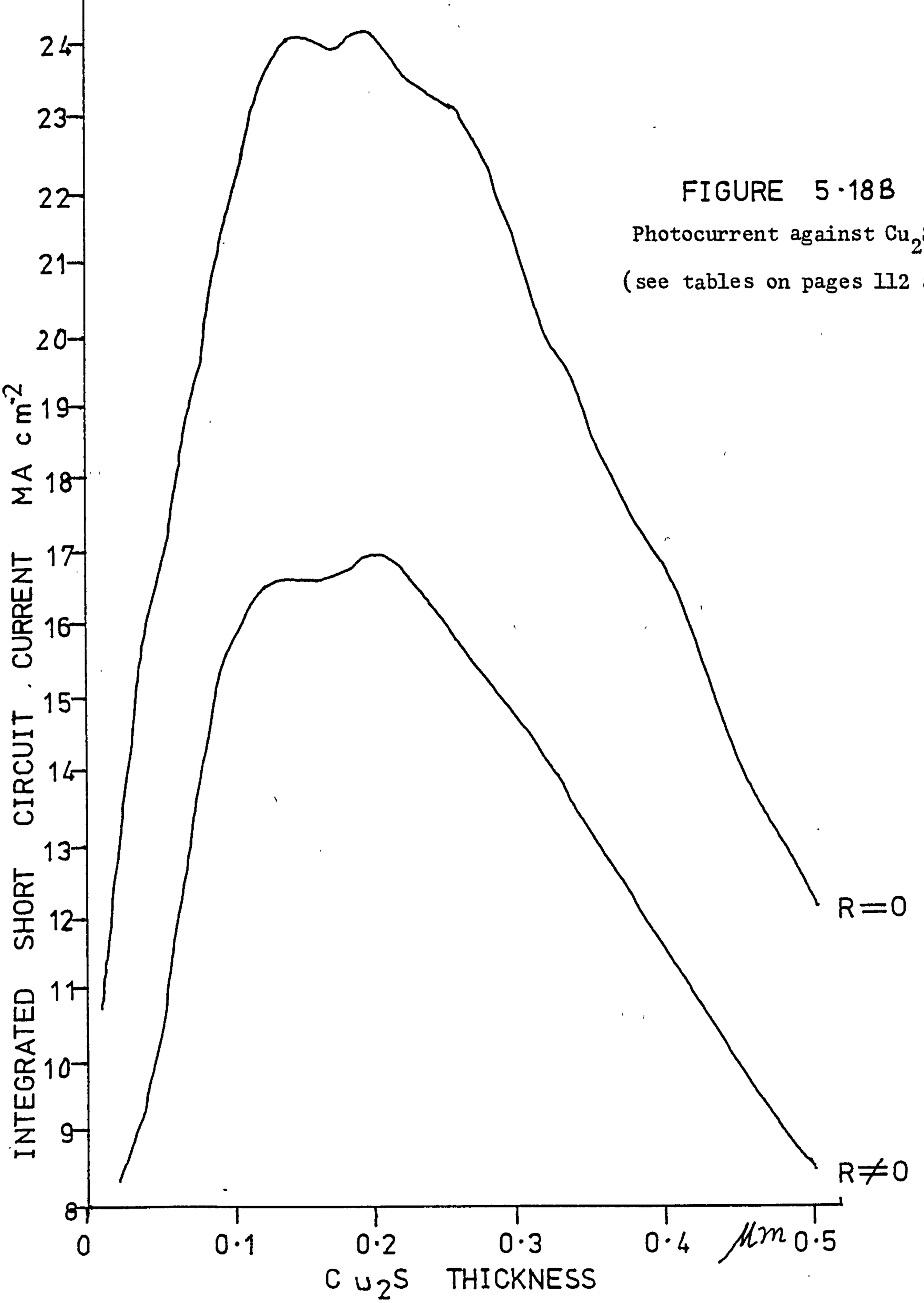

FIGURE 5·18B

Photocurrent against Cu_2S thickness

(see tables on pages 112 and 113)

FIGURE 5-19B

Photocurrent against Cu_2S thickness

(see tables on pages 112 and 113)

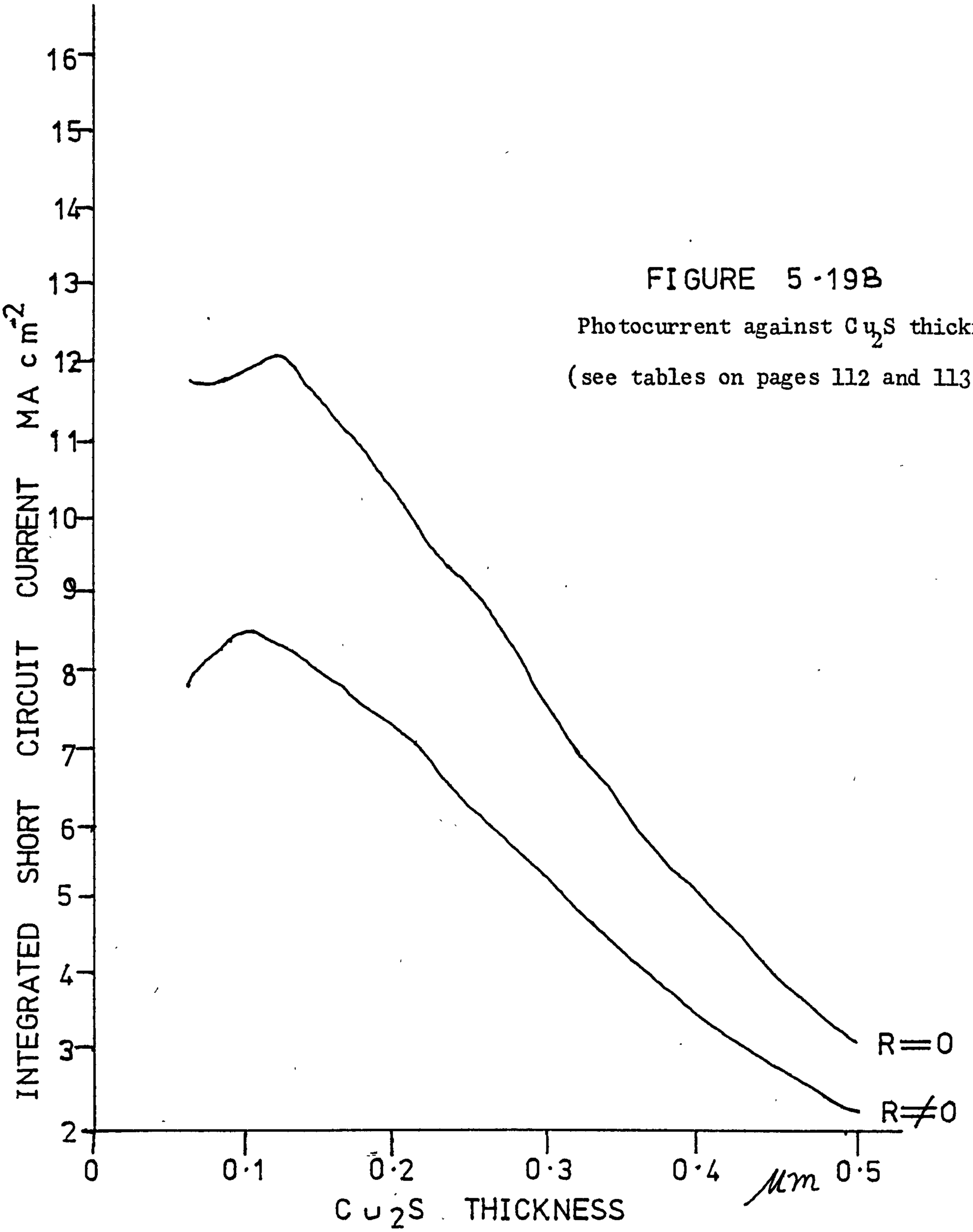

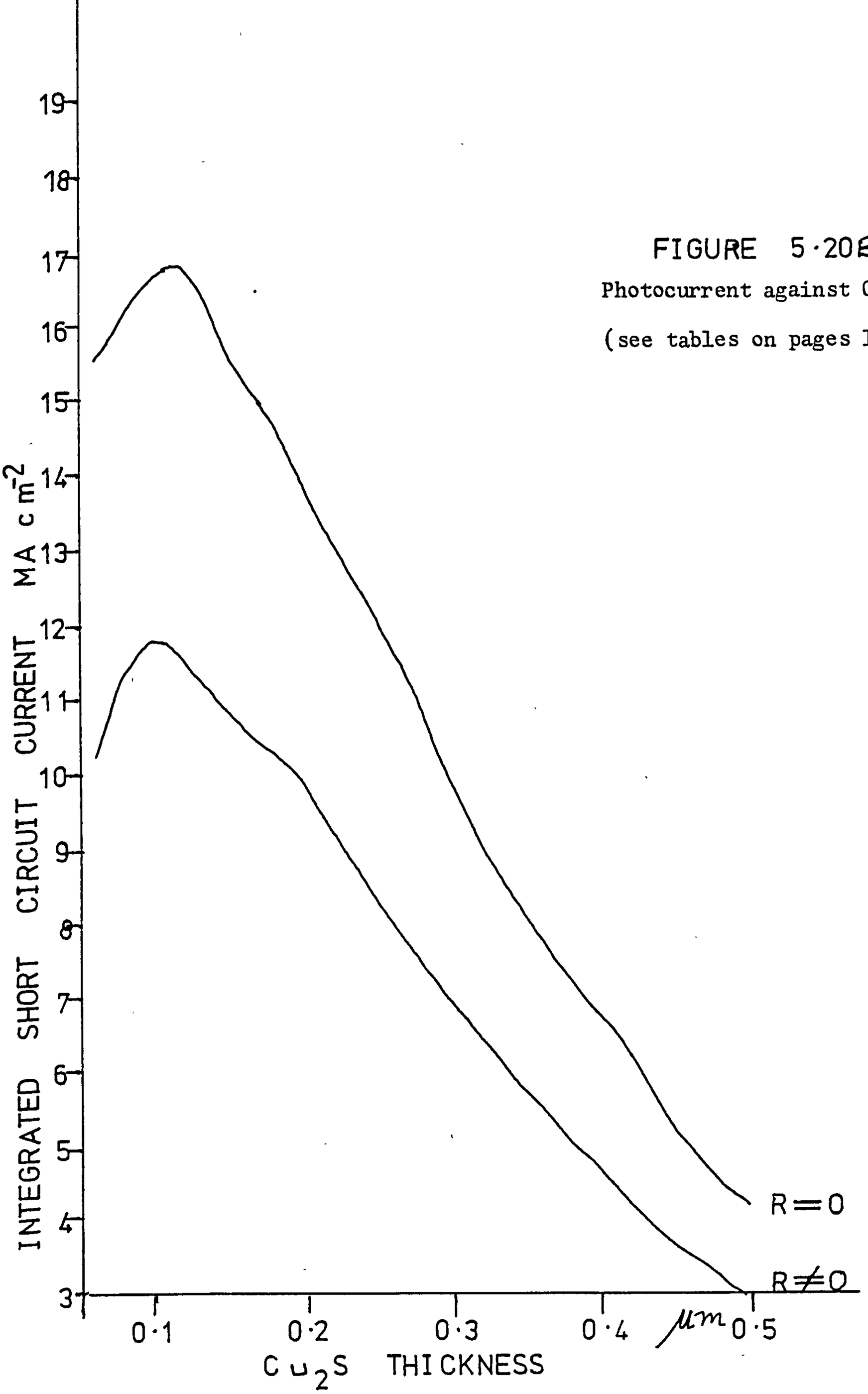

FIGURE 5·20B

Photocurrent against Cu_2S thickness

(see tables on pages 112 and 113)

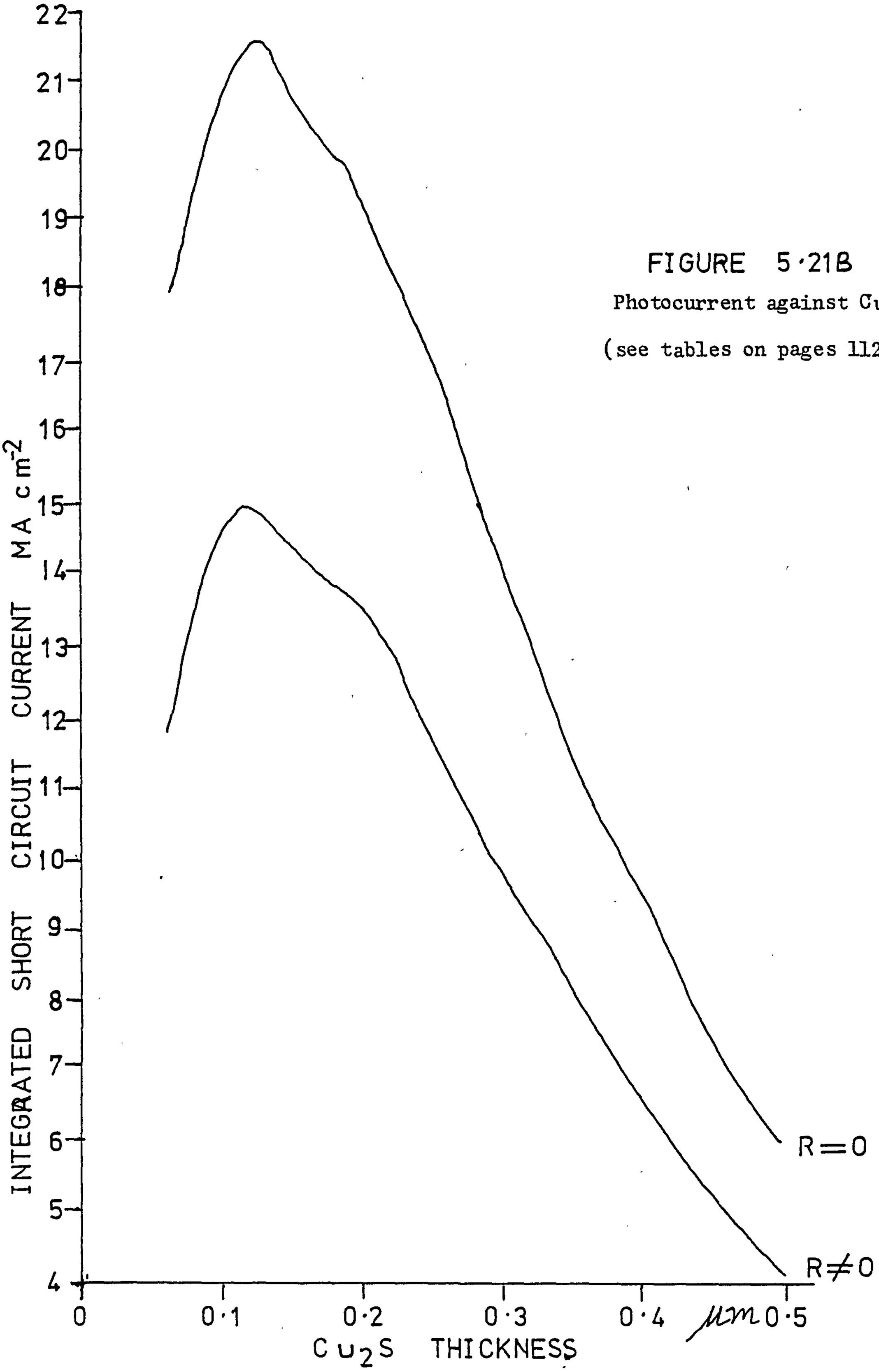

FIGURE 5·21B

Photocurrent against Cu_2S thickness

(see tables on pages 112 and 113)

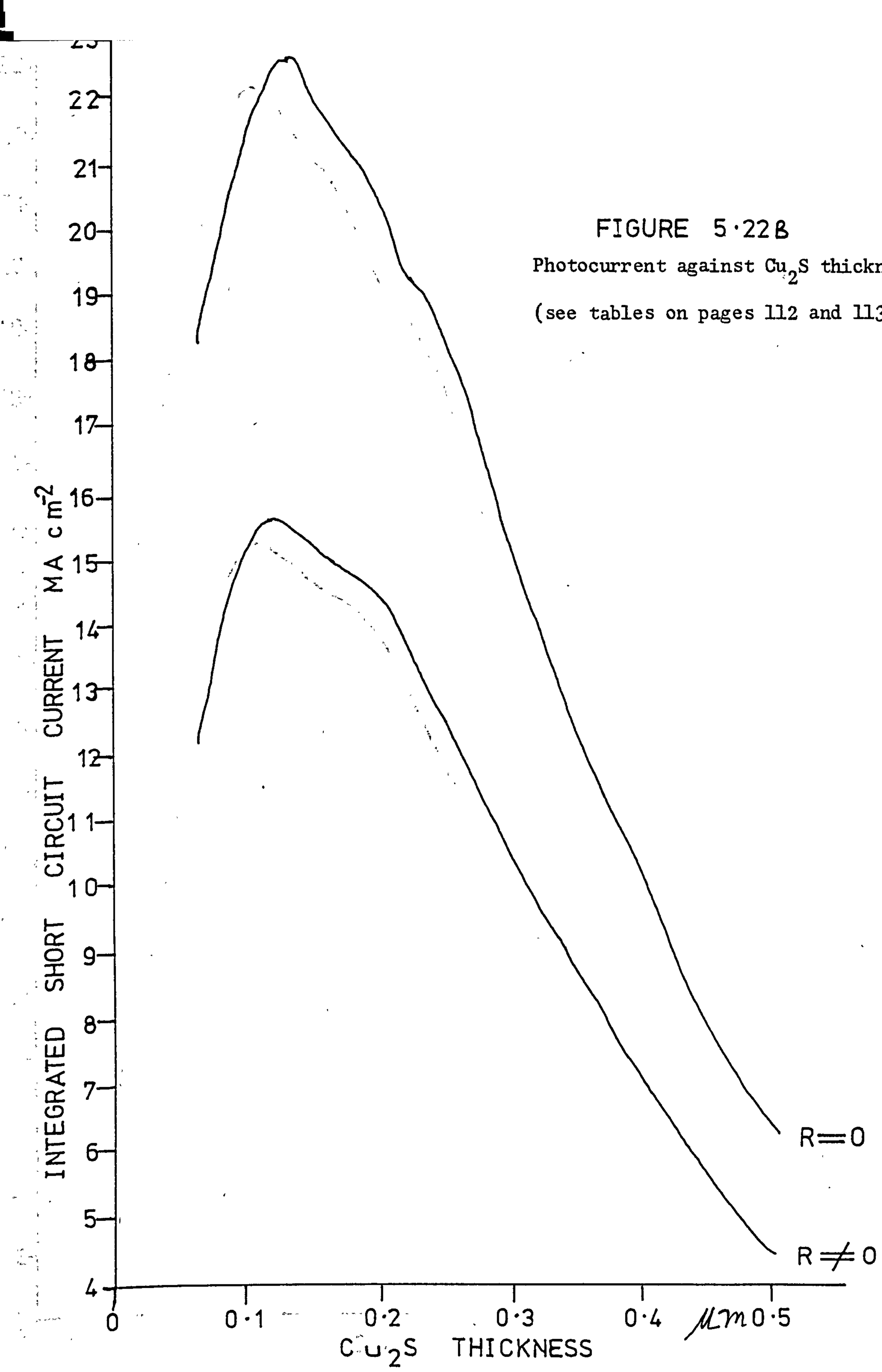

FIGURE 5·22B

Photocurrent against Cu_2S thickness

(see tables on pages 112 and 113)

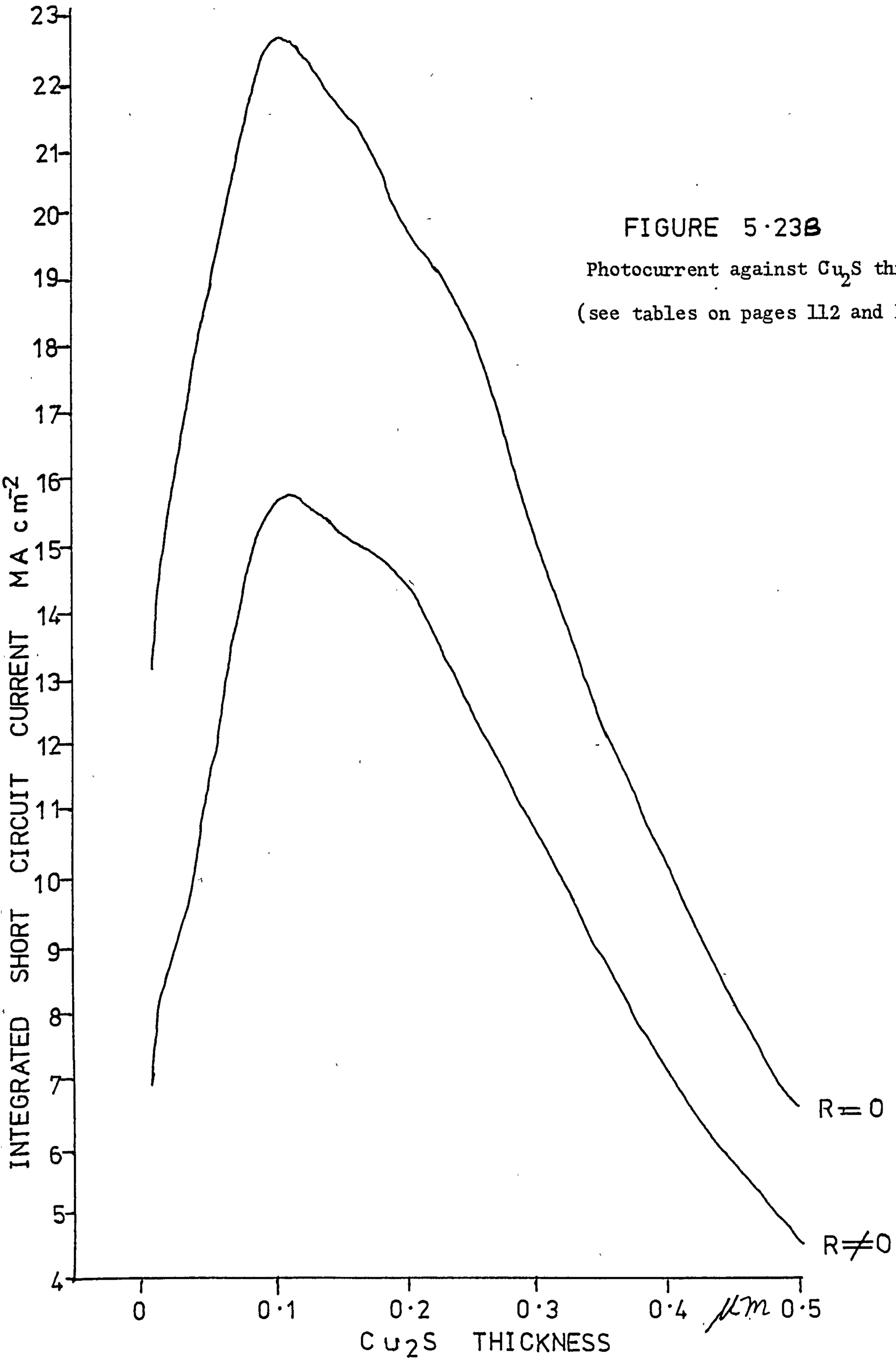

FIGURE 5·23B

Photocurrent against Cu_2S thickness

(see tables on pages 112 and 113)

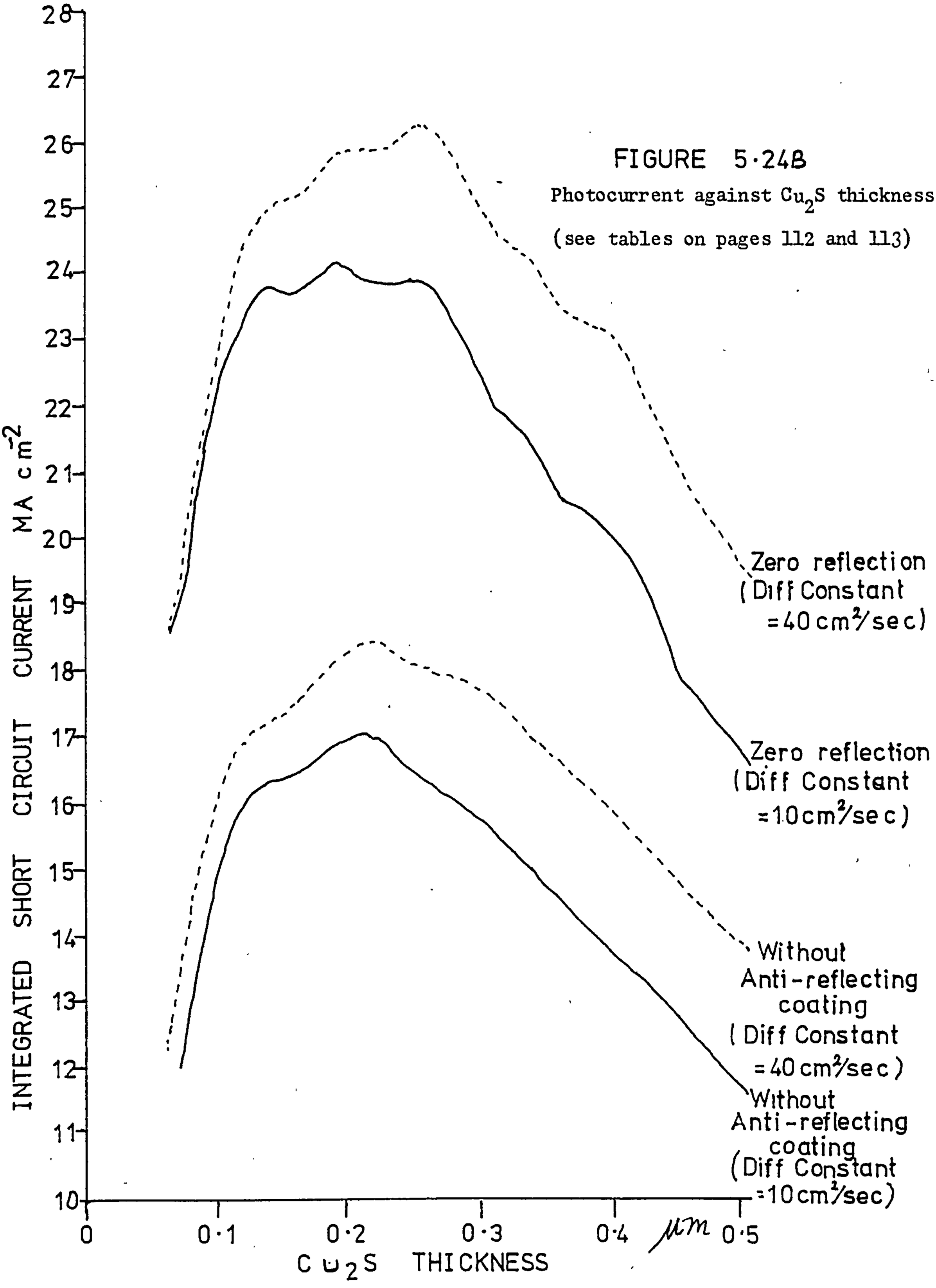

FIGURE 5·24B

Photocurrent against Cu_2S thickness

(see tables on pages 112 and 113)

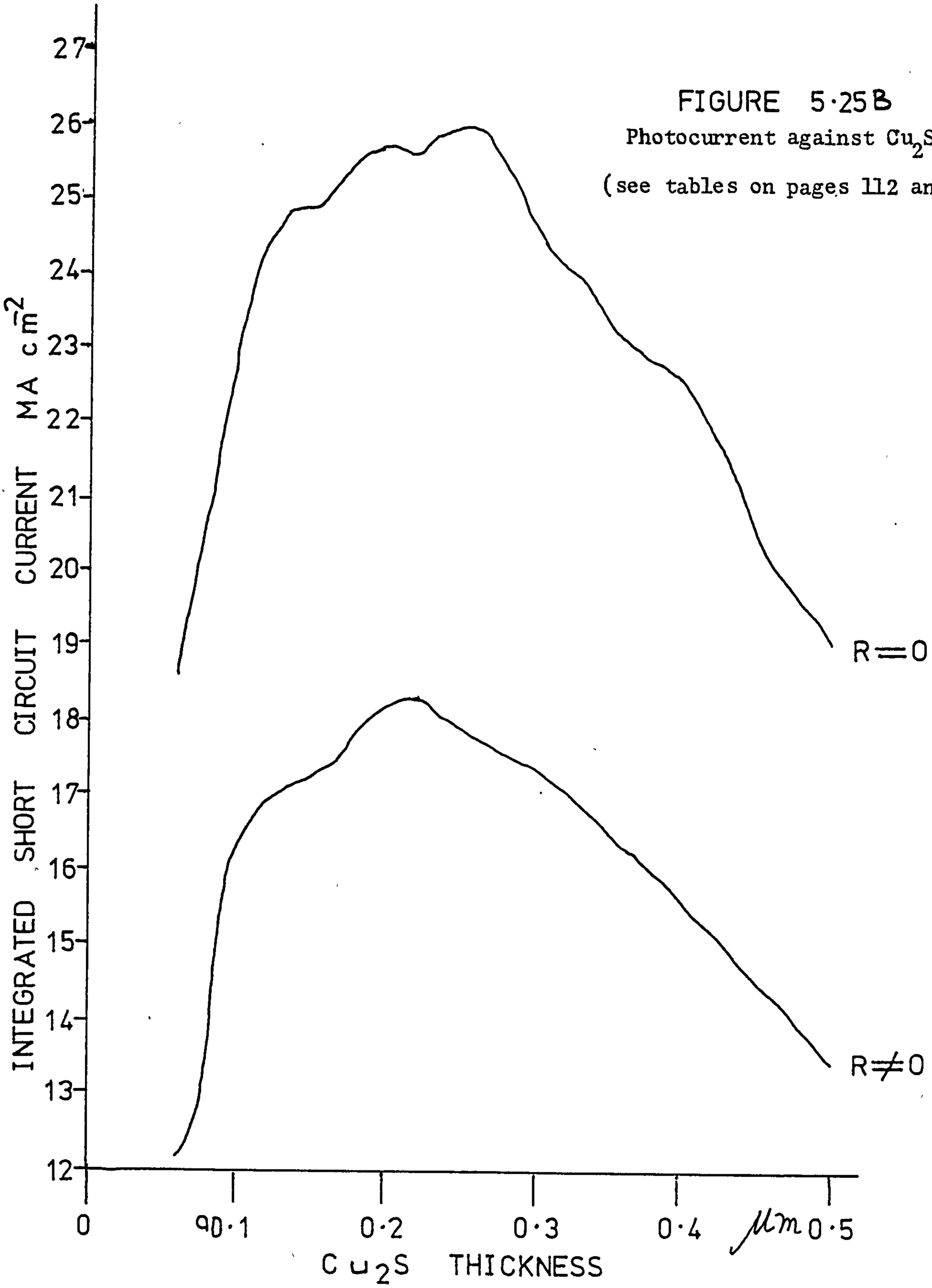

FIGURE 5·25B

Photocurrent against Cu_2S thickness

(see tables on pages 112 and 113)

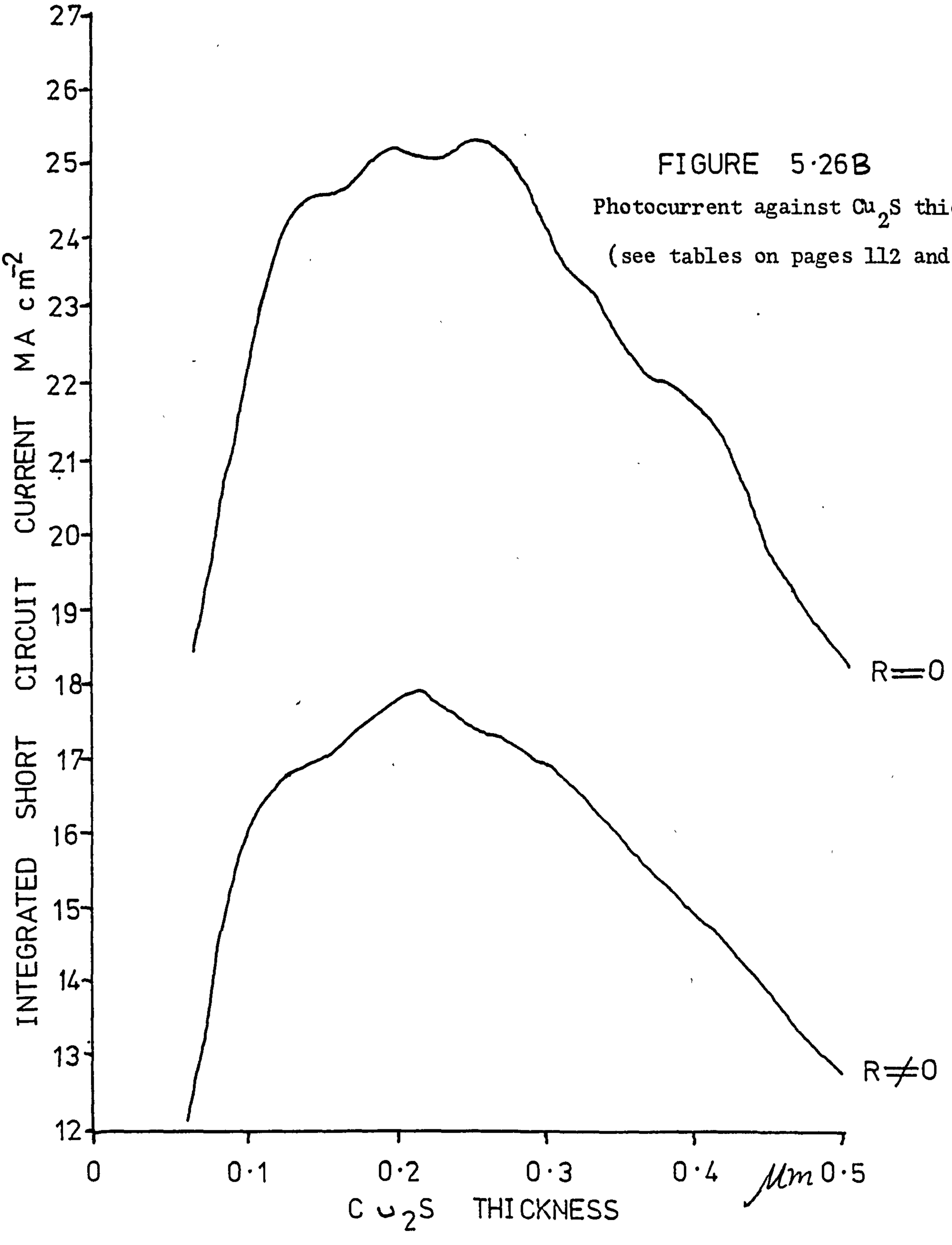

FIGURE 5·26B

Photocurrent against Cu_2S thickness

(see tables on pages 112 and 113)

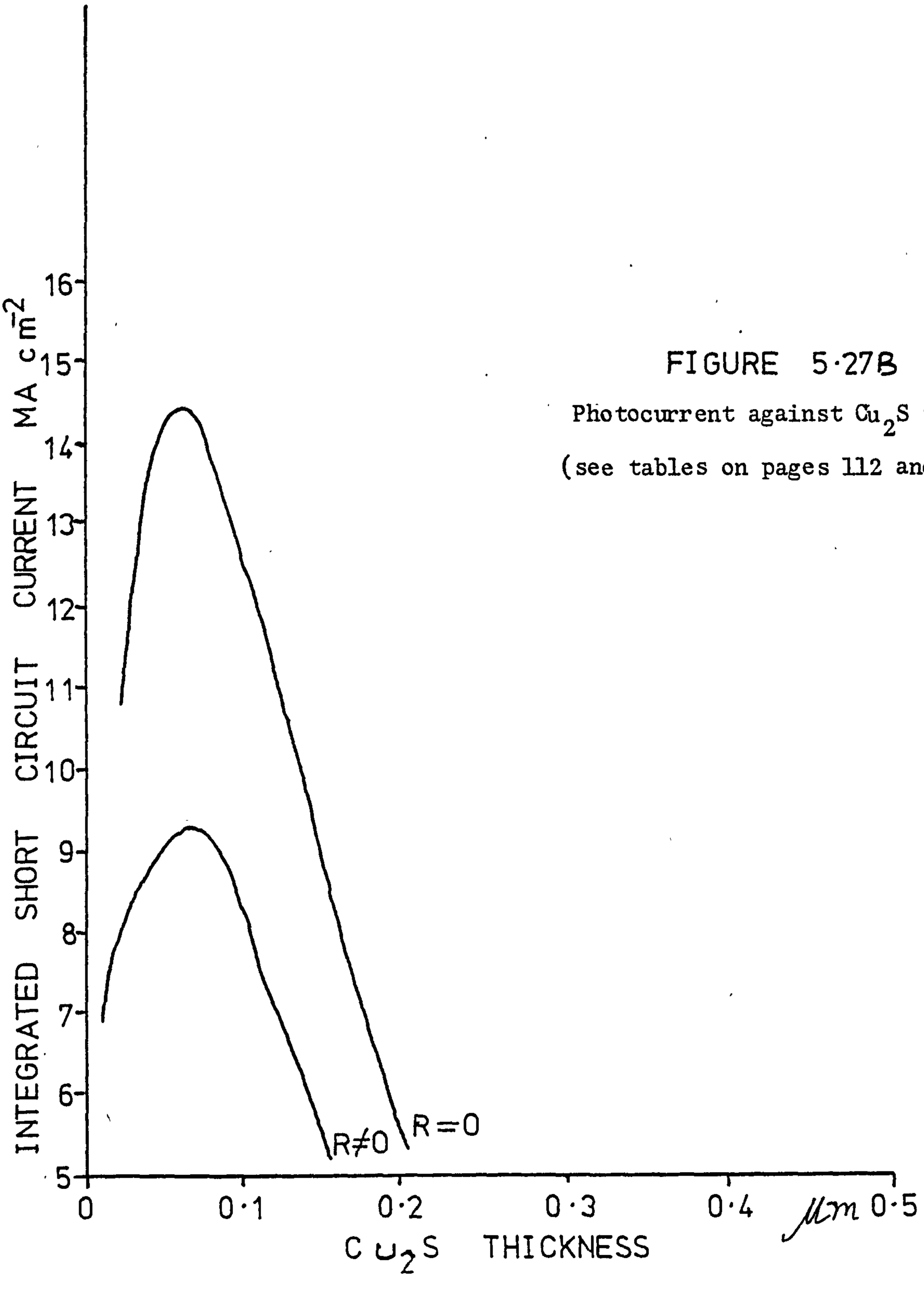

FIGURE 5·27B

Photocurrent against Cu_2S thickness

(see tables on pages 112 and 113)

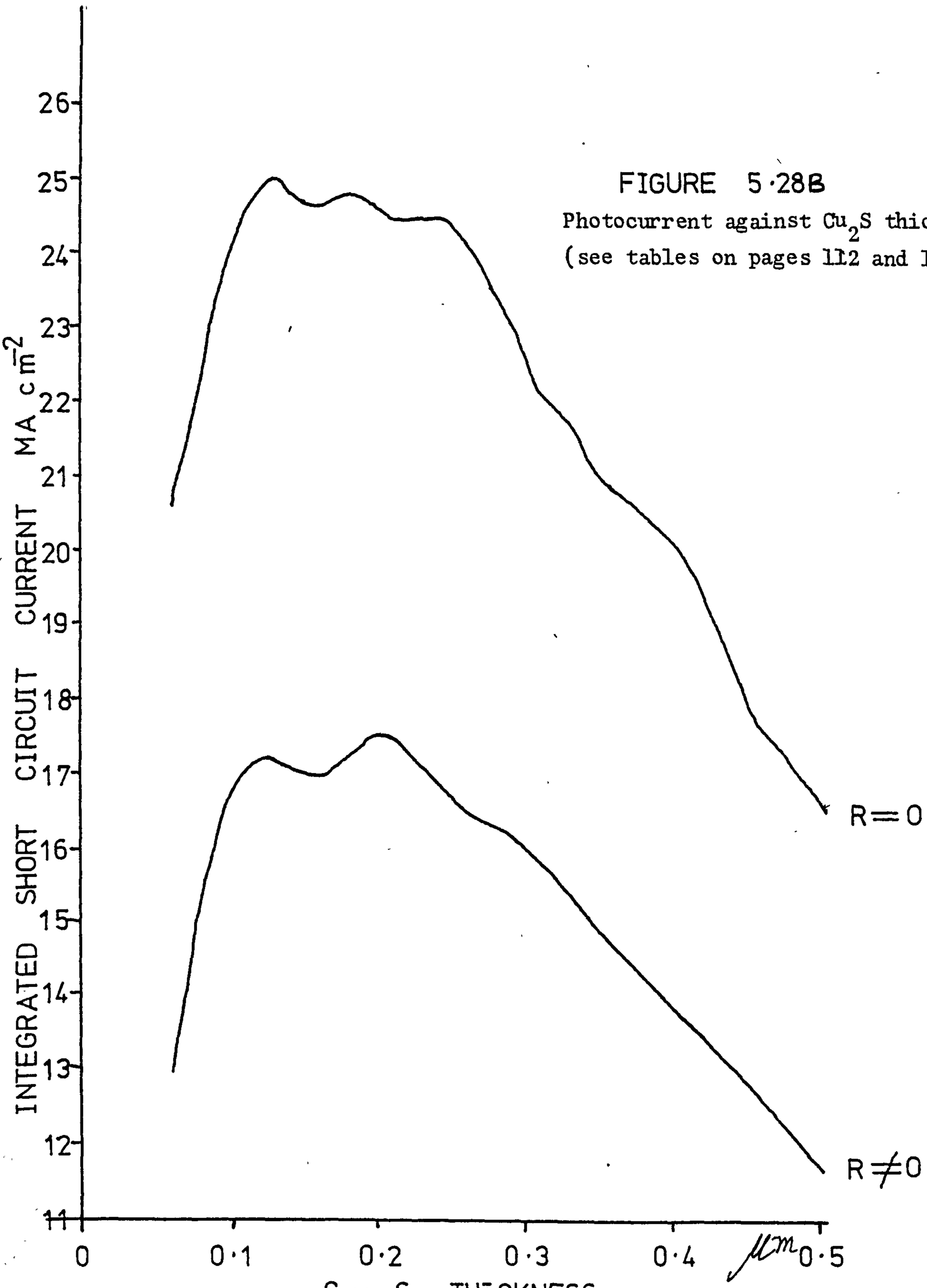

FIGURE 5·28B

Photocurrent against Cu_2S thickness

(see tables on pages 112 and 113)

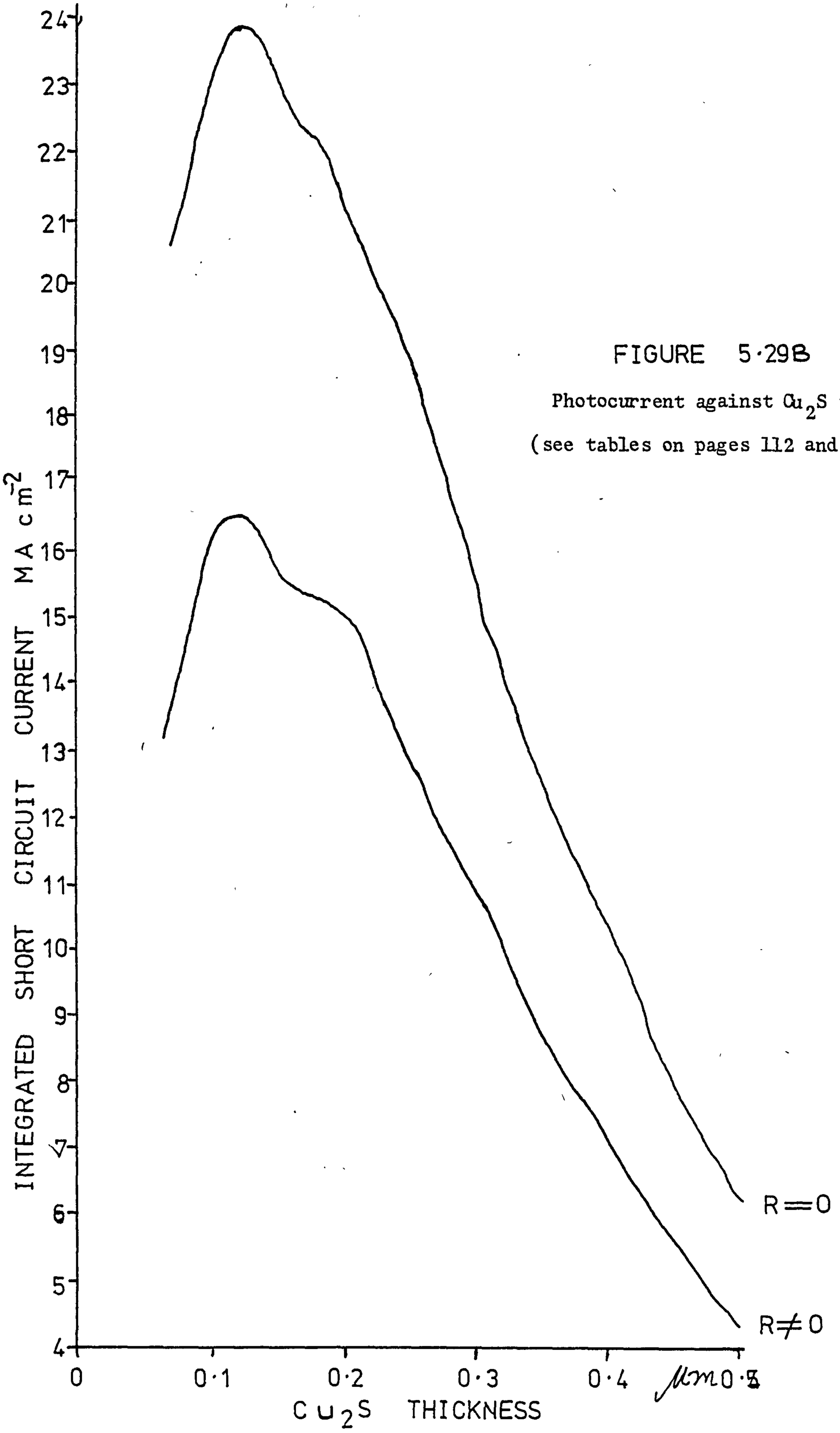

FIGURE 5·29B

Photocurrent against Cu_2S thickness

(see tables on pages 112 and 113)

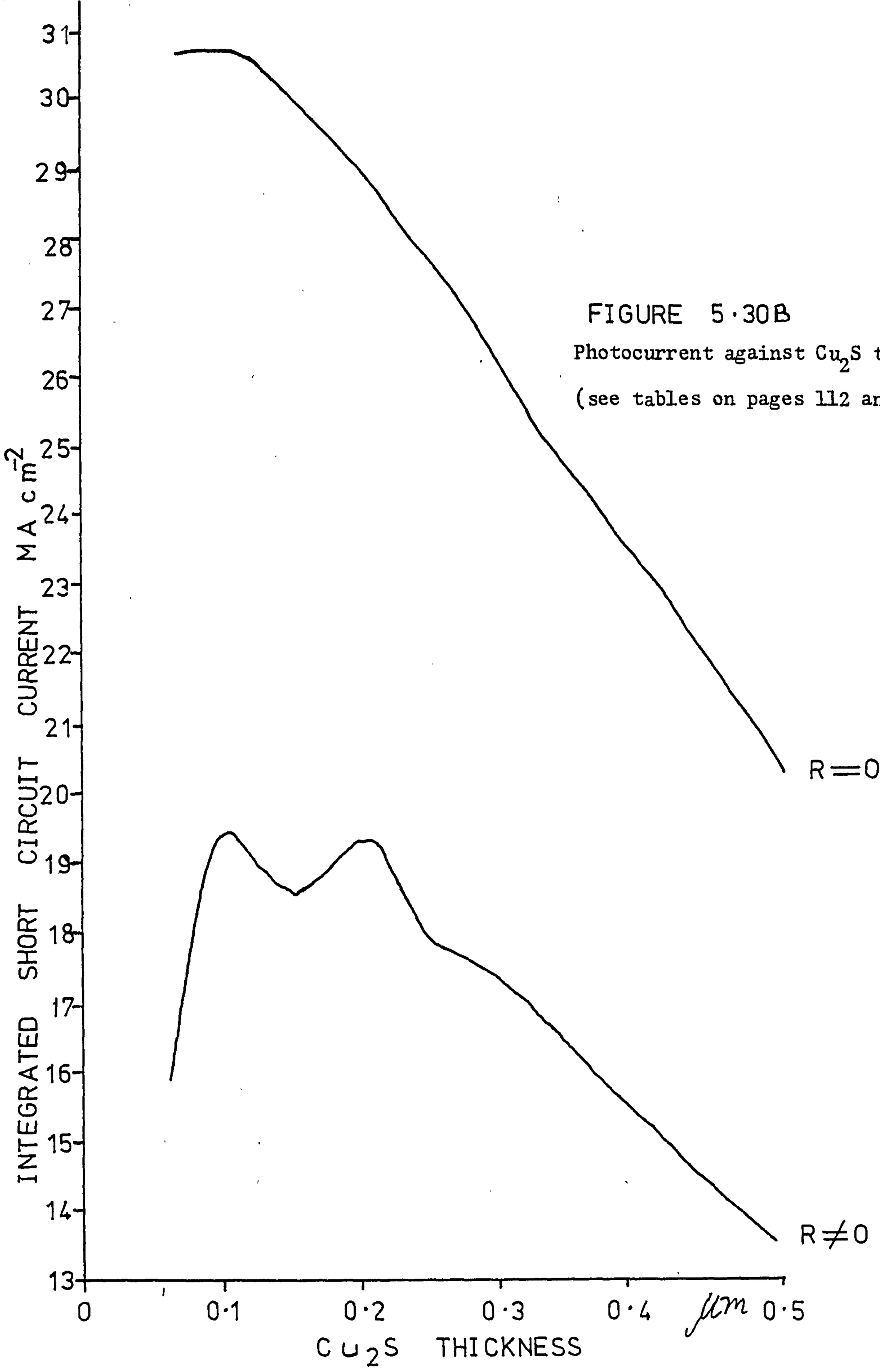

FIGURE 5·30B

Photocurrent against Cu_2S thickness

(see tables on pages 112 and 113)

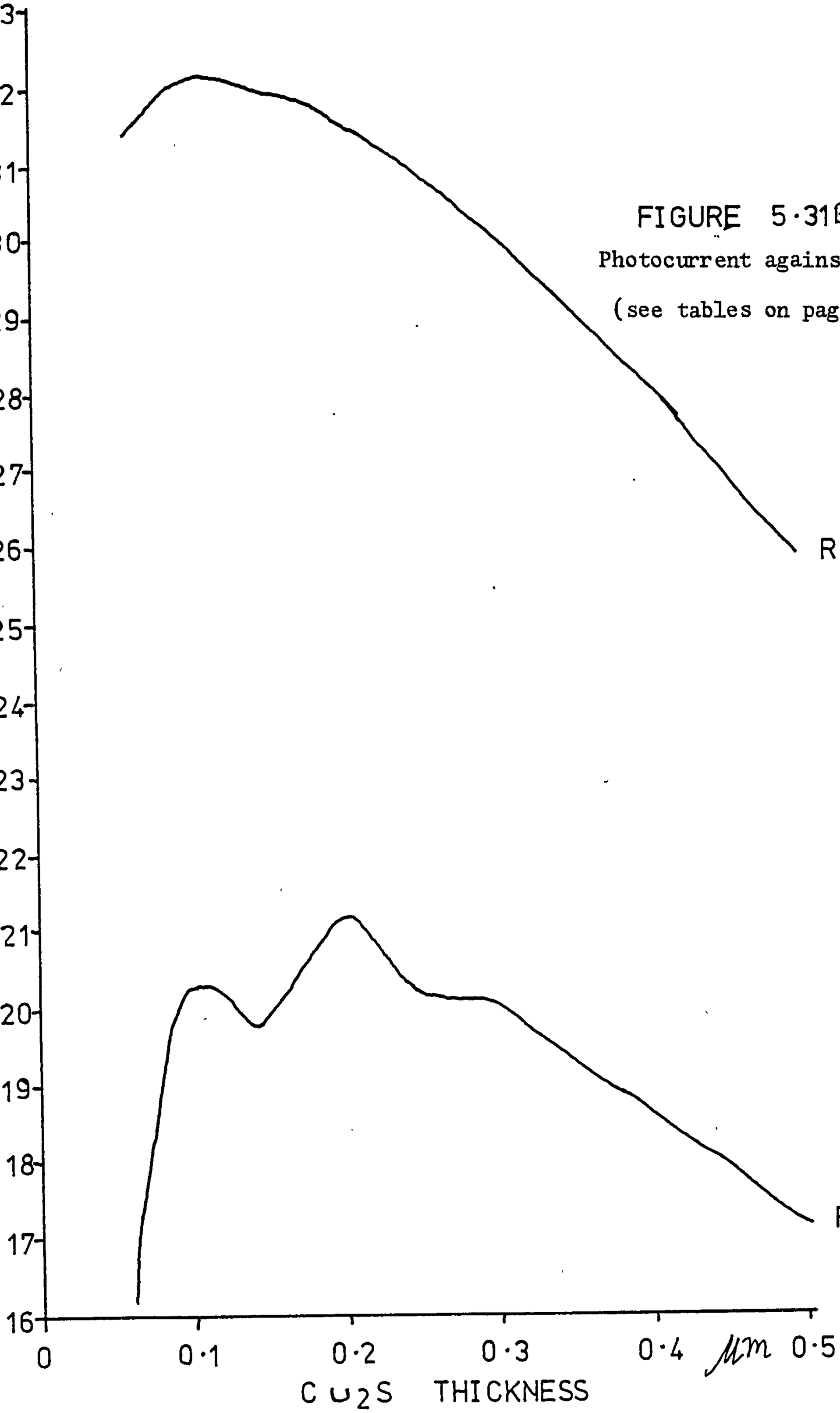

FIGURE 5·31B

Photocurrent against Cu_2S thickness

(see tables on pages 112 and 113)

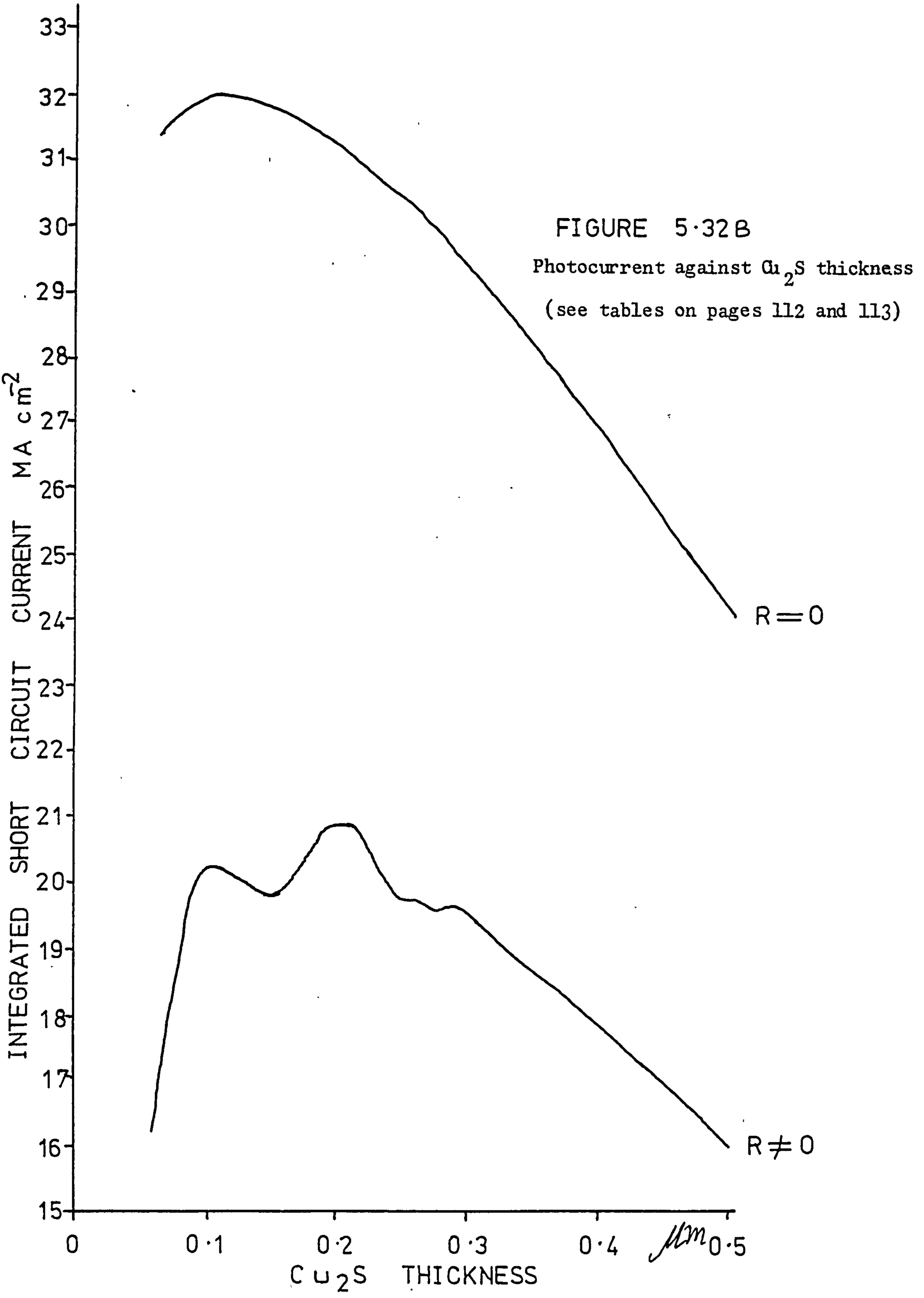

FIGURE 5·32B

Photocurrent against Cu_2S thickness

(see tables on pages 112 and 113)

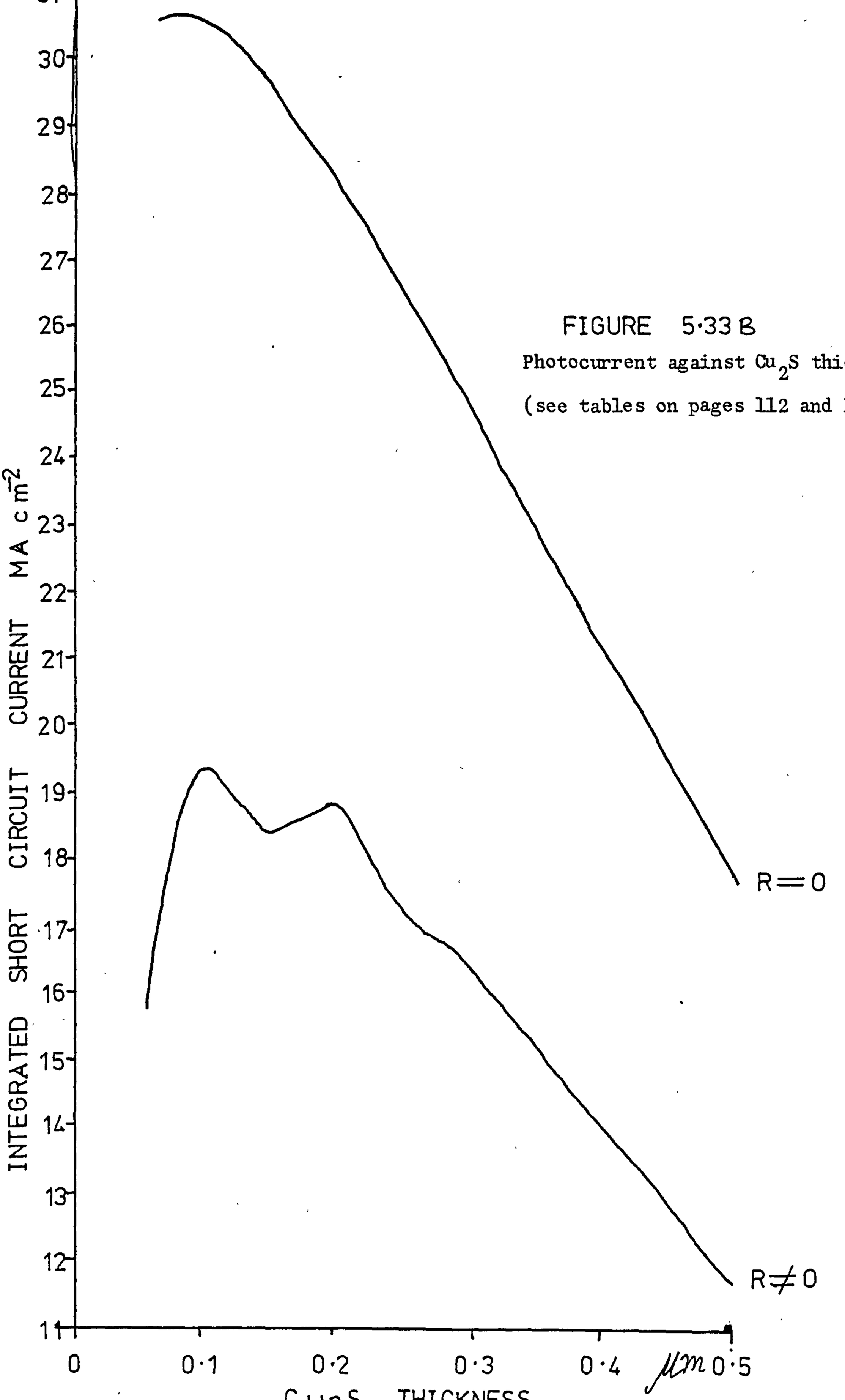

FIGURE 5·33 B

Photocurrent against Cu_2S thickness

(see tables on pages 112 and 113)

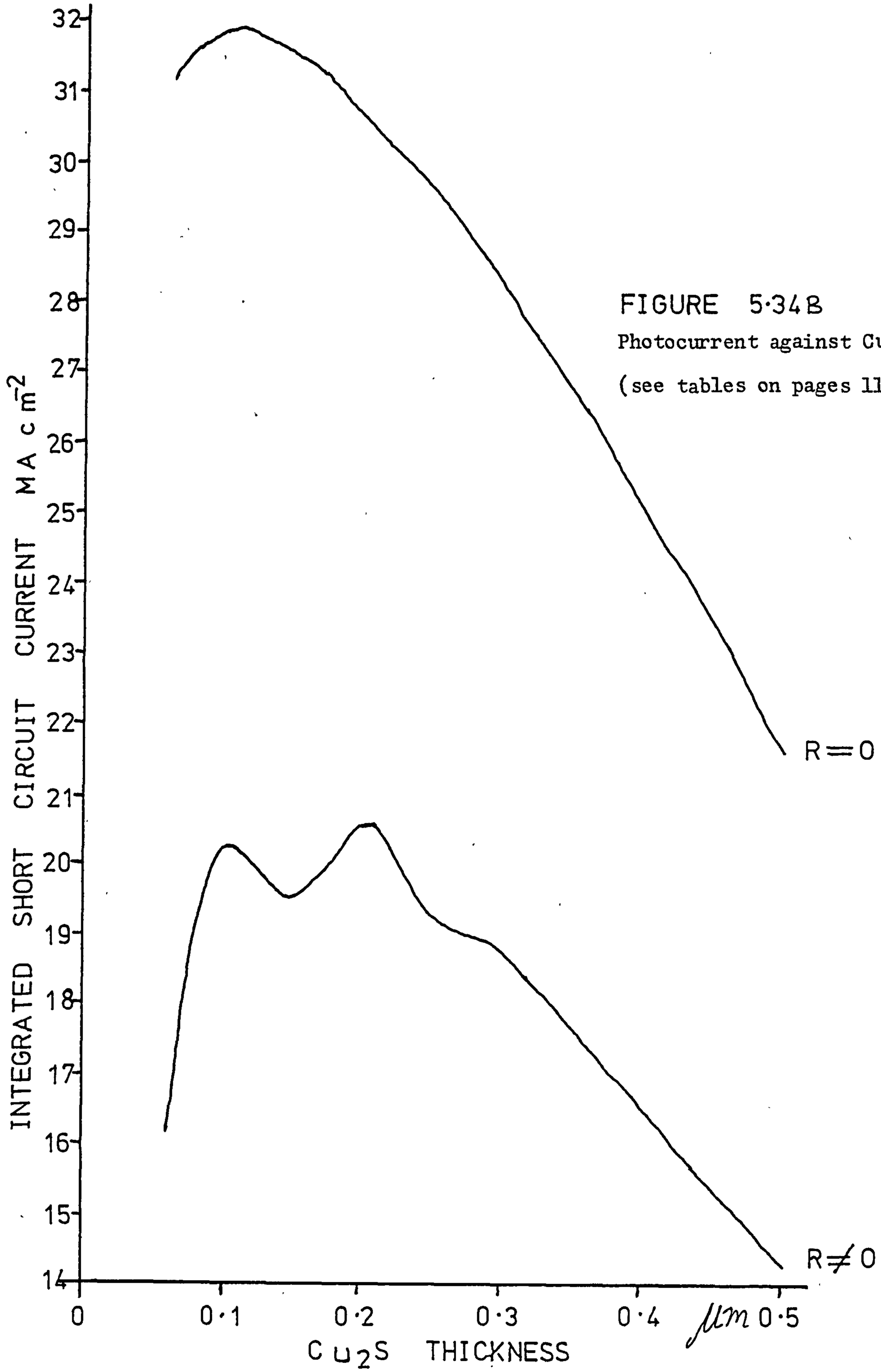

FIGURE 5·34B

Photocurrent against Cu_2S thickness

(see tables on pages 112 and 113)

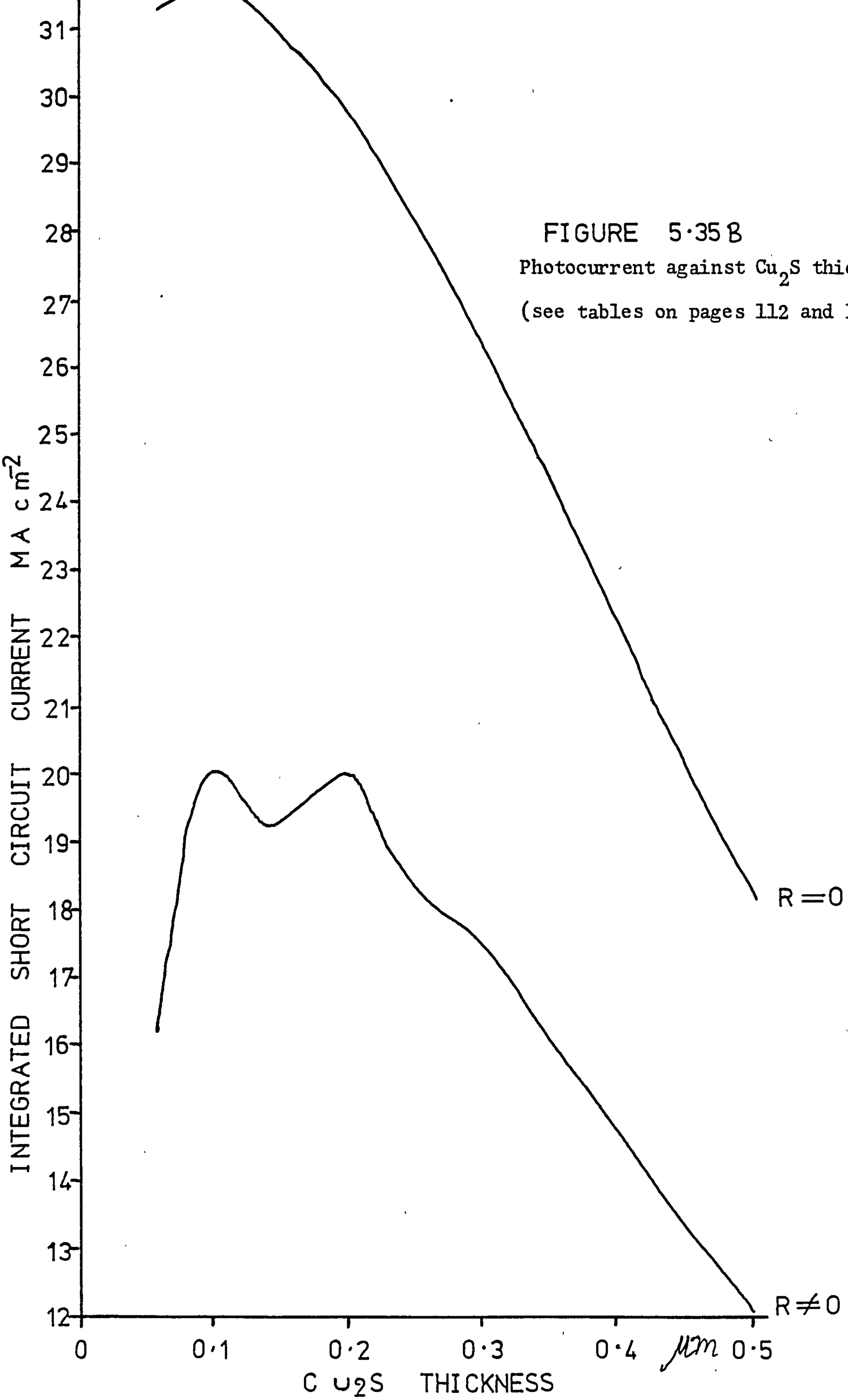

FIGURE 5·35 B

Photocurrent against Cu_2S thickness

(see tables on pages 112 and 113)

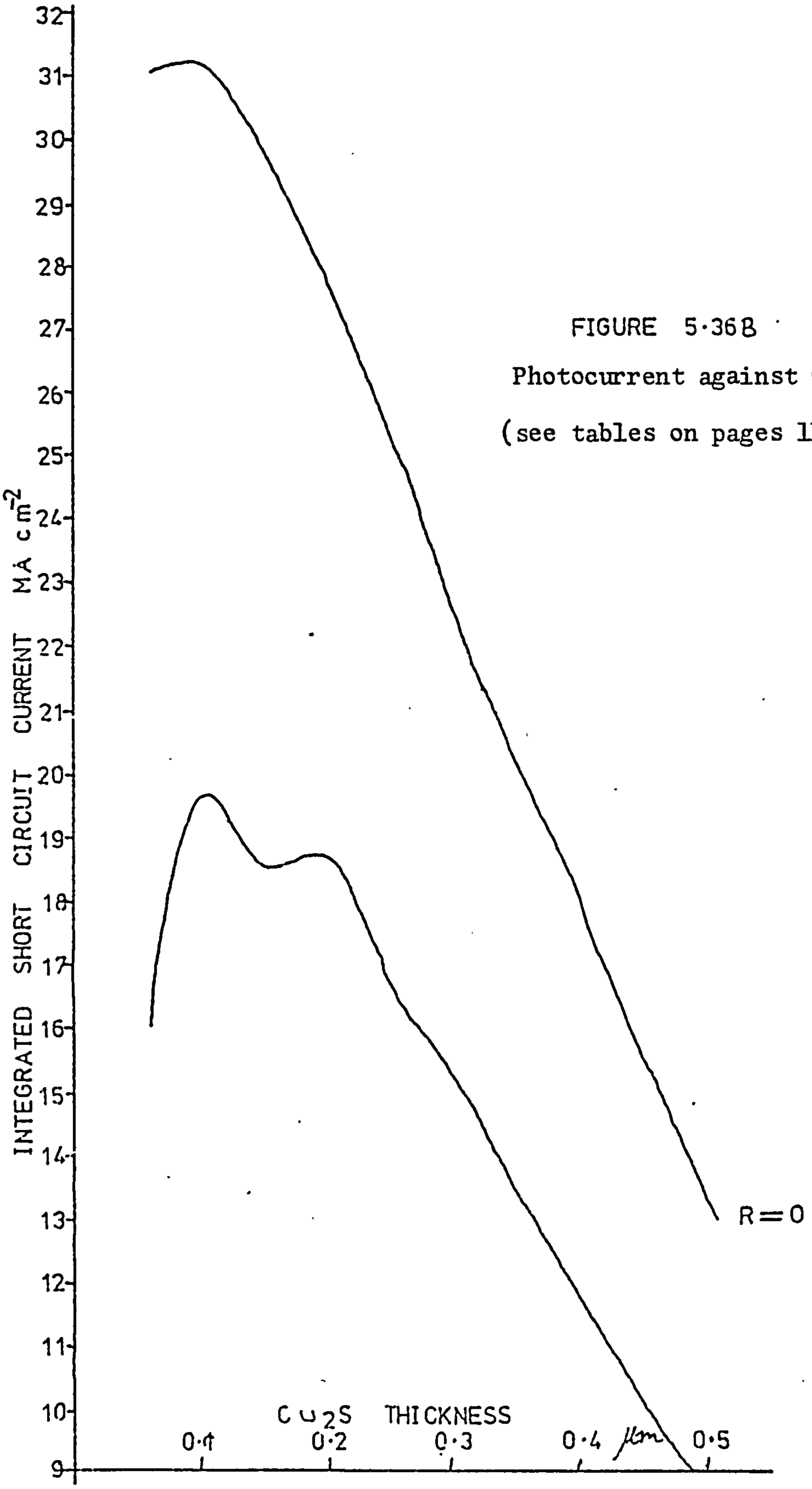

FIGURE 5·36B

Photocurrent against Cu_2S thickness

(see tables on pages 112 and 113)

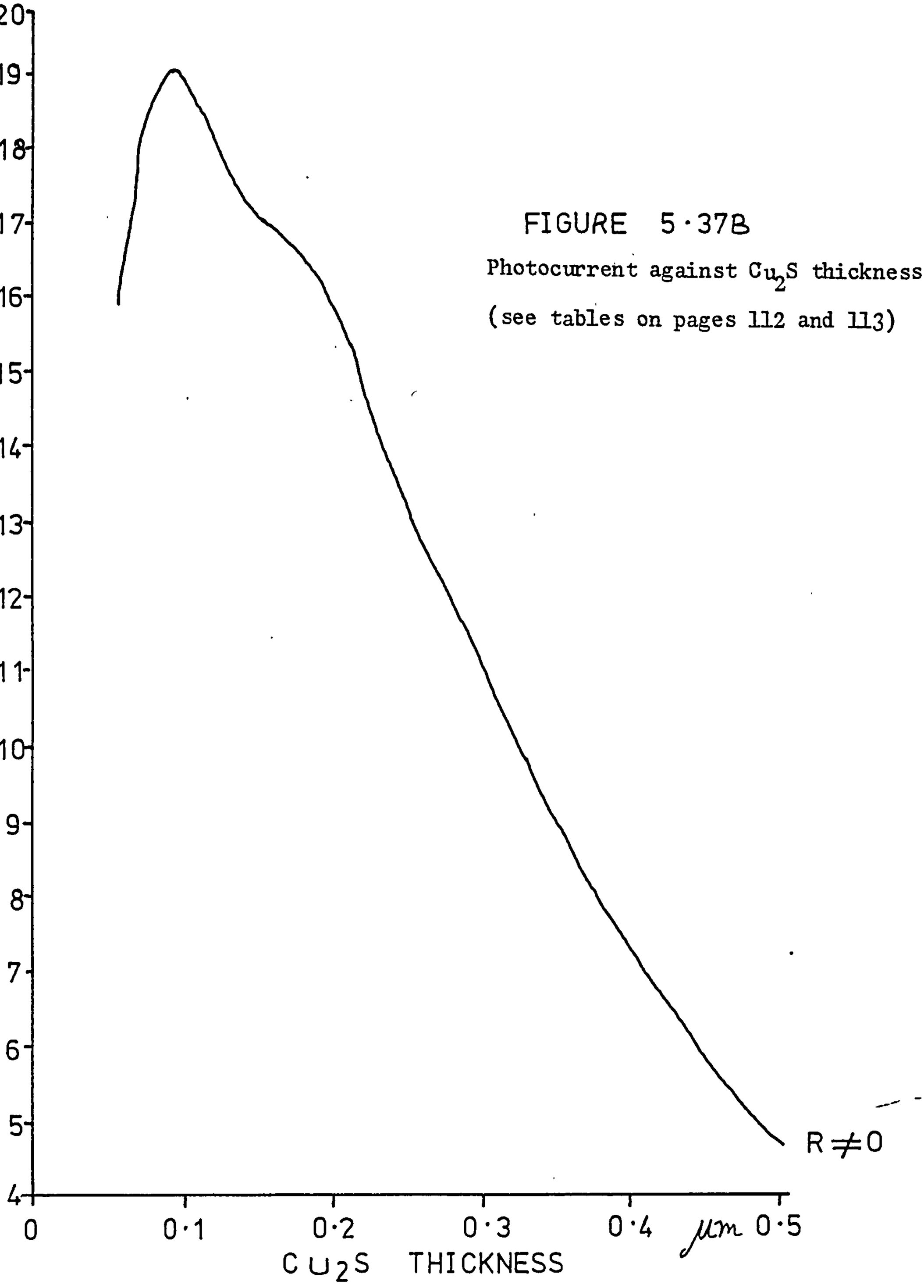

FIGURE 5·37B

Photocurrent against Cu_2S thickness

(see tables on pages 112 and 113)

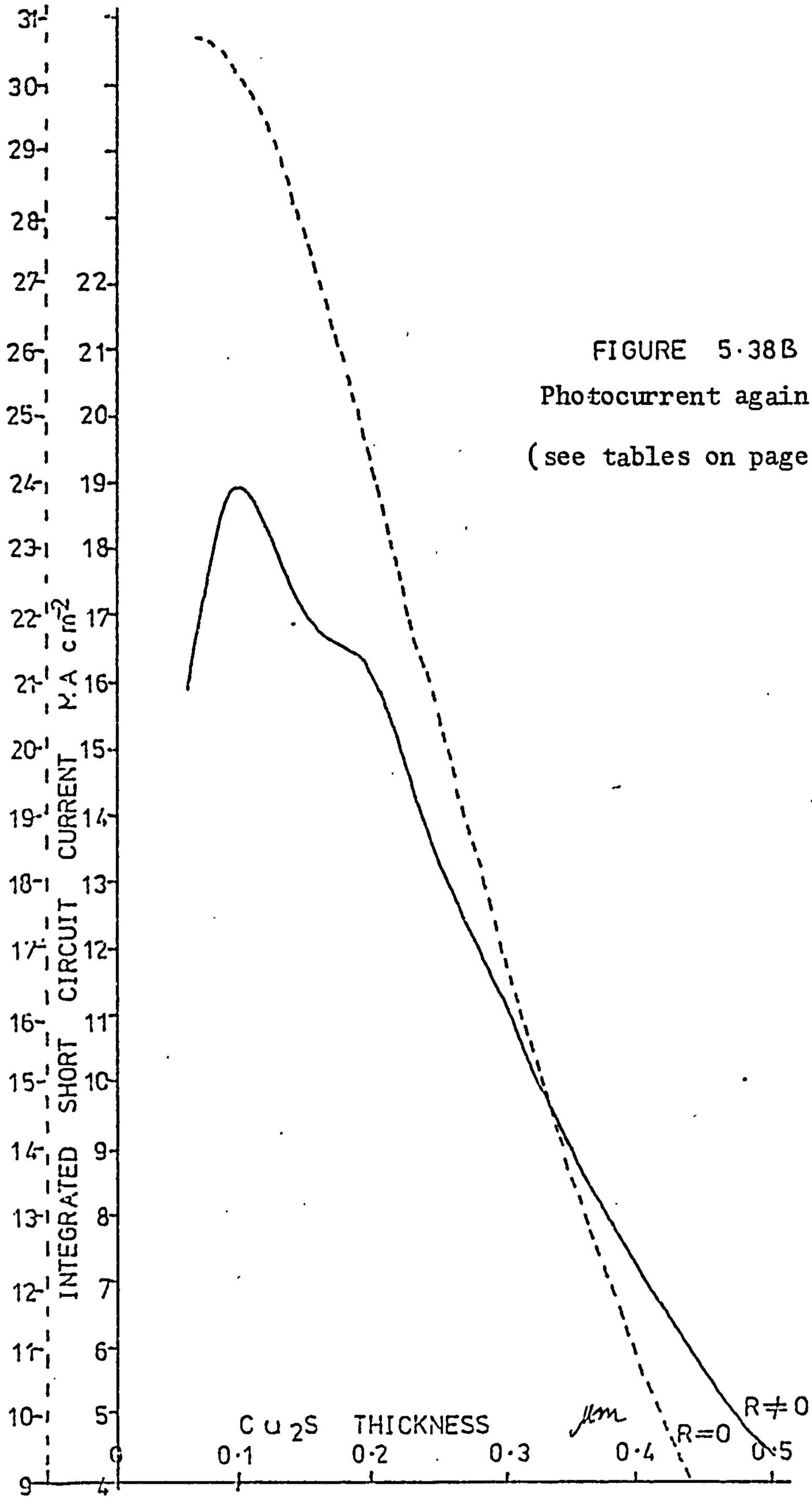

FIGURE 5·38B

Photocurrent against Cu_2S thickness

(see tables on pages 112 and 113)

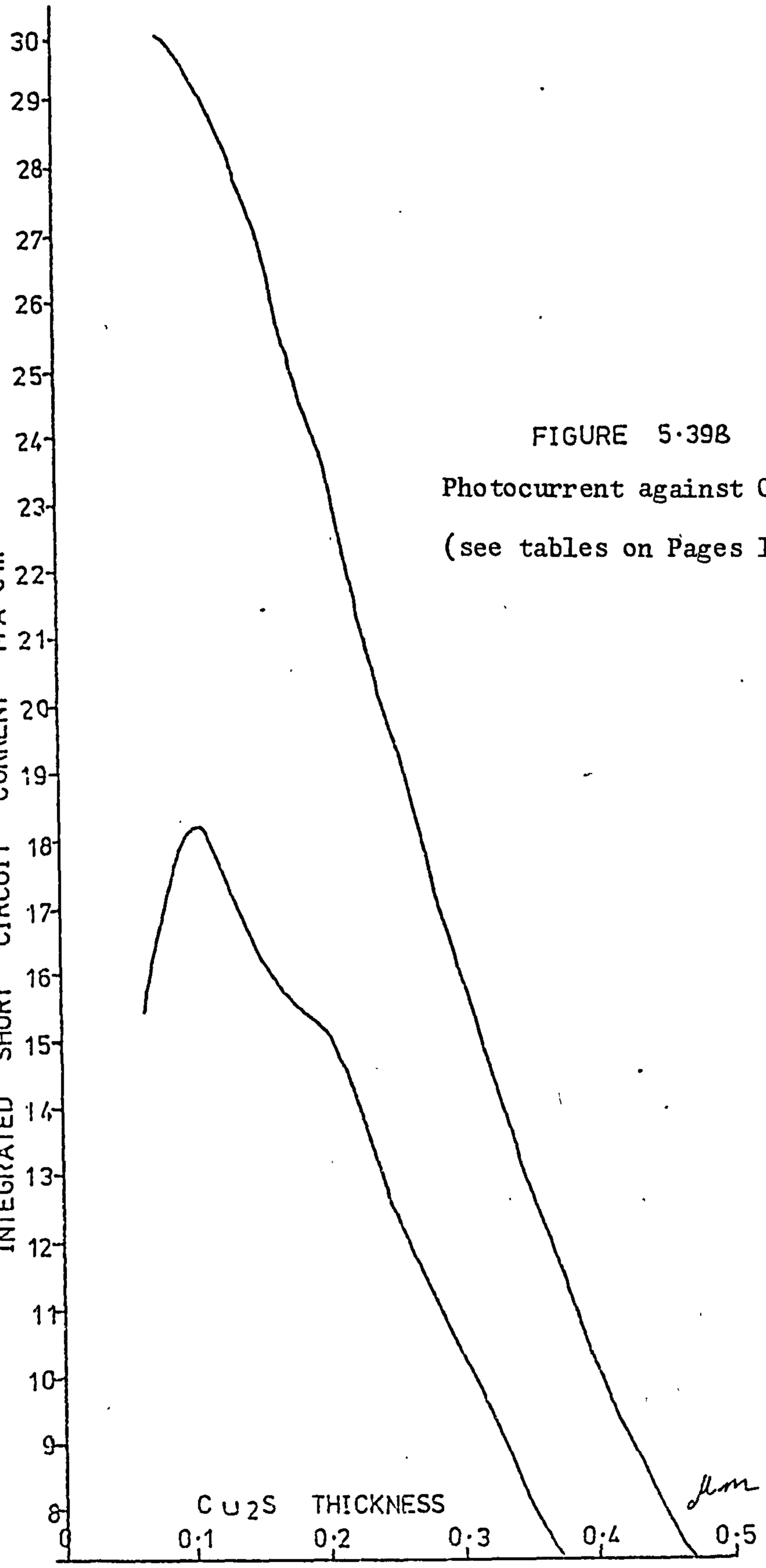

FIGURE 5·398

Photocurrent against Cu_2S thickness

(see tables on Pages 112 and 113)

In figure 5.1B the optimum thickness of the Cu_2S layer for the non-zero R case is 0.11μmand for the zero R case is any value between 0.11 and 0.13μm. The maximum current for the non-zero R case is 8.7 mA/cm^2 and for the zero R case is 12.4 mA/cm^2.

In figure 5.2B the optimum thickness are 0.11 and 0.12μm for the non-zero R and the zero R case, respectively. The maximum corresponding currents are 12.3 and 17.7 mA per cm^2.

In figure 5.3B the peaks have become broader and the maximum values for zero R case lie at 0.19 μm and 0.25 μm with corresponding currents as 24.7 and 24.9 mA/cm^2. For the non-zero R case the maximum value lies at 0.21 μm with a current of 17.4 mA/cm^2.

In figure 5.4B the maximum current for the non-zero R case is near enough 19.4 mA/cm^2 and occurs at all thickness of the Cu_2S between 0.22 to 0.30μm giving a current of 28.2 mA/cm^2. The peaks are again broad.

At a diffusion length of 0.7μm of the minority carriers in the Cu_2S, the optimum thickness of the Cu_2S is reduced as the front surface recombination velocity is increased. The peaks of the curves are also sharper at higher surface recombination velocities .

Without going into any detail it can be seen from figures 5.1B to 5.19B that at higher surface recombination velocities, i.e. 10^6/ 10^7 cm per sec, the optimum thickness remains near enough 0.11μm for the non-zero R case and around 0.12 μm for the zero R case down to 0.3 μm diffusion length. The actual values of the currents at the optimum thickness, and at other thickness for that matter, decrease as the diffusion length is shortened.

Table 5E outlines the changes in the current values at the optimum thickness for different diffusion lengths in the Cu_2S at high front surface recombination velocities for molybdenum substrate.

Table 5F outlines the changes in the current values at the optimum thickness for different diffusion lengths in the Cu_2S at lower surface recombination velocities, i.e. 10^4 and 10^5 cm per sec, for molybdenum substrate.

It can be seen that as the diffusion length is reduced the optimum thickness value continues to decrease at lower surface recombination velocities. The same thing begins to happen at higher surface recombination velocities as the diffusion length begins to fall below 0.3μm. At both high and low surface recombination velocity the effect of it is not only to reduce the short circuit current but also has a tendency to reduce the optimum thickness value for the Cu_2S.

Figure 5.24B shows the current versus Cu_2S thickness curves for a molybdenum substrate at 10^5 cm per sec surface recombination velocity at a diffusion length of 0.5μm and at two different values of the diffusion constant. Increasing the diffusion constant from 10 cm^2 per sec to 40 cm^2 per sec increases both the currents and shifts the optimum thickness values as illustrated in figure 5.24B. Below 0.1μmthere is very little increase in the current when the diffusion constant is increased from 10 cm^2 per sec to 40 cm^2 per sec. At thickness greater than 0.1μm the increase in current becomes quite significant. At 10 cm^2 per sec diffusion constant the optimum thickness at zero R is 0.18μm corresponding to a current of 24.2 mA per cm^2. At 40 cm^2 per sec diffusion constant the optimum thickness at zero R is 0.25μm and the corresponding current equal to 26.3 mA per cm^2. At higher thickness the increase in current is even more significant.

Table 5E Optimum thickness and photocurrent for Cu_2S–CdS - M_o cells

Diffusion Length (Cu_2S) μm	SRV Front cmS^{-1}	Current (Zero R) mA cm^{-2}	Current (non-zero R) mA cm^{-2}	Optimum thickness (zero R) μm	Optimum thickness (non-zero R) μm
0.7	10^7	12.4	8.7	0.11/3	0.11
0.7	10^6	17.8	12.3	0.12	0.10/1
0.6	10^7	12.4	8.6	0.11/2	0.10/1
0.6	10^6	17.75	12.3	0.11/2	0.11
0.5	10^7	12.4	8.65	0.12	0.11
0.5	10^6	17.6	12.3	0.12/3	0.11
0.4	10^7	12.5	8.60	0.11	0.10/1
0.4	10^6	17.5	12.2	0.11/2	0.10/1
0.3	10^7	12.3	8.60	0.12	0.09/10
0.3	10^6	17.3	12.1	0.11/2	0.10/1
0.2	10^7	12.1	8.50	0.12	0.10
0.2	10^6	10.8	11.8	0.11	0.10

CdS diffusion length = 2.0 μm

NB. e.g. 0.11/2 means from 0.11 to 0.12 μm

molybdenum Substrate

Table 5F Optimum thickness and photocurrent for Cu_2S–CdS - M_o cells

Diffusion Length Cu_2S μm	SRV Front cmS^{-1}	Current (zero R) mA/cm^{-2}	Current (non-zero R) mA/cm^{-2}	Optimum thickness (Cu_2S) (zero R) μm	Optimum thickness (Cu_2S) (non-zero R) μm
0.7	10^5	24.7 24.9	17.6	0.19 0.25	0.21 0.21
0.7	10^4	28.2	19.4	0.26	0.22/0.30
0.6	10^4	27.6	19.2	0.25	0.21/3
0.5	10^4	26.8	18.8	0.25	0.21
0.4	10^5	23.6 23.5	16.6	0.18/9 0.13/4	0.20 0.20
0.4	10^4	25.6	18.2	0.18/9 0.24	0.21 0.21
0.3	10^5	22.9	15.8	0.13	
0.3	10^4	24.2	17.0	0.13/4 0.17/9	0.20 0.20
0.2	10^5	21.6	15.0	0.12	0.11
0.2	10^4	22.6	15.8	0.12	0.11/2
0.2	10^0	22.7	15.7	0.11	0.105
0.05	10^4	14.4	9.2	0.05/6	0.06/7

Mo Substrate

CdS diffusion length = 2.0 μm

Table 5G Optimum thickness and photocurrent for Cu_2S–CdS M_o cells

Diffusion Constant (Cu_2S) $cm^2\ S^{-1}$	Diffusion Length (Cu_2S) μm	Optimum Thickness (R=o) μm	Optimum Thickness (R≠o) μm	Current mA cm^{-2} (R≠o)	Current mA cm^{-2} (R=o)
40	0.5	0.25	0.22	18.5	26.3
30	0.5	0.25	0.21	18.2	26.0
20	0.5	0.25	0.21	18.0	25.4
10	0.5	0.18	0.20	17.1	24.2

CdS: Thickness = 10.0 μm

Diffusion length = 2.0 μm

SRV Back = 10^{50} cm S^{-1}

Figures 5.25B and 5.26B show similar current versus Cu_2S thickness curves for diffusion constants equal to 30 cm^2 per sec and 20 cm^2 per sec, respectively, with all the other parameters identical to those for figure 5.24B. At zero R the optimum thickness in figure 5.25B is 0.25 μm corresponding to a current of 26.0 mA/cm^2 and in figure 5.26B the optimum thickness is again 0.25 μm corresponding to a current of 25.4 mA/cm^2. Table 5E summarises the variations in the optimum thickness and the short circuit current as the diffusion constant is altered for a molybdenum substrate.

Graphs of current versus Cu_2S thickness for a zinc substrate are shown in figures 5.28B and 5.29B. In figure 5.28B the front surface recombination velocity is 10^5 cms^{-1} with a diffusion length in the Cu_2S of 0.5 μm. In figure 5.29B the front surface recombination velocity is 10^4 cms^{-1} with a diffusion length of 0.2μ. The diffusion constants in both cases are 10 cm^2 sec^{-1} and the CdS kept at 10.0 μm thick.

Comparison of figures 5.22B and 5.29B show that the curves are similar but that the currents with the zinc substrate are higher by 1.4 mA/cm^2 and 0.9 mA/cm^2 for zero R and non-zero R, respectively, as compared with a molybdenum substrate.

Comparing figures 5.24B and 5.28B the currents again are about 0.8 mA/cm^2 higher with a zinc substrate compared to the molybdenum substrate. It can be seen that the zinc substrate is better than the molybdenum substrate but not dramatically so.

Table 5H summarises similar results as above but for a silver substrate. The first thing to note is the dramatic increase in the short circuit current when the substrate is

Table 5H Optimum thickness and photocurrent for Cu_2S–CdS - Ag cells

Diffusion Length (Cu_2S) μ	SRV Front cmS-1	Optimum Thickness (R=o)(Cu_2S) μ	Current mA cm^2 (R=o)	Optimum Thickness (R≠o)(Cu_2S) μ	Current mA cm^2 (R≠o)
0.7	10^5	0.1	30.7	0.1 0.2	19.4 19.3
0.7	10^4	0.1/3	32.1	0.2	21.1
0.6	10^4	0.1/2	32.0	0.205	20.9
0.5	10^5	0.07/08	30.5	0.10	19.4
0.5	10^4	0.105	31.9	0.1 0.2	20.1 20.6
0.4	10^4	0.10	31.6	0.1 0.2	20.0 20.0
0.3	10^4	0.06/09	31.2		
0.2	10^2			0.1	19.0
0.2	10^4	0.05	30.7	0.1	19.0
0.2	10^5	0.05	30.0	0.1	18.2

A_g Substrate

changed to silver from molybdenum or zinc. This is particularly true for shorter diffusion lengths.

By examining table 5H alone it can be seen that the effect of surface recombination velocity is again to reduce the optimum Cu_2S thickness as well as to reduce the short circuit current. Reducing the diffusion length lowers the current as it does in the case for a molybdenum substrate but not so significantly. For instance at a surface recombination velocity of 10^5 cm per sec the current goes down by 3 mA per cm^2 when shortening the diffusion length from 0.7μm to 0.2μm in the case for the molybdenum substrate, whereas it goes down by 0.7 mA/cm^2 in the case for the silver substrate for R equal to zero.

Figures 5.40B to 5.43B show graphs of the short circuit current versus Cu_2S thickness when the Cu_2S diffusion length is kept at a constant fraction of the Cu_2S thickness. The front surface recombination velocity is kept at 10^4 cm per sec, the diffusion length in the CdS is kept at 2.0μm and the diffusion constants equal to 10 cm^2 per sec for both Cu_2S and CdS.

The Cu_2S diffusion length in figure 5.40B is half the Cu_2S thickness, equal to the Cu_2S thickness in figure 5.41B, twice the Cu_2S thickness in figure 5.42B and five times the Cu_2S thickness in figure 5.43B. The substrate is silver in all the cases.

When the diffusion length is at half the thickness value in the Cu_2S, the optimum value for the thickness when R is not zero is 0.1μm corresponding to a current of 10 mA per cm^2. When R is zero the optimum thickness appears to be around 0.05μm corresponding to a current of about 17.0 mA per cm^2.

FIGURE 5·40B

Photocurrent against Cu_2S thickness

(see tables on pages 155, 156 and 157)

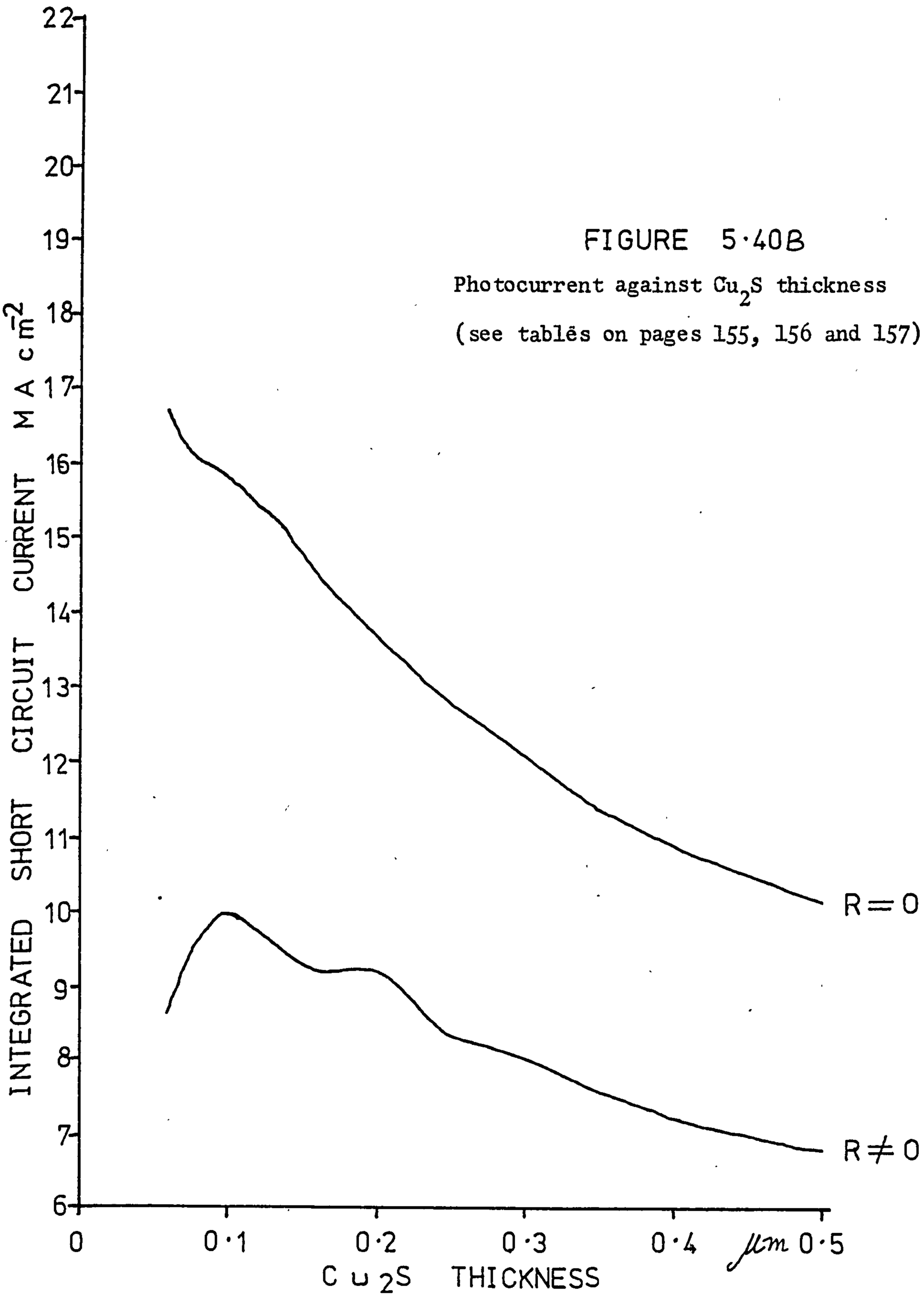

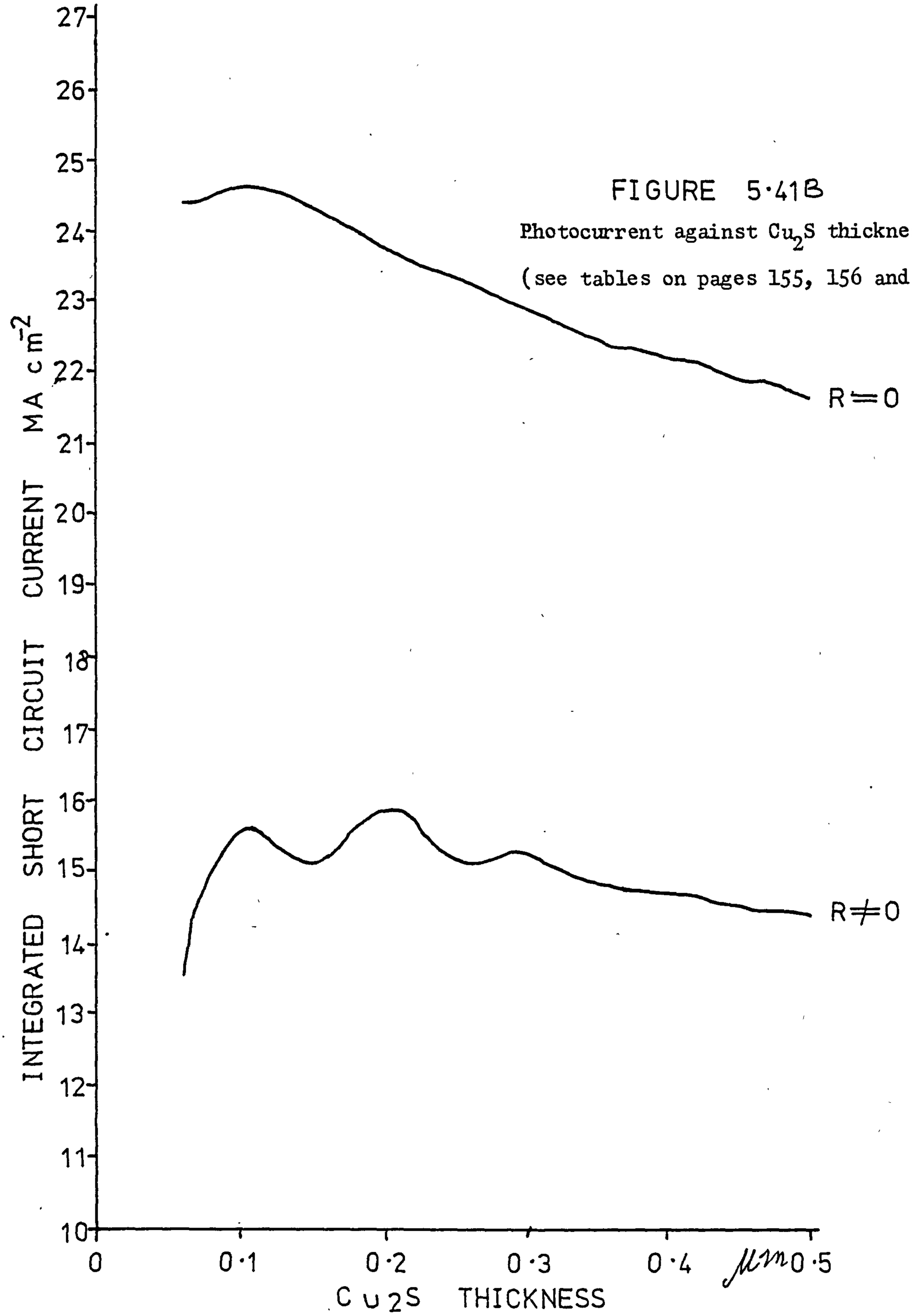

FIGURE 5·41B

Photocurrent against Cu_2S thickness

(see tables on pages 155, 156 and 157)

Photocurrent against Cu_2S thickness (see tables on pages 155, 156 and 157)

FIGURE 5·42B

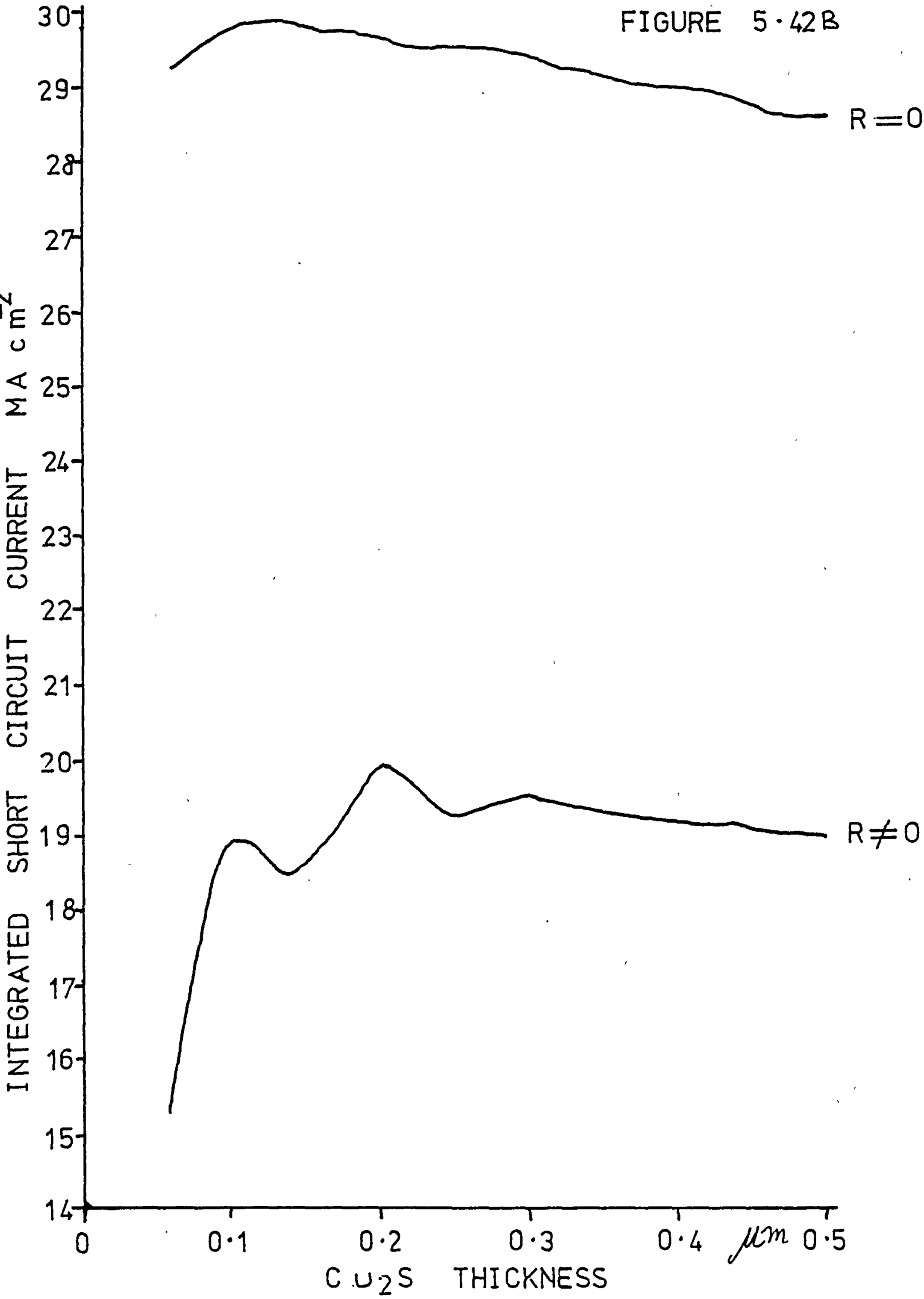

Photocurrent against Cu_2S thickness (see tables on pages 155, 156 and 157)

FIGURE 5·43B

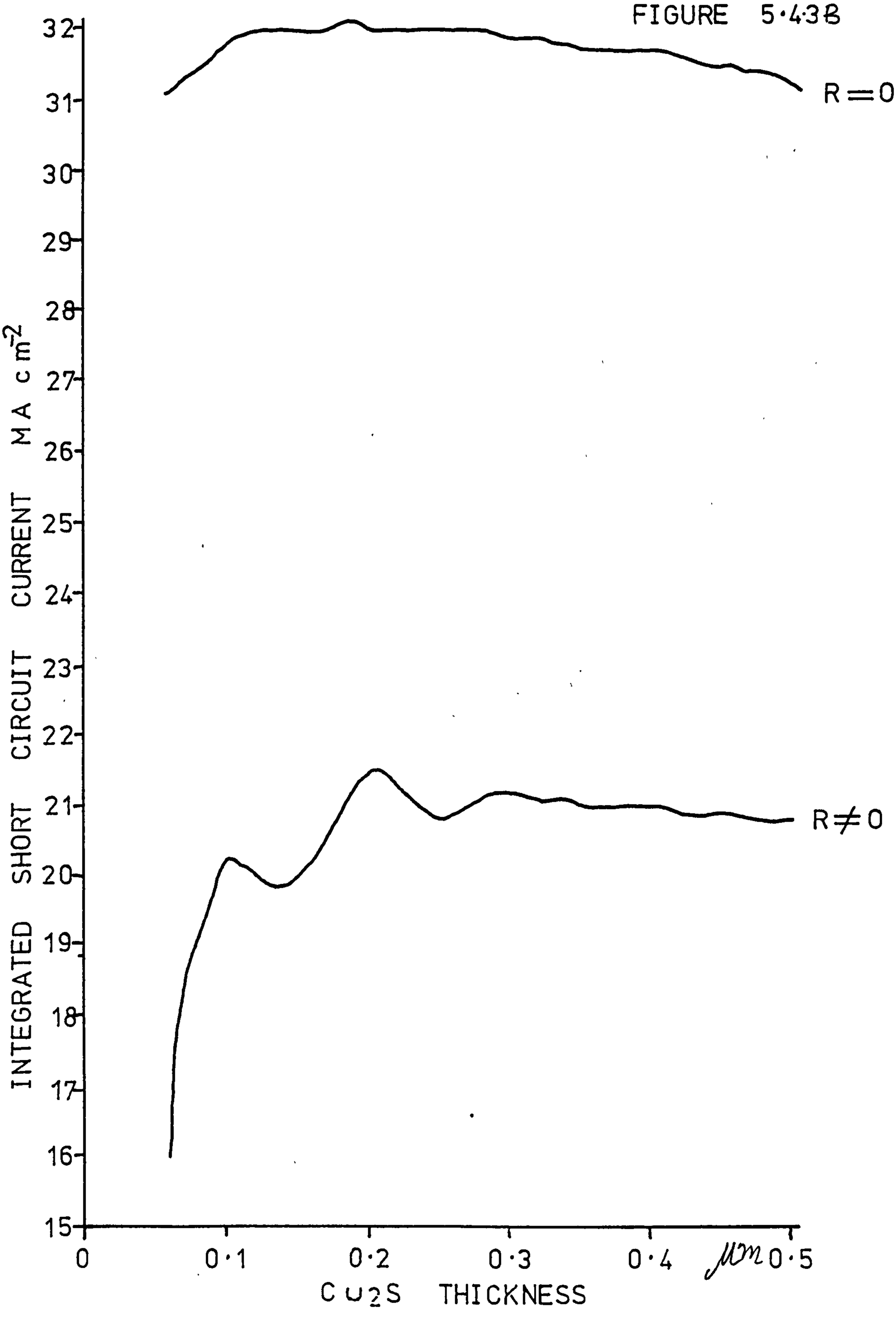

When the diffusion length is equal to the thickness, the optimum thickness for the Cu_2S is 0.09 to 0.12 μm corresponding to a current of 24.6 mA per cm^2 in the zero R case. In the non-zero R case there are two maxima values at 0.1 and 0.2 μm corresponding to currents of 15.6 mA per cm^2 and 15.9 mA per cm^2, respectively.

For the case when the diffusion length is twice the thickness there is a maximum value in the non-zero case at 0.2 μm corresponding to 19.9 mA per cm^2 and a maximum value at 0.1μm corresponding to 18.9 mA per cm^2. In the zero R case there is a very broad maxima peaking at 0.13 μm corresponding to 29.9 mA per cm^2.

The current remains approximately constant at 32 mA per cm^2 from 0.1μm to 0.3 μm thick in the zero R case when the diffusion length is five times the thickness. In the non-zero R case there is a maximum at 0.2μm corresponding to 21.5 mA per cm^2.

As the maximum possible current is 33.3 mA/cm^2 there is very little advantage in making the diffusion length any longer.

CHAPTER 6

ANTIREFLECTIVE COATINGS AND EFFICIENCY OF SCHOTTKY BARRIER SOLAR CELLS

The effect of antireflective coatings has been analysed theoretically and the conditions for maximum transmittance through a metal layer into an absorbing substrate have been derived. In order to compare the theory with experiment, a small programme on Schottky barrier cells was carried out and comparisons made. silver was chosen as the metal for fabricating Schottky barrier cells because of its 'good' optical properties in the visible region.

6.1 Analysis

The solar cell is assumed to be a system of plane parallel sided, homogeneous absorbing layers. The whole solar cell assembly is represented by a theoretical 'effective complex refractive index' given by equation 3.6. The light is assumed to be incident normally. Let this 'refractive index' Z_a equal $\alpha_a - i\beta_a$. For a given wavelength Z_a can be calculated from a knowledge of the optical constants constituting the solar cell assembly.

Let a single layer of refractive index n be applied to the solar cell as an antireflective coating.

The resulting characteristic matrix from equation 3.1 is

$$\begin{vmatrix} B \\ C \end{vmatrix} = \begin{vmatrix} \cos\delta & \frac{i \sin\delta}{n \; Y_V^{-1}} \\ i\, n\, Y_V^{-1} \sin\delta & \cos\delta \end{vmatrix} \begin{vmatrix} 1 \\ Y_V^{-1} Z_a \end{vmatrix} \quad \text{---- 6.1}$$

where $Y_V = \left(\frac{\mu_o}{\varepsilon_o}\right)^{\frac{1}{2}}$ and $\delta = \frac{2\pi}{\lambda} n d$.

(d = thickness of the dielectric layer)

Let the 'effective refractive index' of the assembly including the antireflective layer be $Z = \ell - im$.

From equations 3.6 and 3.7 it can be seen that the transmittance into the solar cell through the antireflecting layer is

$$T = \frac{1}{2Y_V} \text{ Real } (E_s . E_s^* . Z_a^*)$$

$$= \frac{1}{2Y_V} \text{ Real } (Z_a^* . /E_s/^2)$$

where $/E_s/^2 = \frac{4(1-R)}{\text{Real } (BC^*)}$. from equation 3.4

(R = the relectance of the whole assembly including the dielectric layer)

It follows that

$$T = \frac{1}{2Y_V} \text{ Real } \left(\frac{2(1-R) . Z_{a^*}}{\text{Real } (BC^*)} \right) = \frac{(1-R) . \alpha_a}{Y_V \text{ Real } (BC^*)} \quad - - - \ 6.2$$

$$\text{i.e. } \frac{T}{1-R} = \frac{\alpha_a}{Y_V \text{ Real } (BC^*)} . \quad - - - \ 6.3$$

Expression 6.3 represents the potential transmittance through the antireflection coating into the cell, i.e. it is the maximum possible theoretical value. Since there is no absorption in the antireflective layer it is necessarily true that the maximum value in T corresponds to a minimum value in R. Consider the case of a Schottky barrier cell which consists of an absorbing substrate with an absorbing thin film sandwiched between the substrate and an antireflection coating of a dielectric thin film; the characteristic matrix now becomes from equation 2.57

$$\begin{vmatrix} B \\ C \end{vmatrix} = \begin{vmatrix} \cos \delta_2 & \frac{i \sin \delta_2}{n_2 Y_V^{-1}} \\ i n_2 Y_V^{-1} \sin \delta_2 & \cos \delta_2 \end{vmatrix} \begin{vmatrix} \cos \delta_1 & \frac{i \sin \delta_1}{N_1 Y_V^{-1}} \\ i N_1 Y_V^{-1} \sin \delta_1 & \cos \delta_1 \end{vmatrix} \begin{vmatrix} 1 \\ Y_V^{-1} N_s \end{vmatrix}$$

where $\delta_2 = \frac{2\pi}{\lambda} n_2 d_2$, (refers to the AR coating)

$\delta_1 = \frac{2\pi}{\lambda} N_1 d_1$, (refers to the thin absorbing layer)

$N_1 = n_1 - ik_1$ and $N_s = n_s - ik_s$.

The situation is now more complicated but equations 6.2 and 6.3 are still applicable. T now refers to the transmittance into the substrate of complex index N_s through an antireflecting layer of index n_2 and an absorbing metal layer of complex index N_1.

Let $\frac{T}{1-R} = \eta = (\frac{\mu_o}{\varepsilon_o})^{-\frac{1}{2}} \cdot \frac{n_s}{\text{Real } (BC^*)}$ --- 6.4

where n_s is the real part of N_s.

$T = (1-R)\,\eta$ (rewriting equation 6.4). --- 6.5

For a constant thickness of the absorbing film the real part of (BC*) remains constant even when we alter the thickness of the antireflecting layer. This can be seen from 6.1 where a 'complex effective index' $Z_a = \alpha_a - i\beta_a$ refers to the substrate and the thin metal layer together. It follows that

$$B = \cos\delta_2 + \frac{\beta_a \sin\delta_2}{n_2} + i\,\frac{\alpha_a \sin\delta_2}{n_2}$$

$$C^* = Y_V^{-1}(-i(n_2 \sin\delta_2 - \beta_a \cos\delta_2) + \alpha_a \cos\delta_2)$$

$$\text{Real } (BC^*) = Y_V^{-1}(\alpha_a \cos^2\delta_2 + \alpha_a \sin^2\delta_2) = Y_V^{-1}\alpha_a$$

from which $\eta = n_s/\alpha_a$. --- 6.6

As the thickness of the absorbing film is increased α_a will also rise so that η falls. When the thickness of the absorbing film is zero α_a will equal n_s so that

$$\eta = 1.$$

As η remains constant for constant thickness of the absorbing thin film equation 6.5 shows that a minimum value in R corresponds to a maximum value in T, the transmittance into the substrate through the absorbing layer of a given thickness. This would seem to be in contradiction to Hovel (1976) where the implication was that this was not necessarily true. This is important from an experimental point of view when physically depositing an antireflecting coating. One

can monitor the reflectance R directly and the minimum R value will necessarily correspond to the maximum transmittance into the solar cell through the thin metal layer.

The expression for α_a can be calculated from the characteristic matrix. It is found to be

$$\alpha_a = Y_V^{-1} \frac{ef+gh}{f^2+g^2}$$

where $e = du + ck_1 + an_s + bk_s$

$f = a + du + vc$

$g = b + cu + dv$

$h = cu - dk_1 + bn_s - k_s a$,

$u = (n_s n_1 + k_s k_1)/(n_1^2 + k_1^2)$, $v = \frac{(k_s n_1 - n_s k_1)}{(n_1^2 + k_1^2)}$

and $a = \cos \frac{2\pi}{\lambda} n_1 d_1 \cos h \frac{2\pi}{\lambda} k_1 d_1$

$b = \sin \frac{2\pi}{\lambda} n_1 d_1 \sin h \frac{2\pi}{\lambda} k_1 d_1$.

$c = \sin \frac{2\pi}{\lambda} n_1 d_1 \cos h \frac{2\pi}{\lambda} k_1 d_1$

$d = \cos \frac{2\pi}{\lambda} n_1 d_1 \sin h \frac{2\pi}{\lambda} k_1 d_1$.

Equation 6.6 can then be rewritten as

$$\eta = n_s (f^2 + g^2)/Y_V^{-1}(ef + gh) \cdot \qquad \text{- - -} \quad 6.7$$

Equation 6.7 can be used to predict the maximum possible transmittance into the solar cell as the thickness of the thin metal layer is increased.

Returning now to the 'effective refractive index' of the whole assembly including the antireflection layer i.e. $\mathcal{Z} = \ell - im$, from equation 6.1

$$\mathcal{Z} = \frac{\alpha_a \cos\delta + i\,(n \sin\delta - \alpha_a \cos\delta)}{\cos\delta + \frac{\beta_a \sin\delta}{n} + i\frac{\alpha_a \sin\delta}{n}} \cdot \qquad \text{- - -} \quad 6.8$$

The reflectance R of the assembly is given by

$$R = \left(\frac{n_o - (\ell - im)}{n_o + (\ell + im)}\right)\left(\frac{n_o - (\ell - im)}{n_o + (\ell + im)}\right)^* \qquad \text{--- 6.8a}$$

where n_o is the index of the incident medium .

For zero R

$$/\, n_o /= /\ell - im/$$

$$\text{i.e. } n_o = \frac{\alpha_a \cos\delta + i(n \sin\delta - \beta_a \cos\delta)}{\cos\delta + \frac{\beta_a \sin\delta}{n} + i\frac{\alpha_a \sin\delta}{n}} .$$

By comparing the real and imaginary parts the following conditions for zero R are obtained :

$$\text{i.e. } \tan\delta = \frac{(\alpha_a - n_o)\, n}{\beta_a \cdot n_o} \qquad \text{--- 6.9}$$

$$n^2 = n_o\left(\frac{\beta_a^2}{\alpha_a - n_o} + \alpha_a\right) \qquad \text{--- 6.10}$$

$$\text{and from 6.9 } d = \frac{\lambda}{2\pi n} \tan^{-1} \frac{(\alpha_a - n_o).n}{\beta_a \cdot n_o} . \qquad \text{--- 6.11}$$

Equation 6.11 gives the ideal thickness value for an antireflecting layer with an ideal refractive index given by 6.10. Similar expressions have been derived by Schneider (1966).

Equating real and imaginary parts of equation 6.8 we get

$$\ell\left(\cos\delta + \frac{\beta_a}{n}\sin\delta\right) + \frac{m\alpha_a \sin\delta}{n} = \alpha_a \cos\delta \qquad \text{--- 6.12}$$

$$-m\left(\cos\delta + \frac{\beta_a}{n}\sin\delta\right) + \frac{\ell\alpha_a}{n}\sin\delta = n\sin\delta - \beta_a\cos\delta \qquad \text{--- 6.13}$$

eliminating δ from 6.12 and 6.13

$$\ell^2 + m^2 - \frac{\ell}{\alpha_a}(n^2 + \alpha_a^2 + \beta_a^2) + n^2 = 0 .$$

(H A Macleod (1971))

The locus of $(\ell - im)$ i.e. the 'effective index' of the whole assembly, including the antireflecting layer, on the Argand diagram is therefore a circle with a centre at $\left(\frac{n^2 + \alpha_a^2 + \beta_a^2}{2}, 0\right)$

as δ is varied.

The circle passes through the point ($^{\alpha}a - {}^{\beta}a$) and is traced out in a clockwise direction (+) from that point.

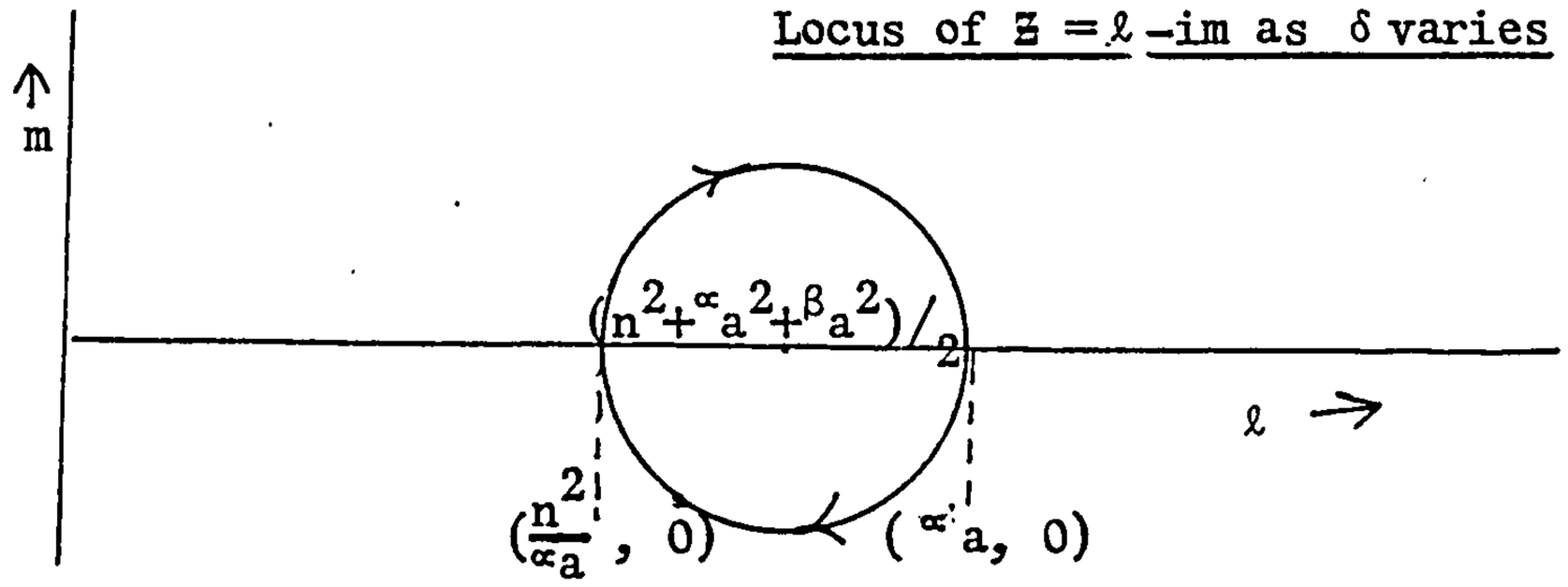

when $m = 0, \ell = {}^{\alpha}a$ or $\frac{n^2}{{}^{\alpha}a}$

In going from the point $({}^{\alpha}a, 0)$ to $\left(\frac{n^2}{{}^{\alpha}a}, 0\right)$ on the Argand diagram for Z the change in phase $\delta = \frac{\pi}{2}$; a quarter wave is equivalent to a semicircle on the Argand diagram.

Let us return now to equations 6.9 and 6.11 with reference to the Argand for Z (diagram below)

when

$Z = n_o$

$R = 0.$

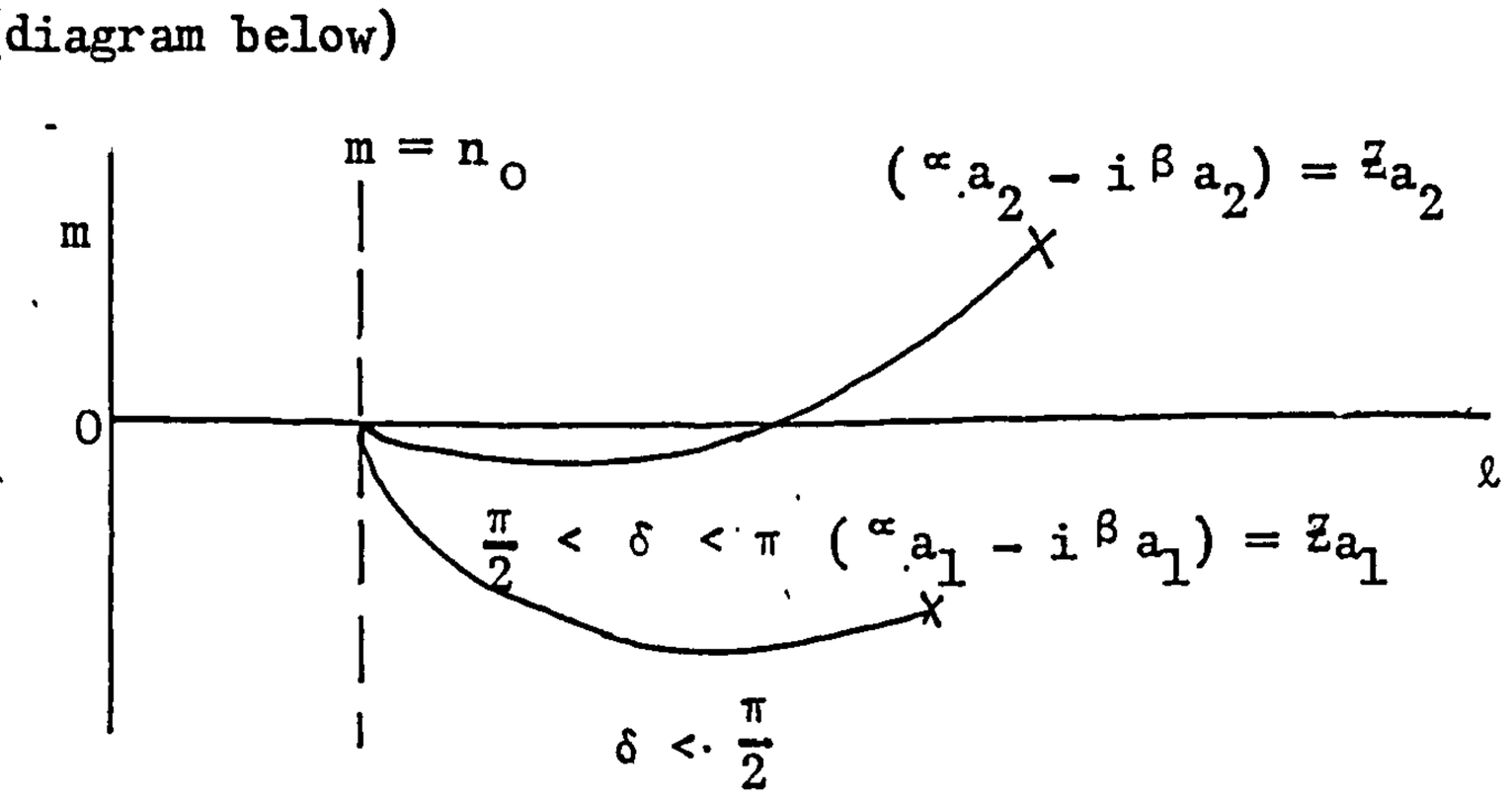

Equation 6.9 gives two alternative values for δ. The correct one is determined by the initial value for $Z_a = {}^{\alpha}_a - i\beta_a$ for the cell before adding the A.R. coating.

If the value of β_a is positive the starting point for Z will lie below m = 0 on the Argand diagram. In this case we take the δ value, given by equation 6.9, that is less than a $\pi/2$.

On the Argand diagram the zero reflectance condition is reached when the locus of Z cuts the $m = 0$ line at $\ell = n_o$ (the refractive index of the incidence medium). If the starting value for Z_a lies above the $m = 0$ the correct value for δ in 6.9 is the one that lies between a quarter wave and a half wave.

From equation 6.10 we can see that the zero reflectance condition cannot be reached if α_a is less than n_o. The forbidden region on the Argand diagram corresponding to this condition is $\ell < n_o$.

Taking the incident medium as air, the reflectance R is given by

$$R = \frac{(1-\ell)^2 + m^2}{(1+\ell)^2 + m^2}$$

i.e. $R(1+\ell)^2 + Rm^2 = (1-\ell) + m^2$

i.e. $(R-1) + 2\ell(R+1) + \ell^2(R-1) + m^2(R-1) = 0$.

This can be rewritten as

$$\ell^2 + m^2 - 2\ell\left(\frac{1+R}{1-R}\right) + 1 = 0 \qquad \text{- - -} \quad 6.14$$

This equation represents a constant reflectance contour on the Argand diagram for Za. It is a circle with a centre at $\left(\frac{1+R}{1-R}, 0\right)$.

By putting $m = 0$ in 6.14

$$\ell = \frac{1+R}{1-R} \pm \frac{2R^{\frac{1}{2}}}{1-R}.$$

The radius of the circle is therefore $\frac{2R^{\frac{1}{2}}}{1-R}$

and the circle cuts the real axis at x_1 and x_2 (diagram below).

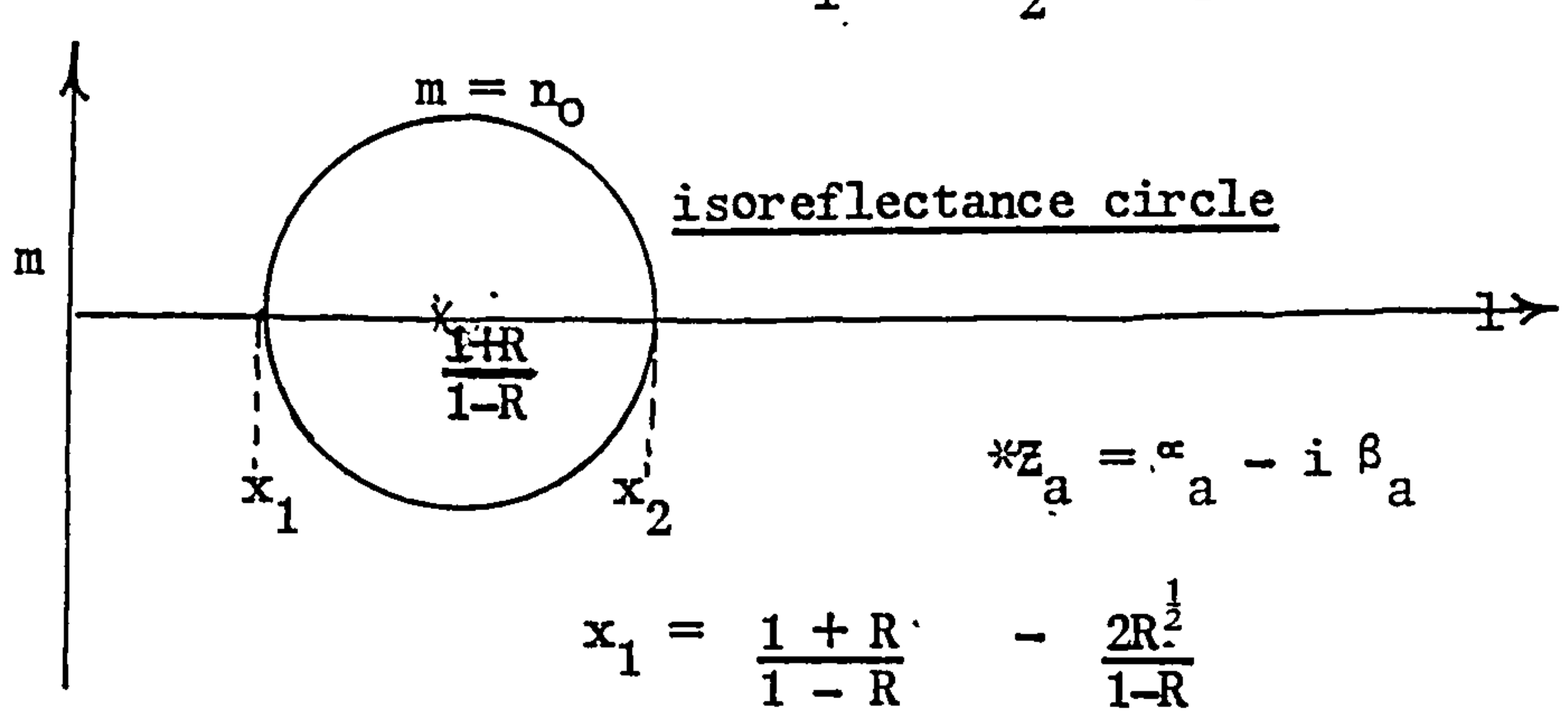

*$Z_a = \alpha_a - i\,\beta_a$

$$x_1 = \frac{1+R}{1-R} - \frac{2R^{\frac{1}{2}}}{1-R}$$

$$x_2 = \frac{1+R}{1-R} + \frac{2R^{\frac{1}{2}}}{1-R}.$$

Equation 6.14 shows us that for any given value for R there is a circle on the Argand diagram such that any value of $\bar{z}$ on that circle will give a reflectance equal to that particular value. We can use this to find conditions for antireflecting, say, down to 5% or 10% in cases where no solutions exist for zero R.

If $\bar{z}_a$ was the starting point on the Argand diagram, that is the 'effective refractive index' of the cell before deposition of the antireflecting coating, then to achieve for example a 10% reflectance, we would have to take the $\bar{z}$ value from $\bar{z}_a$ to any point on the 10% isoreflectance circle. There are only two real values on the isoreflectance circle x_1 and x_2 respectively. x_1 is the lower limiting value such that for real solutions $\bar{z}_a$ must not fall in the region $1 \leq x_1$. It should be noted that

$$x_1 < n_o \quad \text{for} \quad R > 0 .$$

We can now substitute x_1 for no in equations 6.9 to 6.11 to give us the ideal refractive index and thickness for the antireflecting coating in order to reduce R to 10% in this case for instance.

We can also derive general expressions for the ideal thickness and refractive index for an antireflecting coating when x-iy is any point on the isoreflectance contour. x and y are given by the equation

$$x^2 + y^2 - 2x\left(\frac{1+R}{1-R}\right) + 1 = 0,$$

we can rewrite equations 6.12 and 6.13 as

$$x\cos\delta + \frac{\beta_a}{n}\sin\delta + y\frac{\alpha_a}{n}\sin\delta = \alpha_a\cos\delta \qquad \text{- - -} \quad 6.12$$

$$-y\left(\cos\delta + \frac{\beta_a}{n}\sin\delta\right) + \frac{x\alpha_a}{n}\sin = n\sin\delta - \beta_a\cos\delta \qquad \text{- - -} \quad 6.13$$

By eliminating δ we get

$$n^2 = x \left({}^{\alpha}a + \frac{\beta a^2 - y^2 {}^{\alpha}a/x}{{}^{\alpha}a - x} \right)$$

i.e. $$n = \left\{ x \left({}^{\alpha}a + \frac{\beta a^2 - y^2 {}^{\alpha}a/x}{{}^{\alpha}a - x} \right) \right\}^{\frac{1}{2}} , \qquad \text{- - - 6.15}$$

from equation 6.12 above

$$\tan \delta = \left(\frac{{}^{\alpha}a - x}{x\beta_a + y {}^{\alpha}a} \right)$$

i.e. $$d = \frac{\lambda}{2\pi n} \tan^{-1} \left(\frac{a - x}{x\beta_a + y\alpha_a} \right) n \ . \qquad \text{- - - 6.16}$$

Equations 6.15 and 6.16 are general equations of which 6.10 and 6.11 are a special case. Substitution of x by n_o and y by zero results in 6.10 and 6.11.

We are in a position to calculate optimum values for the thickness and refractive index for antireflection coatings even when solutions do not exist for zero reflectance. By gradually increasing the reflectance until a solution appears by use of 6.15 and 6.16 it is theoretically possible to predict values of reflectance below which it is not possible to reduce.

Having found the optimum values for n, the refractive index of the antireflecting layer and the phase thickness δ, it may be that no such material exists. The step may be to find a combination of thin films of available materials whose characteristic matrix is equivalent to the ideal one. Such an ideal combination of thin films is symmetrical (Epstein 1952). Any thin film combination is symmetrical if each half is a mirror image of the other half. The simplest example is a three layer combination in which the central layer is sandwiched between two identical layers.

Let us consider a symmetrical three layer stack p q p, made up of dielectric materials free from absorption and let the characteristic matrix of the combination be

$$\begin{vmatrix} M_{11} & M_{12} \\ M_{21} & M_{22} \end{vmatrix}$$

$$= \begin{vmatrix} \cos\delta_p, & \frac{i \sin\delta}{Y_v\ n_p}p \\ i\ n_p\ Y_v\ \sin\delta_p & \cos\delta_p \end{vmatrix} \begin{vmatrix} \cos\delta_q & \frac{i \sin\delta}{Y_v\ n_q}q \\ i\ n_q\ Y_v\ \sin\delta_q & \cos\delta_q \end{vmatrix} \begin{vmatrix} \cos\delta_p & \frac{i \sin\delta}{Y_v\ n_p}p \\ i\ n_p\ Y_v\ \sin\delta_p & \cos\delta_p \end{vmatrix} \quad \text{- - - 6.17}$$

where

$$M_{11} = \cos\delta = M_{22},$$

$$M_{21} = i\ n\ Y_v\ \sin\delta\ ,$$

$$M_{12} = \frac{i \sin\delta}{Y_v\ n}\ ,$$

where δ and n are the same as in 6.15 and 6.16 .

From 6.17

$$\cos\delta = \cos 2\delta_p \cos\delta_q - \tfrac{1}{2}\left(\frac{n_q}{n_p} + \frac{n_p}{n_q}\right) \sin 2\delta_p \sin\delta_q \quad \text{- - - 6.18}$$

$$\frac{i \sin\delta}{Y_v\ n} = \frac{i}{Y_v\ n_p}\ \left(\sin 2\delta_p \cos\delta_q + \tfrac{1}{2}\left(\frac{n_q}{n_p} + \frac{n_p}{n_q}\right) \cos 2\delta_p \sin\delta_q\right.$$

$$\left. + \tfrac{1}{2}\left(\frac{n_p}{n_q} - \frac{n_q}{n_p}\right) \sin\delta_q\right) \quad \text{- - - 6.19}$$

and

$$i\ n\ Y_v\ \sin\delta = i\ Y_v\ n_p \left(\sin 2\delta_p \cos\delta_q + \tfrac{1}{2}\left(\frac{n_p}{n_q} + \frac{n_q}{n_p}\right) \cos 2\delta_p \sin\delta_q\right.$$

$$\left. - \tfrac{1}{2}\left(\frac{n_q}{n_q} - \frac{n_q}{n_p}\right) \sin\delta_q\right) . \quad \text{- - - 6.20}$$

(H. A. Macleod 1969 P114)

Simultaneous solutions of equations 6.19 and 6.20 gives

$$\left(\frac{n_p}{n} - \frac{n}{n_p}\right) \sin\delta = \left(\frac{n_p}{n_q} - \frac{n_q}{n_p}\right) \sin\delta_q$$

from which

$$\sin\delta_q = \sin\delta\left(\frac{n_q}{n} \frac{(n_p^2 - n^2)}{(n_p^2 - n_q^2)}\right) . \quad \text{- - - 6.21}$$

From 6.18

$$\tan 2\delta_p = \frac{2n_p - n_q}{(n_q^2 + n_p^2)} \cdot \left\{ \frac{\cos \delta_q - \cos \delta}{\sin \delta_q} \right\} \quad ---6.22$$

From a knowledge of n, δ , n_p, and n_q, δ_q and δ_p can be calculated. A single film of index n and phase thickness δ is equivalent to a layer of index n_q , phase thickness δ_q sandwiched between two identical layers of index np and phase thickness δ_p. The index n is known as the Herpin index.

The relative values of n_q and n_p to the Herpin index must be such that

$$\left| \sin \delta \cdot \frac{n_q}{n} \cdot \frac{(n_p^2 - n^2)}{(n_p^2 - n_q^2)} \right| < 1$$

6.2 Theoretical Results

All the equations presented are functions of wavelength and therefore when equations 6.9 to 6.11 for instance, give us ideal values for the refractive index n and the ideal thickness d for the antireflecting layer they are true only for one wavelength.

Ideal values for n and d as functions of wavelengths are presented in figure 6.0. They are given for silver thickness of 100Å and 200Å respectively on a silicon substrate. The ideal value for n in the case for 100Å of silver lies between 2.3 and 2.95 in the wavelength region of 0.4 μm to 1.2 μm .

ZnS with a refractive index of 2.35 in the visible region was chosen as a suitable material for single layer antireflecting coating. The ideal thickness for an antireflecting coating on 100Å of silver on silicon at a wavelength of 0.58 μm is 420Å. The ideal refractive index for the same wavelength is 2.35.

IDEAL ANTIREFLECTING COATINGS (ZERO REFLECTANCE)

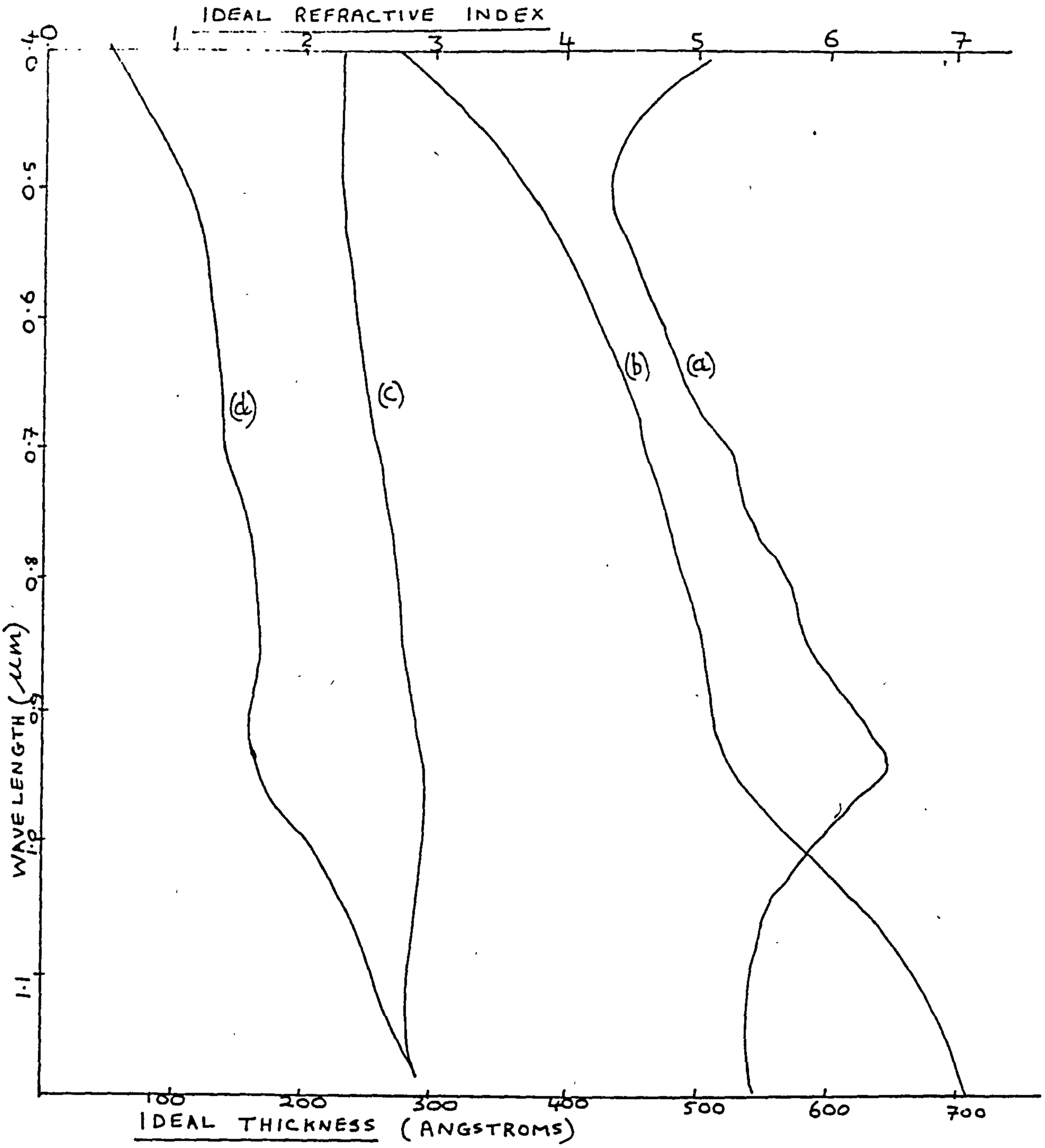

a) Ideal refractive index for 200 Å Ag on Si
b) Ideal thickness for 100 Å Ag on Si
c) Ideal refractive index for 100 Å Ag on Si
d) Ideal thickness for 200 Å Ag on Si

Figure 6.0

The 'effective refractive index' for an assembly of 100Å of silver on silicon lies below the real axis on the Argand diagram (Fig.6.1) and the real part is always greater than 2.0 in the wavelength region of 0.4μm to 1.2μm. It is apparent that real solutions to 6.10 and 6.11 exist. For the same assembly the real transmittance lies well below the potential transmittance (equation 6.3) and the reflectance of the assembly rises from 40% to 60% in the wavelength range of 0.4μm to 1.2μm (Fig. 6.1). It may be possible, in the future, to find or manufacture materials whose refractive index varies with wavelength in an ideal manner but the thickness of the antireflecting layer will still have to be single valued. Therefore by assuming ideal values for n and choosing an ideal thickness value for some central wavelength it is possible to predict the maximum possible transmittance for that particular thickness value for a single layer antireflecting coating (Fig. 6.2). At the wavelength for which the antireflecting coating is optimum the transmittance (real) curve can be seen to be just touching the potential transmittance curve (Fig. 6.2), and the reflectance for the whole assembly at the same wavelength can be seen to be minimum. On the Argand diagram this corresponds to the point where the 'effective refractive index' curve for the assembly cuts the real axis. The part of the curve above the real axis corresponds to values at wavelengths greater than that value for minimum reflectance. The part below the real axis corresponds to values at wavelengths shorter than that value for minimum reflectance.

420Å of ZnS (optimum value at 0.58μm) on 100Å of silver on a silicon substrate gives values for reflectance, transmittance and the 'effective complex index' similar to the latter case (c/f Fig. 6.3 with Fig. 6.2). However, the transmittance values on either side of the minimum reflectance wavelength value are less than in the previous case, in particular in the long wavelength region.

Theoretical results 100 Å Ag on Si

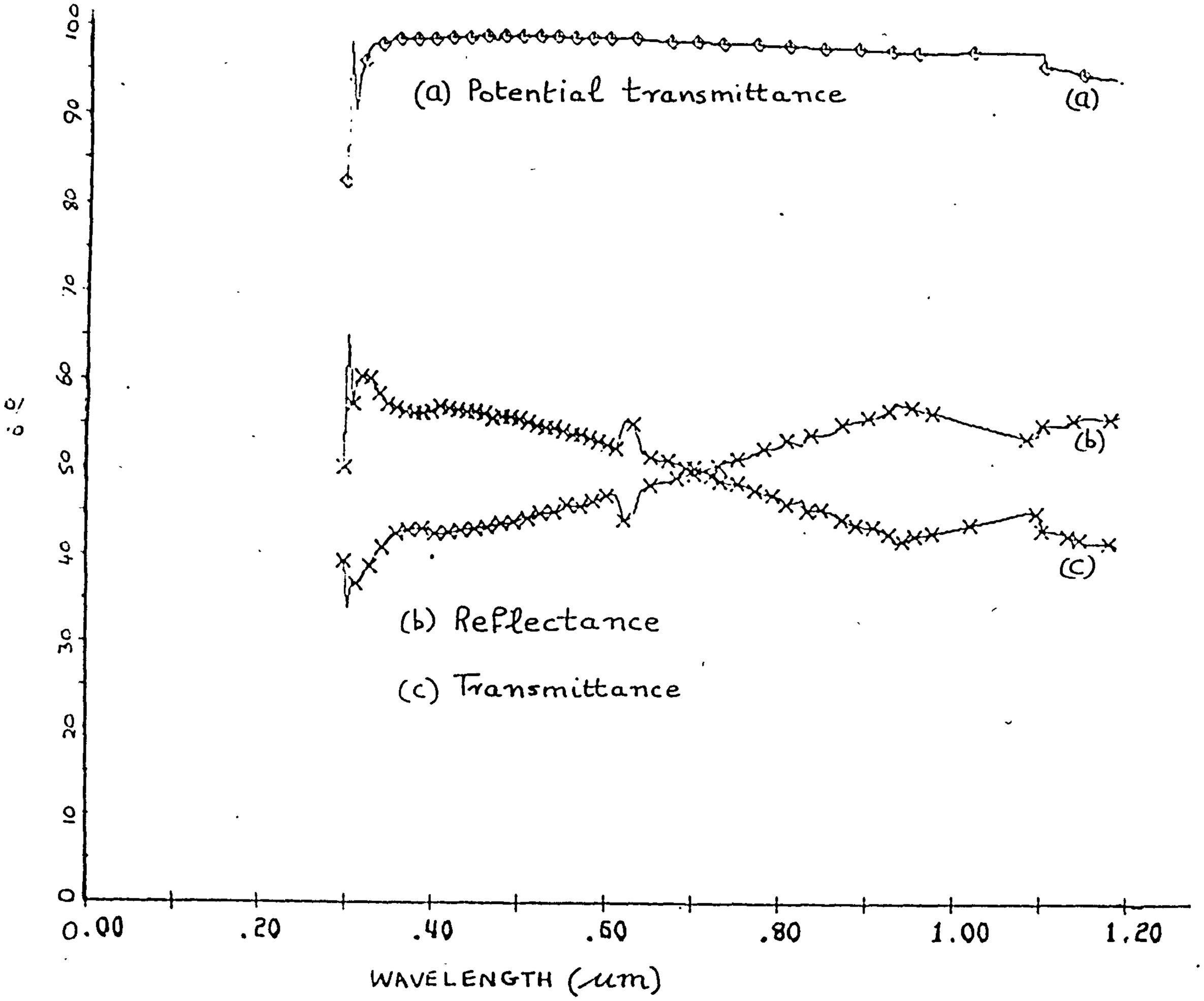

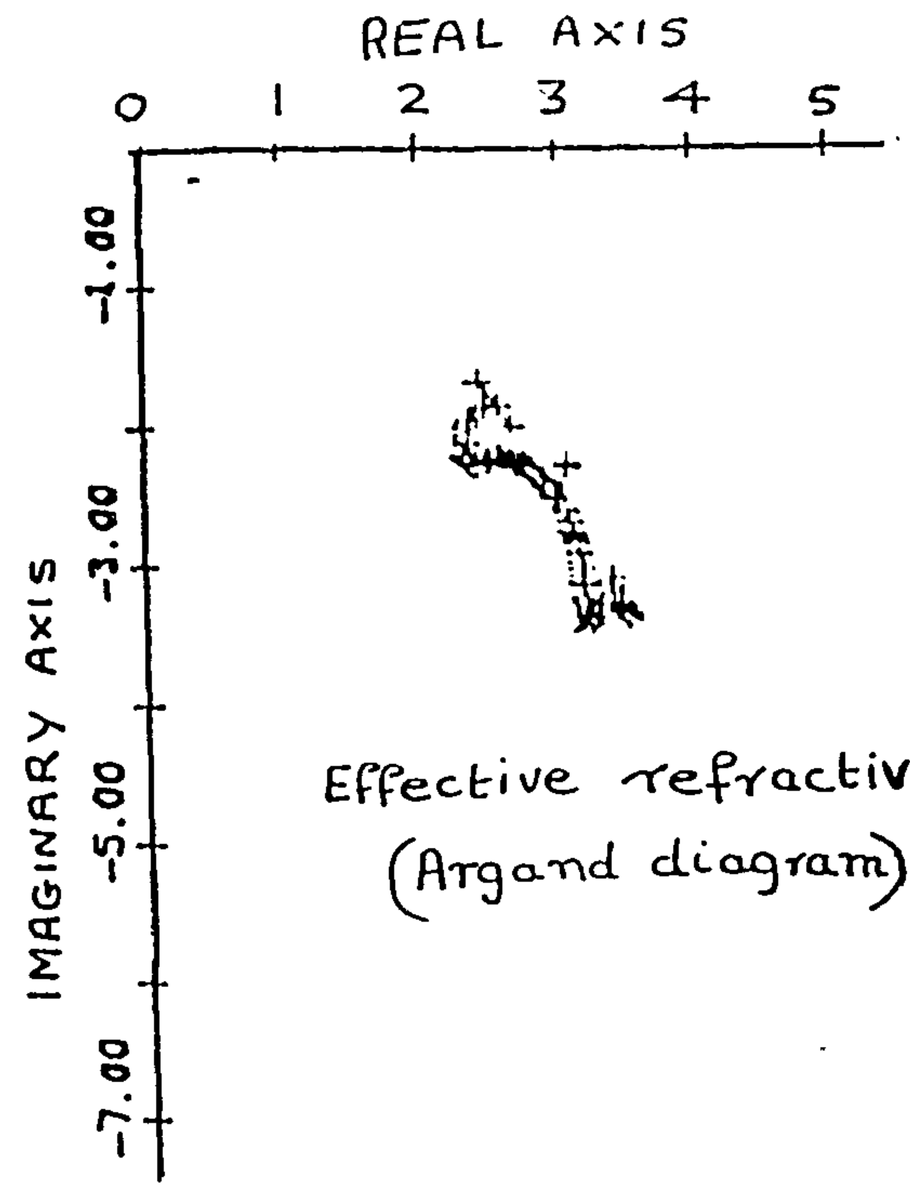

Effective refractive index
(Argand diagram)

FIGURE 6.2 Theoretical results

100 Å of Ag on Si with an antireflecting coating of thickness 420 Å but ideal refractive index

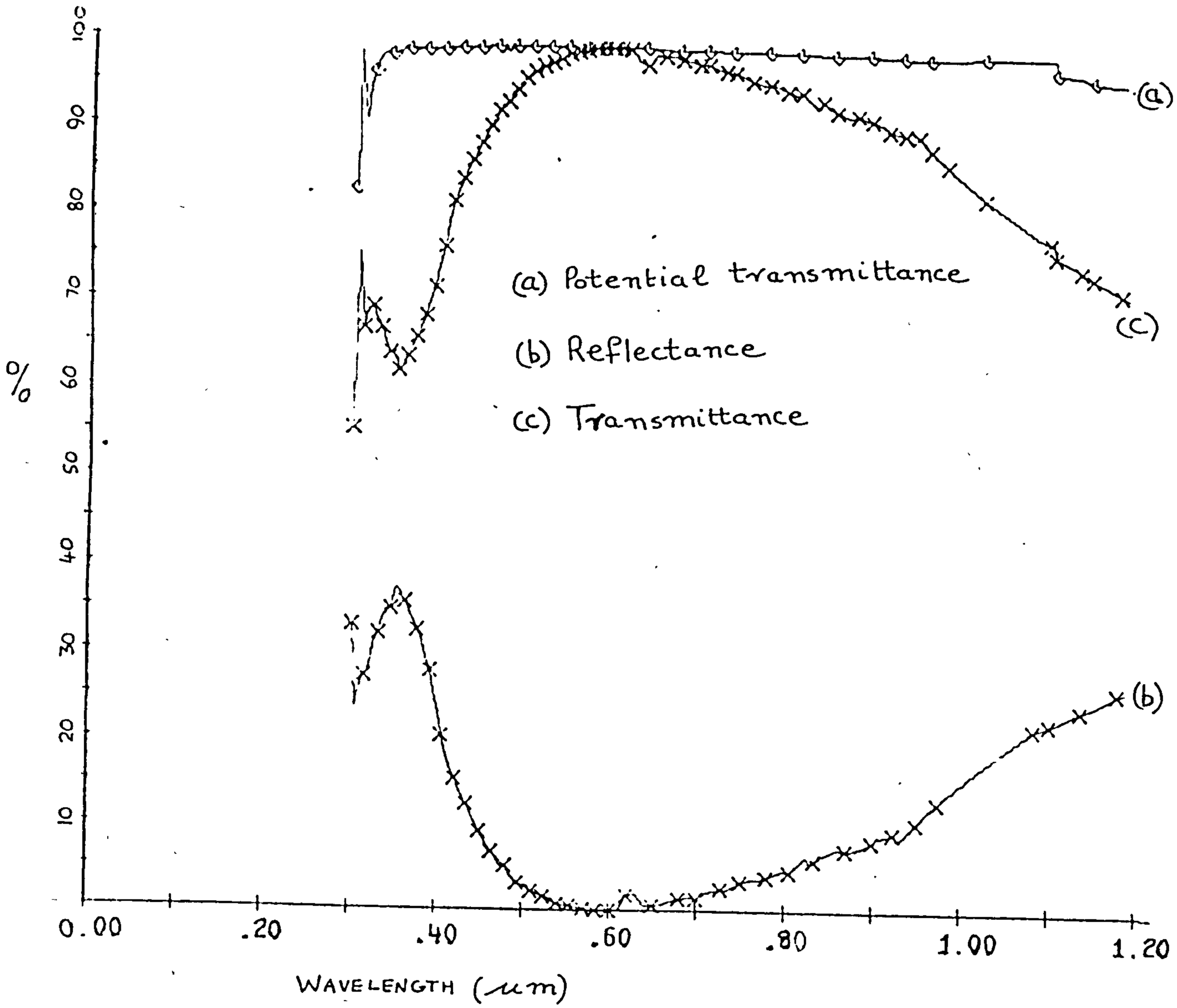

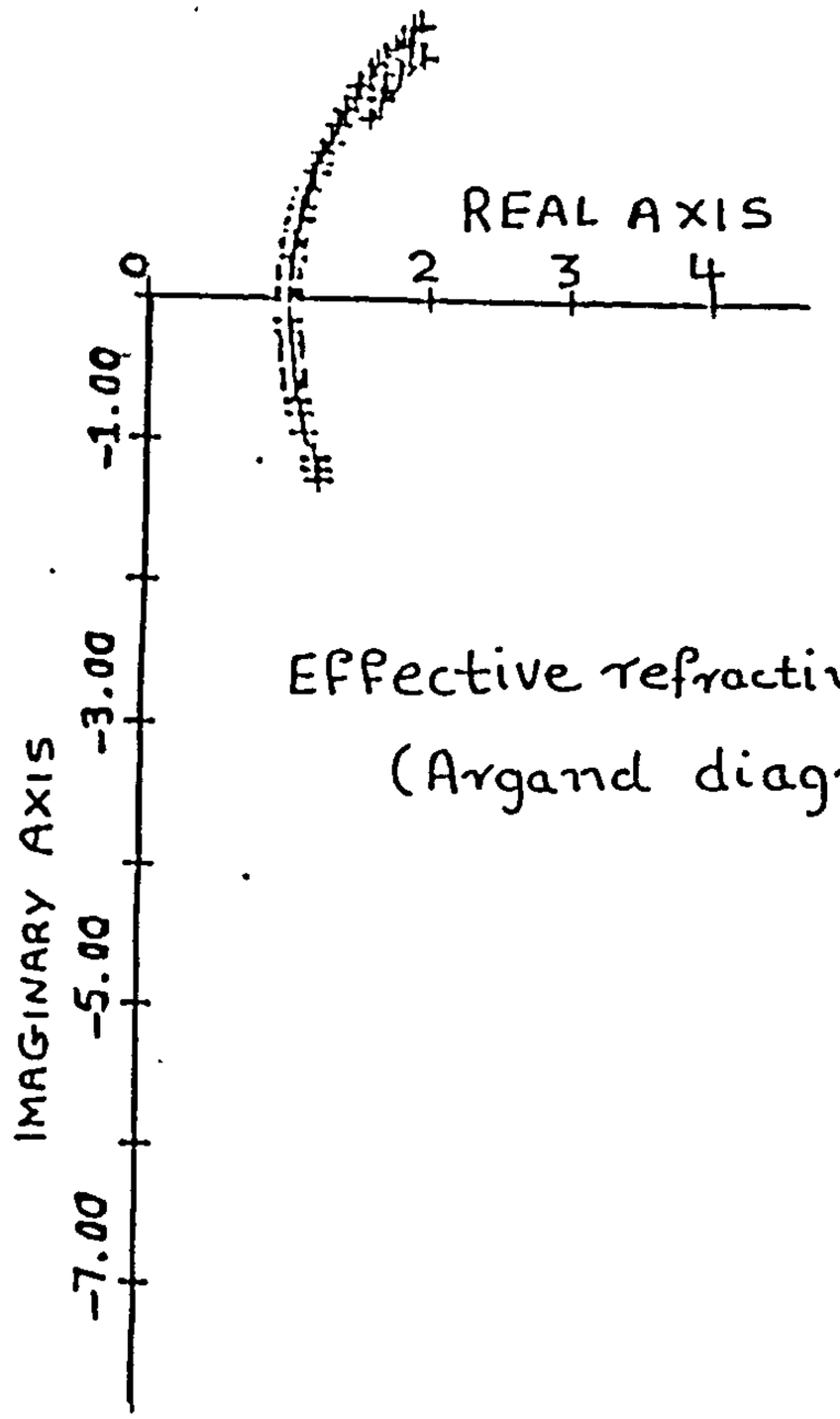

Effective refractive index (Argand diagram)

Transmittance through 200Å of silver into silicon with an antireflecting coating of ideal refractive index and an ideal thickness at 0.5μm wavelength is shown in Fig. 6.4. Unfortunately, there are no suitable dielectric materials with refractive indices approaching the ideal case. Evaporated silicon has an index of 4.4 but is also light absorbing ($k \neq 0$). Results of evaporated silicon substrate are shown in Fig. 6.4. Using evaporated silicon in this way would of course cause electrical complications to the Schottky barrier cell.

Having achieved transmittances such as the ones in Fig. 6.3 with a single layer of ZnS, one could try to improve it further by repeated application of 6.9 to 6.11. This was in fact done and it was found that with cryolite as a second layer, refractive index 1.35 and thickness 790Å, reflectance values in the longer wavelength region would fall. The effect of the second layer was to flatten out the transmittance and reflectance curves (Fig. 6.5) with a small increase in reflectance in the narrow band of minimum reflectance of the single layer antireflecting coating.

It can be seen that minimum reflectance always corresponds to maximum transmittance (Fig. 6.5) into the substrate through the thin metal layer. If the reflectance curve was perfectly flat, i.e. parallel to the obscissa, the 'effective index' curve for the whole assembly on the Argand diagram would be an isoreflectance circle. A curve approaching this circle on the Argand diagram can be seen in Figure 6.5.

Finally, it can be deduced that for the same transmittance into the substrate the higher the refractive indices of the antireflection coatings the thicker can be the metal layer forming the Schottky barrier with the substrate.

FIGURE 6.3

Theoretical results

100 Å Ag on Si with an antireflecting coating of 420Å ZnS

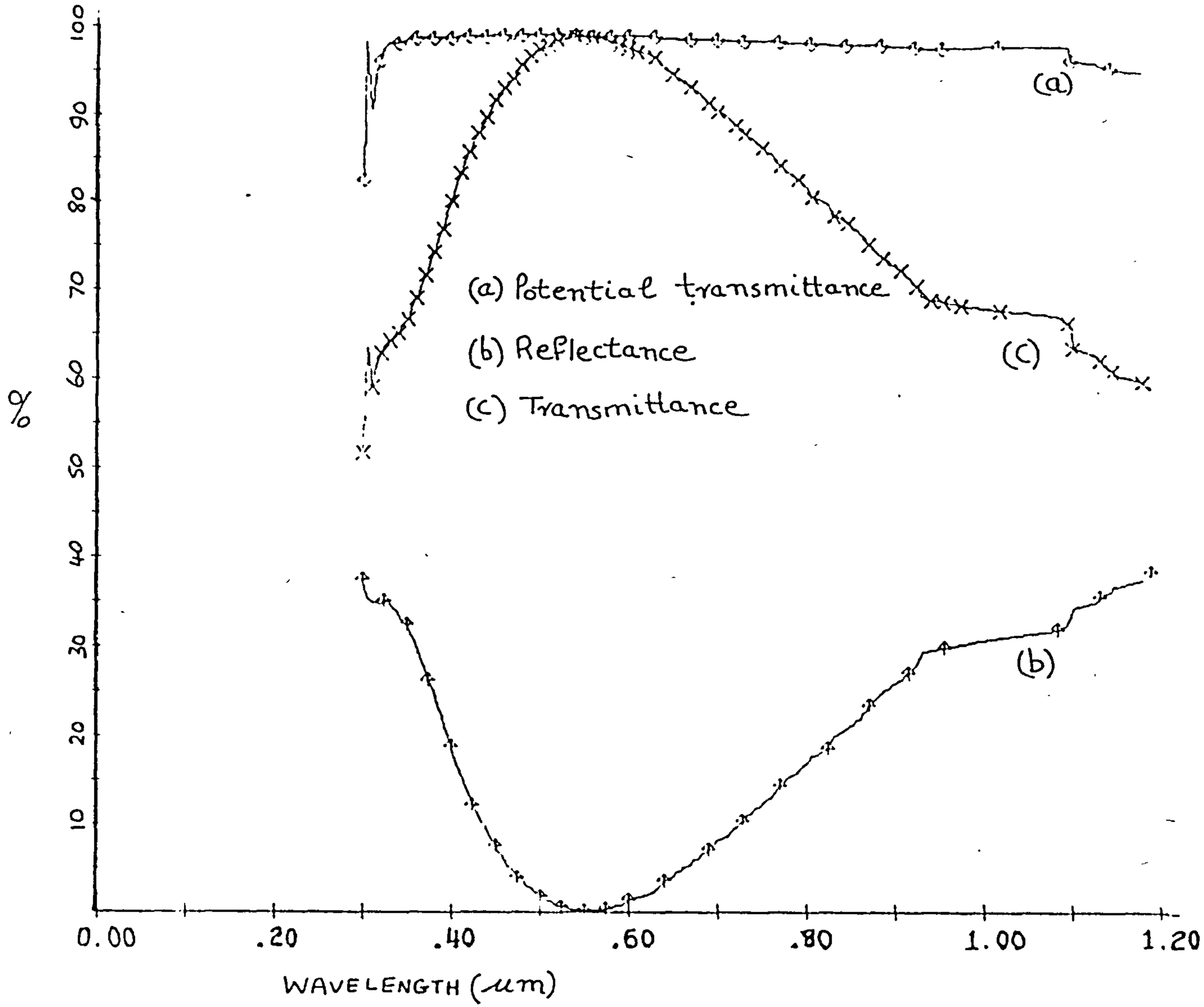

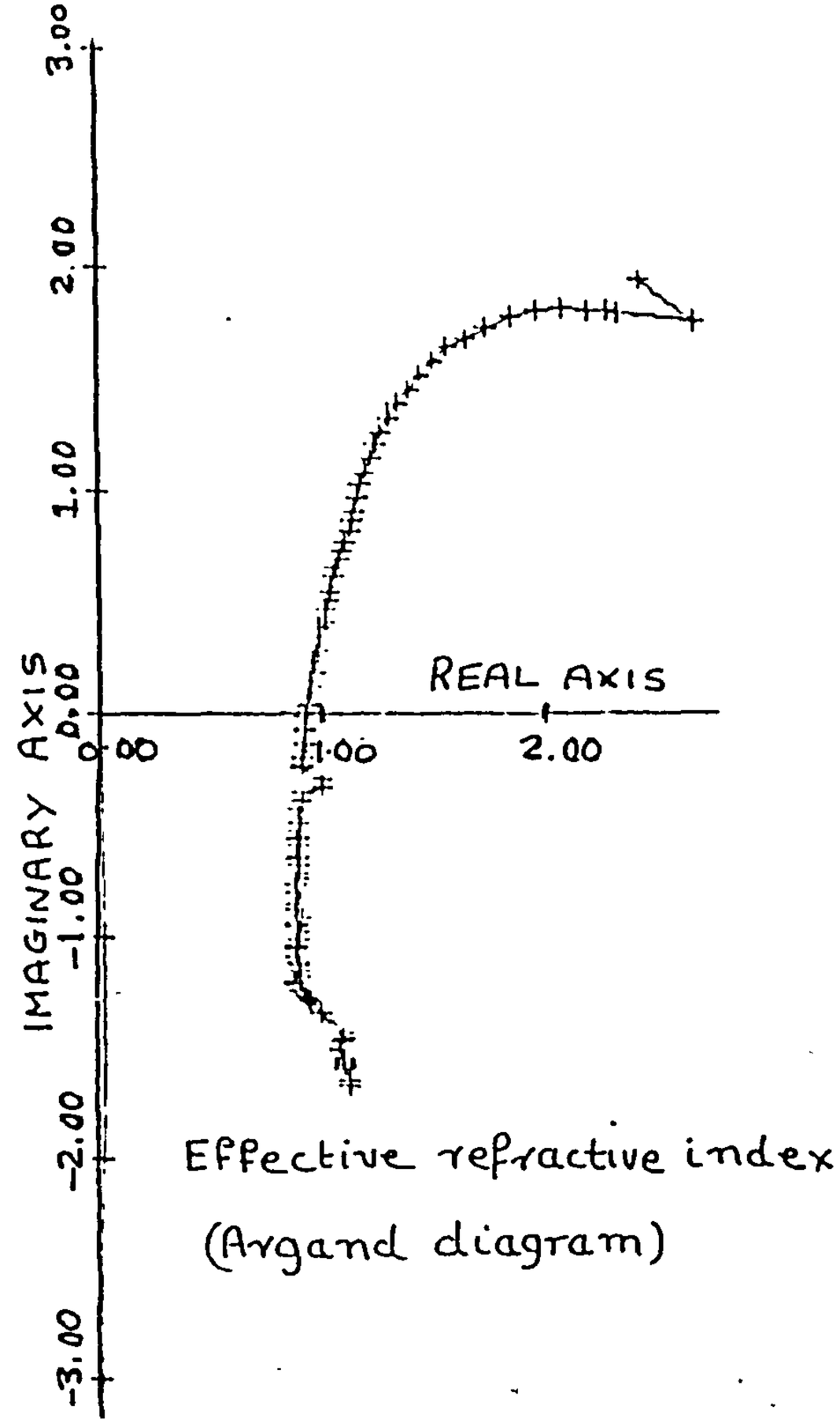

Effective refractive index

(Argand diagram)

FIGURE 6.4

Theoretical results

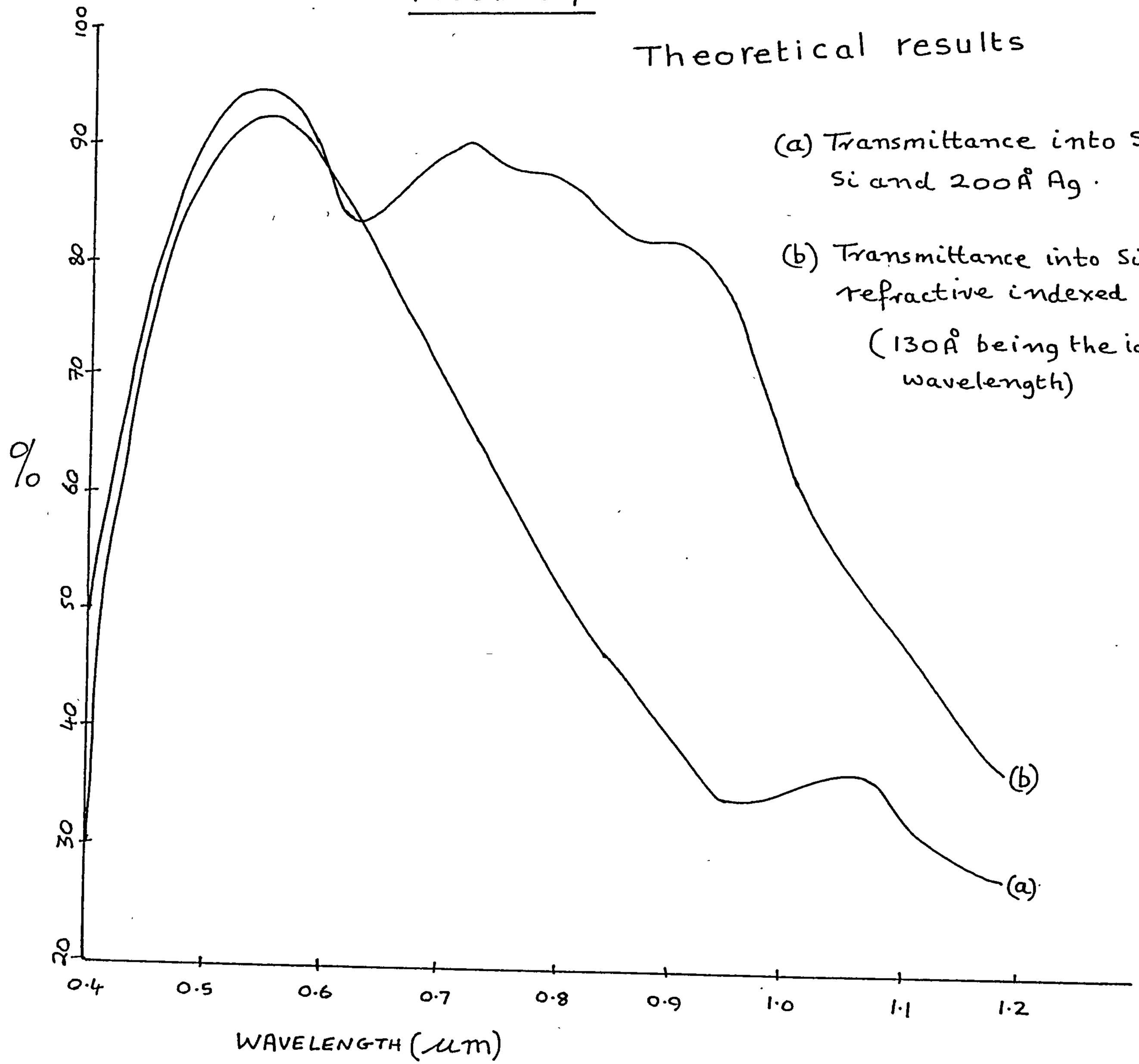

(a) Transmittance into Si through 130Å evaporated Si and 200Å Ag.

(b) Transmittance into Si through 130Å of ideal refractive indexed material and 200Å Ag.

(130Å being the ideal thickness at ~0.5μm wavelength)

FIGURE 6.5 Theoretical results

790 Å Cryolite on 420 Å ZnS on 100 Å Ag on Si substrate

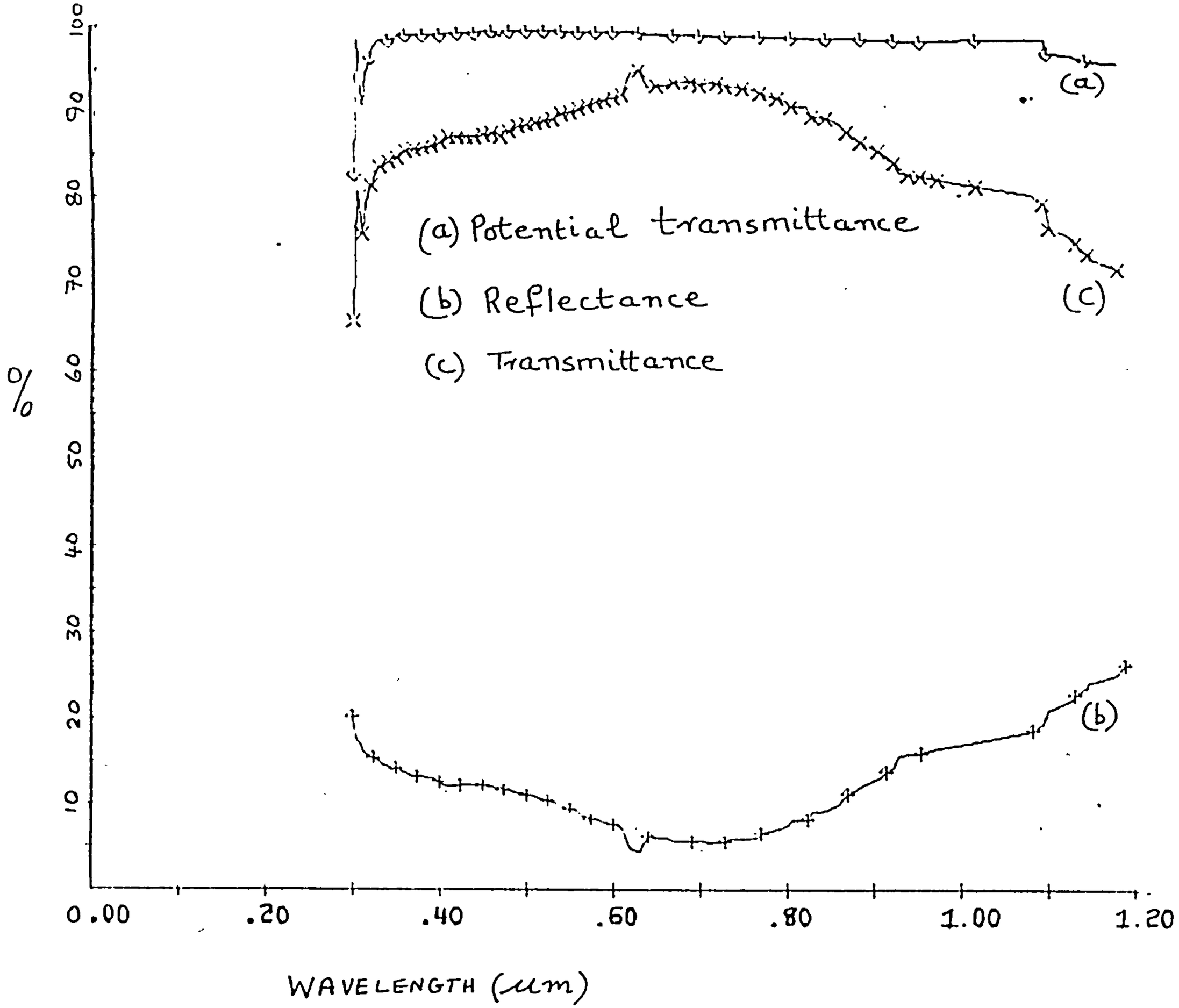

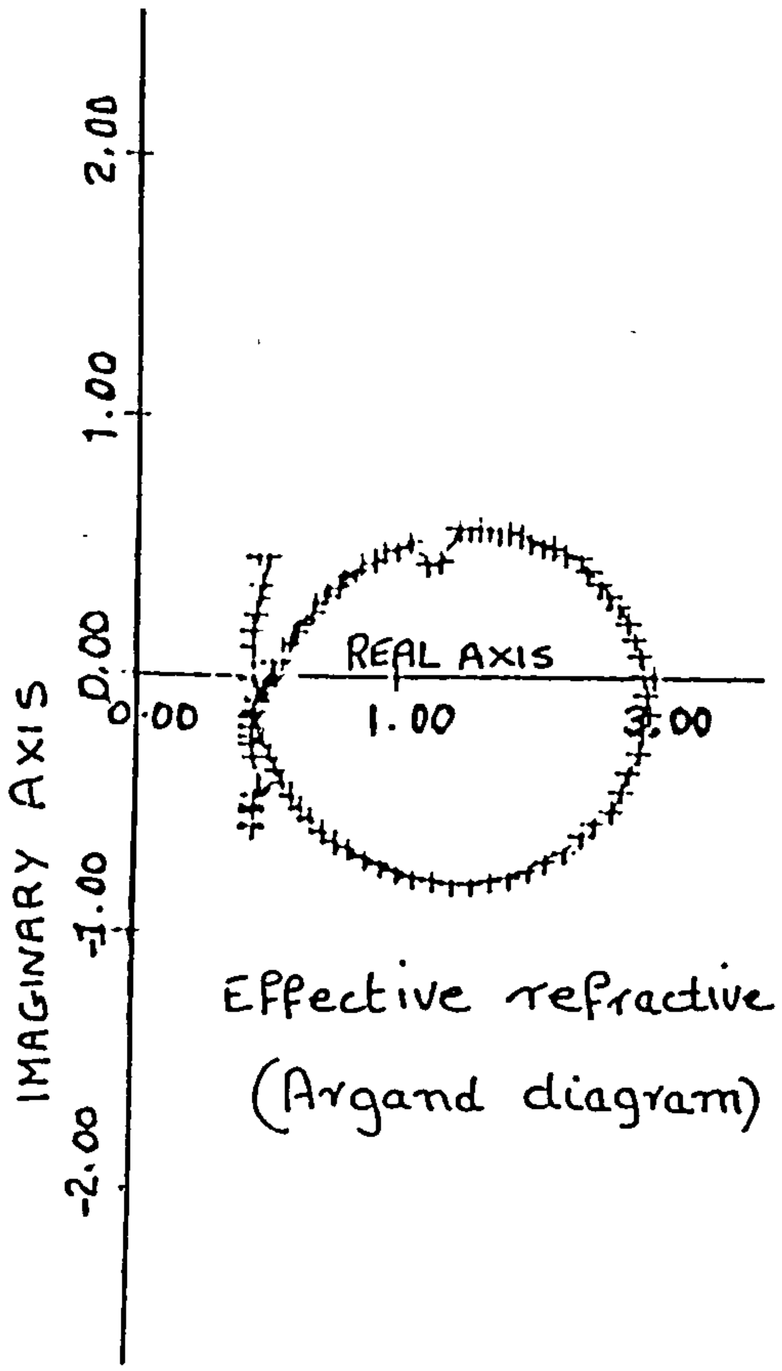

Effective refractive inde
(Argand diagram)

6.3 Experimental Work

A. Optical Properties of Thin Films on Glass

Silver films of differing thickness were evaporated onto glass and the transmission measured. The sheet resistances of the films were also measured. Antireflecting coatings of ZnS were deposited on top of the silver layers. The transmission was again measured. An SP 700A ultraviolet and visible spectrophotometer was used for measuring the optical transmission. The thickness of the deposited thin films was monitored using a 4.5 MHz resonant frequency quartz crystal.

B. Evaporation of Layers on Glass

The depositions were carried out using both the electron gun and the thermal evaporation technique at pressures below 5×10^{-5} torr. Depositions were also carried out using an ion plating plant. For solar cell purposes the silver was required to have high optical transmittance simultaneous to having a low sheet resistance. A bulk thickness of 100Å was found to be a reasonable compromise. To start with the electron gun was used for depositing silver on glass. Both the transmittance and the bulk thickness were measured. The quartz crystal used in measuring the bulk thickness was calibrated first by calculating the transmittance at various thickness of silver (assuming bulk n and k values) and then by measuring silver thickness by an optical interferometer, corresponding to transmittances less than 10% at a wavelength of 0.5μm. $\frac{\Delta f}{\Delta t}$ was found to be $3.6 \text{Hz}\text{Å}^{-1}$ where Δf is the frequency change in the quartz crystal and Δt is the corresponding thickness of the deposited layer. It was decided to carry out further depositions of silver by thermal evaporation. This was because of difficulties arising with the electron gun system. The geometry of the system was such that some of the evaporating silver was finding its way up the electron gun and causing a short circuit in the filament. This was unfortunate as the electron

gun tended to produce more uniform and continuous films at smaller bulk thickness when compared to the thermal evaporation technique. ZnS was still evaporated using the electron gun system. The parameter $\frac{\Delta f}{\Delta t}$ for ZnS was found to be $1.25 Hz\mathring{A}^{-1}$ .. For the thermally evaporated silver the same parameter was found to be $1.84 Hz\mathring{A}^{-1}$ ..

C. Thin Films on Silicon

Thin silver layers were deposited on silicon substrates to form Schottky barrier solar cells. Depositions were carried out using ion plating technique and the thermal evaporation method. Spectral responses, the I/V characteristics and the barrier heights of the diodes were measured. The diode factors were calculated for the cases when the biasing was done both electrically and optically. The effect on the current output of the cell by the addition of an antireflecting coating was also measured.

D. Preparation of Silicon Samples

The silicon substrates were in the form of circular discs diameter 1 cm, P type with a polished face in the (100) plane. The resistivity of the silicon samples was 0.1 ohm cm.

Before the deposition of silver on the polished side of the disc it was first etched with a solution of HF. . The surface of the disc was carefully cleaned with a Q tip which had been previously dipped in a 20% HF solution. This was followed by further careful cleansing with Q tips which had been dipped in deionised water.

The back contacts were made prior to polishing the silicon slice with HF. This was done by first evaporating a thick layer of aluminium, by thermal evaporation on the back unpolished side of the silicon disc. The aluminium covered most of the back surface but not all. The silicon was then placed in a quartz tube at $450^{o}C$ with Argon flowing

through it. It was treated in Argon for about 15 minutes. Two separate wire connections were made to the aluminium at the back of the disc using a silver paste. The disc was then placed in an oven for about two hours at a temperature of 60°C. This enabled the electrical connections to make firm bonds.

The contacts were then tested for 'ohmicity'. A piece of indium wire dipped into indium-mercury makes a very good temporary ohmic contact with P type silicon. This was tested on a I-V curve tracer. This technique was used for making a temporary ohmic contact to that part of the back face of the disc which did not have any aluminium on it. It was verified . that the indium-mercury contact did not touch the aluminium.

The permanent wire connections to the aluminium and the indium-mercury contact were connected to the I-V curve tracer. The characteristics were observed to be rectifying. The current was gradually increased until the characteristics were suddenly observed to be ohmic, i.e. a straight continuous line was observed for both in the forward and reverse bias. The disc was then ready for polishing with HF which was carried out using Q tips to avoid damaging the back contacts.

E. Deposition of Layers onto Silicon

The silicon disc, immediately after the polishing process with HF, was placed in the vacuum chamber ready for evaporation. The clean silicon sample was exposed to the atmosphere for a few minutes while the vacuum pumps were being switched on. When the pressure reached around 2×10^{-5} torr Ag was evaporated onto the substrate through a mask. The area of the evaporated silver formed a circle of diameter 0.5 cm on the silicon surface.

A special copper holder for the mask containing the silicon disc was made such that the disc was in thermal contact with the holder.

The holder was also a heater designed to take its temperature up to 200°C. A thermocouple was attached to the holder to measure the temperature of the silicon disc during the evaporation of silver onto it. It was recognised that the evaporation of silver onto a heated Silicon disc would tend to produce better adhesion of the evaporant to the substrate but if the growth of the oxide layers at high temperatures were to be avoided the evaporating chamber had to be in an ultra-high vacuum region. The temperature of the disc during evaporation of the silver onto it was 30°C. The silver was evaporated by passing a steady current of 22AMPS through a molybdenum boat containing the silver. A shutter was placed between the boat and the substrate until the silver was observed to be evaporating steadily. The shutter was removed and as soon as the required Δf reading was reached it was immediately replaced. The temperature of the substrate during the evaporation process was also noted. The diode was carefully removed from the chamber.

The silicon slice was then carefully removed from its mask and placed inside another one. The second mask shielded half the circular dot already deposited on the substrate.

The silicon slice with its new mask was placed in a new vacuum chamber and a thick layer of gold deposited on top of the semi circle of silver. Using 'Dag' silver paste, electrical connections to a wire were made with the gold contact to the silver layer. The silicon slice was left overnight in a vacuum chamber for the contact to harden. The diode was then ready for making measurements. The short circuit current and the open circuit voltages were measured under the light from a water filtered tungsten lamp of intensity 100 mw cm^{-2}. The unnormalised spectral response under the light from a tungsten iodine lamp was also measured.

The diode was then placed back in the vacuum chamber and an antireflection coating of ZnS was deposited on top of the silver. The short circuit current and the open circuit voltage were again measured. This was followed by measurements of the spectral response curve and the barrier height of the photo-diode. I-V measurements were made and the diode factors calculated both when biased electrically and optically.

F. The Ion Plated Diode

The ion plated diode was fabricated by first etching the polished surface of the P type silicon disc by sputtering the substrate by Argon ions. The sputtering process was carried out in the ion plating plant for 5 minutes. A full description of the ion plating technique is given in I Reid's PhD thesis (Newcastle upon Tyne Polytechnic)* A schematic diagram is shown in figure 6.5.1. showing the layout of the ion plating apparatus. Ion plating is essentially vapour deposition onto a substrate which is the cathode of a glow discharge where the substrate is cleaned and maintained clean by sputtering.

After the silver layer was ion plated onto silicon, top contact was made as described above and a layer of ZnS was then added on to antireflect the solar cell. The same measurements as on the thermally evaporated diodes were then made on the ion plated one.

G. Equipment and Techniques

The vacuum chambers were 12" diameter and the pressures were read using the Pirani, Penning and the ionisation gauges. The vacuum chamber in which silver and ZnS were evaporated was pumped by a turbomolecular pump backed by a rotary pump. The chamber for evaporating Aluminium and gold was pumped by a diffusion pump backed by a rotary pump.

The I-V characteristics of the photocell both in the dark and in the light were plotted directly onto a chart and also measured point by point using a digital voltmeter, an electrometer and a stabilised

* to be published

voltage supply unit for biasing the cell. Equipment for measuring the spectral response and the barrier height was specially constructed. A schematic layout of the apparatus is shown in figure 6.5.2. The photoresponse was measured by mechanically chopping the light at the exit slit of the M2 Grubb-Parsons prism monochromator and focussing it on the Schottky barrier cell. The short circuit current was detected using a phase sensitive detection system. The cell was illuminated from the silver side of the diode.

The monochromator was calibrated in the visible region by detecting the emission lines of mercury, sodium and helium sources. In the infra-red region, suitable for measuring the barrier heights of the silver-silicon contacts, emission spectra lines of a mercury source were used for calibrating the monochrometer in that region (Journal of Research of National Bureau of Standards V45 No.62u.950). A neon-helium gas laser was also used for calibrating the monochromator at 1.153 um wavelength. The resolution of the monochromator was found to be about 200A. This was observed directly from the response to the laser line. The tungsten-iodine lamp was powered by an IBM computer supply unit of 12 volts DC. The ripple in the voltage supply was less than 1 mv so that a stable power supply enabled a stable light output from the lamp.

A Mullard 615 V infra-red detector was used for normalising the response of the Schottky barrier diodes in the region of wavelength where readings were taken for measuring the barrier heights. The relative and normalised* response curve for the infra-red detector was provided by the manufacturer. In the region of interest the response was constant. The response of the Mullard detector was also measured under the light from the tungsten-iodine lamp. The phase sensitive detection system that had been set up was used for measuring this response also. The relative values for the photon flux incident on the infra-red

* normalised response - response per unit incident radiation

Figure 6.5.1

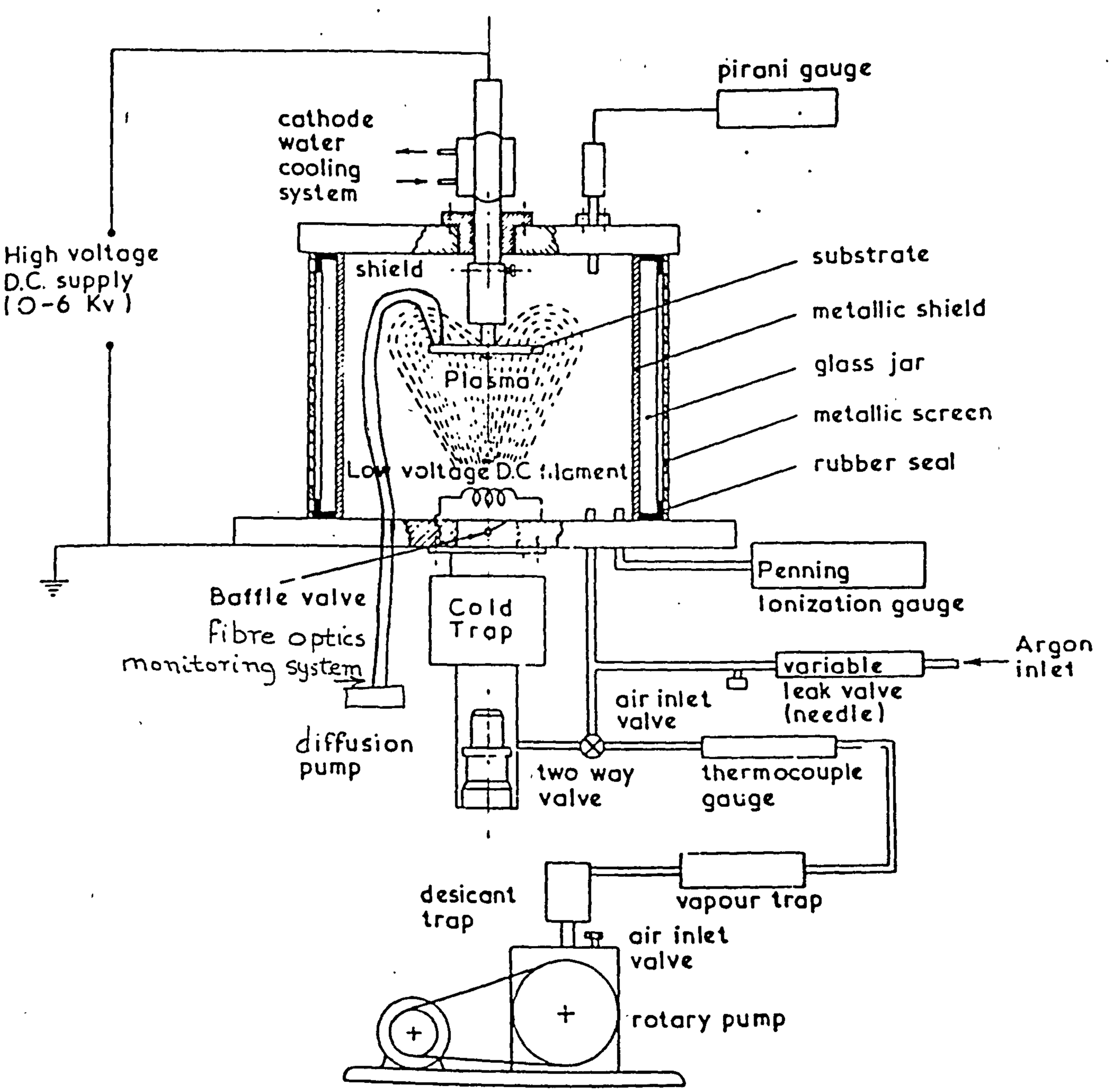

Schematic Layout of the Ion Plating Apparatus

PHOTORESPONSE MEASUREMENT

BLOCK DIAGRAM

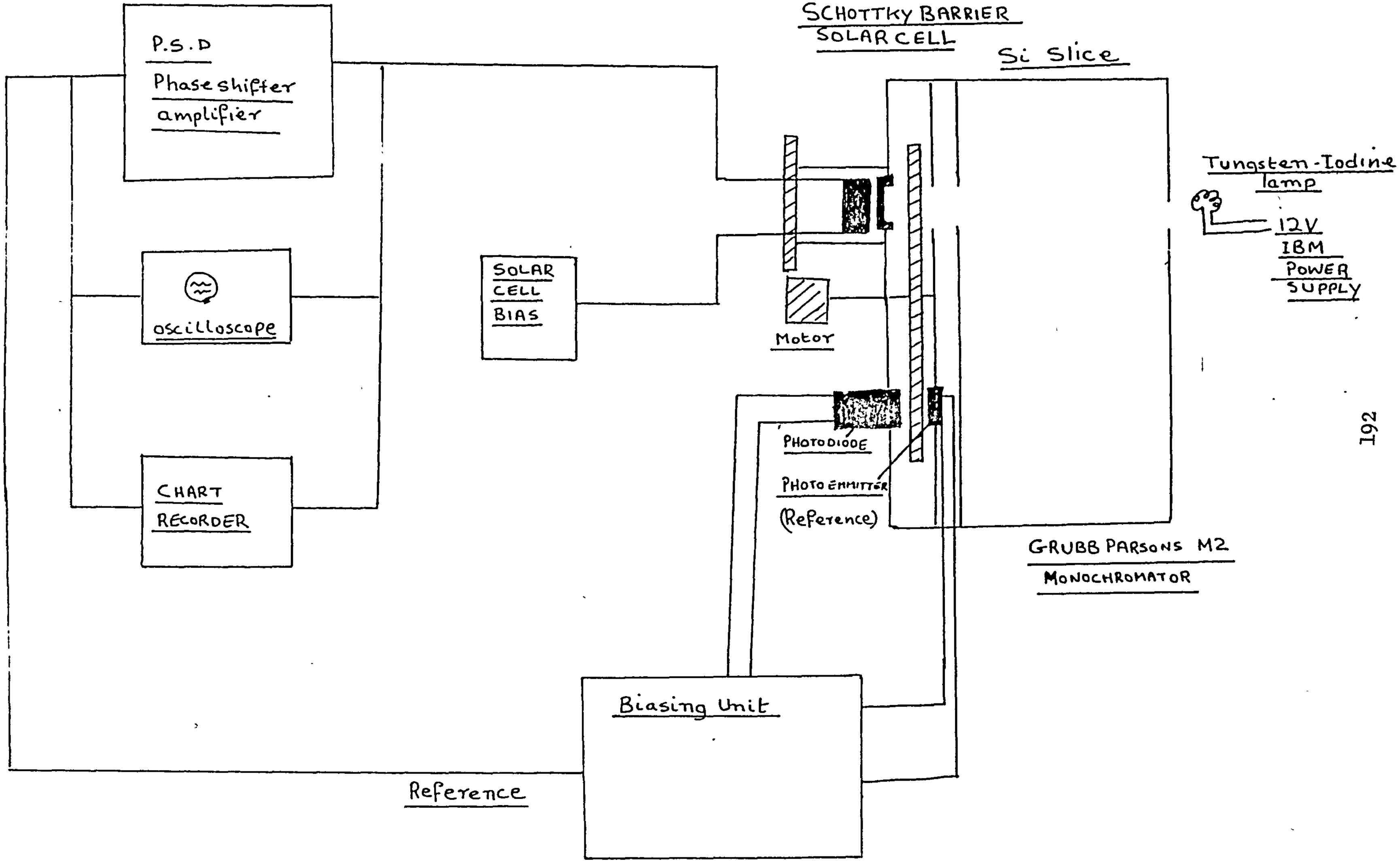

Figure 6.5.2

detector was the same as that incident on the Schottky barrier cell whose normalised response could then be found from the experimentally observed response under the same lamp. By plotting the square root of the relative normalised responses against $h\nu$, the barrier heights of the Schottky photodiodes were measured from the intercept on the h axis (Fowler theory). The diode factors were calculated from the graphs of lnJ versus the voltage across the diode in the dark. From the same graphs the saturation current J_{no} was also calculated. From measurements of V_{oc} the open circuit voltage and the short circuit current J_{sc} and using the equation

$$V_{oc} = \frac{AkT}{q} \ln (J_{sc}/J_{no} + 1)$$

the diode factor A was again calculated. This was taken to be the value in the light. It was realised that J_{no} was not necessarily the same in the dark as in the light.

H. Experimental Results

The experimental results are recorded graphically (figures 6.6 to 6.23) on pages 200 to 217. Titles of these results and the figure numbers are summarised on table 6A. Table 6B contains the measured parameters for the solar cells fabricated in the laboratory.

The remaining theoretical results are shown on pages 218 to 228 but they are discussed, together with the experimental results, on pages 196 to 198.

Table 6A Guide to the experimental results

Figure	
6.6	Comparision of the theoretical and experimental curves for transmittance into glass through silver as a function of silver bulk thickness.
6.7 6.8 6.9 6.10	Experimental transmittance for thermally evaporated silver onto glass both with and without antireflection coatings.
6.11	Unnormalised spectal response measured both with and without antireflection coating of ZnS (thermally evaporated diode 1)
6.12	InJ versus voltage across diode (diode 1)
6.13	I-V measurements directly onto a chart recorder (diode 1) both in the dark and light.
6.14	R Vs $h\nu$ (diode 1) R is the square root of the normalised response.
6.15	Unnormalised spectral response for the thermally evaporated diode 2 with zero bias.
6.16	Unnormalised spectral response for the thermally evaporated diode 2 with a reverse of 2V.
6.17	InJ versus voltage across the diode 2
6.18	R versus hv (diode 2)
6.19	Unnormalised spectal response curve for the ion plated diode with zero bias
6.20	InJ versus voltage across the ion plated diode
6.21	R versus $h\nu$ (ion plated diode)
6.22	I-V measurements directly onto the chart recorder both in the dark and light
6.23	Transmittance through glass with ion plated silver of thickness equal to that deposited on the ion plated diode.

Table 6B Theoretical parameters for the fabricated solar cells

Parameter	Diode 1	Diode 2	Ion Plated Dioc
Diode factor at low voltages i.e. < 0.1 V (dark)	2.0	1.3	1.2
Diode factor at voltages > 0.1V (dark)	8.0	11.4	2.1
Diode factor in the light using $V_{oc} = \frac{AKT}{q} \ln(\frac{J_{sc}}{J_{no}} + 1)$	7.6	1.8	1.7
V_{oc}	70 mV	81 mV	0.35 V
J_{sc}	2.0 μA	9.2 μA	3.92 μA
J_{no}	4.5 μA	1.85 μA	0.11 μA
Active area of cell	0.1 cm^2	0.1 cm^2	0.1 cm^2
Silver thickness	96 Å	100 Å	100 - 140 Å
Oxide thickness	5-20 Å	5-20 Å	no oxide laye
Estimated series resistance	3.5 k$\Omega/\square$	3.5 k$\Omega/\square$	35 $\Omega/\square$
Barrier height	0.67 eV	0.78 eV	0.79 eV
Effective Richardson constant (A cm^{-2} K^{-2})	167	5350	472

6.4 Discussion of Results

Comparison of the theoretical and experimental curves for transmittance into glass through the silver as a function of silver bulk thickness show that the curves superimpose for thickness greater than 300Å (page 200) For values less than 300Å the experimental transmittances are lower than the theoretical ones. This can be explained by the fact that the optical constants, i.e.* n and k are themselves functions of the thickness and structure of the thin film. For thickness greater than 300Å it is reasonable to assume that n and k values are the same as those given in the literature. For thickness below 300Å they must be different (Fig. 6.6). Experimental results of thermally evaporated silver onto glass both with and without ZnS coatings (Figs. 6.7 to 6.10) compare well with the theoretical results of figures 6.24 to 6.26 as well as the results of Anderson et al (1976) who studied thin films of metal in connection with Schottky barrier cells. They reported sheet resistance of 20 Ω/□ for 50Å Cu on 50A Cr with 58% transmittance at 0.6 μm wavelength and 57 Ω/□ for 50Å Ag on 50-Å Cr with 33% transmittance at the same wavelength. In this work a sheet resistance of 5.5 Ω/□ with a transmittance over 50% at 0.6 μm wavelength was measured for 100Å of silver on glass. Anderson et al (1976) used layered metal films with Cr adjacent to Si for good adhesion and high open circuit voltage. The theoretical results (Figs. 6.24 - 6.26) show that the peak transmittance into the substrate and the general shape of the curve depends not only on the antireflecting layer thickness but also on the metal layer thickness. For instance when 175Å of silver on glass is antireflected with ZnS the overall transmittances are not only reduced but the peaks are shifted to the blue end of the spectrum when compared with 100Å of silver on glass.

* n is the refractive index
k is the extinction coefficient

This is due to the absorption in the silver layer. It can be observed that the maximum transmittance always corresponds to minimum reflectance whatever the metal layer thickness.

The experimental values for transmittances are approximately 10 to 15% below the theoretical ones; this could be explained by the incorrect values for n and k being used when making theoretical calculations. An experimentally deposited silver film of 100Å 'bulk'* thickness corresponds to a film of 140Å having n and k values equal to the bulk values (Fig.6.6). This is equivalent to about 15% reduction in the transmittance at least at 0.5 μm wavelength.

Theoretical values for transmittance into silicon through various thickness of Ag are lower than those into glass (Figs. 6.27 and 6.24). The optimum thickness for ZnS as an antireflecting layer on silver on top of silicon will depend on the wavelength. At a wavelength of 0.62 μm for a silver layer of 100Å the optimum thickness for ZnS is 500Å (Fig.6.28). The effect of the oxide layer between 100Å of silver and the silicon substrate is to reduce the reflectance by a couple of per cent at 0.62 μm wavelength.

The theoretical transmittance versus wavelength curves (Figs.6.29 and 6.30) show that as ZnS layer thickness is increased, the general trend for the peak transmittance is to shift to the red end of the spectrum. The effect of the oxide layer is again shown to be negligible on the transmittance. With a ZnS layer of 480Å on silver layer of 100Å thickness the integrated transmittance over the region 0.4 μm to 1.2 μm increases by a factor of 1.6 (Fig. 6.29). The effect of adding a second layer of cryolite thickness 1111Å onto 480Å of ZnS on top of 100Å, 120Å and 175Å of silver layers respectively is shown in Fig. 6.31. The integrated transmittance is increased by a factor of 1.7. This is not significantly greater than with a single layer coating of ZnS. It should

* bulk thickness - density of the thin film is assumed to be the same as for bulk material

be noted that when applying the theory to a solar cell the incident radiation must be taken into account before deciding whether a single or a double layer coating is more suitable. For example, integrated short circuit current could be calculated for particular radiation distribution and the optimum thickness for the antireflecting layer deduced. For AMI radiation the theoretical optimum thickness for ZnS calculated in this way is 450Å (Fig. 6.32) for silver films around 100Å thick. Addition of a cryolite layer increases the current slightly (Fig. 6.19) at AMI radiation where the optimum thickness for the second layer is 600±200Å (Fig. 6.32).

From the theoretical spectral response curve under AMI radiation (Fig. 6.33) it can be seen that the ZnS layer of 450Å on 100Å of silver antireflects mostly in the region containing most AMI radiation. It does not antireflect strongly above 1.0 μm wavelength. The effect of the cryolite layer is also illustrated in Fig. 6.20 where it can be seen to be insignificant. In the strongly antireflecting region the output is doubled by the addition of the ZnS layer. The thickness of the silicon layer was taken as 500μm with a diffusion length of 100 μm for the minority carriers.

The inclusion of a back surface (reflecting) showed that the incident light did not see it in the wavelength region of interest. Some curves of short circuit current versus silicon thickness for a Au -Si-Ag Schottky barrier cell for R=0 and R≠0 are shown in Fig. 6.34. R=0 corresponds to the case of a perfect antireflecting coating. For thin film Schottky barrier cells the back surface can be seen to be important (Fig. 6.34).

6.5 Conclusions

The unnormalised experimental spectral response curves of Fig.6.11 showed that the peak response was approximately doubled by the ZnS layer. This was in agreement with the theoretical predictions.

The high values for the diode factors (Table 6B) for the thermally evaporated diodes would suggest that the simple thermionic-diffusion theory by itself is insufficient to explain the workings of the diodes. There must be other mechanisms at work.

The effects of the oxide layers on the voltage and current mechanisms is the subject of another project in this laboratory and in a more full discussion would certainly need to be taken into account for their effects both on the diode factors and the barrier heights.

The ion plated diode results would be explained more closely by the thermionic-emission theory with diode factors of 2.1 in the dark and 1.7 in the light and having a Richardson constant (effective) of 472A $cm^{-2}\,{}^{o}K^{2}$(Table 6B). The different values for the diode factors when biased electrically and by the light would appear to agree with the qualitative arguements of Card and Young (1976) who pointed out that the charges on the interface states are not the same in the two cases.

Estimates of the series resistances were made from the I-V curves and the very high values for the thermally evaporated diodes were probably the main cause for such low currents (Table 6B). Even a value of 35$\Omega/\square$ series resistance in the ion plated diode was too high and certainly limited the current.

The poor quality of the electrical contacts with 'Dag' paste to the active area of the cells probably accounted for the high series resistance values. The ion plated diode had an overall efficiency approaching 2% and with improved top contacts and a better matching of the antireflecting coating with incident radiation this result could be improved substantially.

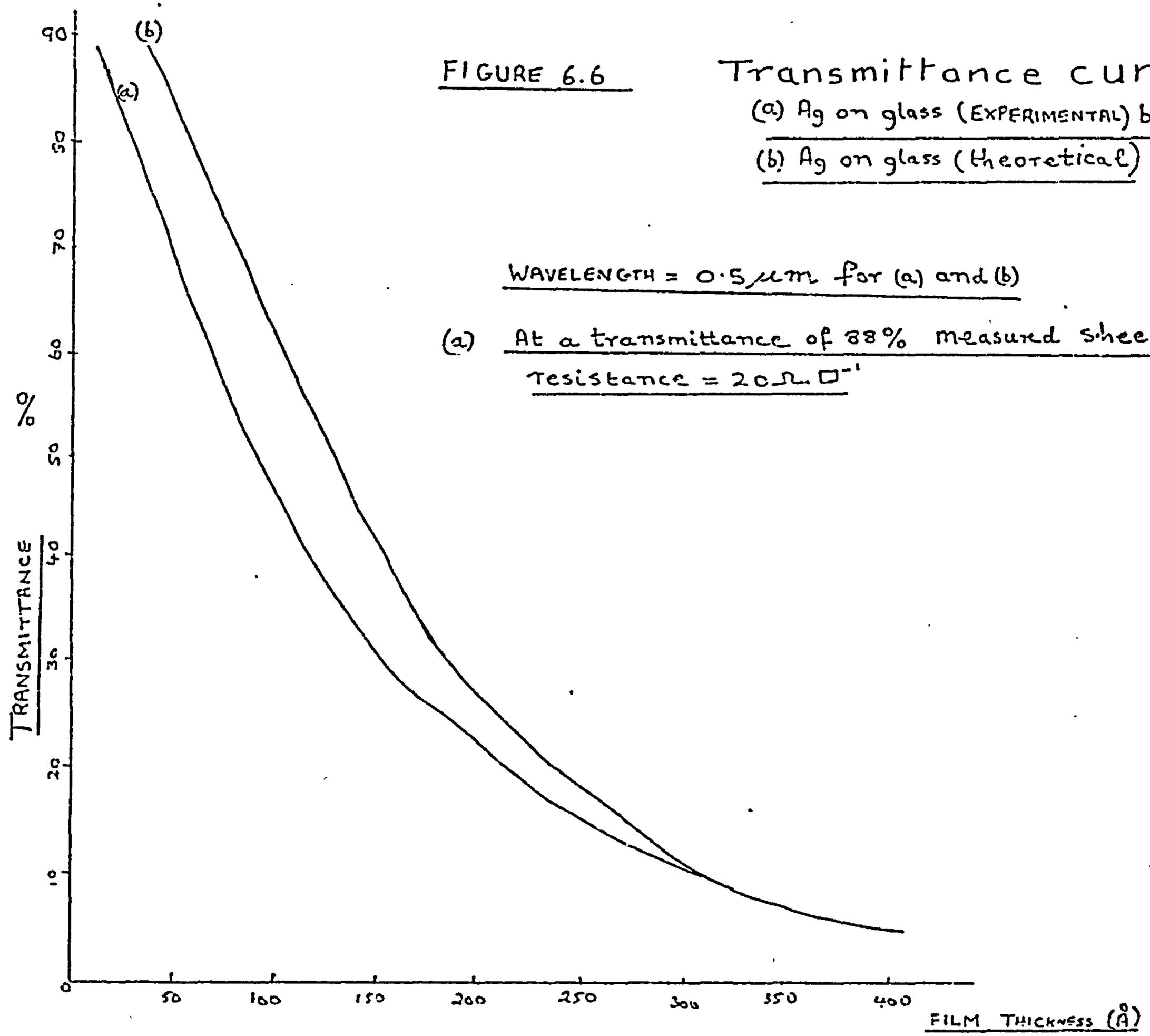

FIGURE 6.6 Transmittance curves

(a) Ag on glass (EXPERIMENTAL) by electron gun

(b) Ag on glass (theoretical)

WAVELENGTH = 0·5 μm for (a) and (b)

(a) At a transmittance of 88% measured sheet resistance = 20 $\Omega.\square^{-1}$

FIGURE 6.7 Experimental results

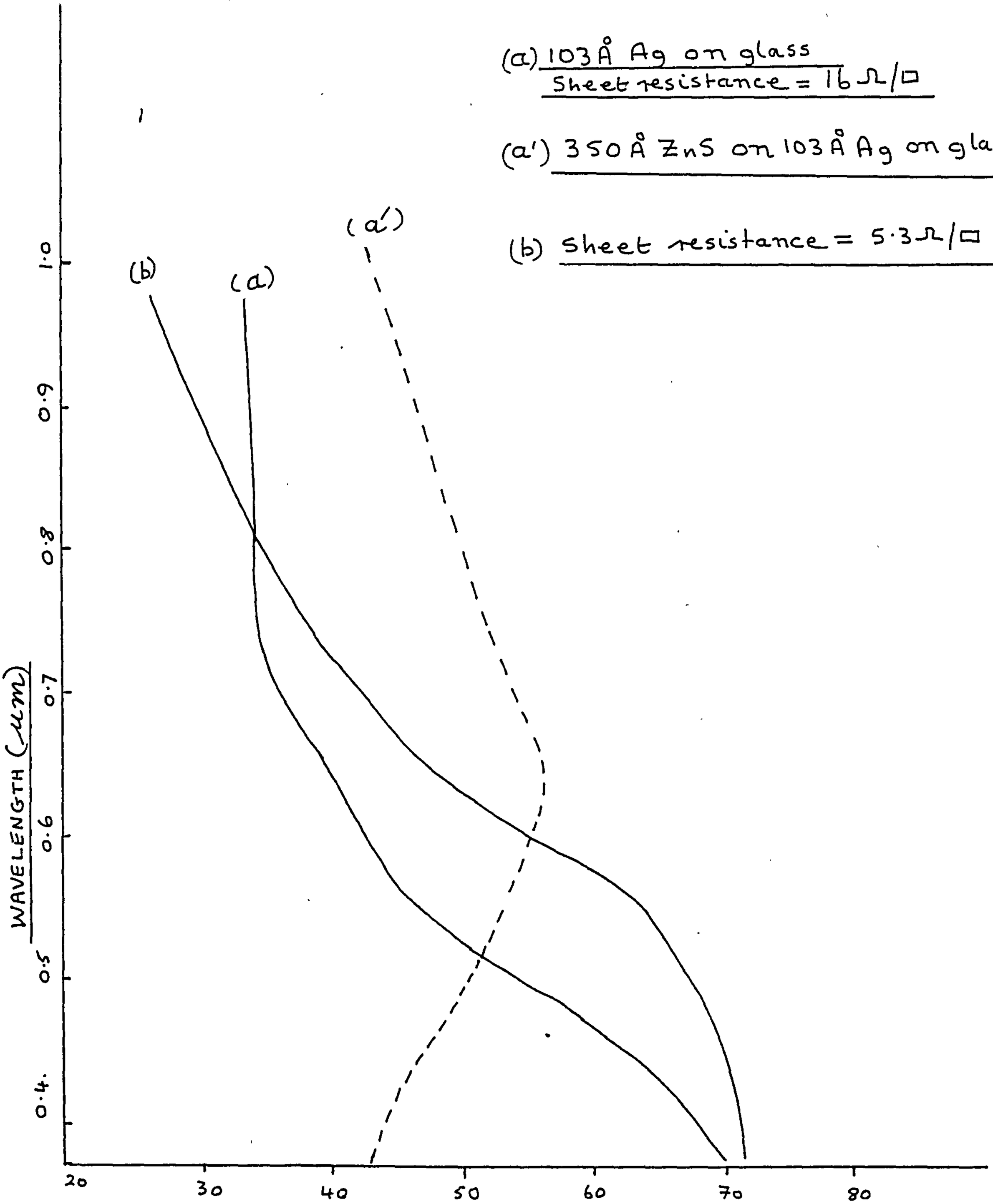

THERMALLY EVAPORATED Ag

ELECTRON GUN EVAPORATED ZnS

FIGURE · 6. 8 Experimental results

(a) 100 Å Ag on glass ; sheet resistance = 5·5 Ω □⁻¹

(b) 90 Å Ag on glass ; sheet resistance = 10·0 Ω □⁻¹

(c) 100 Å Ag on glass + 300 Å ZnS (antireflecting coating)

(d) 90 Å Ag on glass + 300 Å ZnS (antireflecting coating)

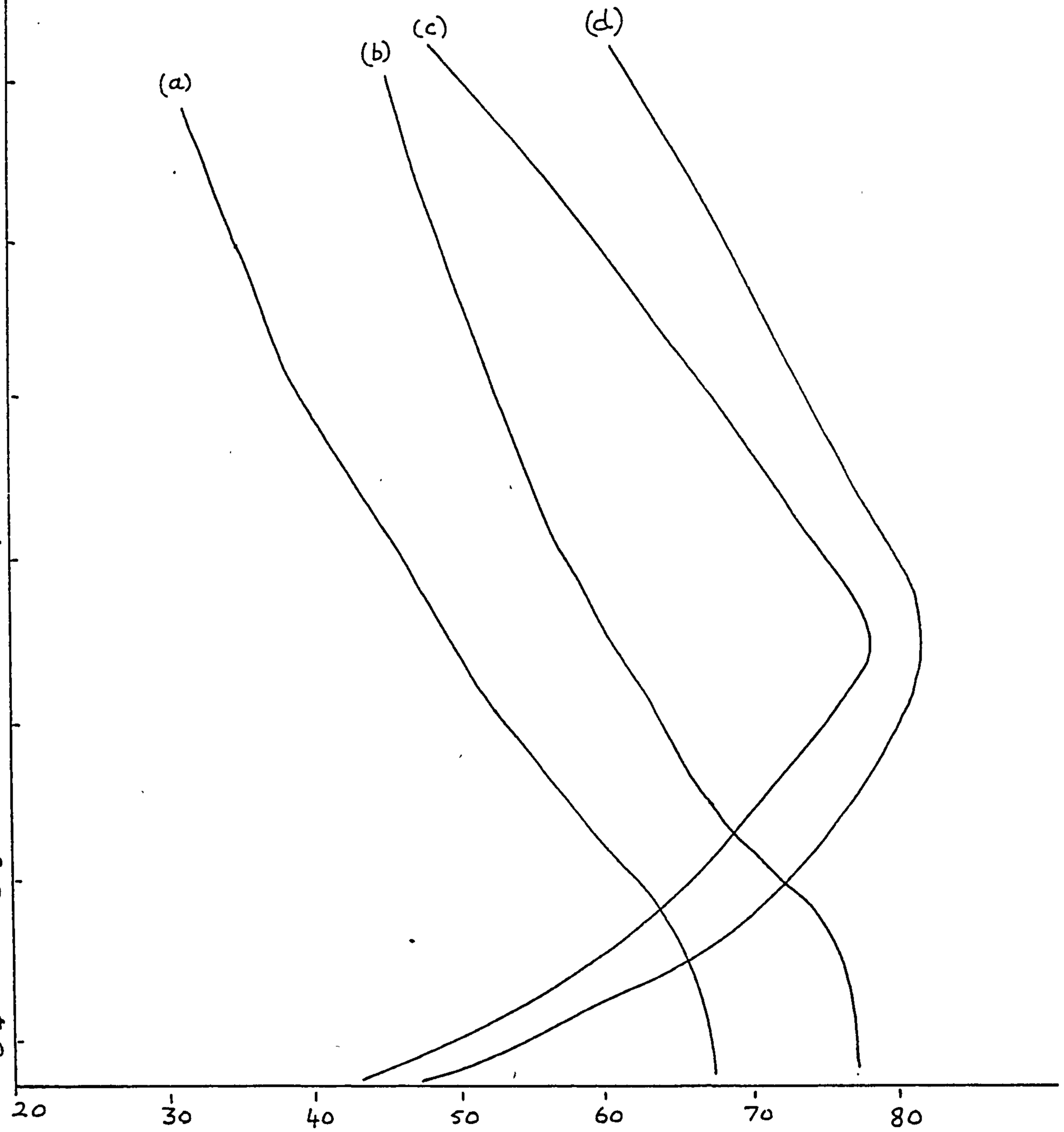

Thermally evaporated Ag

Electron gun evaporated ZnS

FIGURE 6.9 Experimental results

(a) 107 Å Ag on glass

(b) 430 Å ZnS on 107 Å Ag on glass

(c) 92 Å Ag on glass

d) 300 Å ZnS on 92 Å Ag on glass

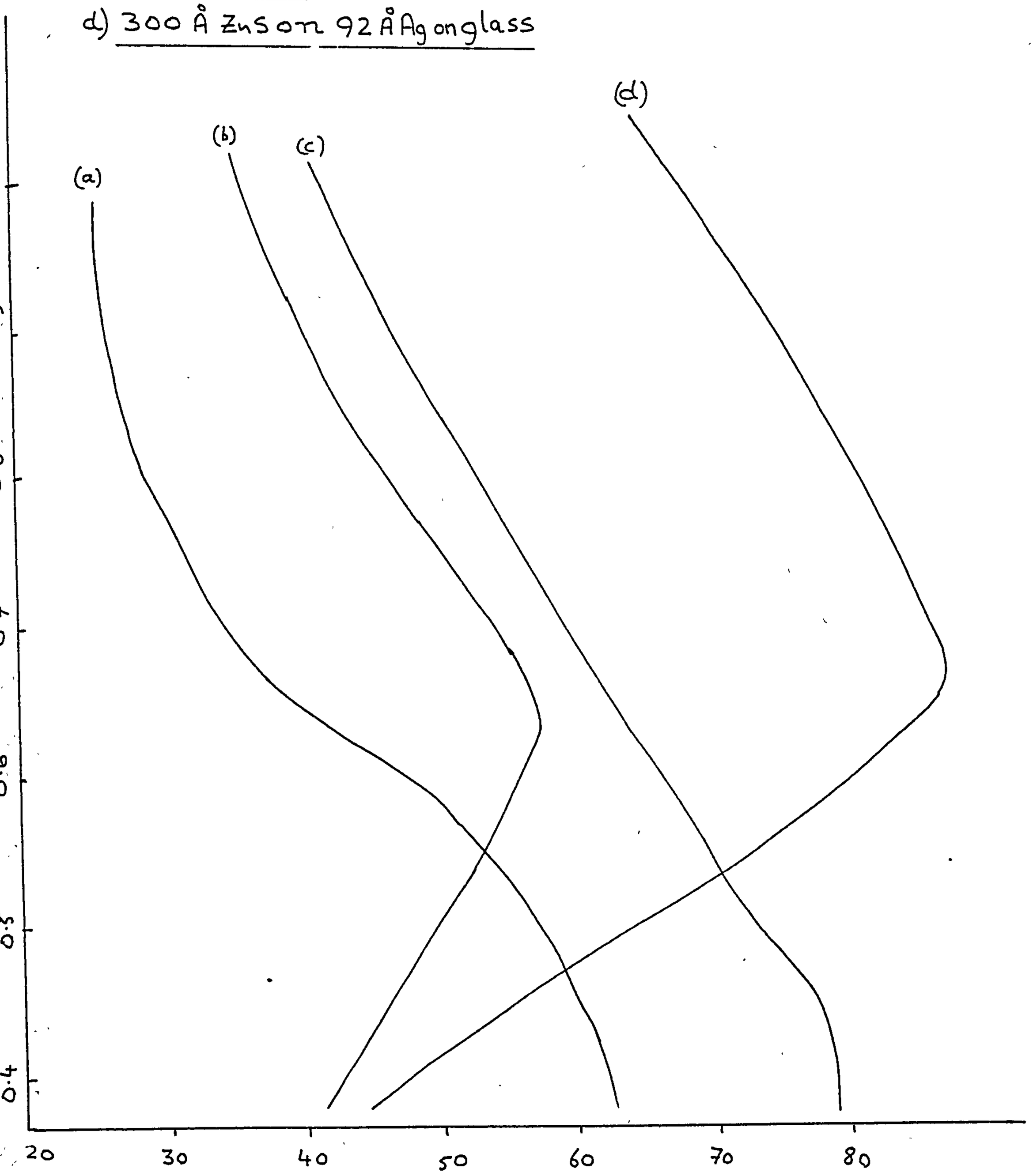

THERMALLY EVAPORATED Ag

ELECTRON GUN EVAPORATED ZnS

FIGURE 6.10 Experimental results

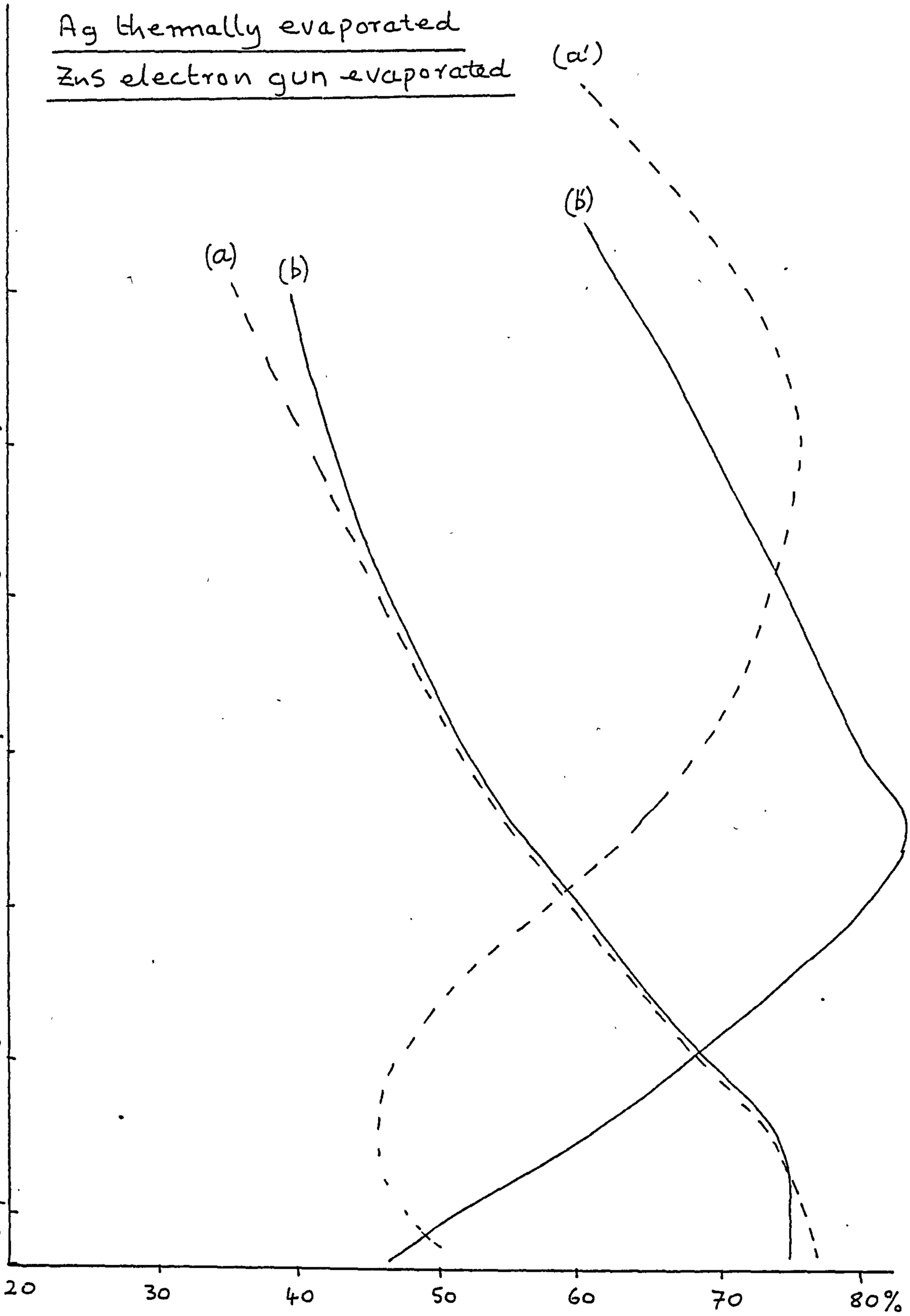

(a) 100 Å Ag on glass; sheet resistance = 9.5 Ω/□

(a') 700 Å ZnS on 100 Å Ag on glass

(b) 103 Å Ag on glass

(b') 340 Å ZnS on 103 Å Ag on glass

Experimental results

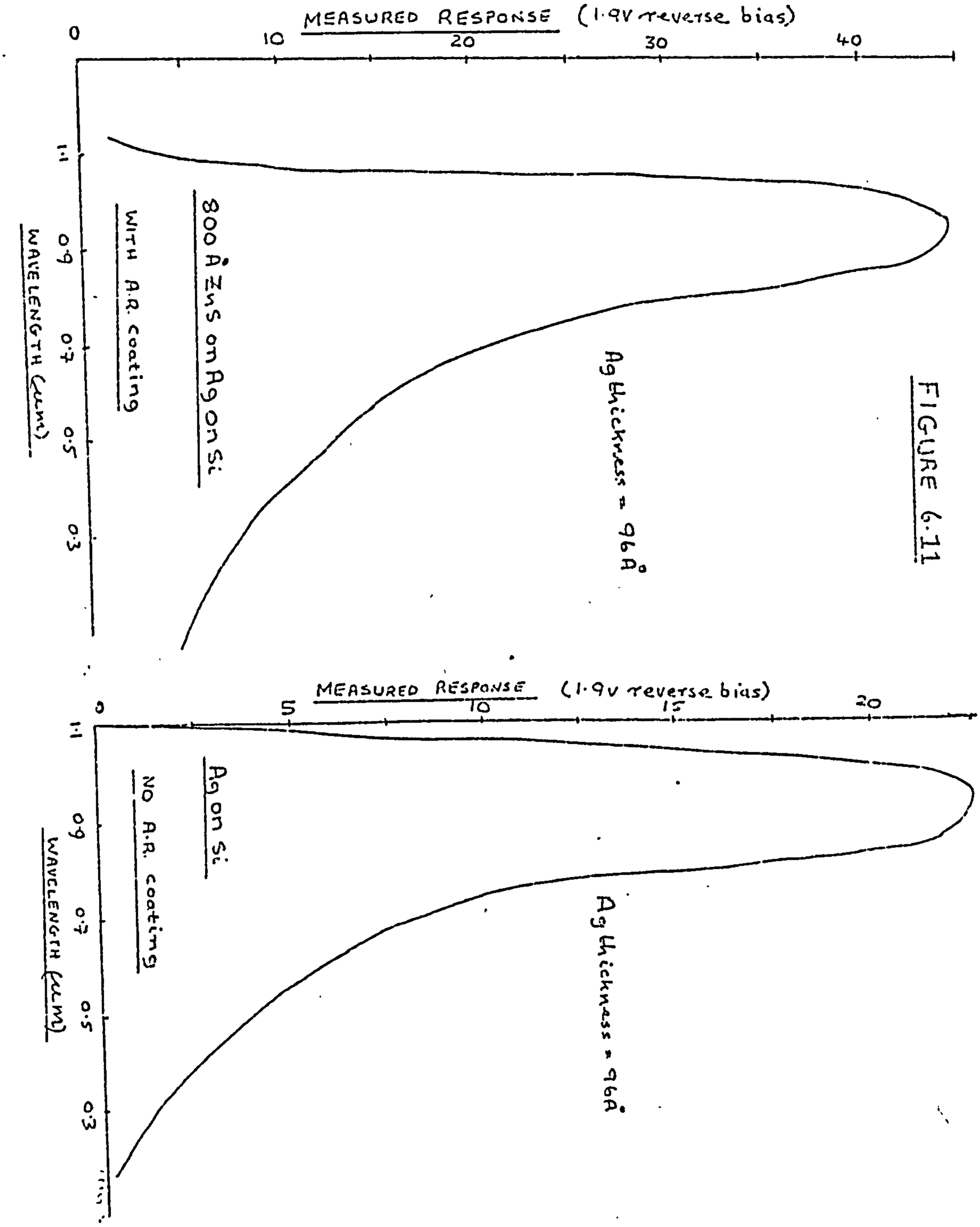

FIGURE 6.11

FIGURE 6.12 Experimental results

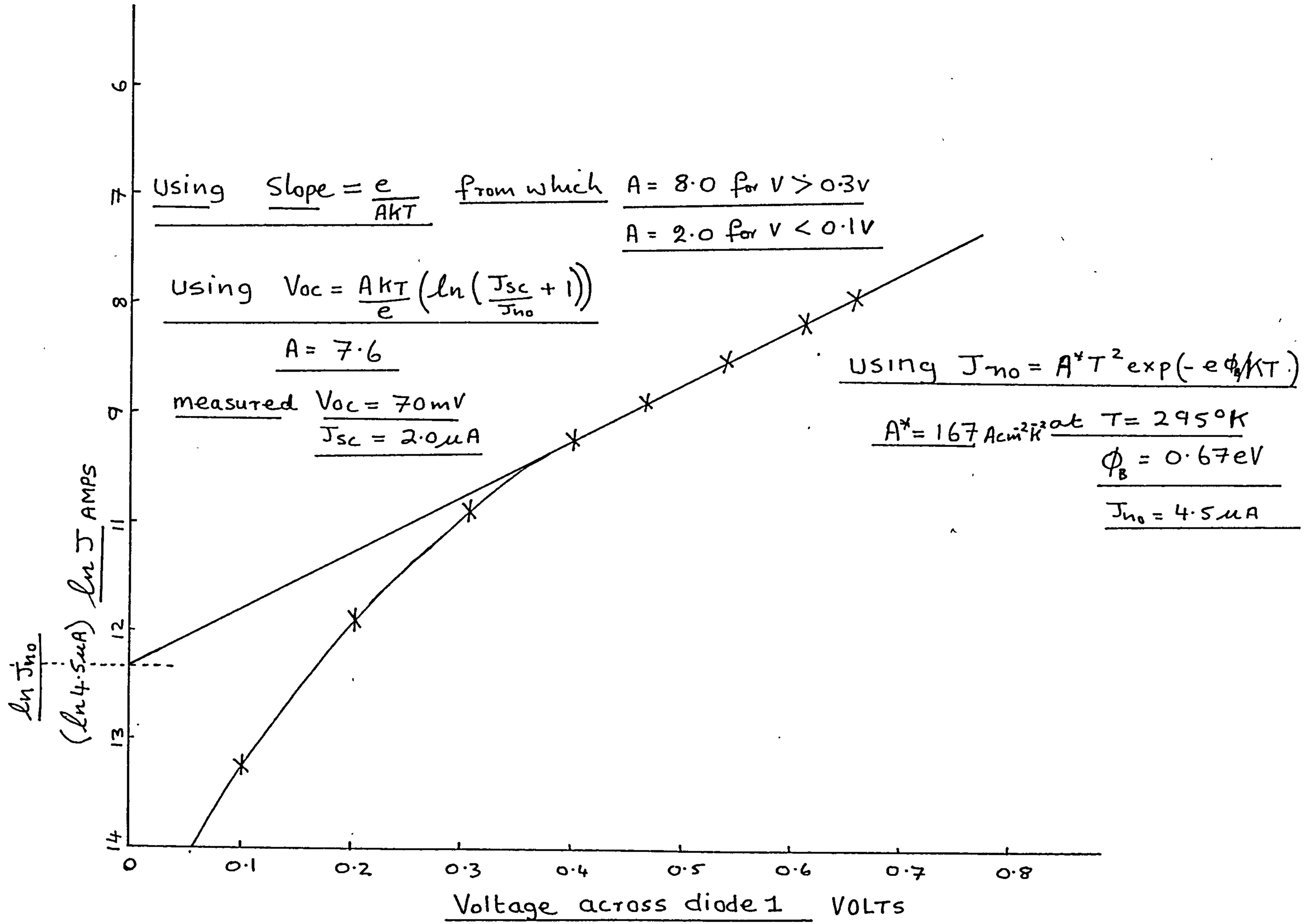

FIGURE 6.13 Experimental results

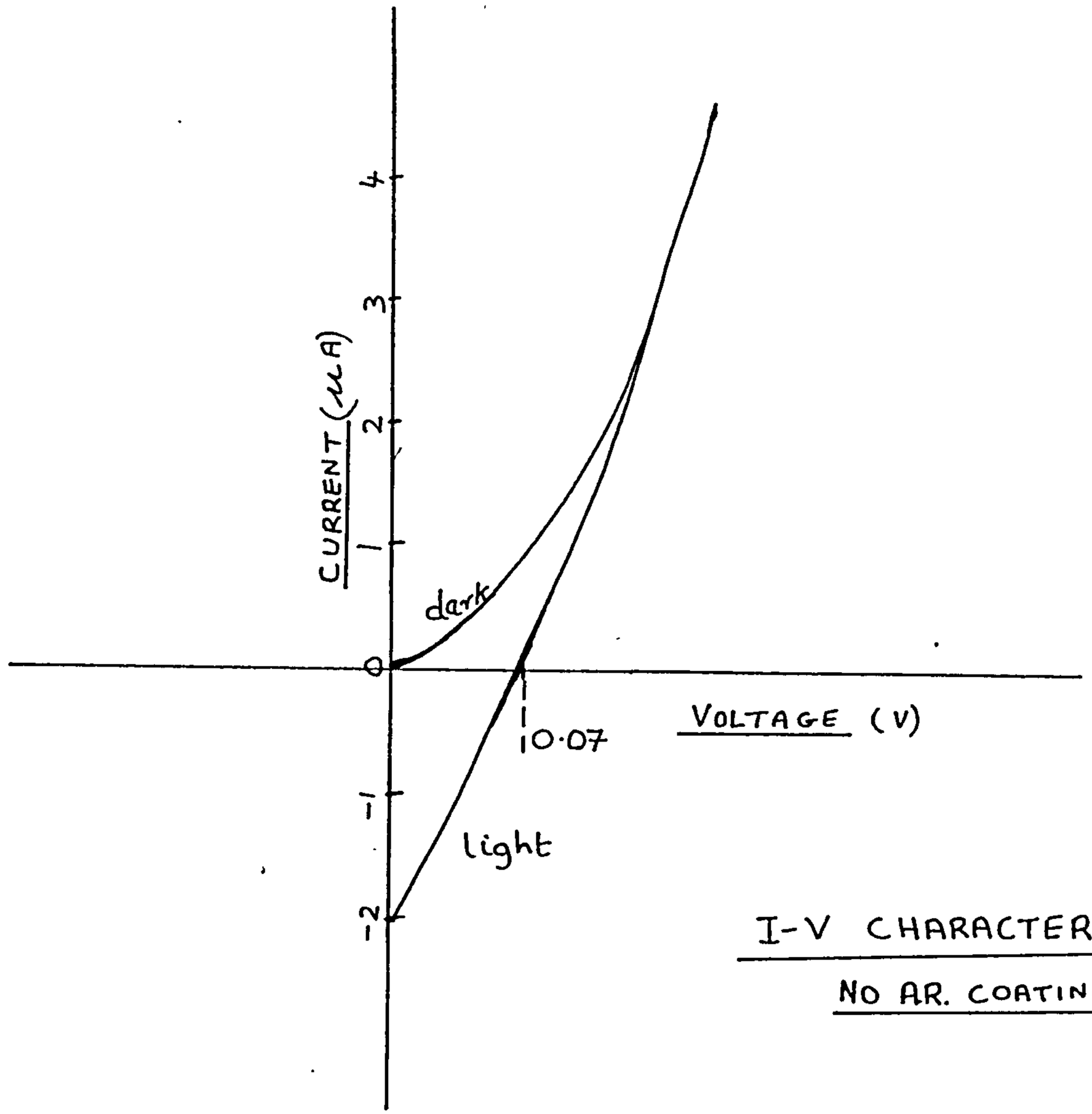

I-V CHARACTERISTIC OF DIODE 1

NO AR. COATING

Experimental results

FIGURE 6.14

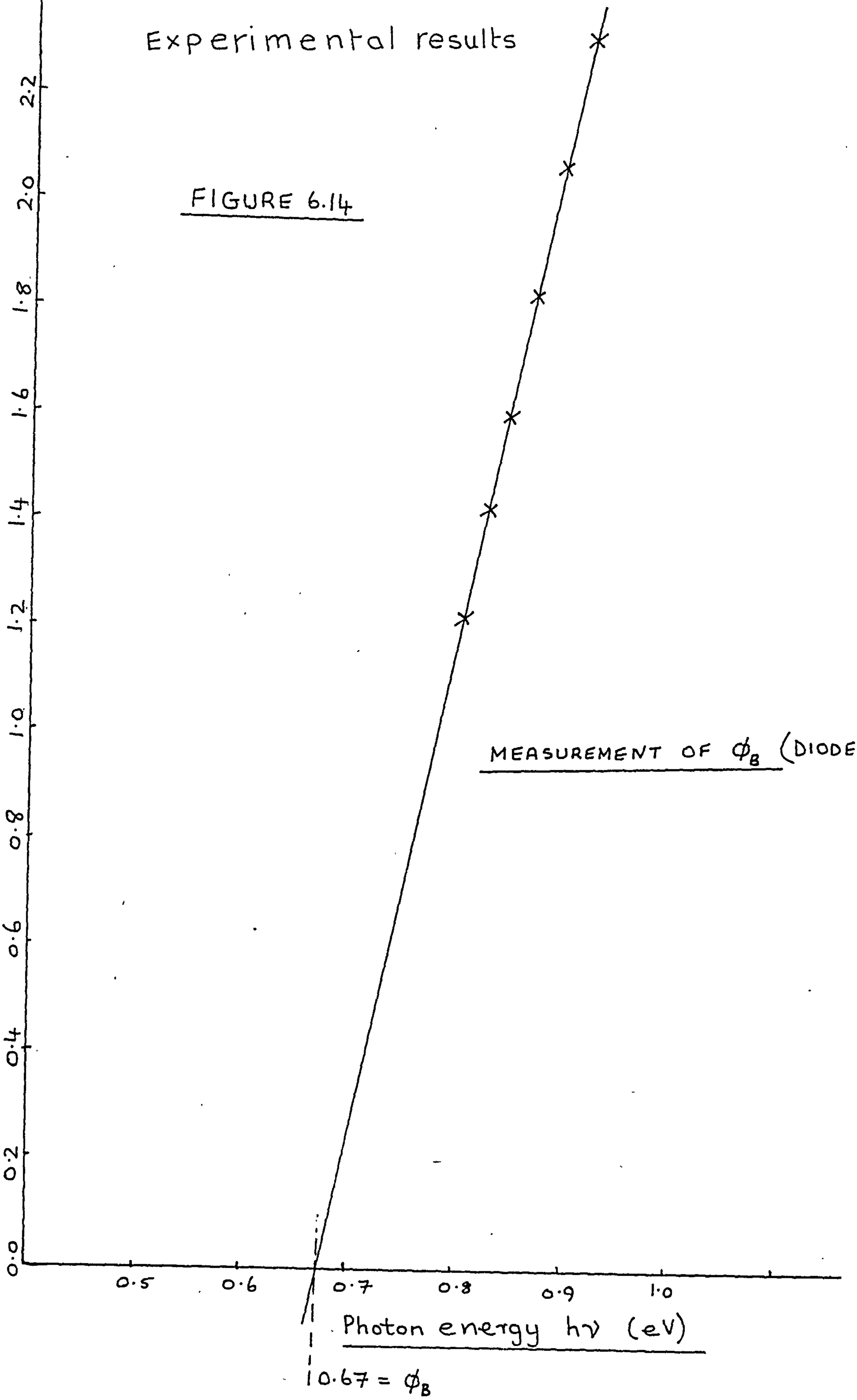

MEASUREMENT OF ϕ_B (DIODE 1)

FIGURE 6.15

Experimental results

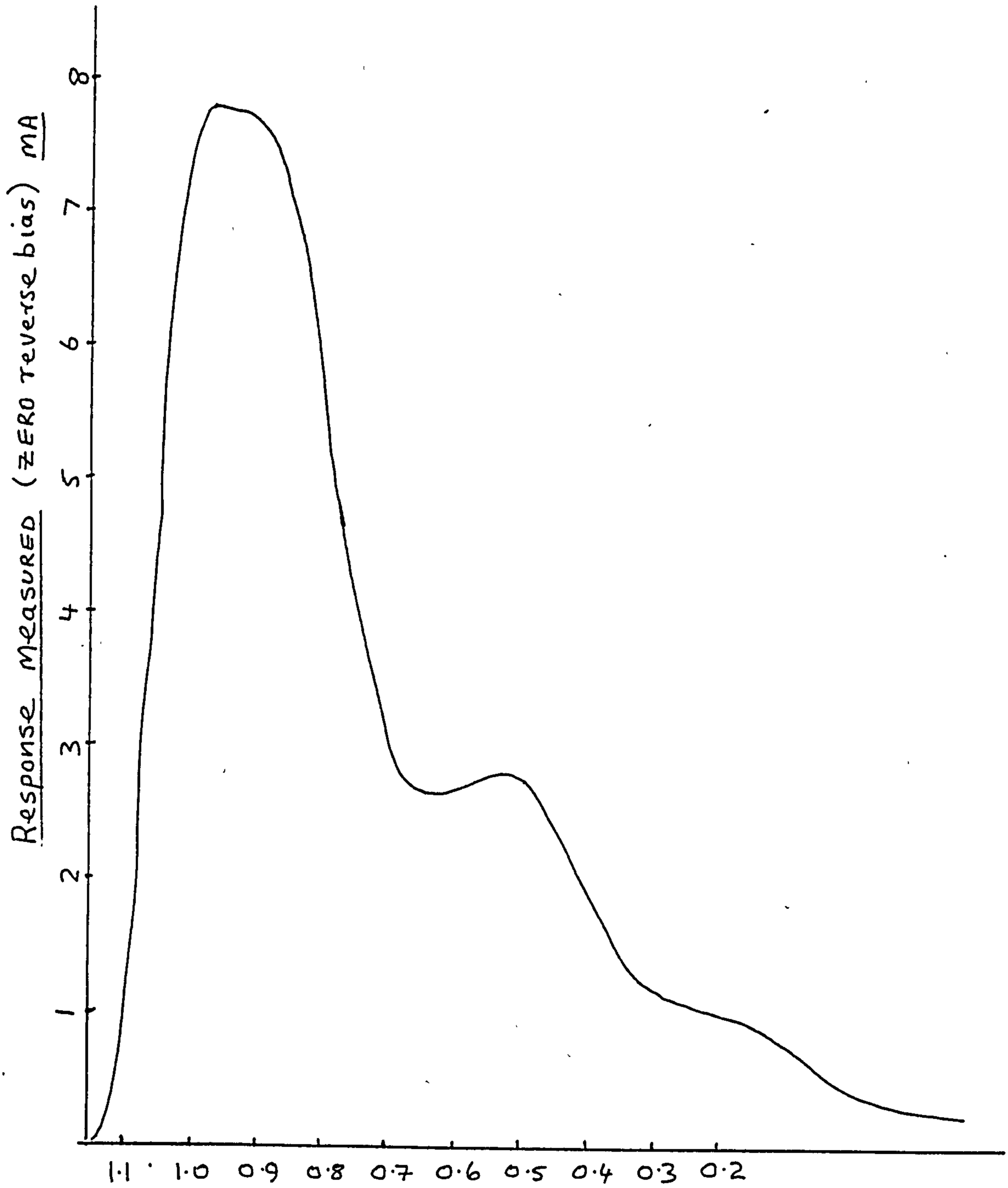

DIODE 2

FIGURE 6.16

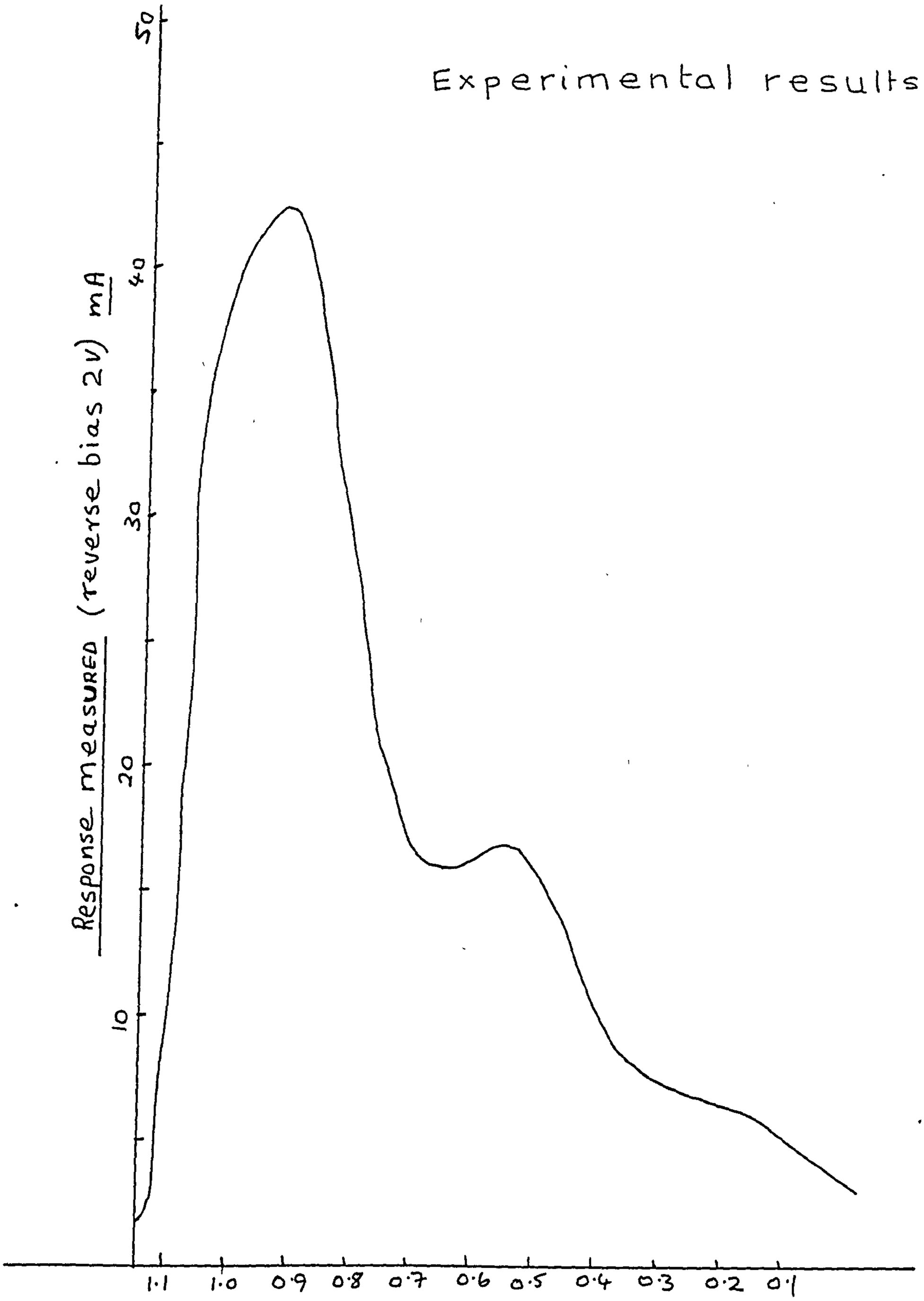

DIODE 2

FIGURE 6.17

Experimental results

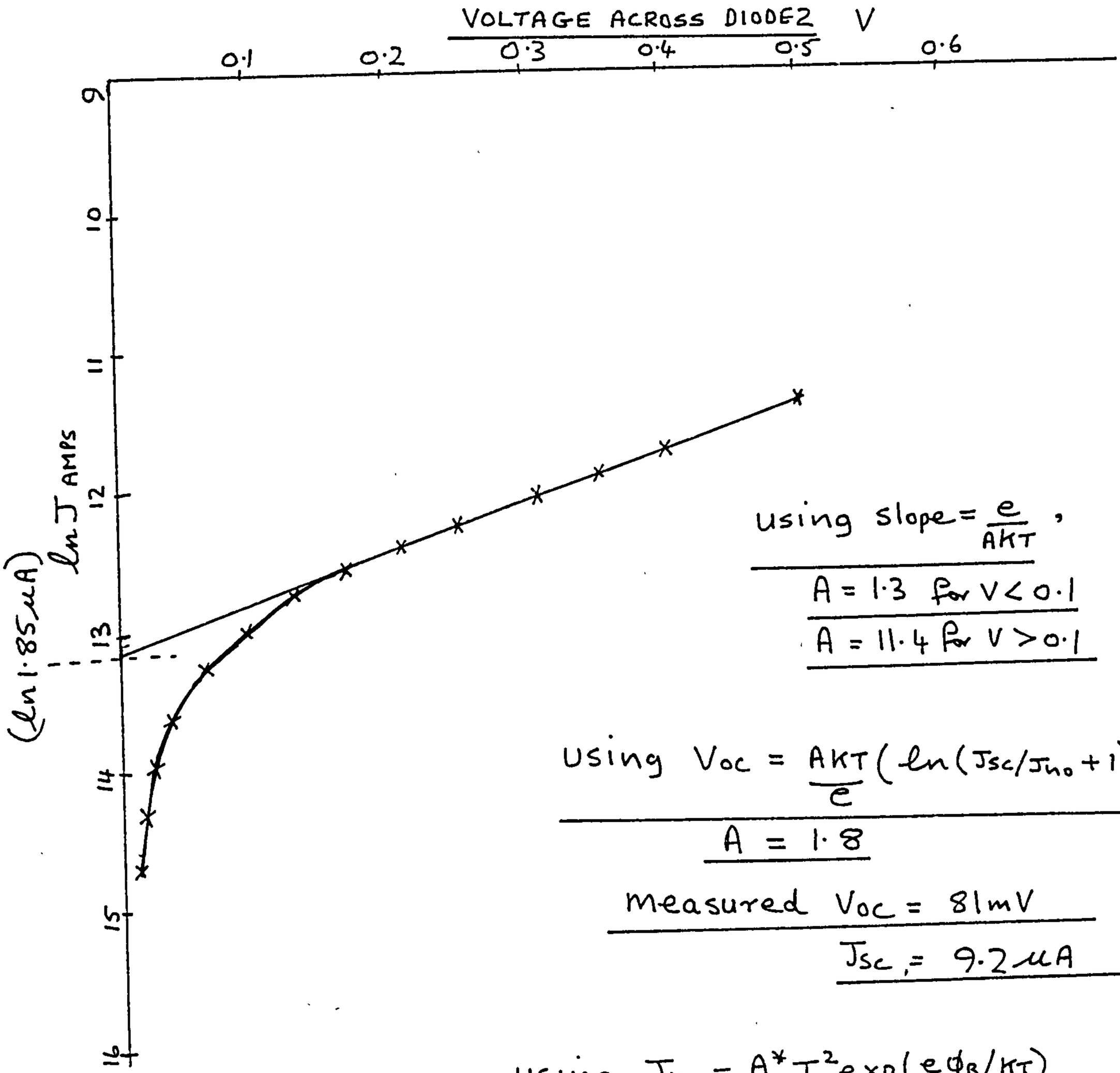

Using slope = $\frac{e}{AKT}$,

A = 1·3 for V < 0·1

A = 11·4 for V > 0·1

Using $V_{OC} = \frac{AKT}{e}\left(\ln(J_{SC}/J_{no} + 1)\right)$

A = 1·8

measured V_{OC} = 81mV

J_{SC} = 9·2 μA

Using $J_{no} = A^* T^2 \exp(e\phi_B/KT)$

A^* = 5350 A cm^{-2} K^{-2} at T = 295°K

ϕ_B = 0·78eV

FIGURE 6·18

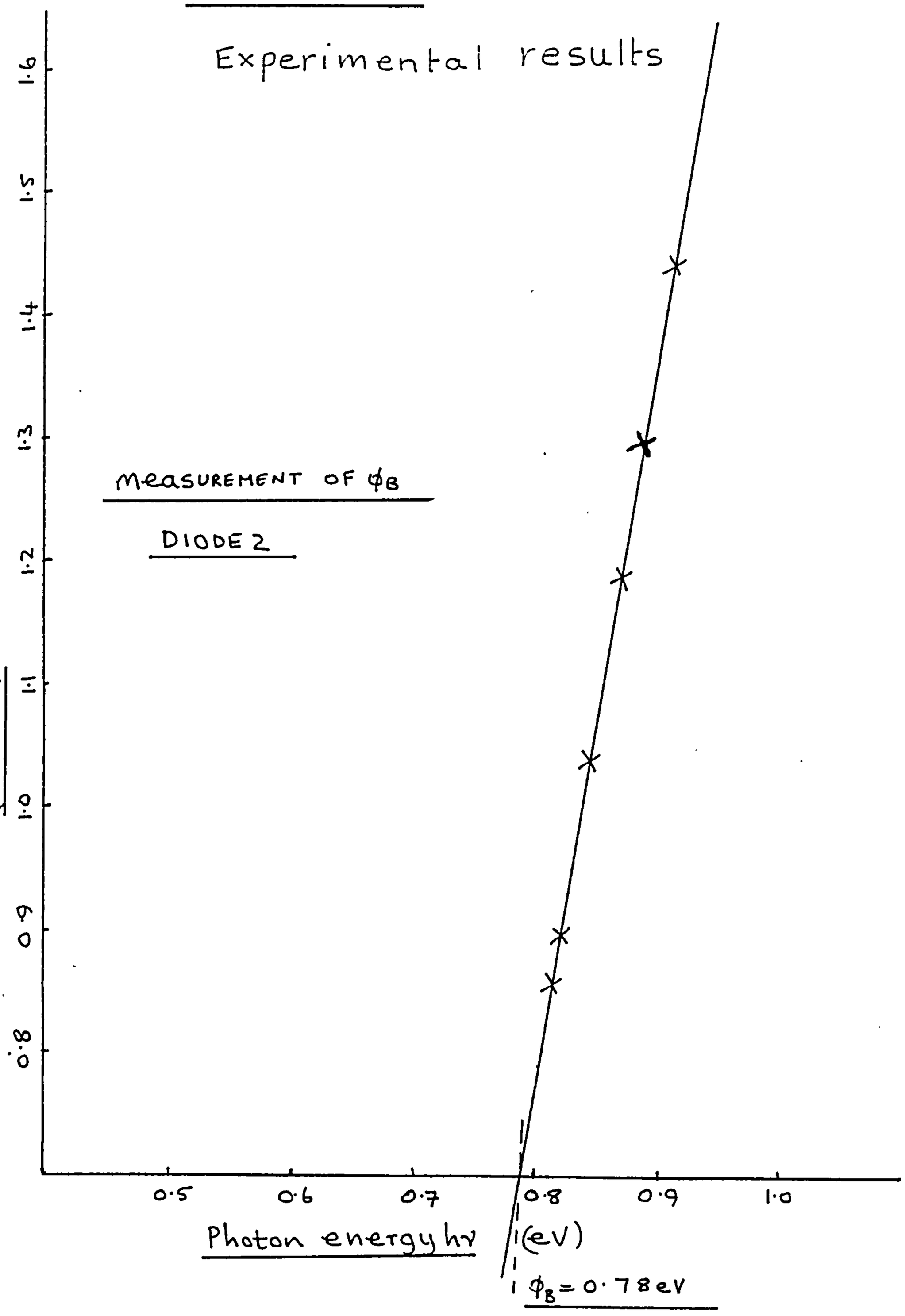
Experimental results
measurement of ϕ_B
Diode 2
$\left(\frac{\text{Response}}{}\right)^{\frac{1}{2}}$
1·9
1·5
1·4
1·3
1·2
1·1
1·0
0·9
0·8
0·5
0·6
0·7
0·8
0·9
1·0
Photon energy hν (eV)
$\phi_B = 0·78$ eV

FIGURE 6·19

Experimental results

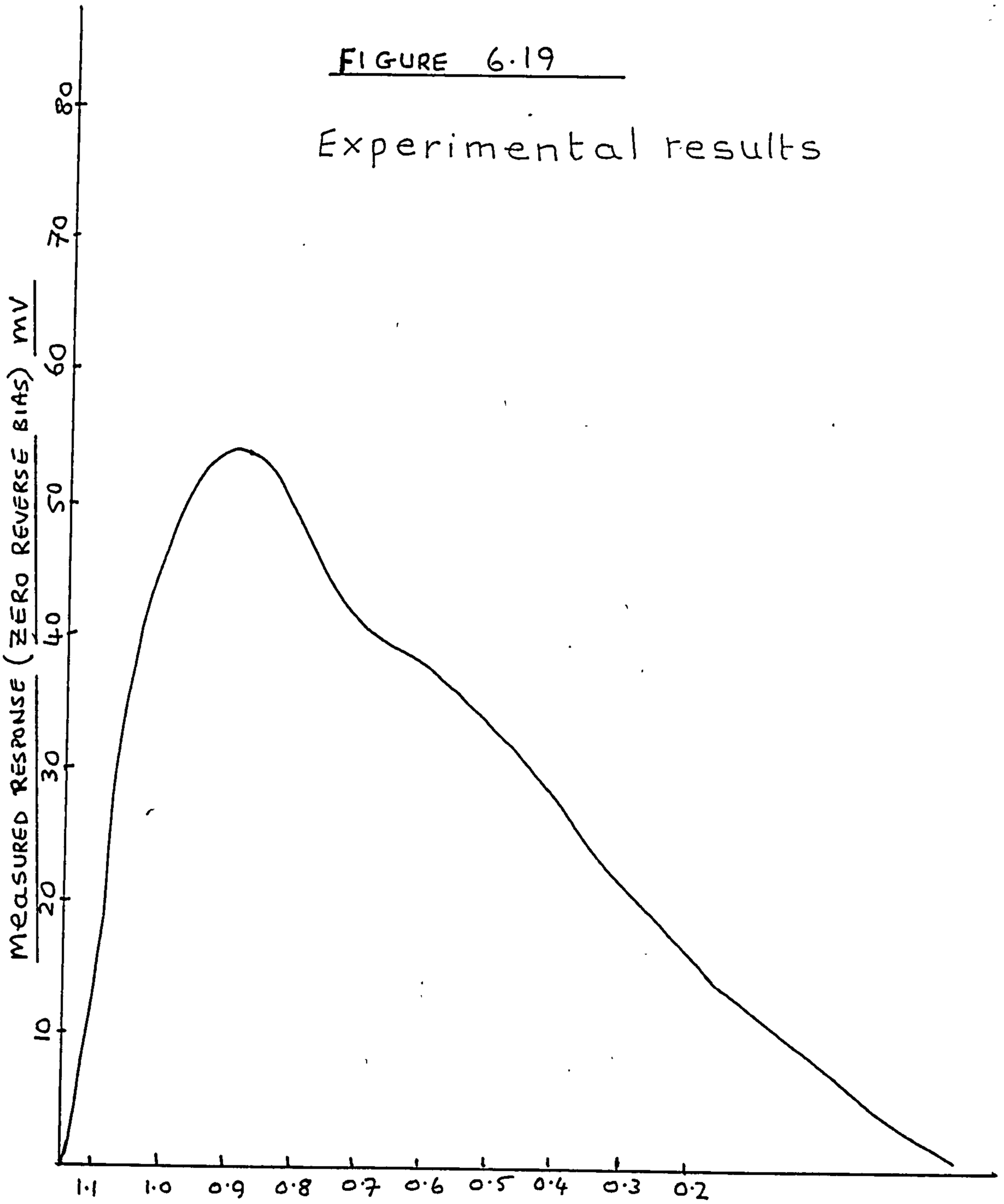

ION PLATED DIODE

FIGURE 6.20

Experimental results

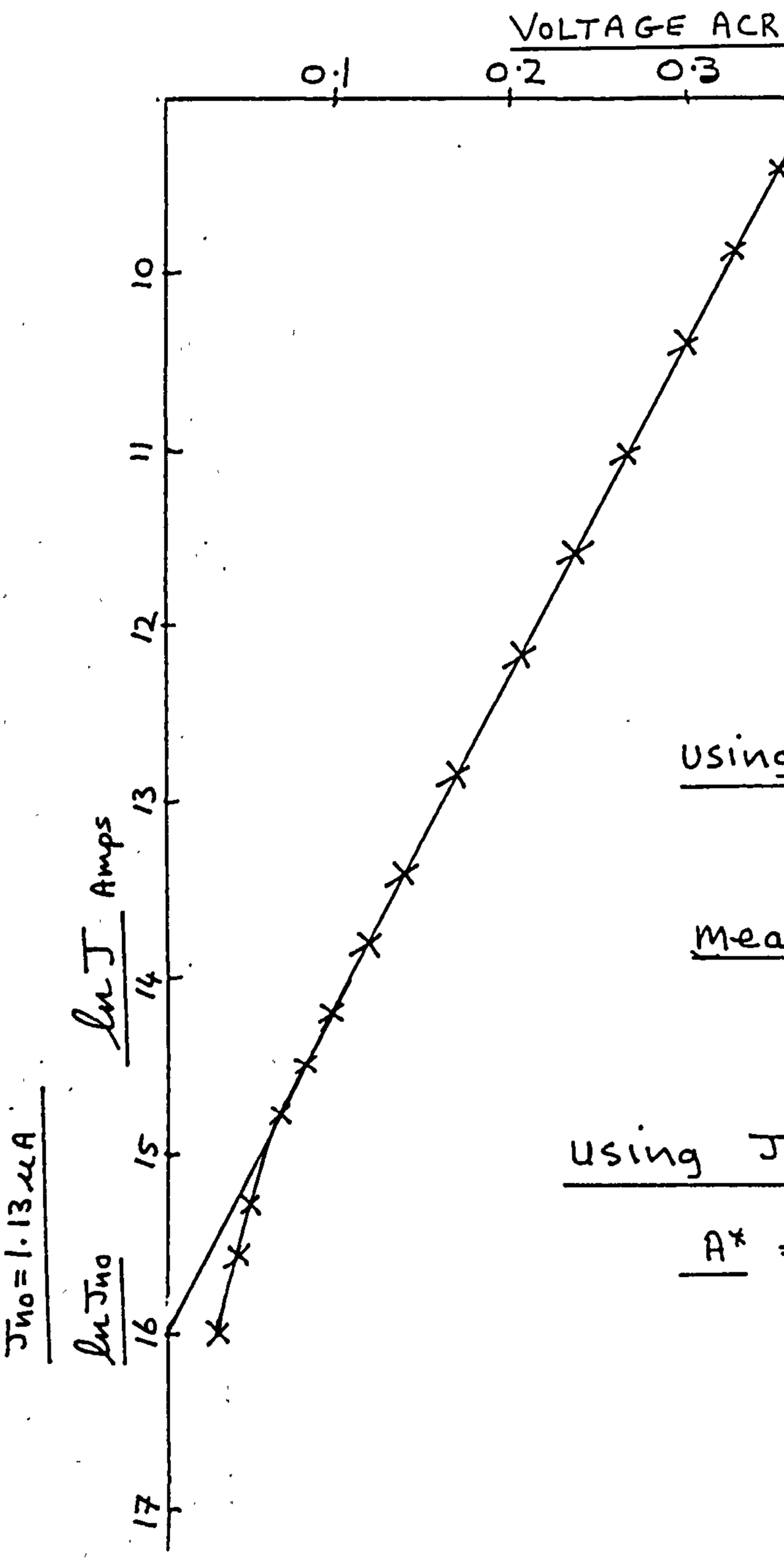

Using slope = $\frac{e}{AkT}$,

$A = 2.1$ for $V > 0.1V$

$A = 1.2$ for $V < 0.1V$

Using $V_{oc} = \frac{AkT}{e}\left(\ln\left(J_{sc}/J_{no}+1\right)\right)$

$A = 1.7$

measured $V_{oc} = 0.35V$

$J_{sc} = 392\mu A$

Using $J_{no} = A^* T^2 \exp(e\phi_B/kT)$

$A^* = 472\ A\,cm^{-2}K^{-2}$ at $T = 295°K$

$\phi_B = 0.79eV$

FIGURE 6·21

Experimental results

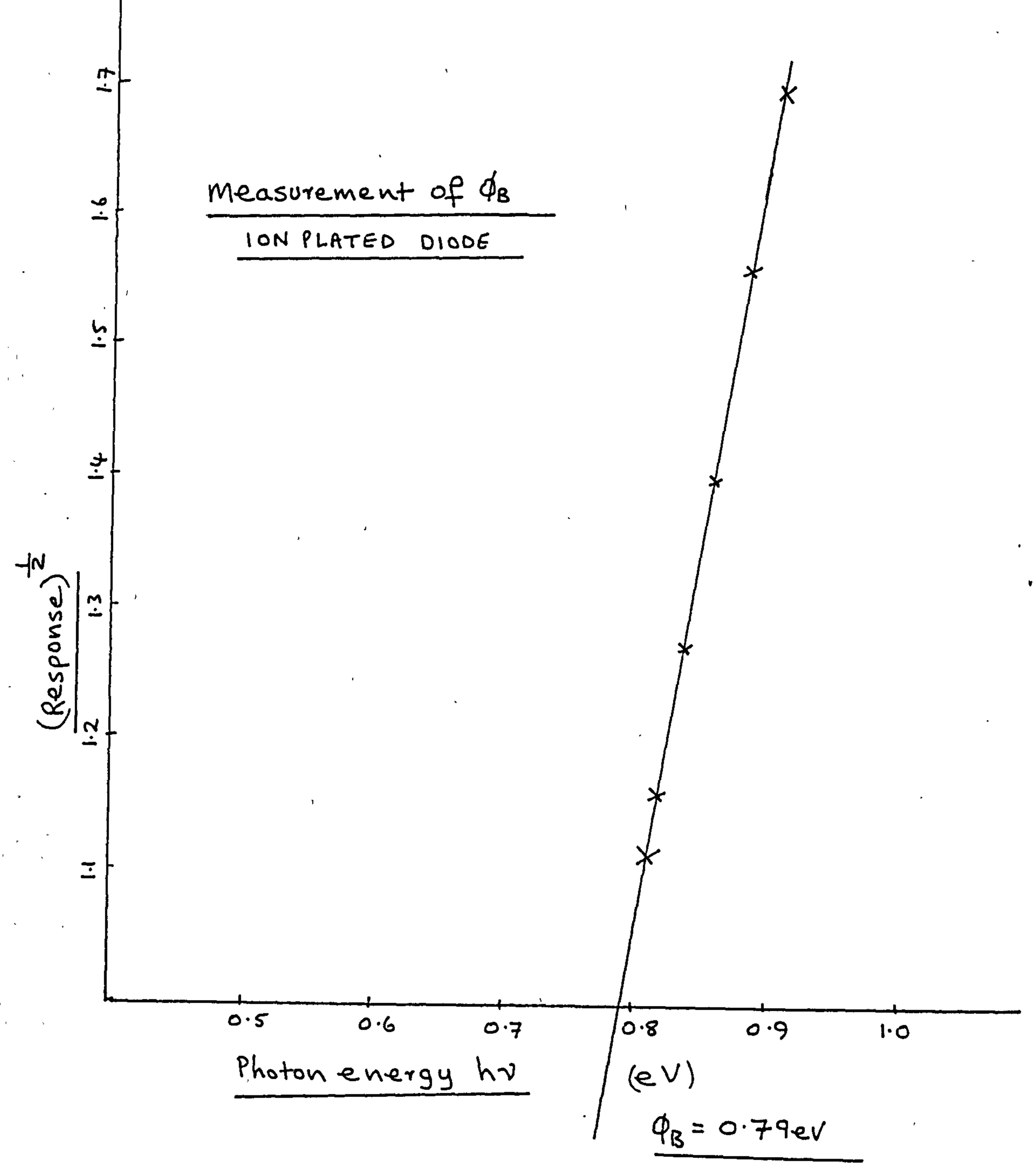

FIGURE 6.22

Experimental results

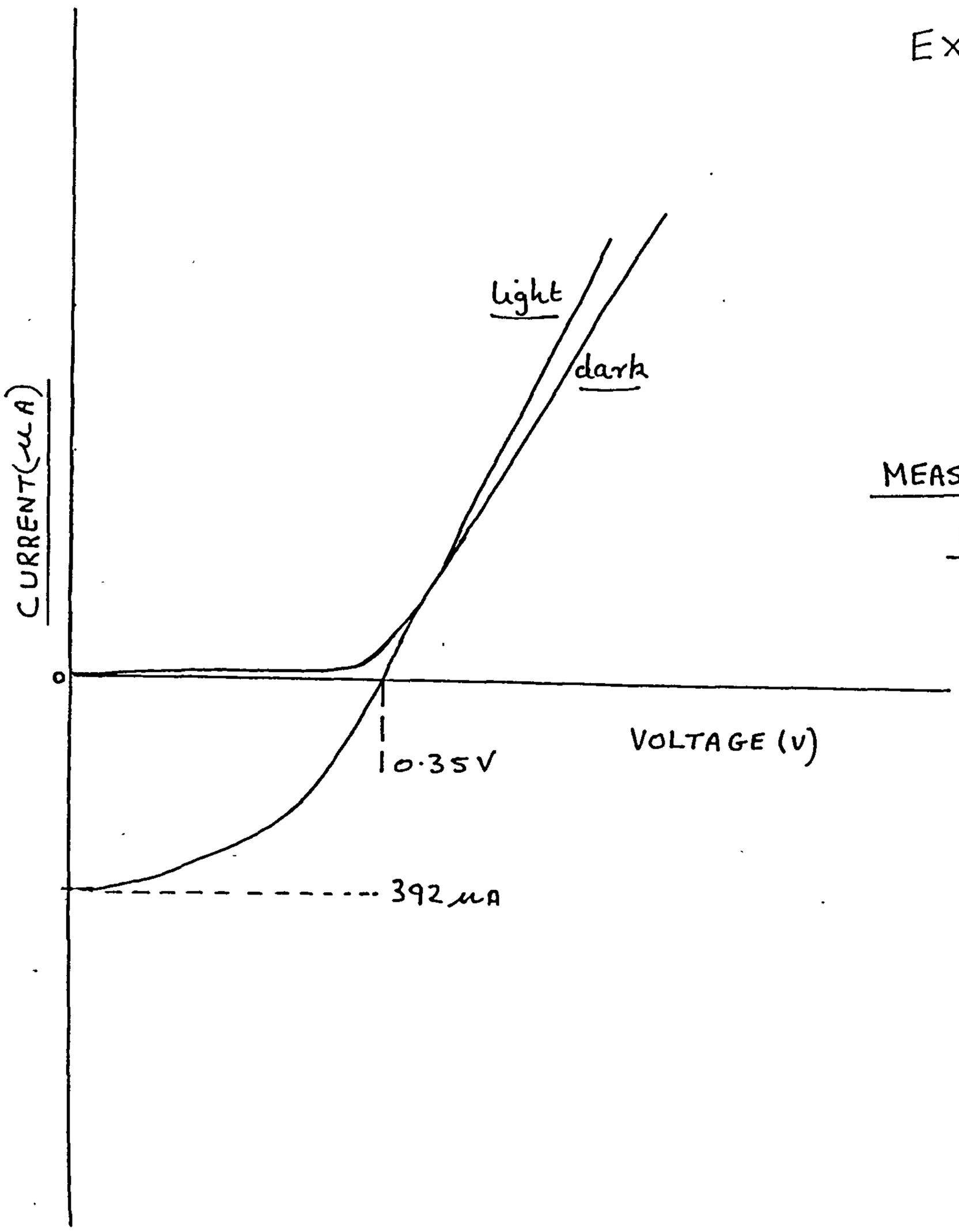

MEASURED I-V CHARACTERISTICS

FOR THE ION-PLATED DIODE

FIGURE 6.23 Experimental results

Experimental curve of ion plated Ag onto glass of thickness equal to that of the Ag layer on the ion plated diode

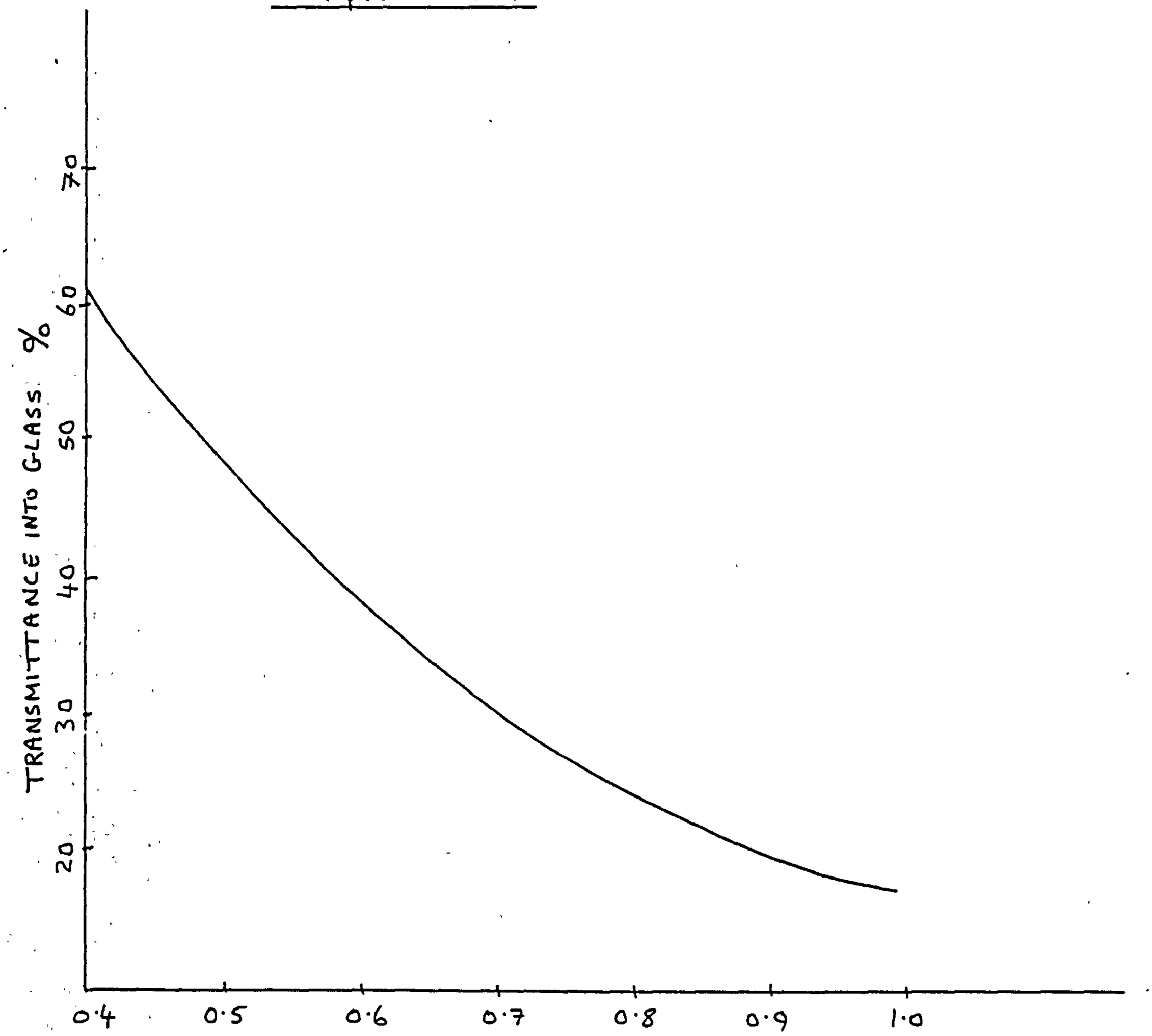

FIGURE 6.24

WAVELENGTH = 0·62 μm

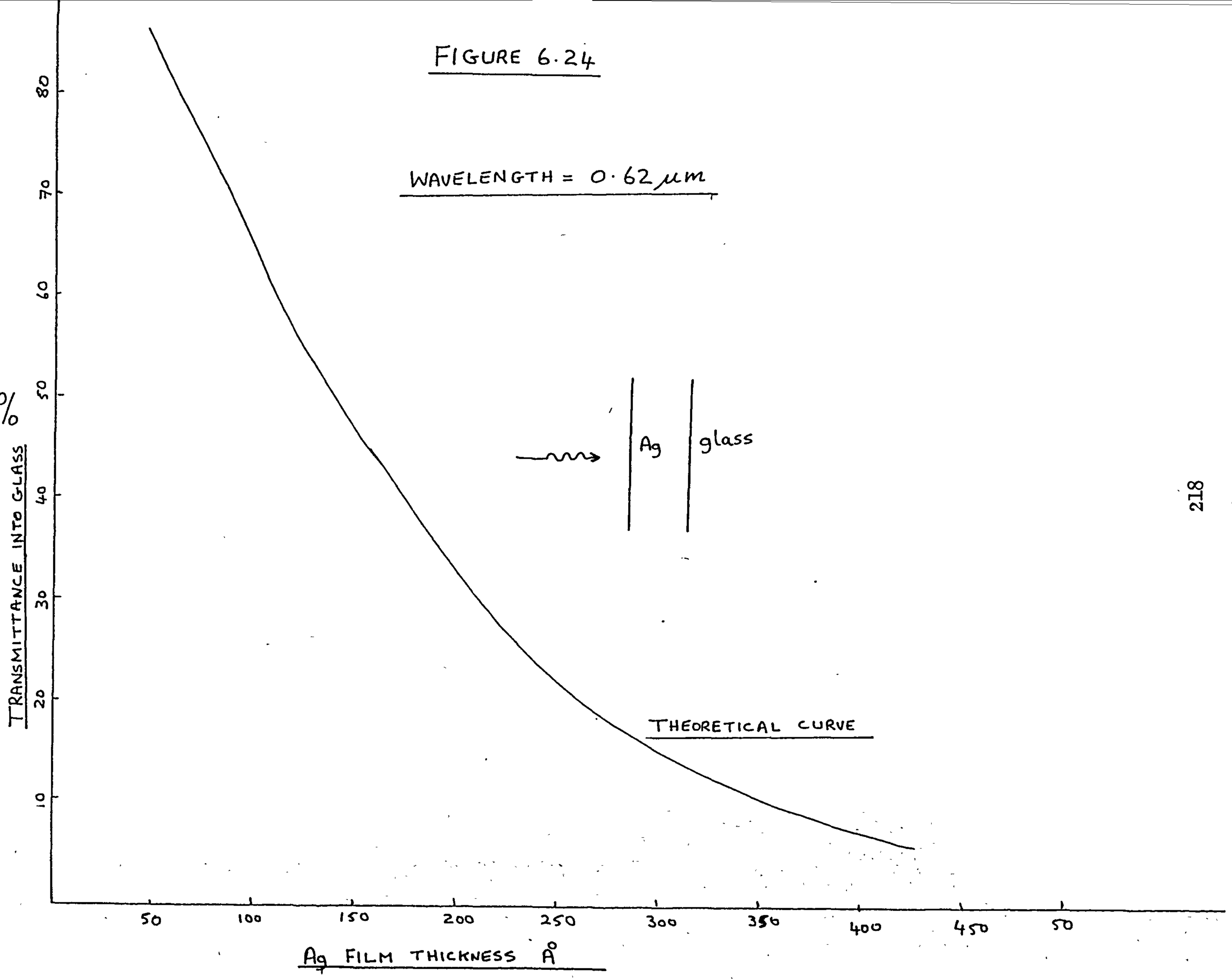

FIGURE 6.25

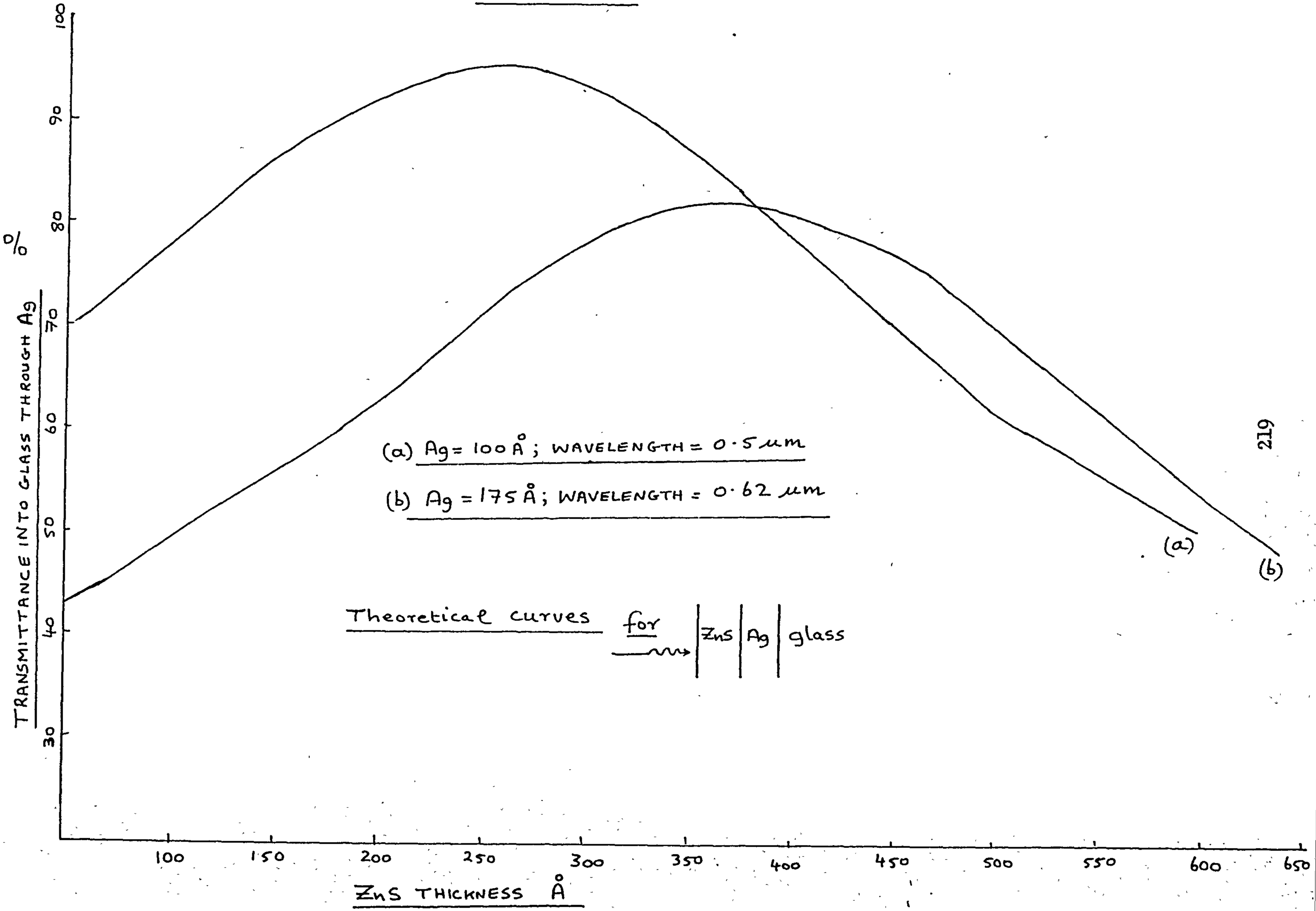
%
TRANSMITTANCE INTO GLASS THROUGH Ag
100
90
80
70
60
50
40
30
100
150
200
250
300
350
400
450
500
550
600
650
ZnS THICKNESS Å
(a) Ag = 100 Å ; WAVELENGTH = 0·5 μm
(b) Ag = 175 Å ; WAVELENGTH = 0·62 μm
(a)
(b)
Theoretical curves for ~~> | ZnS | Ag | glass

FIGURE 6.26

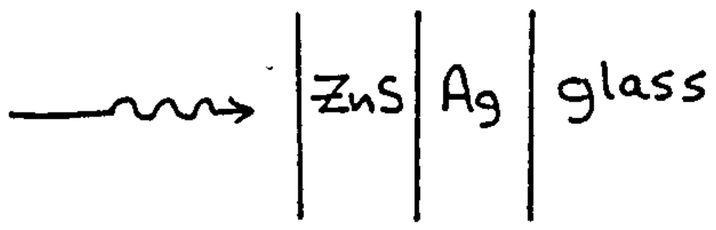

THEORETICAL CURVES

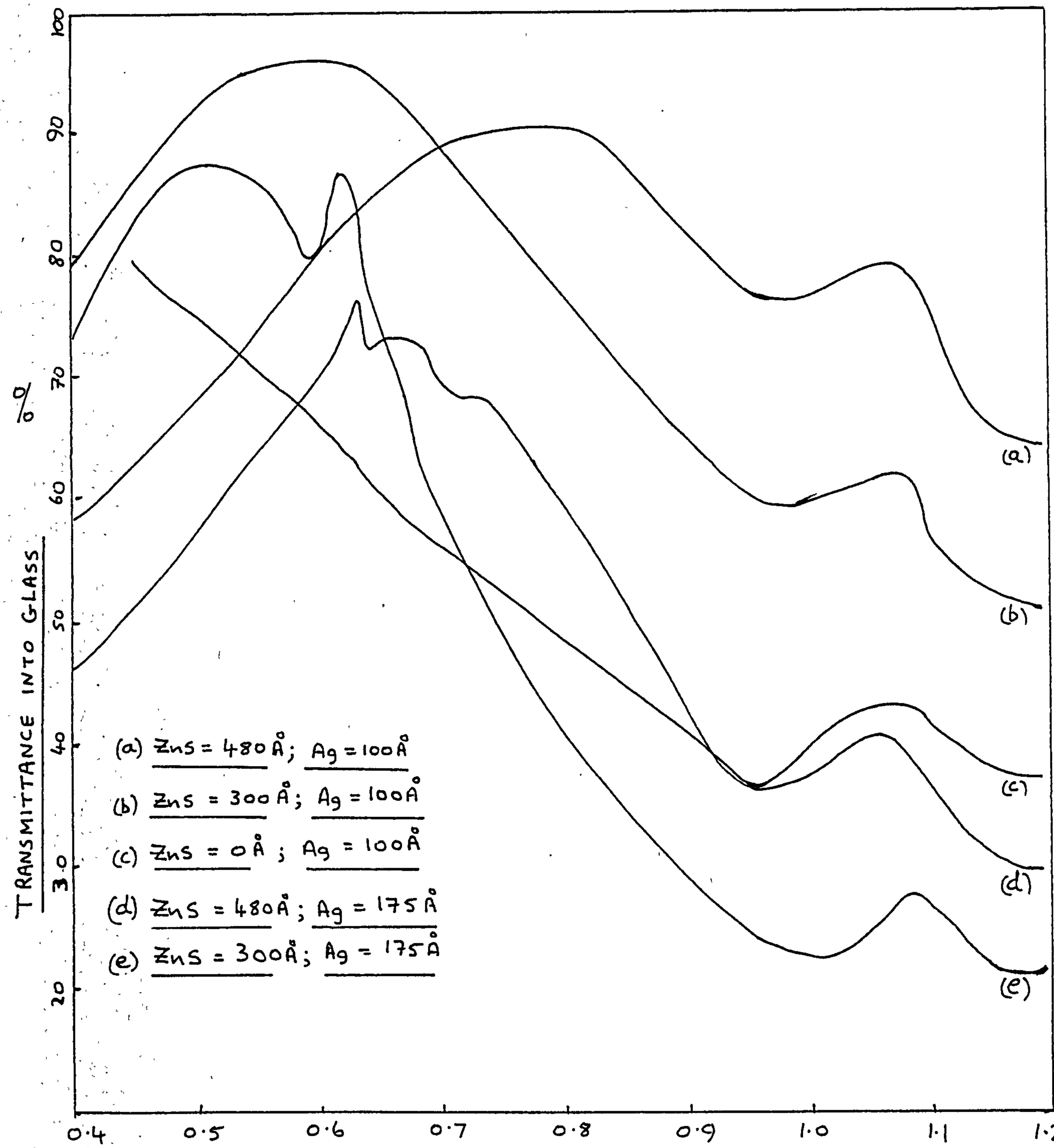

(a) ZnS = 480 Å; Ag = 100 Å

(b) ZnS = 300 Å; Ag = 100 Å

(c) ZnS = 0 Å ; Ag = 100 Å

(d) ZnS = 480 Å ; Ag = 175 Å

(e) ZnS = 300 Å; Ag = 175 Å

FIGURE 6.27

WAVELENGTH = 0·62 μm

TRANSMITTANCE INTO Si

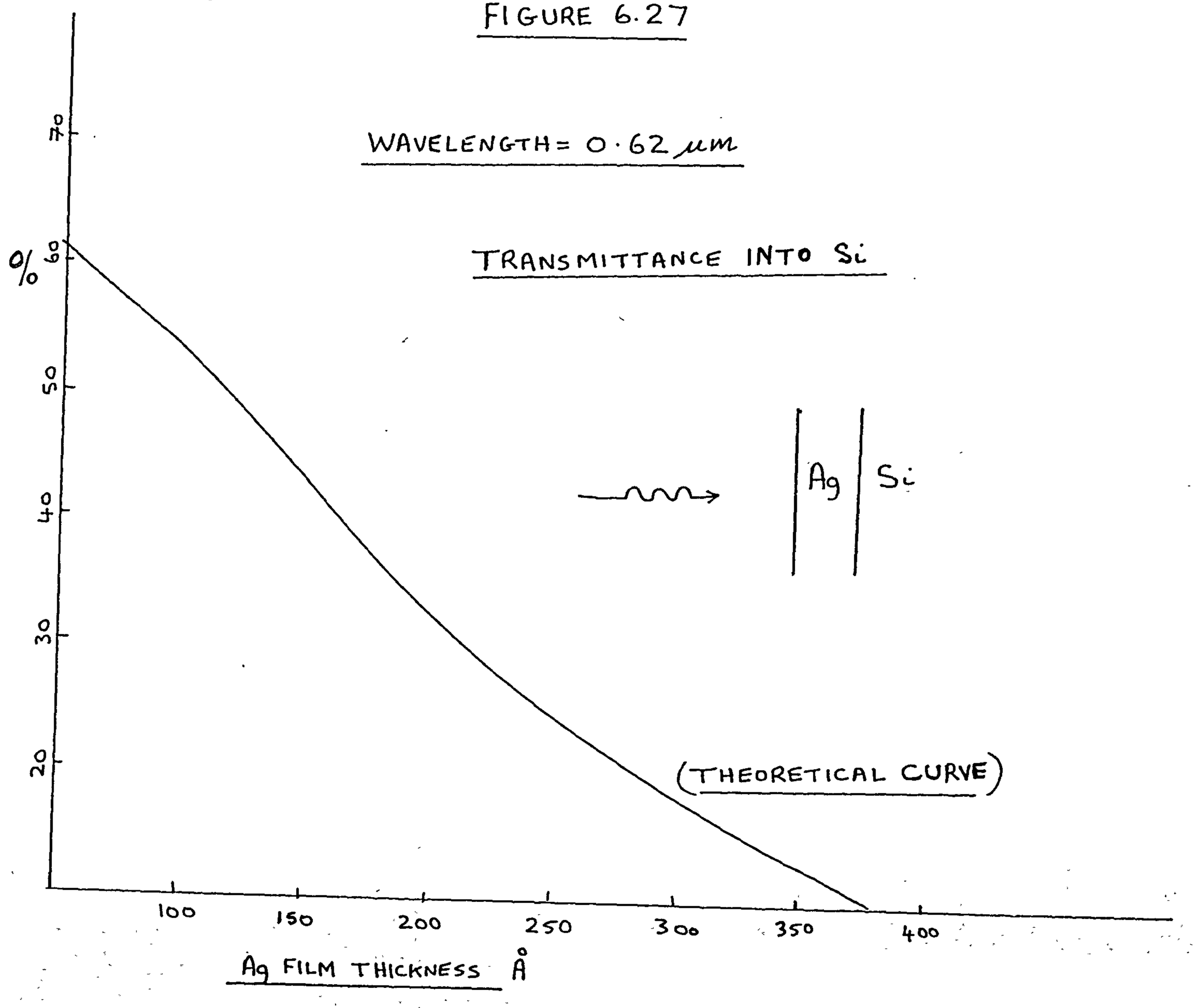

FIGURE 6.28 Theoretical results

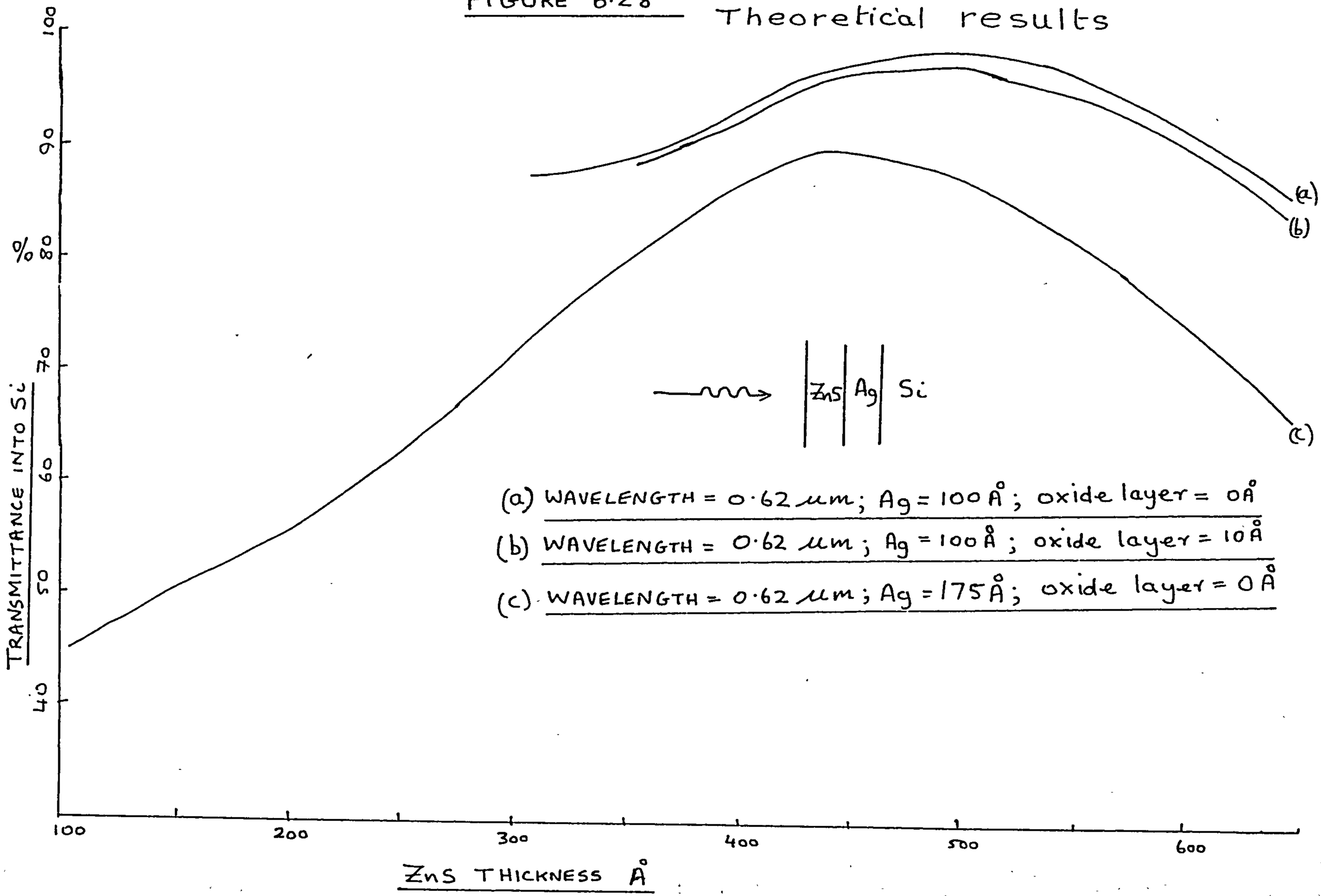

(a) WAVELENGTH = 0·62 μm; Ag = 100 Å; oxide layer = 0Å

(b) WAVELENGTH = 0·62 μm; Ag = 100 Å; oxide layer = 10Å

(c) WAVELENGTH = 0·62 μm; Ag = 175 Å; oxide layer = 0 Å

FIGURE 6.29

Theoretical results

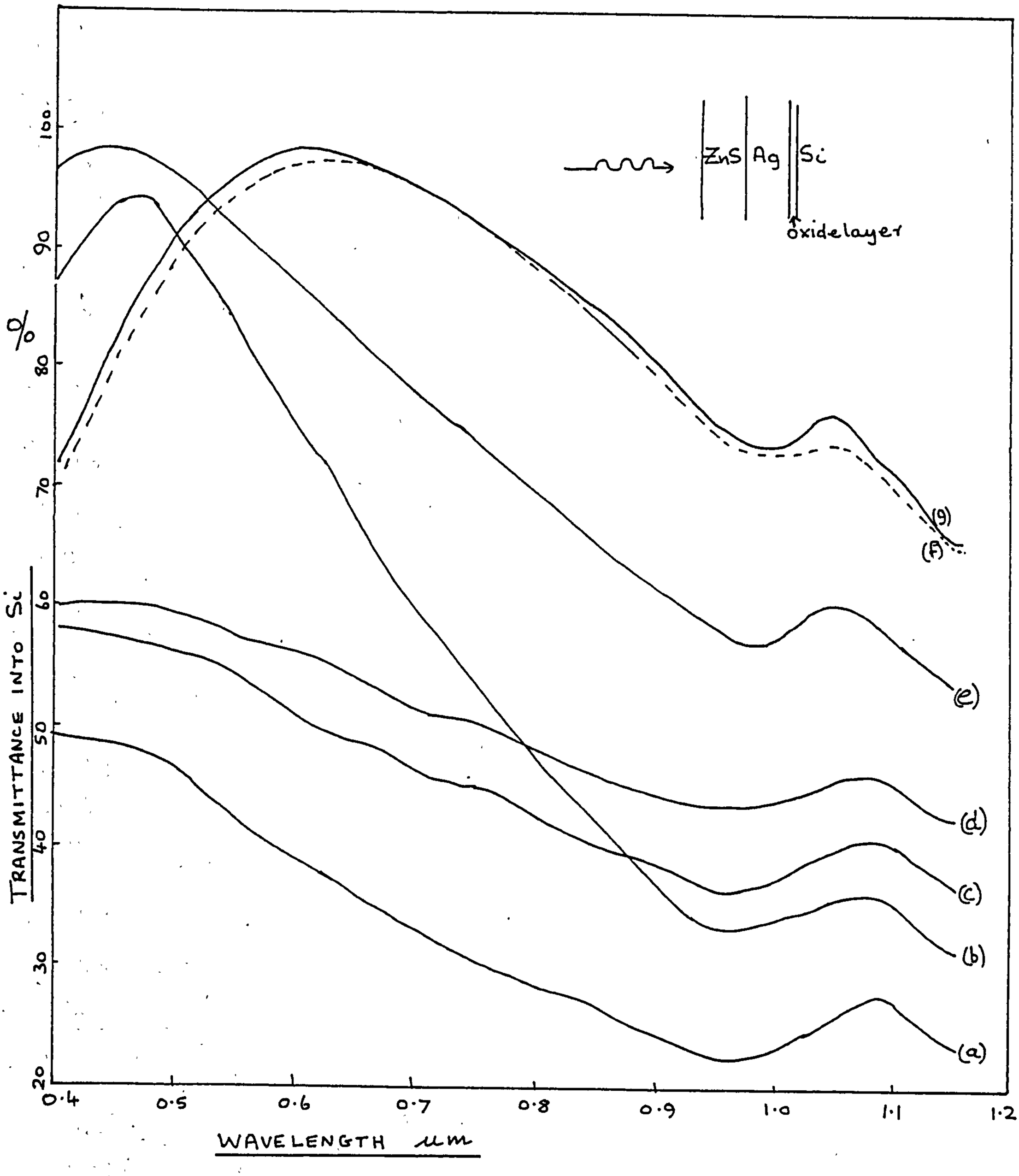

(a) Ag thickness = 175 Å ; No ZnS layer ; No oxide layer

(b) Ag thickness = 175 Å ; ZnS = 300 Å ; No oxide layer

(c) Ag thickness = 120 Å ; No ZnS layer ; No oxide layer

(d) Ag thickness = 100 Å ; No ZnS layer ; No oxide layer

(e) Ag thickness = 100 Å ; ZnS = 300 Å ; oxide layer = 20 Å (SiO_2)

(f) Ag thickness = 100 Å ; ZnS = 480 Å ; oxide layer = 20 Å (SiO_2)

(g) Ag thickness = 100 Å ; ZnS = 480 Å ; No oxide layer

FIGURE 6.30

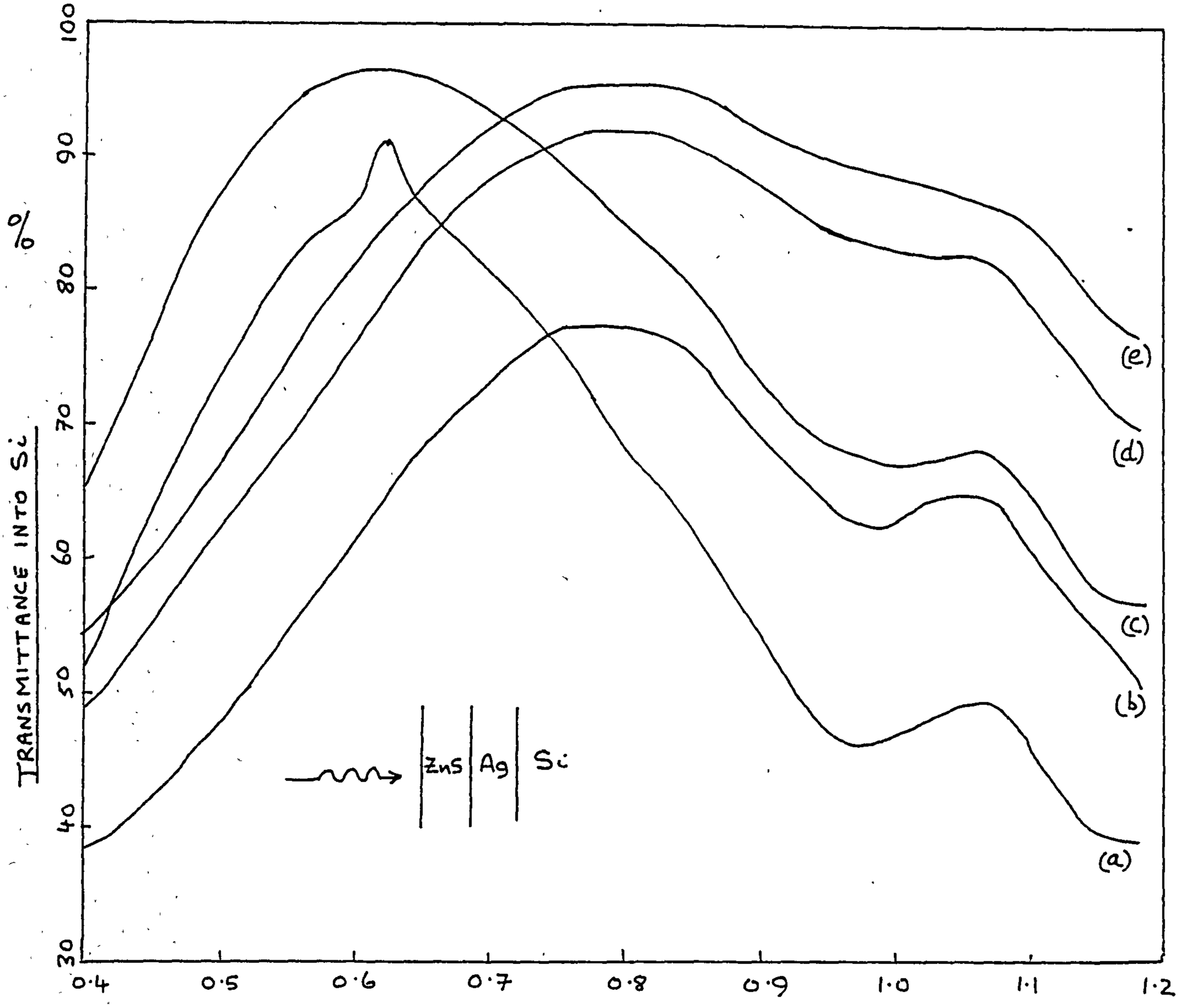

(a) Ag = 175 Å ; ZnS = 480 Å

(b) Ag = 175 Å ; ZnS = 650 Å

(c) Ag = 120 Å ; ZnS = 480 Å

(d) Ag = 120 Å ; ZnS = 650 Å

(e) Ag = 100 Å ; ZnS = 650 Å

FIGURE 6·31

Theoretical results

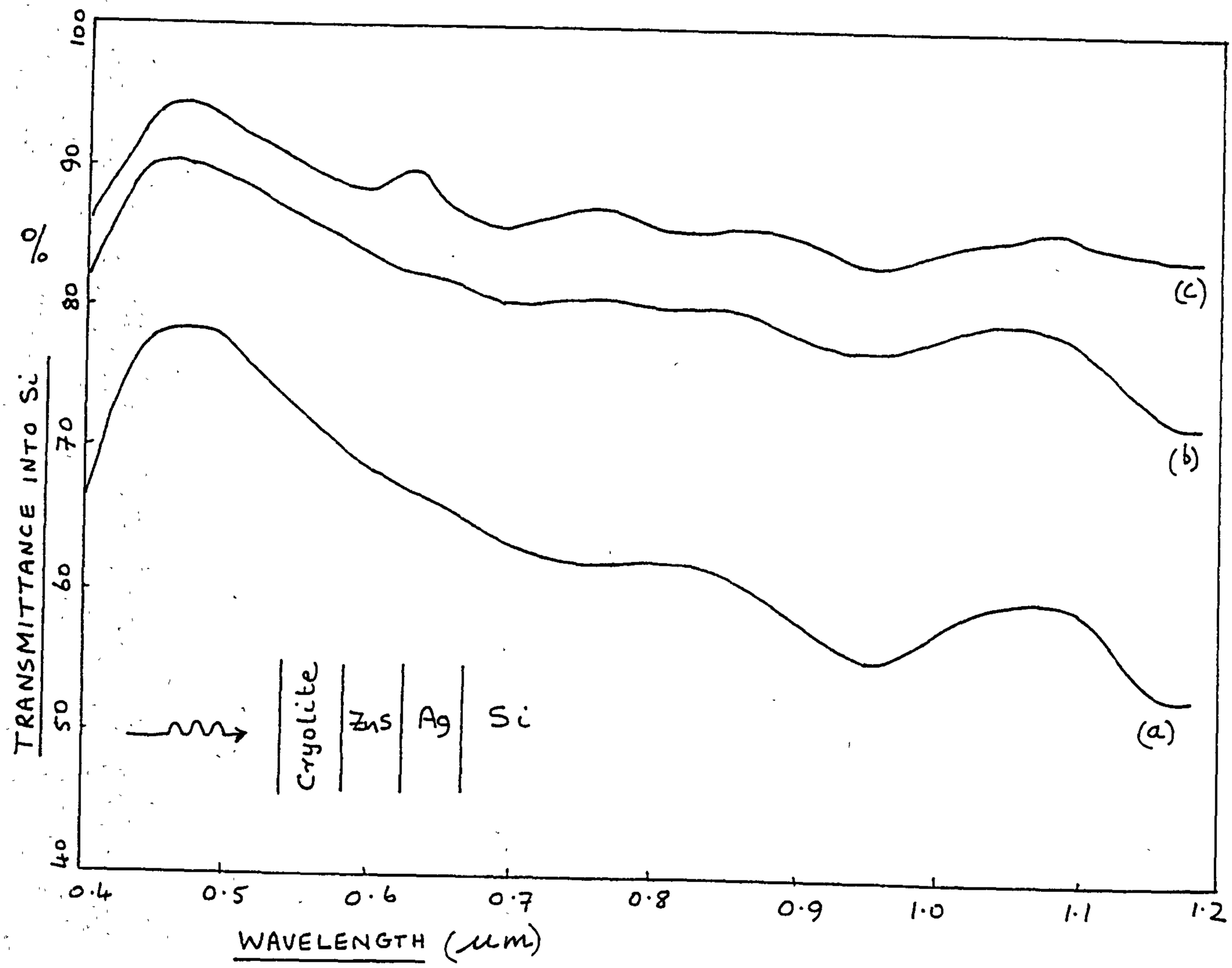

(a) Ag = 175 Å ; ZnS = 480 Å ; Cryolite = 1111 Å

(b) Ag = 120 Å ; ZnS = 480 Å ; Cryolite = 1111 Å

(c) Ag = 100 Å ; ZnS = 480 Å ; Cryolite = 1111 Å

FIGURE 6.32

Theoretical results

Ag on Si

Si thickness = 500 μm ; L = 100 μm ; $\tau = 2.5 \times 10^{-6}$ s.

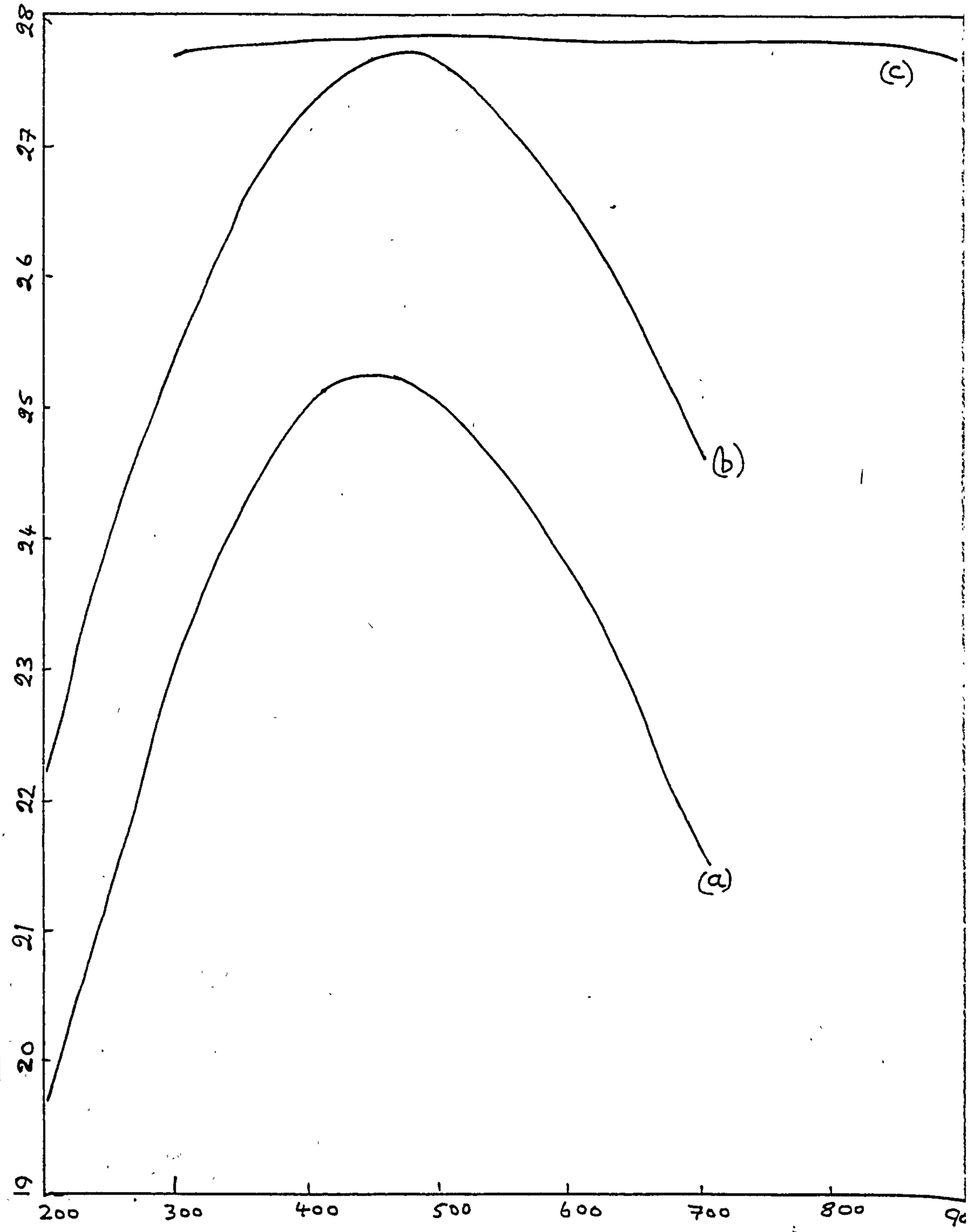

(a) Ag = 140 Å ; No Cryolite layer

(b) Ag = 100 Å ; No Cryolite layer

(c) Ag = 100 Å ; ZnS = 450 Å

FIGURE 6.33 Theoretical results

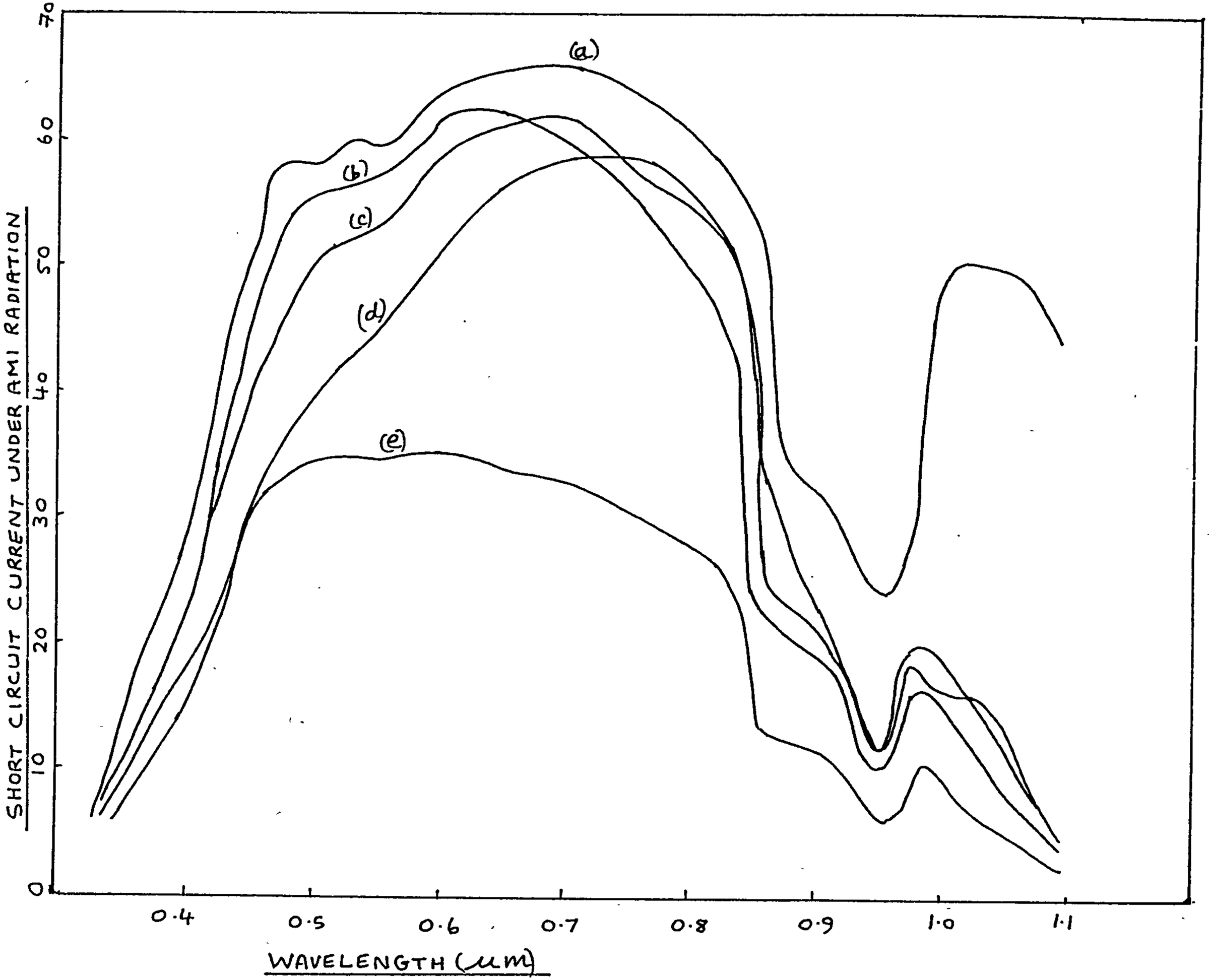

Ag on Si

Si thickness = 500 μm; L = 100 μm;
$\tau = 2.5 \times 10^{-6}$ s

(a) CURRENT EQUIVALENT OF AMI RADIATION

(b) Ag = 100 Å; ZnS = 450 Å; NO Cryolite

(c) Ag = 100 Å; ZnS = 450 Å;
Cryolite = 600 Å

(d) Ag = 100 Å; ZnS = 650 Å; NO Cryolite

(e) Ag = 100 Å; NO A.R. coating

FIGURE 6.34 Theoretical results

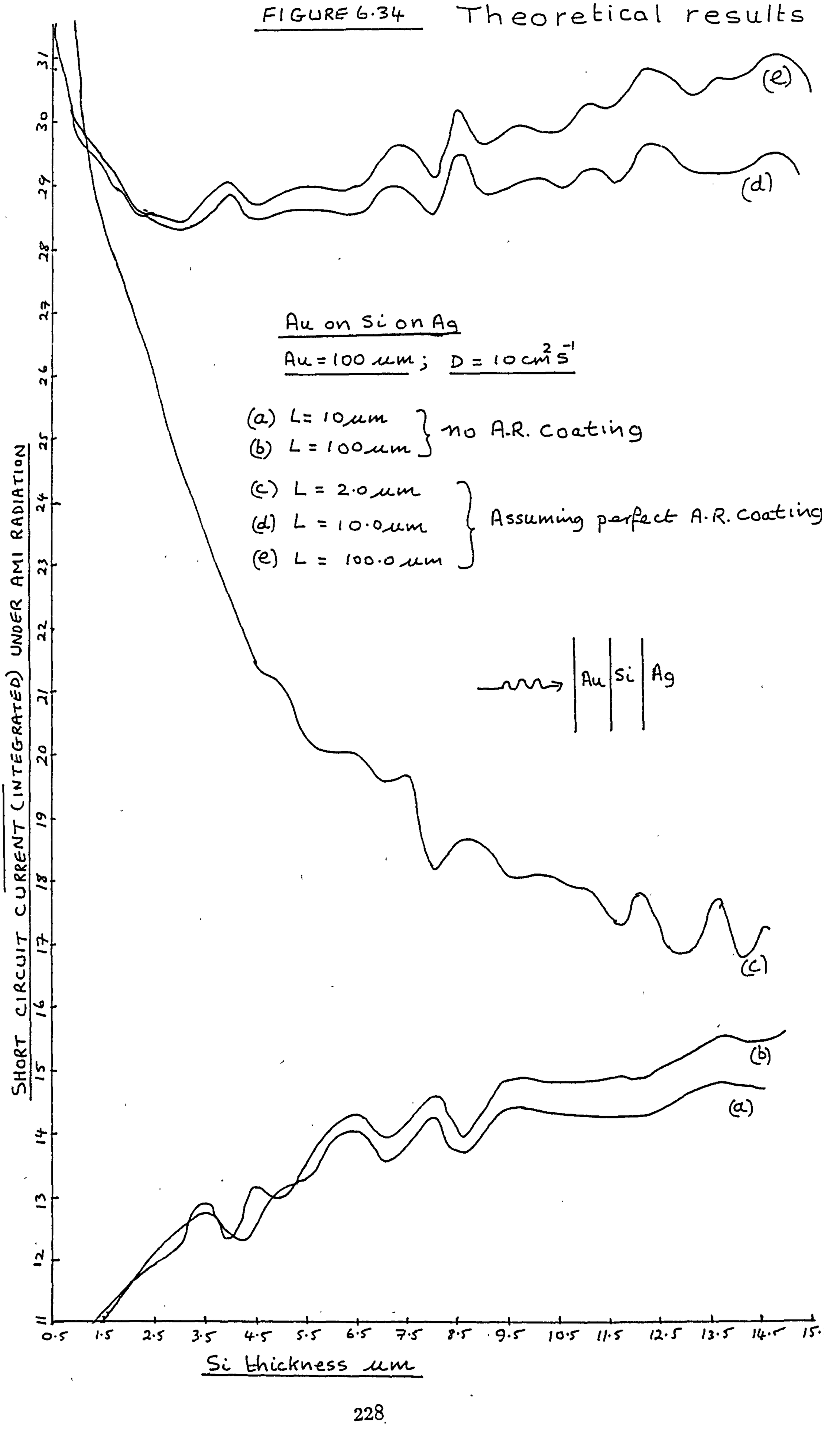

CHAPTER 7

COMPARATIVE RESULTS FOR SOME THIN FILM CELLS

In the following work the data for Copper Sulphide in the chalcosite phase (Cu_2S - CdS cells are most efficient in this phase) was taken from Mulder, (Mulder, 1973). The incident radiation was taken to be AMI in intensity and spectral distribution and the data of Thakoekora (Thakoekora, 1976) was used as in Chapter 5.

7.1 The Cadmium Sulphide-Cuprous Sulphide Cells

Figure 7.2 shows the short-circuit current as a function of the thickness of the cuprous sulphide layer for three values of electron diffusion length and for the two extreme conditions of system reflectivity: R = 0 assumes a perfect optical match to air i.e. all the incident radiation enters the first layer whilst for $R \neq 0$ the assembly has the reflectivity calculated for optically flat layers of the specified thickness, and the structure evident in these curves is due partly to the variation of reflectivity with Cu_2S thickness. The reflectivity of poly-crystalline films depends on their surface topography, and the surface roughness of films in solar cells gives rise to fairly low values of reflectivities. The peak currents shown in Figure 7.2 are larger than those calculated by Rothwarf (1975) and the optimum cuprous sulphide thickness are smaller. This is due partly to the choice of a silver substrate, but mainly to the effect of multiple passes of the light through the cuprous sulphide and the depletion layers, as can be seen in Figure 7.4.

The current depends critically on both the diffusion length and the surface recombination velocity, and Figure 7.3 shows the current at optimum cuprous sulphide thickness as a function of outer surface recombination velocity for three values of electron diffusion length. These results suggest that the diffusion length should be greater than 0.4μm and the surface recombination velocity less than about 10^4 cm.s^{-1} if efficient current collection is to be achieved, in broad agreement with the conclusions of Rothwarf (1975).

The importance of the optical properties of the back-surface contact is immediately apparent from Figure 7.4 which shows the photogenerated current as a function of cuprous sulphide thickness for silver, zinc and molybdenum substrate. The reflectivity of zinc and molybdenum is less than that of silver, causing the current to be lower, particularly at the smaller thicknesses.

Figure 7.5 shows a flying spot scan of the current from a dry-barrier formed cell with a molybdenum substrate, half of which was coated with silver. The increase in current on the side with the silver substrate is very evident, the increase being of the order of 20% - 30%, as would be expected from Figure 7.4 for a cuprous sulphide thickness of about 0.15μm.

7.2 The Cadmium Sulphide - Indium Phosphide Cell

The optical constants of indium phosphide used were those given by Seraphin and Bennett (1967). Figure 7.6 shows the photocurrent as a function of cadmium sulphide thickness for a range of minority carrier diffusion lengths for a configuration in which

the light enters through the cadmium sulphide. In all cases, it can be seen that a larger current is to be expected as the cadmium sulphide thickness is reduced.

The dependence of the photocurrent on the indium phosphide thickness is shown in Figure 7.7 for both silver and zinc back-surface contacts, and the advantages of using a silver substrate is again obvious.

The effect on the photocurrent of outer surface recombination velocity is shown in Figure 7.8, and it can be seen that this parameter is not critical for cadmium sulphide thickness greater than about 1μm.

7.3 The Cadmium Sulphide - Copper Indium Selenide Cell

The optical constants of copper indium selenide were not available, so they were calculated on the assumption of direct absorption and an energy gap of 1.eV. The electron mobility in copper indium selenide was taken to by 150 $cm^2V^{-1}S^{-1}$. Figure 7.9 shows the variation in photocurrent as a function of the thickness of copper indium selenide in a $CdS - CuInSe_2$ - substrate configuration. For a silver substrate the optimum copper indium selenide thickness is about the same as the optimum thickness of cuprous sulphide in the $CdS - Cu_2S$, but the effect of using a zinc substrate is even more pronounced.

The effect of varying the thickness of the cadmium sulphide layer is shown in Figure 7.10. The variations are similar to those for the $CdS - InP - Ag$ system, or for the $CdS - Cu_2S - Ag$ system and the effect of changing the minority carrier diffusion length is also similar.

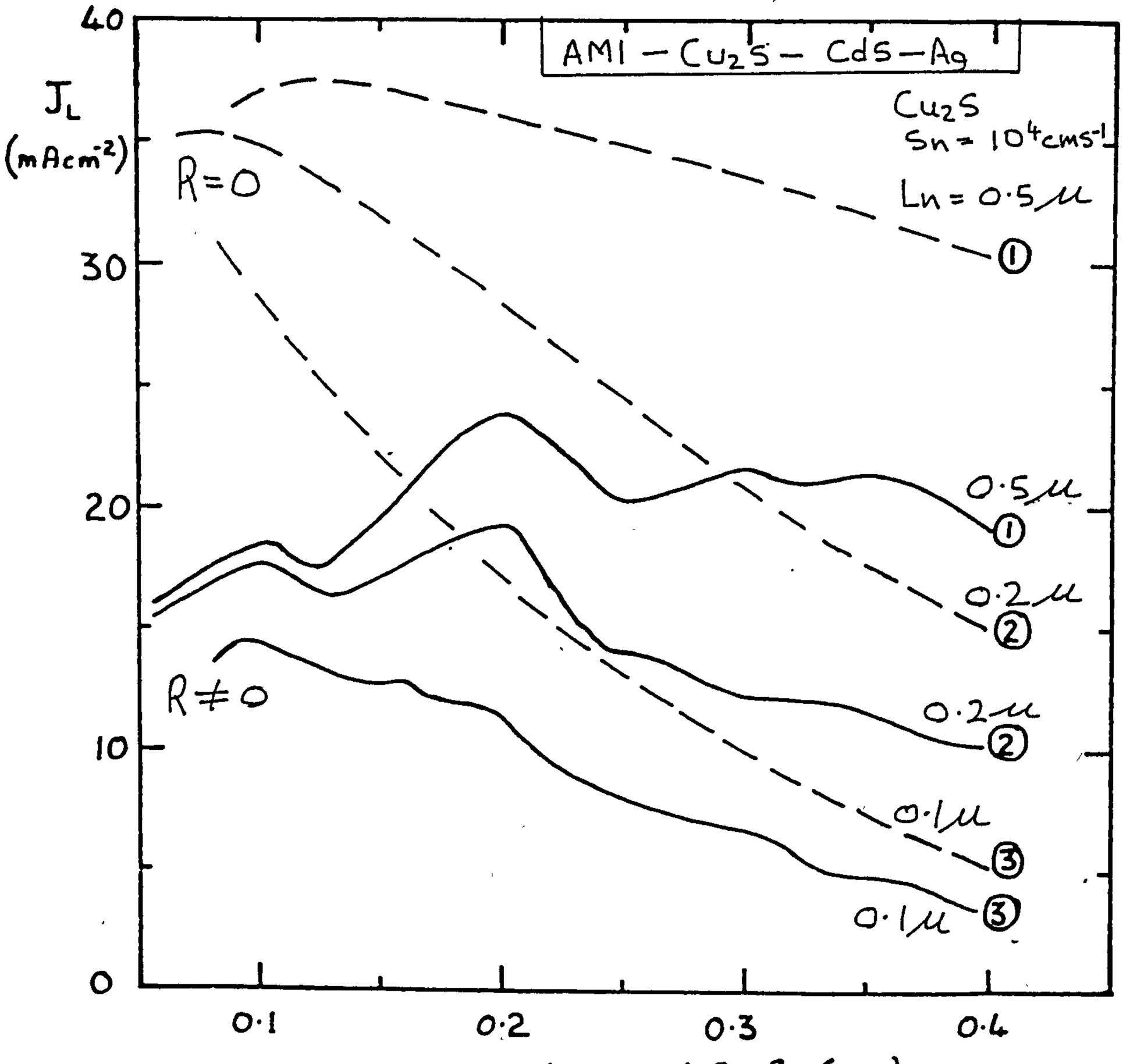

Figure 7.2 Current against Cu_2S thickness on 10 CdS

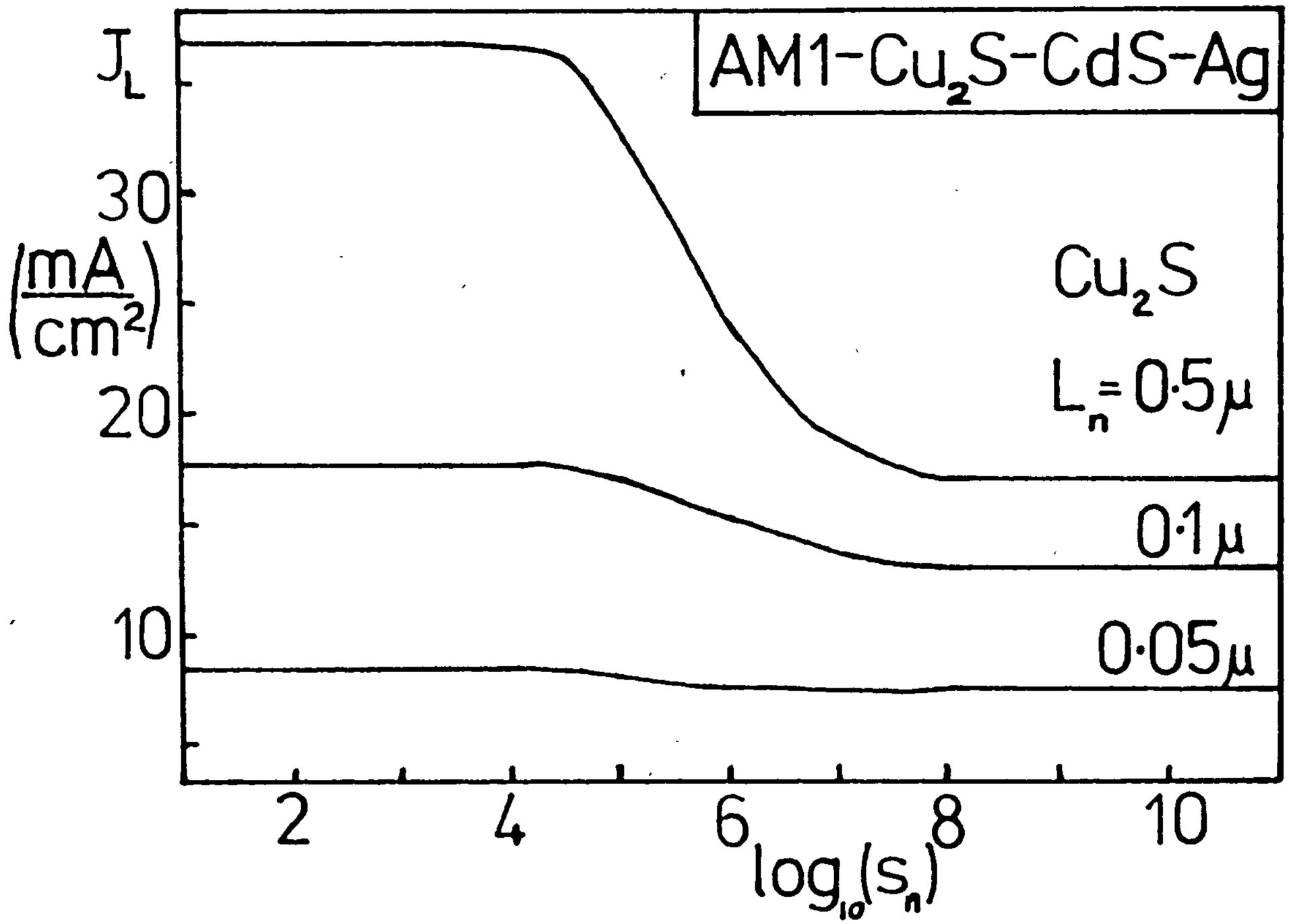

Figure7.3 Photogenerated current (mA cm^{-2}) as a function of outer surface recombination velocity (cm s^{-1}) for 0.2μ Cu_2S on 10μ CdS

on 10μ CdS

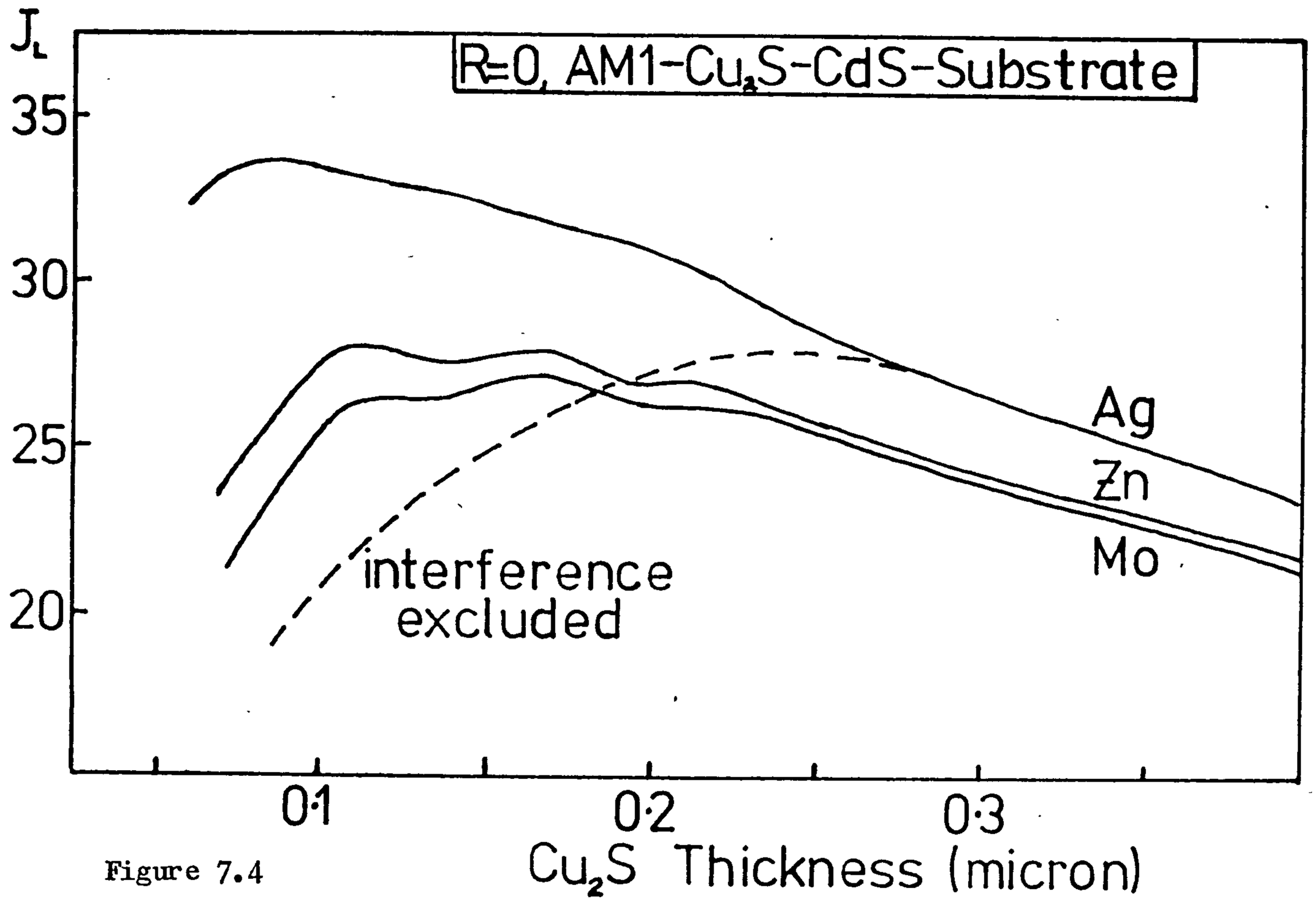

Figure 7.4

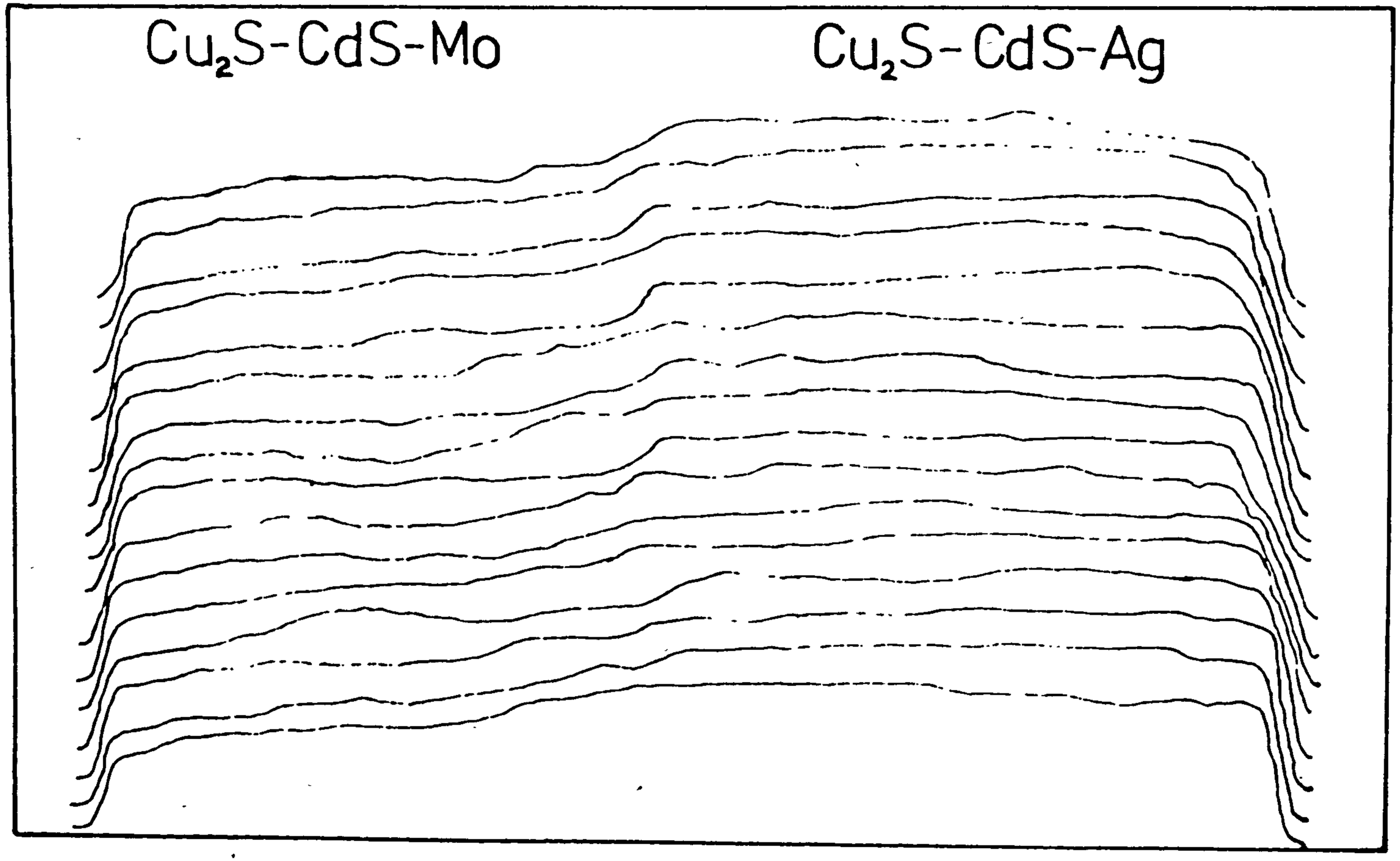

Figure 75 Flying spot scan across a cell with a half silvered molybdenum substrate.

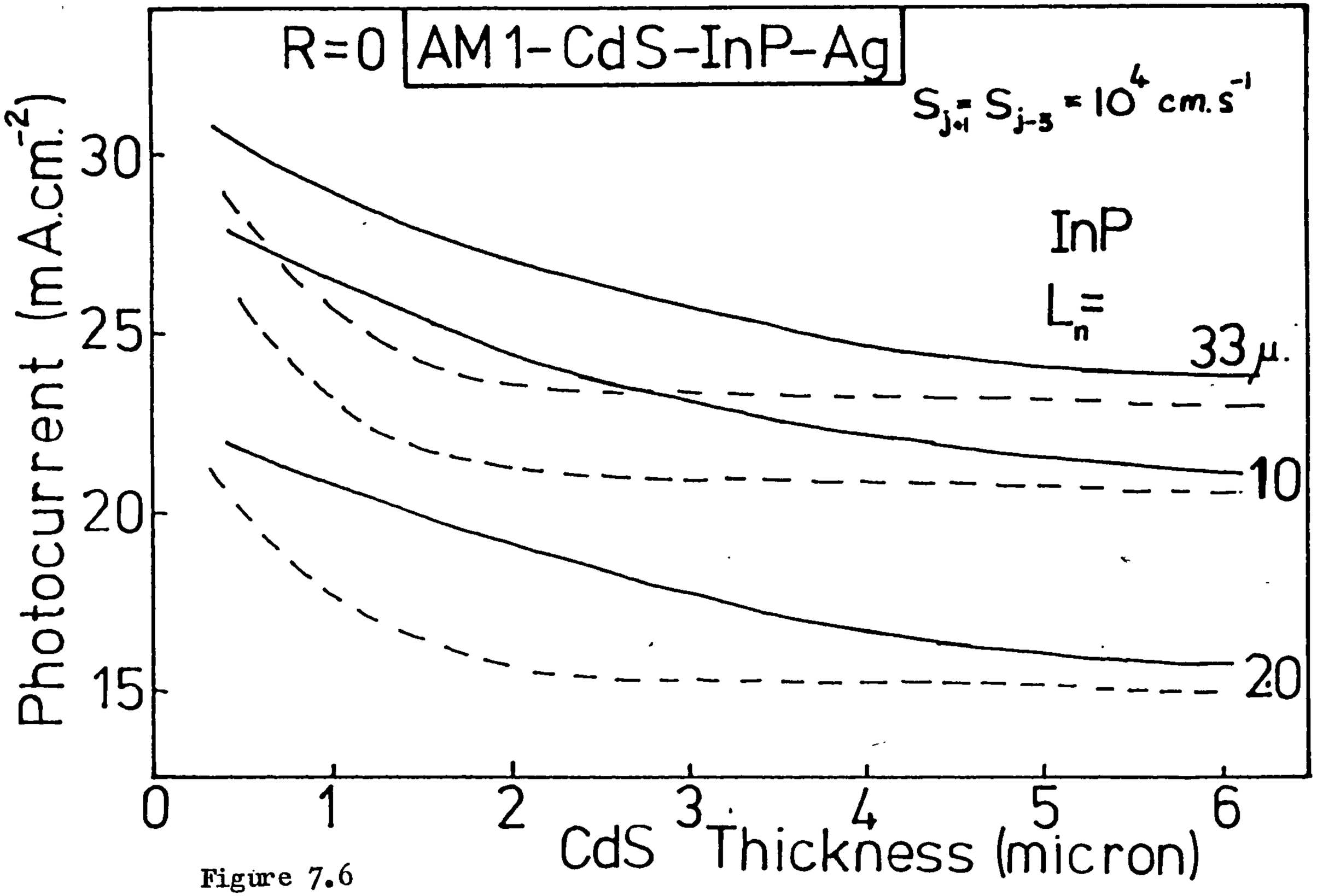
R=0
AM1-CdS-InP-Ag
$S_{j-1} = S_{j-3} = 10^4$ cm.s^{-1}
InP
L_n =
33 μ.
10
20
Photocurrent (mA.cm^{-2})
30
25
20
15
0
1
2
3
4
5
6
CdS Thickness (micron)

Figure 7.6

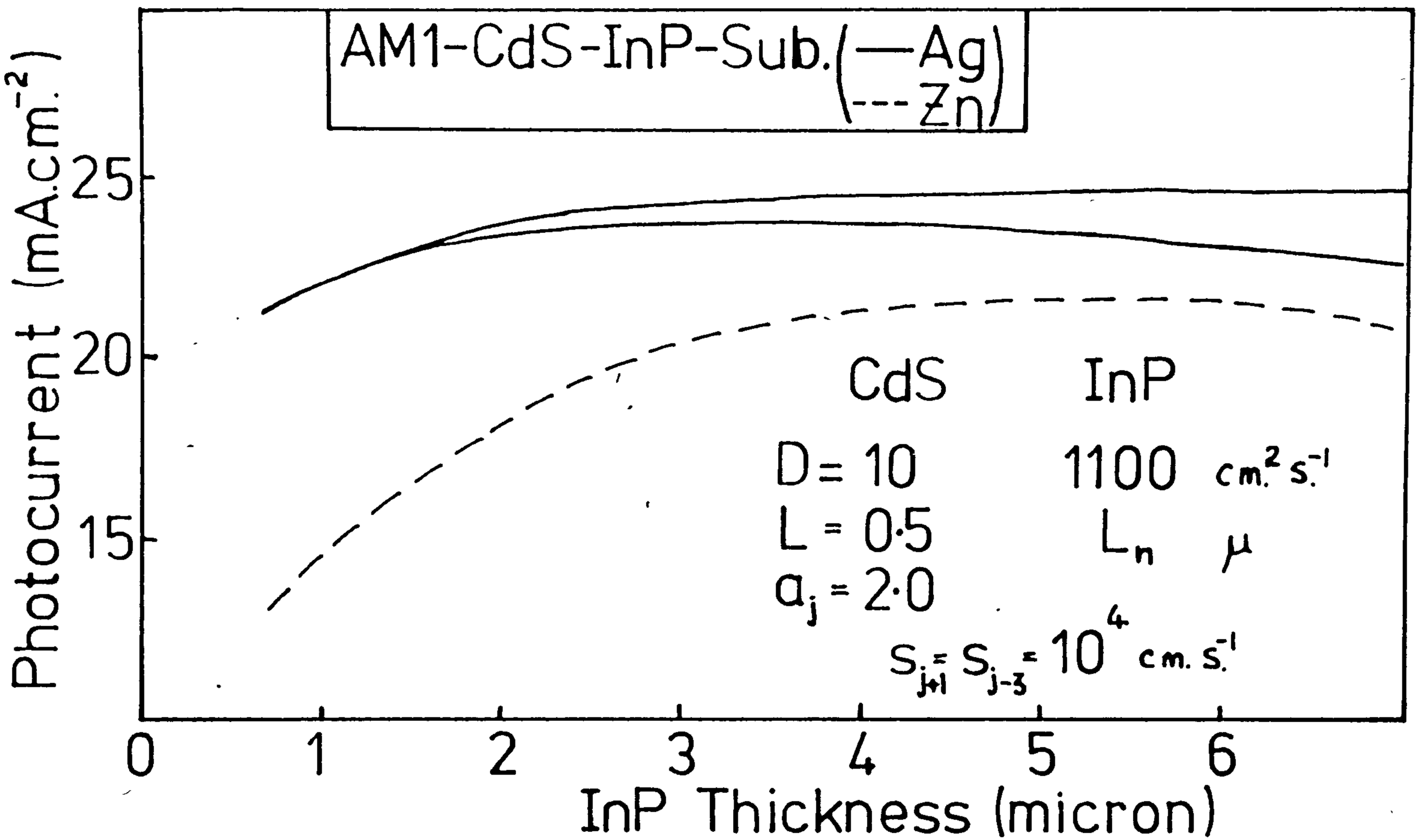

Figure7.7 Photogenerated current (mA cm^{-2}) as a function of InP thickness.

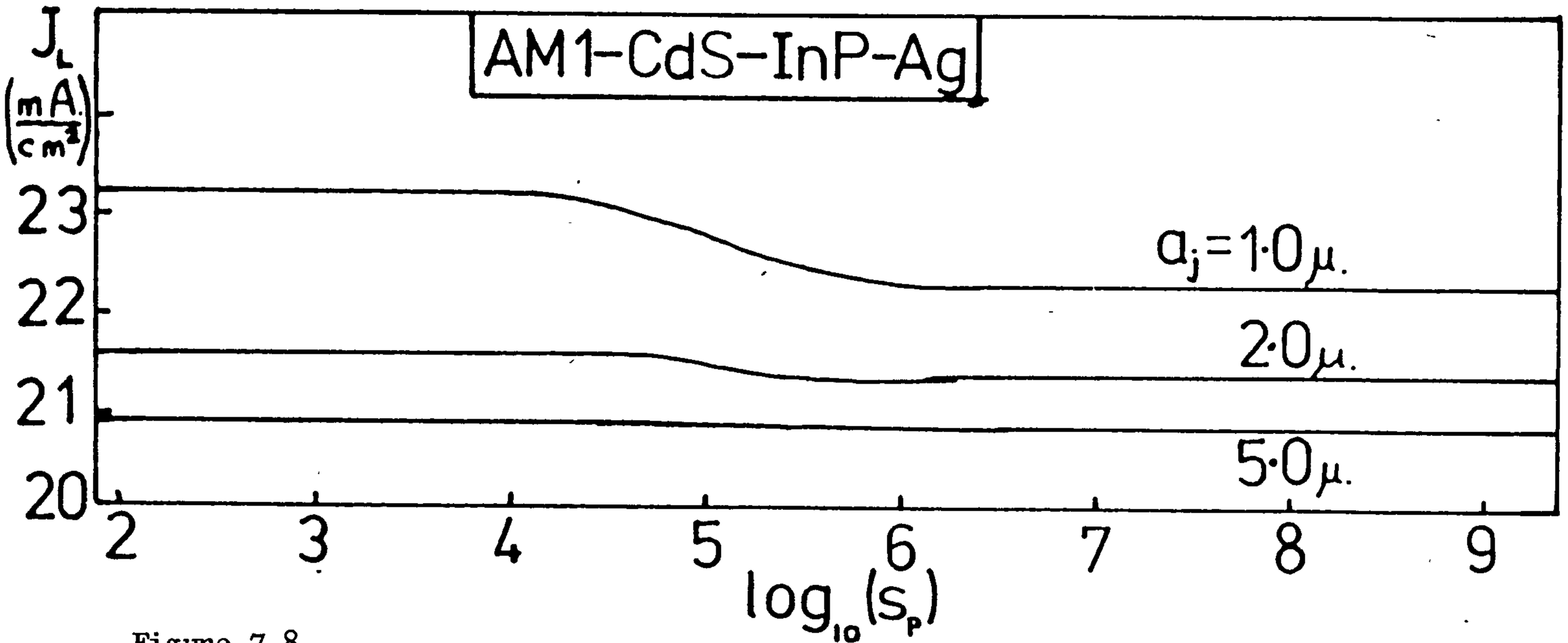
AM1-CdS-InP-Ag
J_L $\left(\frac{mA}{cm^2}\right)$
23
22
21
20
a_j=1·0μ.
2·0μ.
5·0μ.
2
3
4
5
6
7
8
9
$\log_{10}(S_p)$

Figure 7.8

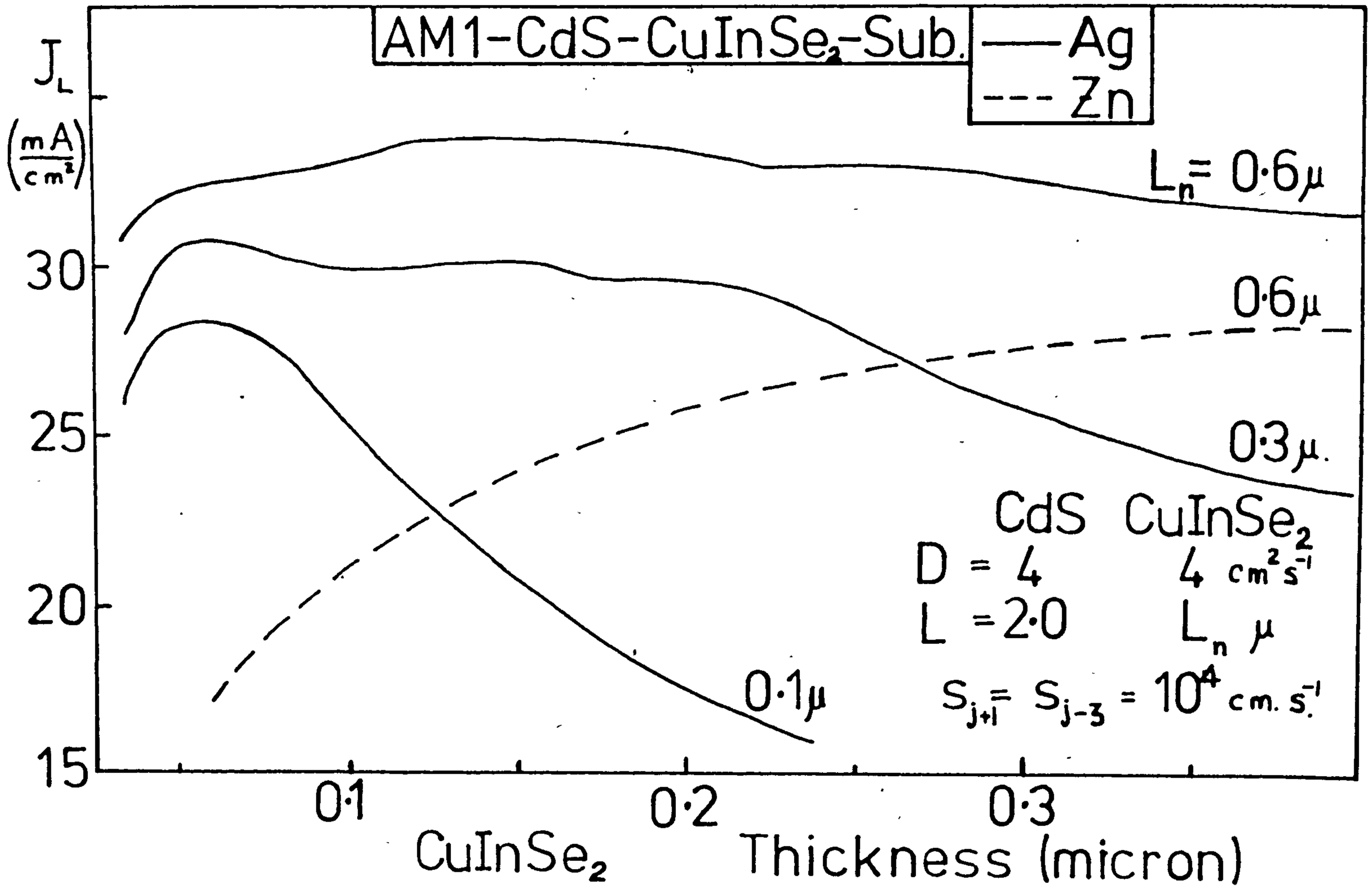

Figure7.9 Photogenerated current as a function of $CuInSe_2$ thickness for 2.0μ thick CdS

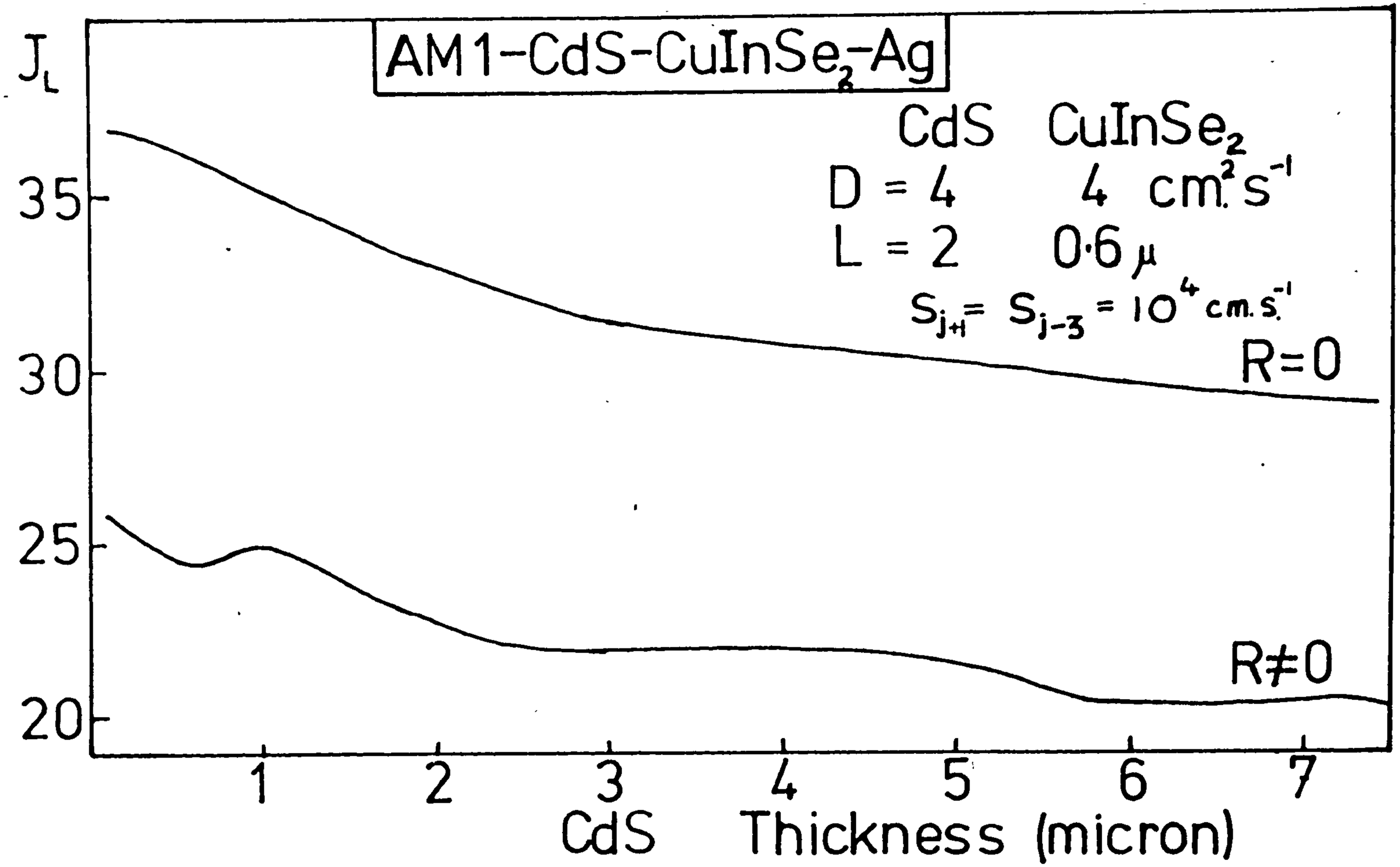

Figure7.10 Photogenerated current (mA cm^{-2}) as a function of CdS thickness for 0.2μ thick $CuInSe_2$.

CHAPTER 8

CONCLUSIONS

The work for this thesis was carried out in stages. In the first stage a general theory for thin film solar cells was developed taking into account the optical effects in thin films. Photogeneration rate as a function of position was computed by solving Maxwell's equations in a cell assumed to be composed of optically flat parallel layers. The photo current was next computed and the effects of varying the transport parameters, the substrate and layer thickness were observed for heterojunction thin film solar cells. In addition to the work on Cu_2S - CdS cells the other hetero-junction devices analysed were CdS - CuI Se_2 and CdS - InP cells.

Next, an analysis of the theory of anti-reflection coatings as applied to solar cells in general was carried out. This was followed by calculations for Schottky barrier cells. These cells are difficult to anti-reflect because the top metal layer absorbs light without making any contribution to the generation and collection of the photo current. Finally, an experimental programme on Schottky barrier cells was carried out to make some comparisons with the theoretical results. In addition to making supplementary apparatus necessary in the deposition of thin films in the vacuum chambers, a unit was specially con-structed and built for making spectral response and barrier height measurements.

Heterojunction Cells

The model of thin film solar cells presented in this paper predicts that the photogenerated current is significantly affected by interference effects within the cell and also by the optical properties of the substrate. The experimental evidence shown in Figure 7.4 offers strong support for the prediction that silver is a much better substrate material than molybdenum on purely optical criteria, but of course the substrate must also act as an ohmic contact and a nucleation surface for the inner layer, and these requirements also influence the choice of substrate material Boer (1977).

Boer (1977) has suggested that interference will play a very minor part in determining the photogenerated current in thin film solar cells, since the coherence of the wave fronts will be destroyed by strong scattering, and this does seem to occur in the 30μm - 50 μm thick CdS films used in "Clevite" type processes. In dry-formed cells using on 5μm-10μm thick CdS films, strong interference peaks from both the Cu_2S and CdS layers can be seen in transmission, and in these cells therefore the photogenerated current must be influenced by interference effects.

In a solar cell, the power output is decreased if the series resistance is too high. The sheet resistivity of the outer layer determines the grid requirement, and hence influences the power conversion efficiency and the cost of production (Hill, 1978). The Cu_2S thickness for optimum efficiency of Cu_2S-CdS cells may thus be somewhat greater than those shown in Figures 7.2 and 7.4 and the requirements of low sheet resistivity will determine the minimum thickness of CdS required in CdS-InP-Ag and CdS-$CuInSe_2$-Ag cells.

Anti-reflection Coatings on Solar Cells

It is clear from the results presented in the thesis that a simple anti-reflection coating can lead to a very significant increase in the intensity of radiation reaching the silicon depletion layer, and the resultant increase in electrical output has been observed many times by many workers. The use of multi-layer coatings does not seem to lead to a significant improvement in transmittance over that for a single layer coating for the materials considered, but it should be noted that although these materials are amongst the best optical coating materials available at present, their optical constants are not optimum for the AR coating of SB or MIS solar cells. For a 100 Å thick silver film on silicon, zinc sulphide is quite similar to the ideal material, but a coating with a higher refractive index would enable a thicker metal layer to be used whilst retaining the same transmittance, and this would be of great value in reducing the series resistance of large area cells. Unfortunately the high index materials tend to be absorbing and are thus unsuitable for use in optical coatings.

When designing an SB or MIS solar cell, it is relatively straightforward to calculate the transmittance into the silicon for any number of layers of insulator, metal or AR coating using the techniques described in Chapter Six provided that the optical constants are known. When metal layers only a few Å thick are used, these layers rarely show either continuous coverage or bulk optical constants, but the assumption of uniform planar layers with bulk optical constants seems to give a good first approximation in calculating an optimum AR coating. Once a coating material has been chosen with optical constants close to the calculated ideal values, the optimum thickness of a single layer coating can be

determined in practice by reflectance measurements during deposition, since for non-absorbing coating, maximum transmittance necessarily coincides with minimum reflectance.

The performance of the anti-reflection coatings discussed above and of all those so far used on SB or MIS cells, is poor compared to those on glass or semiconductor materials where high transmittance can be achieved over a wide wavelength range. The problem lies in the metal layers which have refractive indices with very small real parts, large imaginary parts and very high dispersion. It is therefore extremely difficult to design a coating which will give an effective refractive index which cuts the real axis on the Argand diagram close to unity over a wide range of wavelengths.

Experimental Work

The experimental work was carried out essentially to compare with the theoretical results. Schottky barrier cells were chosen to compare the AR coating theory, being particularly difficult to anti-reflect because of the metal layer.

Electron beam evaporation, thermal evaporation and ion-plating techniques were utilised in the fabrication of Schottky barrier cells. When monitoring the deposition of either the silver or the zinc sulphide films, it is often convenient to monitor the layers deposited on a pyrex glass substrate close to the silicon slice. Theoretical curves for silver on glass, silver on silicon and zinc sulphide on Ag/glass were calculated assuming the layers are of uniform thickness with optical constants equal to the bulk values. It has been found that these conditions are most closely met if the layers are ion-plated or deposited carefully by electron beam evaporation. Thermally evaporated films thicknesses around 100 Å have optical constants

which differ significantly from the bulk values and silver films of 100 Å thickness have many pin-holes. Ion-plated silver films have a much smaller pin-hole density and this would seem to be the better deposition method.

The experimental transmittances were approximately 10 to 15% below the theoretical ones, and this could be explained by the incorrect refractive index and extinction coefficient values being used when making the theoretical calculations.

The results of the experiment support the theoretical predictions that multilayer anti-reflection coatings on a Schottky barrier cell do not significantly improve the output.

The peak spectral response was roughly doubled by the single ZnS AR coating. This was in agreement with the theoretical predictions.

The high values for the diode factors (Table 6B) for the thermally evaporated Schottky barrier solar cells suggested that the single thermionic-diffusion theory by itself is insufficient to explain the current mechanisms.

The ion-plated diode results would be explained more closely by the thermionic emission theory with diode factors of 2.2 in the dark and 1.7 in the light (Table 6B). The different values in the diode factors when biased electrically and by the light involved appear to agree with the qualitative assessments of Card and Yang (1976) who pointed out that the interface charges are different in the two cases.

The experimental results for thermally evaporated silver on glass both with and without ZnS coatings compare well with the results of Anderson et al (1976).

Conclusion

For the first time a theory for solar cells has been presented which takes into account optical interference within the solar cells. The results of the theory were very significant and showed that as a result of enhanced absorption of light due to optical interference, current collection is improved compared to models of cells in which interference effects are excluded. The optical properties of the substrate were also shown to affect significantly the current collected. The experimental evidence presented in Chapter 7 supports the theory of thin film solar cells presented in the thesis.

The theory for anti-reflection coatings on solar cells (chapter 6 and Gandham et al 1979) shows for the first time why it is not possible to anti-reflect the solar cell completely and enables one to calculate the maximum limit of transmittance into the device and the corresponding ideal refractive indices and thicknesses for the anti-reflection coating. It thus allows one to use the optically closest available material for anti-reflecting that particular solar cell. Oxide layers in Schottky barrier cells were shown to be of negligible significance optically on the photogenerated current.

The experimental results would suggest that the ion-plating technique can produce thin, yet continuous metal films compared to the other methods (evaporation, electron beam) in the fabrication of Schottky barrier cells. The ion-plating technique should also produce AR coatings which are more robust and with greater adhesive properties.

The general theory for the thin film solar cell can initially be used for optimising the short circuit current by optically

matching the component layers of the device to produce maximum absorption of the light as close as possible to the depletion region of the cell. The complex refractive index for the whole assembly can then be calculated from a knowledge of the optical parameters of the device layers. The AR coating theory presented in Chapter 6 can then be used for calculating the optimum AR coating for maximum transmittance into the cell. The actual deposition of the AR coating could be monitored by observing the reflectance of the whole assembly. As pointed out in Chapter 6 the maximum transmittance into the cell will necessarily coincide with minimum reflectance.

In the case of a Schottky barrier cell where the optical properties of the top metal layer may not necessarily be the same as the metal bulk properties, the effective refractive index for the whole cell including the metal thin film could be measured experimentally using ellipsometry. The effective refractive index could then be fed into the AR coating theory and the optimum AR coating for the cell calculated from the point of matching the material and thickness for maximum transmittance into the cell.

The optimum AR coating does not necessarily produce zero reflectance but results in a reflectance value below which it is theoretically not possible to reduce.

Again for the first time the theory for the "interference" cell was extended to include constant electric fields and equations for calculating the photogenerated currents in such a cell have been presented. The analysis was further extended to obliquely incident light.

It is possible to carry out further work based on this thesis.

Computation of the equations for the photogenerated current in a cell with impurity gradients can be carried out. It is expected that the photogenerated current would rise as a result of these gradients but they are also likely to cause a rise in the dark currents in thin film solar cells thus cancelling each other out. The existing theory can be extended to include junction fields thus presenting an even fuller picture of a solar cell.

If one could measure the insolation in a particular geographical area then "optimisation techniques" could be used for calculating an ideal refractive index and thickness over an extended wavelength range for that particular region by incorporating the equations already presented in the "optimisation programme". The entire work could be extended for obliquely incident light.

REFERENCES

ANDERSON R. L., Solid State Electronics 5, 341 (1962).

ANDERSON W. A., Delahoy A. E., Milano R. A., Applied Optics 15, 1621 (1976).

BOER K. W., Phys. Stat. Sol. (a) 40, (2) 355 (1977).

CARD H. L., Yang E. S., Applied Phys. Lett. 29, 57 (1976).

CHOO S. C., Solid State Electronics 11, 1069 (1968).

CUMMEROW R. L., Physics Rev. 95, 16 (1954).

CASPERD A. N., Phd. Thesis, Newcastle upon Tyne Polytechnic (1979).

DE VOS A., Energy Conversion 16, 69, (1976).

DOLEGA U., S. Naturforsch, 18, 653 (1963).

EVANS D. A. and P. T. Landsberg, Solid State Electronics 6, 169 (1963).

DALE F. and P. Smith, J Applied Phys. 27, 777 (1956).

ELLISS B. and Moss, Solid State Electronics, 13, 1, (1970).

* GANDHAM B., Hill R., MacLeod H. A. and M. Bowden, Proceedings of the EEC Photovoltaic Conference in Luxembourg p.1121 (1977).

GODLEWSKI M. P., Baraona C. R. and Brandhurst, 10th PVSC 1973, p.212 Ref.38.

HEAVONS O. S., "Optical Properties of Thin Solid Films", Butterworths, London (1954).

HILL R. "Thin Film Solar Cells" in "Active and Passive Thin Film Devices" (1978) Academic Press.

HOVEL H. J., "Semi Conductors and Semi Metals" Vol.II Academic Press N.York (1975).

HOVEL H. J., J Applied Physics 47, 4968 (1976).

ILES P. A., J Vac. Science Techn. 14, 1100 (1977).

KOSSELL et al "Physics of Thin Films" Vol.5, 1 (1969).

LANDSBERG P. T., Solid State Electronics 18, 1043 (1975).

LANDSBERG P. T., and Klimpke, Proc. Royal Soc. London A 354, 101 (1977).

LOFERSKI J. J., J Applied Phys. 27, 777, (1956).

LOFERSKI J. J., and Wysocki, RCA Rev. 22, 38 (1961).

MACLEOD H. A., "Thin Film Optical Filters", Adam Hilger, London (1969).

MACLEOD H. A., Optica Acta 19, 1 (1971).

* GANDHAM B., Hill R., MacLeod H. A. and M. Bowden, Solar Cells Vol.1 1, (1979).

MAKOTA et al, J Applied Physics 46, 8 (1975).

MALLINSON J. R. and P. T. Landsberg, Proc. R. Soc. London A355, 115-130 (1977).

MARTINUZZ I. S. and O. Mallen, Phys. State Solid, (a) 16, 339 (1977).

MILNES A. G. and D. L. Feucht "Heterojunction and Metal Semi Conductor Junctions" Academic Press (1972).

MOSS T. S., Solid State Electronics 2, 222 (1961).

MOSS T. S., "Optical Properties of Semi Conductors" Butterworth, London (1959).

MULDER B. J., Phys. State Solid (a) 13, 79, (1972), 15, 409, (1973).

NEWMAN P. C., Electronics Letters 1, 265, (1965).

PRINCE M. B., J Applied Phys. 26, 534 (1955).

RAPPAPORT P., RCA, Review 21, 373 (1959).

RIBEN A. R. and D. L. Feucht, Solid State Electronics 9, 1055 (1966).

ROTHWARF A., 13 IEEE Photovoltaic Specialists, Conference, Washington DC (1978).

ROTHWARF A., Int. Workshop on CdS Solar Cell P.9 NSF-RANN AER 75-15858.

ROTHWARF A. and K. W. Boer, Prog. Solid State Chem. 10, 71 (1975).

SAH C. T., Noyce R. N. and Schokly, Proc. Inst. Radio Eng. 45, 1288 (1957).

SCHNEIDER M. V., Bell System Tech. Journal 45, 1611 (1966).

SHARMA B. L. and R. K. Purohit, "Semi Conductor Heterojunctions" Pergamon (1974)

SERAPHIN B. D. and H. E. Bennett, "Semi Conductors and Semi Metals" Vol. III Academic Press N.York (1967).

STIRN R. J. and Y. L. M. Yeh, Proc. 10th Photovoltaic Specialists Conference Pages 15-24 IEEE N.York (1974).

STERN M., Solid State Physics Vol. 15 (1963) Academic Press.

SZE, "Physics of Semi Conductor Devices" Wiley (1969).

THAKAEKORA M. P., Proceedings of Symposium on Solar and Energy Utilisation Washington (NASA Goddard Space Flight Centre, Greenbelt Md. 1974).

VAN OPDORP J. M., Thesis Technische Hogeschool Eindhoven (1969).

WANG E. Y., Yu F. T. S., Simms V. L., Brandhurst H. W. and J. D. Broder. Proceedings 10th Photovoltaic Specialists Conference Pages 168-173 IEEE N. York (1974).

WOLF M., Proc. IRE 48, 1246 (1960).

WOLF M., Proc. IEEE 51, 674 (1963).